Connecting the Observed Properties of Exoplanet Populations to Their Formation

CONNECTING THE OBSERVED PROPERTIES OF EXOPLANET POPULATIONS TO THEIR FORMATION

By

MATTHEW J. ALESSI, M.SC.

A Thesis Submitted to the School of Graduate Studies in Partial Fulfillment of the Requirements for the Degree of Doctor of Philosophy in Physics

McMaster University

Descriptive Note
DOCTOR OF PHILOSOPHY (PHYSICS and ASTRONOMY) 2020
McMaster University (Physics and Astronomy) Hamilton, Ontario
AUTHOR: Matthew J. Alessi, M.Sc. (McMaster University)
SUPERVISOR: Dr. Ralph E. Pudritz
NUMBER OF PAGES: xvii, 271

Abstract

The wealth of exoplanetary data as displayed on the mass-semimajor axis and mass-radius distributions reveal a tremendous amount of information constraining our understanding of their formation. We link the variety of outcomes shown in exoplanet populations to the observed ranges of protoplanetary disk properties using the core accretion model of planet formation. For this purpose, we consider a population synthesis framework that samples disk properties' observationally-constrained distributions as inputs to thousands of planet formation models. Planet traps are a key feature of our approach in that they are barriers to rapid type-I migration, and are sites of early stages of the core accretion process in our models. We show that a low setting of forming planets' atmospheric envelope opacities $\kappa_{\rm env} \simeq 10^{-3}$ cm^2 g^{-1} is necessary to achieve a range of gas giants' orbital radii that agrees with the data. At this low setting of $\kappa_{\rm env}$, X-ray ionization and its related dead zone results in a clear separation between hot Jupiters and warm gas giants near 1 AU. When radial dust drift is included in our models, the rapid migration of solids into the ice line makes it a crucial trap for the formation of super Earths and warm gas giants. The ratio of the formation frequency of these two planet types has an interesting dependence on the initial disk radius R_0, with intermediate $R_0 \simeq$50 AU producing the largest super Earth population, and both larger and smaller disk sizes forming more gas giants. When including disk chemistry, the range of disk radii over which planet formation in traps occurs leads to a wide range of solid compositions, from ice rich planets (up to 50% ice by mass) to dry, Earth-like compositions. We show planet compositions and post-disk atmospheric photoevaporation to be two key factors affecting the mass-radius distribution of our populations.

Co-Authorship

Chapters 2, 3, and 4 of this thesis contain original scientific research written by myself, Matthew Alessi. In each of these chapters corresponding to accepted or submitted papers with listed co-authors, I was the primary writer and corresponding author, leading the development of the theoretical framework and analysis of results. All calculations have been performed by me, with the exception of the contributions of co-authors, which are listed below.

Chapter 2 of this thesis has been published as an article in the peer-reviewed journal Monthly Notices of the Royal Astronomical Society (MNRAS). The reference to this work is,

Alessi M., & Pudritz R. E., 2018, MNRAS, Volume 478, pp. 2599-2617.

My supervisor, Prof. Ralph Pudritz, is the second author of this paper. Prof. Pudritz assisted in the direction of this research, interpretation of results, and aided with writing during the editing process.

Chapter 3 of this thesis has also been published as a peer-reviewed article in MNRAS. The reference to this work is,

Alessi M., Pudritz R. E., & Cridland A. J., 2020, MNRAS, Volume 493, pp. 1013-1033.

My supervisor, Prof. Ralph Pudritz is the second author, and assisted with writing in the editing process, and contributed to the development of the paper through assisting in the direction of research and interpretation of results. Dr. Alexander J. Cridland is the third author, who is credited with merging the dust evolution code with the framework of our protoplanetary disk model. Dr. Cridland also assisted with running the dust evolution code.

Chapter 4 of this thesis has been published as a peer-reviewed article in MNRAS. The reference to this work is,

Alessi M., Inglis J., & Pudritz R. E., 2020, MNRAS, Volume 497, pp. 4814-4833.

The second author, Julie Inglis, is credited with running the planetary structure and atmospheric

photoevaporation calculations that are presented in chapter 4. J. Inglis contributed to the writing of portions of the model section in chapter 4 that are related to planetary structure and atmospheric photoevaporation: sections 4.2.3, 4.2.4, Appendix B, & Appendix C. J. Inglis is also credited with creating figure 4.4 in section 4.2.3. The third author is my supervisor, Prof. Ralph Pudritz, who is credited for his role in contributing to the development of this work through his assistance in the direction of research and interpretation of results. J. Inglis & Prof. Pudritz also aided with editing during the writing process.

All previously published material has been reformatted to conform to the required thesis style. I hereby grant an irrevocable, non-exclusive license to McMaster University and the National Library of Canada to reproduce this material as part of this thesis.

Acknowledgments

There are many people to whom I express my gratitude for their support throughout this thesis. I would first of all like to thank my supervisor Prof. Ralph Pudritz for his mentorship during my graduate studies at McMaster. I look back fondly over the years we have worked together, and through this time your guidance, patience, and expertise has been paramount to my development as a scientist. Your passion for astrophysics has been a consistent source of inspiration for me, and I am proud of the work we have achieved together.

I also thank the members of my supervisory committee, Profs. James Wadsley and Christine Wilson. Your individual perspectives on this project provided great insight and guidance. I thank Dr. Yasuhiro Hasegawa for many beneficial discussions and exchanges over the course of this thesis, and for hosting my visit to Caltech and NASA JPL during my Ph. D. studies. I also thank Prof. Yann Alibert for his time spent as my thesis' external examiner and the insightful comments he provided.

I thank all my fellow office mates, research group members, and graduate students, both past and present, for the camaraderie and lasting memories of office shenanigans and doing our best on the softball field with Liquid State. I particularly thank Samantha Benincasa, Alex Cridland, Corey Howard, & Ben Pearce for the emotional support, helpful scientific discussions, and for putting up with my puns (for which at least 1 in 10 were good; but I cannot ask them to thank me here for those, because *thesis* my acknowledgements section, after all). I also extend my thanks to all other members and staff of the McMaster Physics & Astronomy department for making it such an enjoyable work environment. To the secretarial staff and the members of RHPCS computational support, thank you for all your hard work in making our day-to-day lives run smoothly.

Outside of the department, I thank all my friends and family for their love and support during my studies. I thank my parents, John and Tamara, my sister Danielle, and my mother-in-law Marlene

for their support and encouragement in my education.

Finally, I extend my deepest gratitude to my wife Janelle, who has stood by my side through all of this. You are my constant source of inspiration, emotional support, and encouragement, and I would be lost without you. Thank you for always believing in me, and for everything you do to make our lives better. September 2016 not only marked the start of my PhD, but also the month where you surprised me with our adored dog Luna. You have kept me grounded when my studies were overbearing, and the achievements I have made over recent years is a testament to how strong I feel with you by my side. I love you.

"Let the truth of love be lighted, let the love of truth shine clear.

Sensibility, armed with sense and liberty.

With the heart and mind united in a single, perfect, sphere."

Cygnus X-1 Book II: Hemispheres, Rush, Hemispheres, 1978

–Neil Peart (1952-2020)

Contents

List of Figures

List of Tables

List of Acronyms & Abbreviations

AD	Ambipolar Diffusion
ALMA	Atacama Large Millimeter/submillimeter Array
AU	Astronomical Unit
DSHARP	Disk Substrutures at High Angular Resolution Project
M-a	Planetary mass - semimajor axis (e.g. M-a diagram/distribution)
MHD	Magnetohydrohynamics
M-R	Planetary mass - radius (e.g. M-R diagram/distribution)
MRI	Magnetorotational instability
SPHERE	Spectro-Polarimetric High-contrast Exoplanet REsearch
TESS	Transiting Exoplanet Survey Satellite

Chapter 1

Introduction

Beyond our Solar system, over 4000 planets orbiting other host-stars have been discovered. These planets' properties, such as their masses, orbital radii, and sizes, display a tremendous amount of diversity, many of which contrast significantly with planets of the Solar system (Borucki et al., 2011a; Batalha et al., 2013; Rowe et al., 2014). This diversity challenges our understanding of what a typical planetary system's properties are. From a formation standpoint, how is such a large range of planet properties achieved?

In the standard nebular hypothesis, planet formation takes place in protoplanetary disks surrounding stars in their final stages of formation. In very recent years, images of these disks' dust distributions have been obtained with *ALMA* (i.e. ALMA Partnership et al. 2015) and *SPHERE* (i.e. van Boekel et al. 2017). These observations have revealed a striking amount of substructure in disks, such as gaps, rings, and asymmetries. Remarkably, each of these features can be caused by the presence of forming planet(s) (Jang-Condell & Turner, 2012; Dong et al., 2015b), and thus may be regarded as indirect observations of planet formation "in action". Additionally, protoplanetary disks themselves are seen to possess a range in properties, such as masses and radii, that will directly influence outcomes of planet formation.

The goal of this thesis is to connect the observed diversity in disk and exoplanet properties through planet formation theory. From an observational standpoint, the timeline of planet formation is bracketed on either end, with initial formation conditions revealed through disk observations and exoplanet properties exhibiting outcomes of planet formation processes. Our planet formation theory will therefore be constrained by the data in its ability to use measured ranges of disk properties

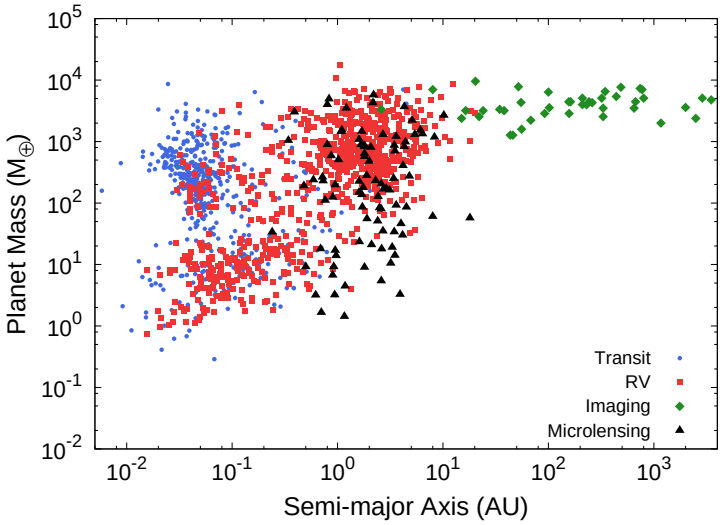

Figure 1.1: The observed planet mass semi-major axis diagram is shown, while indicating each planets' initial discovery method. Clusters of data points indicate the existence of different planet classes such as super Earths, hot Jupiters, and warm Jupiters. These data were compiled using the NASA exoplanet archive (https://exoplanetarchive.ipac.caltech.edu/), current as of May 27, 2020.

as inputs and achieve correspondence with the observed distribution of exoplanet properties. As exoplanet and disk observations are then paramount in our understanding of planet formation and shaping our theory, we will first outline the main results of these observations here.

In figure 1.1, we start by presenting a key diagram that reveals many results of exoplanetary observations: the mass semi-major axis (hereafter M-a) diagram. Regions in the M-a space with a high density of data points indicate the existence of planet populations (Chiang & Laughlin, 2013). For example, we see a collection of data points indicating the existence of gas giants with masses $\gtrsim$ 100 $M_\oplus$ at small orbital radii $a_p \lesssim 0.1$ AU. This M-a region corresponds to the population of hot Jupiters, having masses comparable to the Solar system gas giants, but orbital radii smaller than the closest planet to the Sun, Mercury. At somewhat larger orbital radii, we see another collection of massive planets $M_p \gtrsim 100$ $M_\oplus$ with orbital radii $0.6 \lesssim a_p \lesssim 6$ AU. This population, referred to as warm Jupiters, is the largest population of gas giants, which indicates that planet formation produces massive planets near $a_p \sim 1$ AU as opposed to very short period orbits, as is the case for hot Jupiters.

By far the largest collection of data points on the M-a diagram corresponds to low-mass planets

($\sim$ 1-30 $M_\oplus$) with orbital radii between 0.01-1 AU. These low-mass planets are referred to as super Earths ($1 \lesssim M_p \lesssim 10$ $M_\oplus$) and Neptunes ($10 \lesssim M_p \lesssim 30$ $M_\oplus$). As the M-a diagram shows this planet class to be the most numerous, it indicates that planet formation produces many more low-mass super Earths as opposed to massive gas giants.

In figure 1.1, we show each planets' discovery method, most of which are initially detected through the radial velocity or transit method. In the case of the radial velocity method, planet detection takes place through measuring the host-star's periodic motion about the planet-star centre of mass. The period and amplitude of the host-star's radial velocity curve can be used to determine the planet's orbital period and mass ($M_p \sin i$, modulo the inclination angle i of the system which is often unknown), respectively. Since the radial velocity of the host star about the centre of mass is induced by the planet's gravity, it will be biased to the detection of massive, close-in planets, as these will induce the largest radial velocity amplitudes. This bias strongly favours the detection of hot Jupiters, for instance. Conversely, low-mass planets, or planets on large orbits are harder to detect as they induce small motions in their host-stars. In these examples, the planets' radial velocity signals can become comparable to the detection limit, set by telescope measurement error and stellar motions (pulsation and/or surface convection) that add noise to a star's radial velocity in the absence of planet-induced motions (i.e. see Lovis & Fischer 2010).

The transit detection method corresponds to observing a periodic temporary decrease in the host star's measured flux, caused by a planet crossing the face of the host-star and blocking a fraction of the light in the case of a system observed nearly edge-on. The amount of light blocked is proportional to the planet's surface area $\propto R_p^2$. By measuring the fractional decrease in the stellar flux, one can discern the planet's radius R_p, with the period of transits indicating the planet's orbital period. The transit method will be biased, then, to the detection of large planets which block larger fractions of light from the host star. In the case of sufficiently small planets, the fractional decrease in the stellar light curve from transits will be small and comparable to the detection limit. This is set by noise in the star's light curve, caused by telescope stability and stellar variability (Howard et al., 2012). Additionally, small orbital periods are also favoured in the transit method as they require the host star to be monitored for a shorter time-duration.

While the radial velocity method was used to make some of the first exoplanet discoveries (Mayor & Queloz, 1995; Butler & Marcy, 1996; Marcy & Butler, 1996), the majority of exoplanets have been discovered with the transit method, owing to the *Kepler* space-based mission, designed to detect

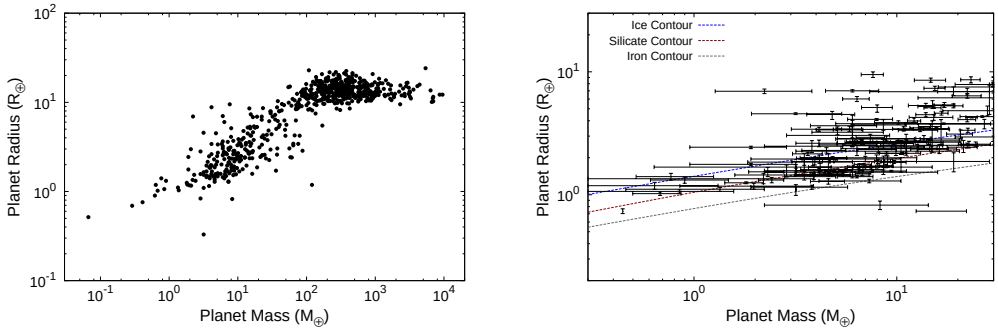

Figure 1.2: **Left:** The observed exoplanet mass radius diagram is shown across the full range of planet masses. **Right:** We show the low-mass range of the mass-radius distribution, including observational uncertainties. We include M-R contours corresponding to uniform composition models to illustrate the observed sample's range in mean densities. These data were compiled using the NASA exoplanet archive, current as of May 27, 2020.

Earth-like planets around Sun-like stars (Koch et al., 2010; Borucki et al., 2011b). The *Kepler* mission detected the majority of known exoplanets, and revealed the large number of super Earths and Neptunes previously mentioned. Current and future observations from *TESS* (the Transiting Exoplanet Survey Satellite) will continue to improve our understanding of exoplanets through additional transit detections, particularly around M-dwarf stars (Barclay et al., 2018).

In figure 1.2, we plot another key exoplanet diagram; the mass-radius (hereafter *M-R*) diagram. When both a planet's radius and mass have been measured (through a transit and radial velocity observation, respectively), the mean density can be deduced, and is most clearly shown through the M-R diagram. Particularly in the low-mass range, planets display a range of radii, and therefore a range of mean densities at any given mass.

We highlight the interesting variety in mean densities among low-mass planets by plotting mass-radius curves corresponding to uniform composition models computed with planetary structure calculations (discussed further in section 1.4, and chapter 4 Appendix B). These three solids - iron, silicate, and ice - are the standard categories of solid materials present in the Solar nebula available for planet formation, with ice being the lightest material and iron being the densest. These contours, therefore, estimate the maximum and minimum planet radius that can be achieved at a given mass, assuming the planet is composed of only solid materials. The observed data's distribution with respect to these contours shows that, for a subset of planets, the range in planet radius (or mean density) at a given mass can be attributed to a range in solid compositions.

However, a portion of the observed data lies at a larger radius than the M-R ice contour. As ice is the lightest solid material available for forming planets, this therefore indicates the presence of a gaseous envelope on a significant portion of these planets. In the case of planets with atmospheres, (which, if present, set a planet's transit radius in the upper atmospheric layers - defined where the optical depth to stellar radiation is roughly unity), differences in planet radii are achieved through differences in atmospheric scale height. The scale height is set by the planet's surface gravity (i.e. its mass), and its temperature as set by its proximity to its host star. In this regard, a planet's total mass, atmospheric mass, and orbital radius - all resulting from planet formation - play a key role in setting the atmospheric scale height and overall radius of a planet.

In figure 1.3, we show a third key exoplanet diagram: the eccentricity - semi-major axis relation. A planet's eccentricity $0 \leq e \leq 1$ indicates the degree to which its orbit deviates from that of a perfect circle (e=0) with high values of e indicating a highly eccentric, non-circular orbit. A planet's orbital eccentricity can be inferred through deviations in the host star's radial velocity curve from a perfectly sinusoidal profile that corresponds to a circular orbit. In sufficiently high-e orbits, however, planets will have small perihelion distances (defined as the closest planet-star distance during a planet's orbit) and tidal dissipation from the host-star's gravity will reduce the orbital eccentricity. This leads to an upper-limit on e at a given a_p, as indicated in figure 1.3 by the dashed line, which has been estimated by assuming significant tidal dissipation at a perihelion distance of 0.03 AU.

The eccentricity - semi-major axis diagram shows that exoplanets display a wide range of orbital eccentricities. At a given a_p, planet eccentricities range from 0 (circular orbits) to high e values near the orbit's upper-limit. These rather high eccentricities can be contrasted with the Solar System planets that have nearly perfectly circular orbits, with the mean orbital eccentricity among Solar system planets being e=0.06 (Winn & Fabrycky, 2015). As we will discuss further in section 1.2, planet formation in the protoplanetary disk phase is expected to result in near-circular orbits, and planet eccentricities (driven, for example, by mutual gravity between multiple forming planets) are exponentially damped by torques from disk material (i.e. see review in Kley & Nelson 2012). On this basis, high planet eccentricities allude to the effects of post-disk phase dynamics. For example, gravitational scattering of one or more planets that form in a system can lead to the remaining planet(s) acquiring a high e from the gravitational exchange (Chatterjee et al., 2008). The exoplanet eccentricity distribution indicates that such dynamics effects that drive high planet eccentricities are common.

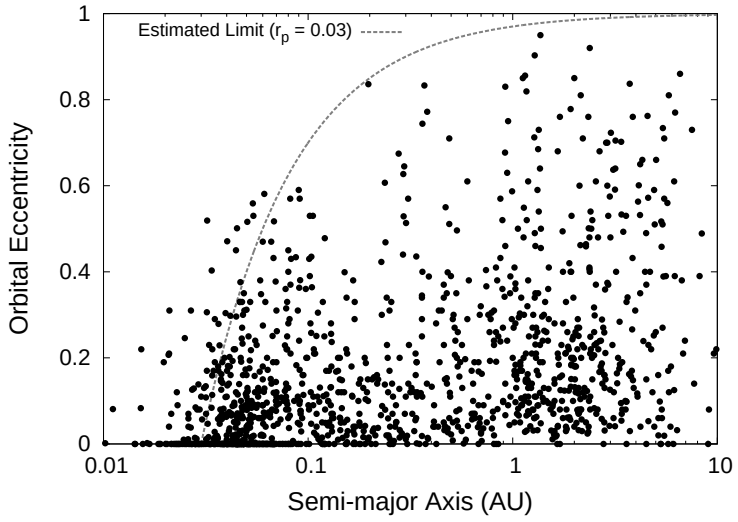

Figure 1.3: The observed eccentricity - semi-major axis relation is plotted. The dotted line indicates a perihelion distance of 0.03 AU, used to estimate an upper-eccentricity limit where tidal dissipation damps high-eccentricity orbits. Across the full range of orbital radii, planets display a wide range of eccentricities from circular orbits up to near this high-eccentricity limit. These data were compiled using the NASA exoplanet archive, current as of May 27, 2020.

The biases in the observational methods through which planets are detected are an important factor to consider when interpreting the above exoplanet distributions. For example, both the transit and radial velocity methods (that have detected the vast majority of known exoplanets) are biased to detecting massive planets on short orbits. These biases result, for example, in detecting hot Jupiters in figure 1.1 at a higher frequency than what is truly present in a random, unbiased sample of stars. Is the separation between the hot and warm Jupiter populations truly present in exoplanet populations, or is this caused by the high detection rates of hot Jupiters due to observational bias? Additionally, gas giants at large orbital radii $a_p \gtrsim 10$ AU are detected via direct imaging, and figure 1.1 shows that there are a small number of these planets observed. The observed frequency of large-period gas giants raises the question if planets at such separations from their host stars truly are rare, or if their small number of detections is also a result of observational biases.

Occurrence rate studies provide insight on the above questions by combining the observed exoplanet frequencies with knowledge of each detection method's observational biases to estimate true, unbiased planet occurrence rates. The understanding of detection methods' biases can be applied, for example, throughout the planetary mass semi-major axis space to correct the observed frequen-

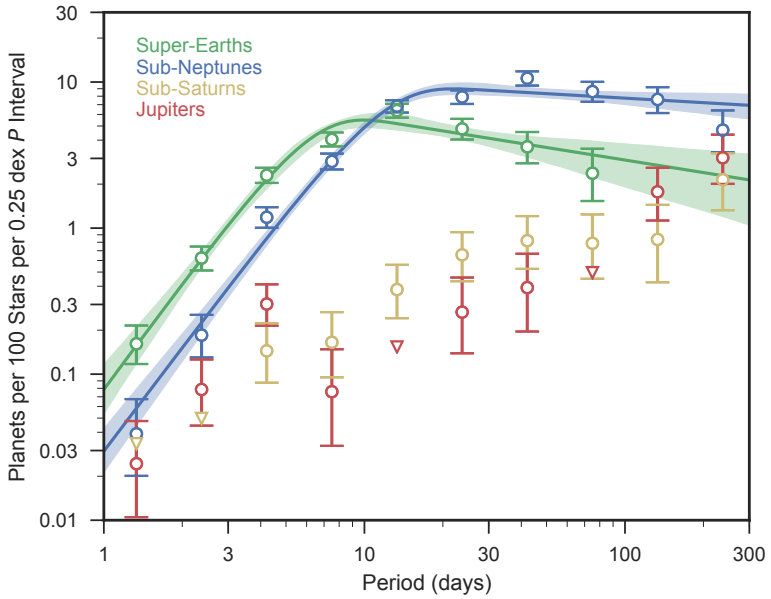

Figure 1.4: The planet occurrence rate - orbital period relation is shown for *Kepler* planets, binned into four planet mass categories. Reproduced with permission from Petigura E.A., Marcy G.W., Winn J.N., et al., 2018, AJ, 155, 89. DOI:10.3847/1538-3881/aaa54c, figure 7, ©AAS.

cies throughout the M-a diagram. This bias-correction was done on the *Kepler* data set by The California-Kepler Survey, where high spectral-resolution observations of planet hosting stars in the *Kepler* sample were performed to accurately measure stellar properties, reducing observational uncertainties on planet transit radii (Petigura et al., 2017; Johnson et al., 2017).

In figure 1.4 we show a result of this survey, where we plot planet occurrence rate vs. orbital period (related to semi-major axis through Kepler's third law) for four different planet classes (Petigura et al., 2018). In the case of super Earths and Neptunes, their occurrence rates are seen to increase until a period of about 10 days, with roughly a constant (or shallow decreasing with orbital period) occurrence rate at larger orbits. The occurrence rate profiles of sub-Saturns and Jupiters are roughly a power-law with steady increase with orbital period, a result also found in Santerne et al. (2016). The Jupiter occurrence rate profile shows that, when corrected for observational bias, hot Jupiters are indeed more rare than warm Jupiters at larger orbits $\sim$ 1 AU. Such a conclusion is not readily obtained from the uncorrected M-a data. There is a slight decrease in the occurrence rate near 10 days ($\sim$ 0.1 AU), but the orbital radius-extent of this decrease is smaller than what is indicated through the separation between the hot- and warm-Jupiter populations in the M-a diagram. We

note that the *Kepler* host stars require multiple transits to be observed and are therefore limited by the extent of the mission, resulting in an upper-limit to orbital periods of 300 days ($\sim$ 0.9 AU).

The above result can be complemented by occurrence rate studies for radial velocity observations whereby planets at larger orbital radii can be detected, as was done for the Keck doppler survey in Cumming et al. (2008) and Bryan et al. (2016). While Cumming et al. (2008) find that the gas giant occurrence rate increases with orbital radius up to $a_p = 3$ AU, Bryan et al. (2016) find that the occurrence rate of gas giants decreases with orbital radius for $a_p >$ 3-10 AU. The combined result of these two papers shows that the occurrence rate of gas giants reaches a maximum in the $a_p \simeq$ 3-10 AU range, indicating that the warm Jupiter population is, in fact, the largest population of gas giant planets. This result can be discerned from the uncorrected M-a data, although the hot Jupiter and warm Jupiter populations appear much more comparable in frequency. Additionally, the above result of Bryan et al. (2016) (analyzing data for which gas giants at orbits out to 20 AU were detectable through radial velocity) shows that the occurrence rate of long-period gas giants are indeed more rare than warm Jupiters after the observations are bias-corrected.

We now highlight key observational findings pertaining to protoplanetary disks. As disks are the formation environment for planets, understanding their properties is crucial for constraining planet formation timescales. Our understanding of planet formation is being transformed through recent highly-resolved (sub-)mm disk images revealing solid dust distributions and substructures.

In figure 1.5, we show a grid of mm-disk observations for disks in the DSHARP (Disk Substructure at High Angular Resolution Project) survey observed with ALMA (Andrews et al., 2018). This sample of disks displays an exceptional amount of substructure such as gaps, rings, and asymmetries. These features can reveal underlying processes taking place within disks, such as the presence of forming planets that cannot be directly observed. Alternatively, they can be related to disk features or instabilities that cause inhomogeneities in the dust distribution (not related to planets). Gaps, for example, have been linked to the position of volatile condensation fronts (Zhang et al., 2015). However it has been ruled out that all observed gaps coincide with volatile ice lines, as gap locations do not scale with host-star luminosity (van der Marel et al., 2019). Under the assumption that gaps are formed through planet-disk gravitational torques, gap positions and widths have been used to constrain forming planet masses and orbital radii (i.e Dong & Fung, 2017). The suite of observed disks in figure 1.5 also shows that this sample of disks possesses a range of dust radii.

In figure 1.6, we further explore the range in disk radii from both an observational and numerical

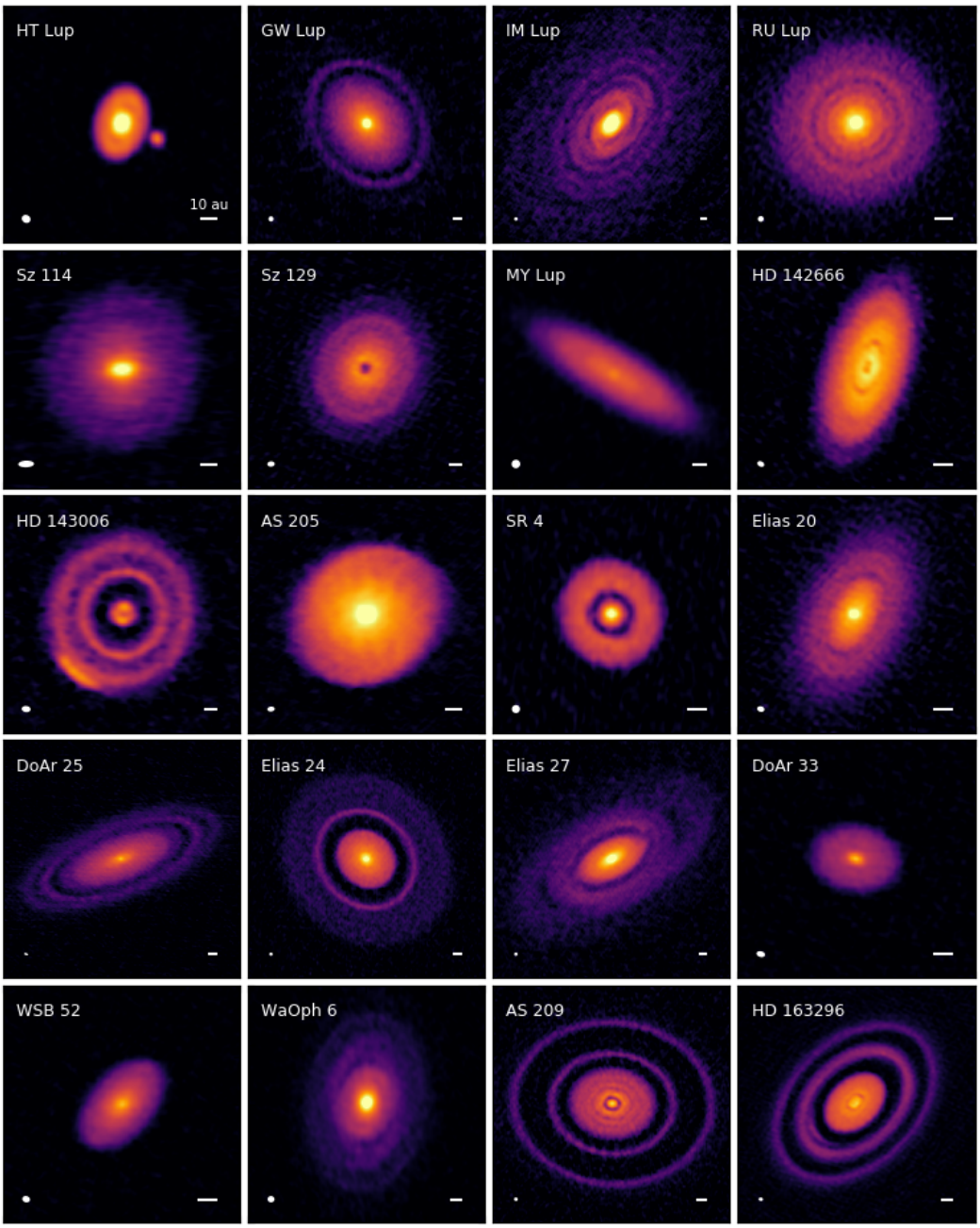

Figure 1.5: A suite of protoplanetary disks observed in the DSHARP survey, revealing a range of disk sizes, and features including gaps, rings, and asymmetries. The x- and y-axes (not shown in the image) correspond to the angular offsets from the disks' centres (offsets in right ascension $\Delta\alpha$ and declination $\Delta\delta$, respectively). These are unique for each image, ranging from $\pm$ $\sim$1 milliarcseconds to $\pm$ $\sim$a few 100 milliarcseconds (see a complete listing in Huang et al. 2018b). Beam sizes and 10 AU scale bars are shown in the bottom left, and bottom right corners of each panel, respectively. We refer the reader to Andrews et al. (2018) for a full listing of beam angular dimensions corresponding to each image, ranging from $\sim$ 50-130 milliarcseconds. Reproduced with permission from Andrews S. M., Huang J., Pérez L. M., et al., 2018, ApJ, 869, L41. DOI:10.3847/2041-8213/aaf741, figure 3, ©AAS.

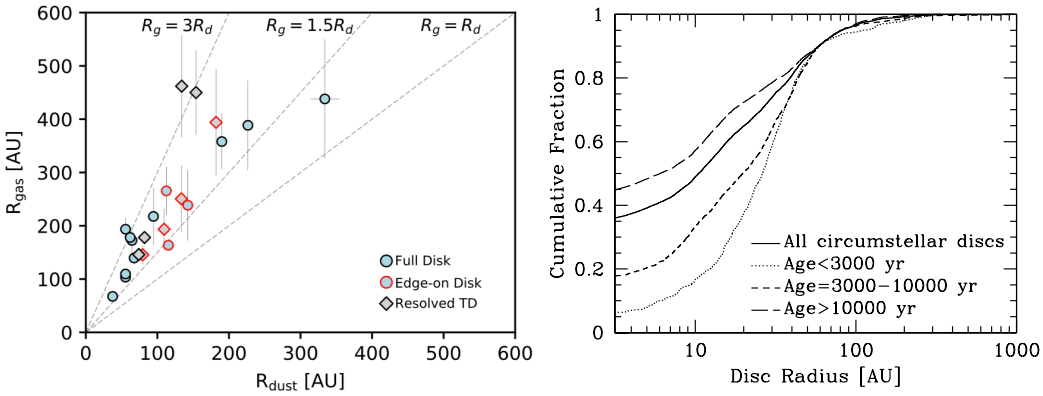

Figure 1.6: **Left:** The observed gas and dust disk radii of Lupus protoplanetary disks are shown, revealing a range in both quantities and a scaling of $R_{\rm gas}$ ∼1-3$R_{\rm dust}$ in the sample. Reproduced with permission from Ansdell M., Williams J.P. Trapman L., et al., 2018, ApJ, 859, 21. DOI:10.3847/1538-4357/aab890, figure 8 (top left panel), ©AAS.
Right: The cumulative distribution of protoplanetary disk radii resulting from a suite of hydrodynamic core collapse models is shown, also revealing a range of disk radii from formation. Reproduced with permission from Bate, M. R., 2018, MNRAS, 475, 5618. DOI:10.1093/mnras/sty169. Figure 14 (top, centre panel).

perspective. The left panel shows gas and dust-disk radii in the Lupus sample observed with ALMA in Ansdell et al. (2018), probing the dust through mm-emission and the gas through CO isotopologue lines. This figure not only shows that there is a range in both observed gas and dust disk radii, but that they scale with the gas disk radius $R_{\rm gas}$ being 1-3 times larger than the dust disk radius $R_{\rm dust}$. While modest differences in gas and dust disk radii have been attributed to optical depth effects (Facchini et al., 2017), large discrepancies with $R_{\rm gas} \gtrsim 3R_{\rm dust}$ indicate a large degree of grain growth and/or radial dust drift that transports solids from the outer disk inwards - mechanisms we will further explore in section 1.1.2.

The right panel of figure 1.6 shows a cumulative distribution of disk radii resulting from simulations of protoplanetary disk formation involving the hydrodynamic collapse of protostellar cores (Bate, 2018). This figure shows that a wide range of disk radii is also achieved from a numerical approach. As we will discuss further in section 1.1, MHD effects (specifically, magnetic braking), can have a significant effect on protostellar collapse models and resulting disk radii (Tomida et al., 2015; Masson et al., 2016). Nonetheless, both pure hydrodynamic and MHD collapse models produce an interesting range of disk radii, a result also found from observations. Since this quantity (along with disk mass) directly influences planet formation timescales, its observationally and numerically inferred range will lead to an interesting variety in planet formation outcomes.

High-resolution disk images have recently allowed direct observation of planet formation as it's taking place, such as in the PDS 70 (Keppler et al., 2018) and MWC 297 (Ubeira-Gabellini et al., 2020) systems. However, as direct observation of planet formation is not feasible aside from select cases, planet formation theory is relied upon to connect the two endpoints of observational data: protoplanetary disks and exoplanet distributions. Furthermore, the tremendous amount of data pertaining to disks and exoplanets that has become available in recent years provides invaluable constraints on planet formation models.

The goal of this thesis is to develop a complete picture of planet formation that includes key mechanisms that shape the M-a and M-R relations such as planet migration, dust evolution through radial drift, disk chemistry, and post-disk atmospheric mass loss. Our theory will be shaped in its ability to connect the observed protoplanetary disk and exoplanet data. Throughout this thesis, we use the method of planet population synthesis whereby thousands of planet formation models are computed, in which we sample from observationally constrained distributions of host-star and disk data. We thus achieve comparisons between full distributions of computed and observed planet populations. Through these comparisons, and use of the available observational constraints, we are able to not only investigate key mechanisms of the planet formation process and their effect on the M-a and M-R distributions, but also constrain parameters and timescales related to these various aspects of our model.

The remainder of this thesis chapter will give a synopsis of our approach, outlining observational and theoretical constraints. We organize as follows: In section 1.1, we give an overview of modelling protoplanetary disk evolution, including disk chemistry, and dust evolution; section 1.2 discusses planet formation and migration during the protoplanetary disk phase, and we overview important post-disk phase planet evolution mechanisms in section 1.3; we describe planet structure modelling necessary for computing planet radii in section 1.4, and the method of population synthesis used throughout this thesis in section 1.5; lastly, in section 1.6, we give an overview of our approach and main results for remaining thesis chapters.

1.1 Protoplanetary Disk Evolution

In the standard nebular hypothesis, planets form out of material present within the circumstellar disk, which is concurrently being accreted onto the protostar as it evolves onto the main sequence. As

several crucial processes (disk chemistry, dust evolution, planet formation and migration) are taking place within the protoplanetary disk environment, it is paramount to have a detailed understanding of the densities and temperatures throughout, as well as their time-evolution.

Protoplanetary disk formation takes place through the gravitational collapse of a protostellar core. This sets the initial disk conditions, such as its mass, radius, metallicity, and composition. The turbulent motion present within the core results in an overall distribution of specific angular momenta throughout the collapsing regions (Li et al., 2014). In the classical, purely hydrodynamic treatments of star formation, protoplanetary disk formation is a consequence of conservation of angular momentum during collapse (Terebey et al., 1984). A non-zero specific angular momentum prevents some material from falling directly onto the protostar, and rather onto an orbit at a radius depending on the value of the specific angular momentum. However, if a magnetic field is present within the collapsing region, magnetic braking will also have an effect on this process, exerting a torque on collapsing material and reducing its angular momentum (Mellon & Li 2009; Seifried et al. 2012; Hennebelle et al. 2016; see also review Pudritz & Ray 2019). The significance of this process can be quantified via the mass-to-magnetic flux ratio Φ, with small values of Φ indicative of strong magnetic braking. The degree of magnetic braking will affect the resulting initial disk radius, with strong magnetic braking leading to smaller disk radii than what would be achieved in a pure hydrodynamic collapse (Tomida et al., 2015; Masson et al., 2016).

Basic considerations of total angular momentum conservation indicate that, as the protostar accretes disk mass, a portion of disk material must be transported outwards. Consequences of this process are seen in the Solar System. One finds that the rotational angular momentum of the Sun is significantly smaller than orbital angular momentum of Jupiter, illustrating that the process(es) governing disk dynamics must act to transport mass inwards and angular momentum outwards. In this section we focus on the two main proposed mechanisms that drive disk evolution: the magnetorotational instability (MRI) and magnetohydrodynamic (MHD) disk winds. We will give a brief physical overview of both of these processes in what follows.

We first, however, outline the equation governing disk evolution. The theory presented in Lynden-Bell & Pringle (1974) sees disk evolution driven through a generalized disk viscosity ν. This viscosity causes a torque, and angular momentum exchange, between disk material at neighbouring radii that orbit at different rates due to the gradient in orbital frequency Ω. Without having to consider *what* causes this disk viscosity, its action throughout the disk leads to the following form of the disk surface

density Σ evolution equation (Lynden-Bell & Pringle, 1974),

$$\frac{\partial \Sigma}{\partial t} = \frac{3}{r}\frac{\partial}{\partial r}\left[r^{1/2}\frac{\partial}{\partial r}\left(r^{1/2}\nu\Sigma\right)\right] , \tag{1.1}$$

where t is the time during disk evolution and r is the disk radius. Equation 1.1 is a type of diffusion equation that evolves on a so-called viscous (diffusion) timescale,

$$\tau_{\rm vis} \simeq \frac{r^2}{\nu} . \tag{1.2}$$

The disk's viscous timescale, set by the strength of the effective viscosity ν, therefore quantifies the timescale over which disk evolution occurs. As discussed further in section 1.5, protoplanetary disk lifetimes can be observationally inferred by determining the fraction of stars in young clusters showing infrared excesses generated by radiation from the disk photosphere (i.e. Hernández et al. 2007; Ribas et al. 2014). Through this approach, one infers typical disk lifetimes of 1-10 Myr. Another constraint is obtained through inferring accretion rates onto a protostar from observed Hα emission (Gullbring et al., 1998; Hartmann et al., 1998). Both constrain the above viscous timescale, and therefore the strength of the effective viscosity.

When considering the molecular viscosity of disk material, one finds that its strength is too weak, and that it results in viscous disk evolution timescales that are several orders of magnitude longer than observed disk lifetimes, indicating that molecular viscosity cannot be the source of the disk's effective ν (Armitage, 2010). While disks' low molecular viscosities (and high Reynolds number) suggest they should be prone to hydrodynamic instabilities that generate turbulence, Keplerian disks also satisfy the Rayleigh stability criterion (having an increasing specific angular momentum with radius) contradicting this intuition (Pringle, 1981).

Rather, turbulence in Keplerian disks has been shown to be generated through magnetic stresses via the magneto-rotational instability (MRI; Balbus & Hawley 1991). The MRI is an instability that arises due to an electro-magnetic coupling between disk material on neighbouring orbits. The gradient in orbital frequency $\mathrm{d}\Omega/\mathrm{d}r < 0$ throughout the disk leads to the distance between adjacent (i.e. at radii r and $r + \delta r$) gas parcels to increase, further increasing their electromagnetic force, which becomes a runaway process. As the MRI is a MHD effect, it requires a low-level of ionization to persist throughout the disk in order to operate. Turbulent fluid motions will cause mixing or

coupling between neighbouring disk regions, resulting in an effective turbulent viscosity. Given that turbulent eddies will be generated on a scale of roughly the disk scale height H, and that they will be subsonic (having speeds less than the local sound speed c_s), Shakura & Sunyaev (1973) give the following α-parameterization of turbulent viscosity,

$$\nu = \alpha c_s H \ . \tag{1.3}$$

Settings of the disk α between $\sim 10^{-4}$-10^{-2} give viscous timescales (equation 1.2) that correspond reasonably with observed disk lifetimes. Using this viscosity parameterization (equation 1.3) gives rise to self-similar solutions of the disk evolution equation 1.1 if power-law disks are assumed (Lynden-Bell & Pringle, 1974).

Many works that model disk evolution have done so by assuming evolution is driven via MRI-induced turbulence. However, recent observations inferring the strength of turbulence in protoplanetary disks have indicated that disks show lower levels of turbulence than may have been expected based on the above considerations. For example, through observing line-broadening in the TW-Hya disk, Flaherty et al. (2018) constrain the amount of disk turbulence that is present giving an upper limit of $\alpha_{\rm turb} < 0.007$. Additionally, Pinte et al. (2016) find that a large degree of dust settling is required to obtain an optimal fit between their modelled dust distribution and the observed dust distribution of HL-Tau. The significant amount of dust settling that is required results in a best-fit value of $\alpha_{\rm turb} \simeq 3 \times 10^{-4}$. Lastly, recent constraints on $\alpha_{\rm turb}$ have resulted from Rosotti et al. (2020), who use DSHARP sub-mm continuum disk data to study dust properties confined within pressure traps (see also Dullemond et al. 2018). Their results constrain $\alpha_{\rm turb}$ over a large range 10^{-4} - several $\times 10^{-3}$ by considering factors governing dust evolution in disks (see section 1.1.2).

The above observational constraints on the degree of turbulence in disks are in early stages of development, and they do not entirely rule out turbulence as driven through MRI. They do, however, pose a limit to its strength (i.e. $\alpha_{\rm turb} \sim 10^{-2}$, a common setting used in models, exceeds these observed upper limits). As modelling disk evolution under MRI-generated turbulent viscosity has traditionally been the standard approach, we continue our discussion of disk evolution under this mechanism before discussing the alternate scenario of MHD disk-winds.

The generation of turbulent vortices via MRI is suppressed by diffusivities η related to non-ideal MHD effects: Ohmic dissipation of currents that generate a magnetic field and Ambipolar diffusion

of a magnetic field with respect to charged particles (Turner et al., 2007; Bai & Stone, 2011). By equating the MRI growth timescale (set by the Alfvén speed $v_{\rm A}$) and dissipation timescale (set by η) on arbitrary length scale λ, one can derive the following criteria for MRI to be active through the Elsasser number (Simon et al., 2013),

$$\Lambda \equiv \frac{v_{\rm A}^2}{\eta\Omega} \lesssim 1 \ , \tag{1.4}$$

where Ω is the Keplerian orbital frequency. This condition states that in order to operate, MRI must generate turbulence faster than it is dissipated.

Generation of MRI-turbulence has been studied most extensively in semi-analytic disk models under the assumption that Ohmic dissipation is the non-ideal MHD effect that acts to suppress the MRI. We first outline results of this approach before discussing results pertaining to other non-ideal MHD effects and more complex models. Among non-ideal MHD effects, Ohmic dissipation has been shown to be strongest at the disk midplane (Bai, 2011), and its related diffusivity η_o has the form (Matsumura & Pudritz, 2003),

$$\eta_o = \frac{234}{x_e} T^{1/2} \, {\rm cm}^2 \, {\rm s}^{-1} \ , \tag{1.5}$$

where T is the local disk temperature. Since, in the case of MRI, turbulence is driven by magnetic stress, one can scale the Alfvén speed as $v_{\rm A}^2 \sim \alpha_{\rm turb} c_s^2$, denoting that α is caused by *turbulence* with this mechanism. Using equation 1.5, the MRI criterion (equation 1.4) can be used to estimate the ionization fraction x_e required in order for the MRI to operate. One finds that even quite low-levels of ionization $x_e \gtrsim 10^{-13}$ are sufficient in order to sustain the MRI and drive disk turbulence (Gammie, 1996).

The dependence of the MRI on ionization fraction raises the question of what causes disk ionization. Thermal ionization fractions on the order of one part in 10^{12} can only be achieved at very small disk radii $\lesssim 0.1$ AU where the temperature is sufficiently high. High energy radiation, such as X-rays generated by accretion of disk material onto the host-star, or interstellar cosmic rays, can ionize disk material across its entire extent (Armitage, 2011). When determining the ionization rate caused by each of these sources at a particular location in the disk, one needs to consider to what degree they are attenuated. For example, when calculating the ionization rate at the disk midplane, one needs to account for the factors by which each source is attenuated by disk material along the ionizing radiation's path.

Since the disk surface density Σ is, generally, a decreasing function of radius, the above consider-

ation indicates that, along the disk midplane, the ionization fraction will decrease with radius. This gives rise to the disk *dead zone*, a region in the inner disk where the ionization fraction is insufficient for the MRI to operate and generate turbulence. This results in a so-called *layered accretion* model (Gammie, 1996), where the dead zone exists in the inner disk region near the midplane, but has MRI being sustained in the upper scale heights of the disk's vertical extent (where ionizing radiation has yet to be sufficiently attenuated, leading to sufficient x_e).

Of particular importance is the outer boundary of the dead zone, defined at the point on the disk midplane where the ionization fraction is large enough for the operation of the MRI. Outside of this outer edge, sufficiently large ionization fractions persist down to the disk midplane due to the low disk surface density $\Sigma(r)$. Along the disk midplane, then, there will be a transition between an inner, laminar region, and an outer turbulent region. This inhomogeneity has a significant effect on disk structure and on related planet migration arising through planet-disk torques (i.e. is the location of a planet trap - see section 1.2.1). The dead zone also has an inner boundary at the point at small disk radius where thermal ionization results in a sufficient ionization fraction to sustain MRI.

Including the dissipating effect of ambipolar diffusion (hereafter AD) can complicate the simple layered accretion picture of Gammie (1996) that only considers MRI suppression via Ohmic dissipation. When studying MRI-suppression through these non-ideal MHD terms, Ohmic dissipation is found to be strongest in the higher-density regions of the disk (i.e. near the disk midplane) while AD is found to be most significant in lower-density regions (Armitage, 2011). As a result, AD can suppress MRI in the upper regions of a disk's vertical extent (i.e. Bai & Stone, 2013), precisely where the layered accretion model predicts MRI to operate (above the midplane dead zone) in order to maintain the disk's radial angular momentum exchange. With Ohmic dissipation suppressing MRI near the midplane, and AD suppressing at higher vertical extents, Bai & Stone (2013) find that angular momentum exchange can be achieved through the launching of a disk wind as opposed to MRI which is suppressed across almost the entirety of the disk's vertical extent. Another result of AD's dominance at low densities is that it can suppress MRI at the midplane in the outer disk ($\gtrsim$ 30 AU, i.e. Simon et al., 2013).

Adding yet further complexities is the inclusion of the Hall effect as the third non-ideal MHD term that typically is most significant at intermediate densities, and is dependent on the magnetic field's geometry with respect to the disk fluid's motion (Armitage, 2011). A fully self-consistent treatment of these non-ideal MHD effects on disk evolution demands a numerical approach relating

each non-ideal effect's diffusivity to disk chemistry (Bai & Stone, 2013; Lesur et al., 2014; Gressel et al., 2015; Bai et al., 2016; Mori et al., 2019; Gressel et al., 2020). These numerical models of the complex problem of disk evolution are repeatedly showing that: (1) MRI can be suppressed over large regions of the disk's vertical and radial extents; (2) disks are therefore quite laminar (at least, to a larger degree than expected based on traditional viscous evolution models); and (3) that disk evolution (angular momentum exchange) can be handled through the launching of a disk wind.

Following these numerical results, we now consider MHD disk winds as an alternative method of driving evolution. In this mechanism, angular momentum exchange is caused by open magnetic field lines exerting torques on disk material. In the upper layers of the disk, where the magnetic pressure dominates over gas pressure, a consequence of this torque will result in disk material being driven outwards along the magnetic field lines in a disk wind (Blandford & Payne, 1982; Pudritz & Norman, 1986). By conservation of angular momentum, there will be a related inflow velocity (i.e. accretion) in disk material towards the midplane. Adding the contribution of an MHD disk wind results in the following changes to the surface density evolution equation 1.1 (Suzuki et al., 2016; Chambers, 2019),

$$\frac{\partial \Sigma}{\partial t} = \frac{3}{r}\frac{\partial}{\partial r}\left[r^{1/2}\frac{\partial}{\partial r}\left(r^{1/2}\nu\Sigma\right)\right] + \frac{1}{r}\frac{\partial}{\partial r}\left(r v_w \Sigma\right) + \dot{\Sigma}_{\rm outflow} \ . \tag{1.6}$$

Here, the first term corresponds to the disk evolution related to turbulent viscosity, as in equation 1.1. The second term is related to the radial velocity of disk material driven by the disk wind v_w. In the Chambers (2019) formalism, this scales with the wind-induced velocity at 1 AU, v_0 as follows,

$$v_w \sim v_0 \left(\frac{T}{T_0}\right)^{1/2} \ ; \tag{1.7}$$

where T is the midplane temperature, and T_0 is the temperature at 1 AU (see section 5.2 for further details). Lastly, as wind-driven evolution causes both disk accretion *and* an outflow, there is a third term in equation 1.6 representing the outflow surface density rate $\dot{\Sigma}_{\rm outflow}$ which can be a function of disk radius r and time t. For example, in the Chambers (2019) disk model, the wind-driven outflow is,

$$\dot{\Sigma}_{\rm outflow} \sim \frac{\Sigma v_0}{r_0}\left(\frac{r}{r_0}\right)^{-3/2} \ , \tag{1.8}$$

scaling with the wind-induced disk radial velocity v_0 at reference radius $r_0 = 1$ AU. The outflow's

time-dependence comes in the form of the decreasing surface density Σ. Equation 1.8 shows that a wind-driven outflow will preferentially remove disk material in high Σ regions and small radii (Suzuki et al., 2010). Disk wind theory predicts a ratio between the mass-loss rate from the outflow and the disk accretion rate of $\dot{M}_{\rm wind}/\dot{M}_{\rm disk} \sim 0.1$ (as derived in Pudritz & Norman 1986). This theoretical result has been confirmed observationally for a large sample of systems (Watson et al., 2016).

We note that the form of the surface density evolution equation presented in equation 1.6 is quite general, in that one can investigate disk evolution with different settings of the strengths of turbulent viscosity and wind-driven accretion and outflow. For instance, one can consider the pure turbulent viscosity case or the pure wind-driven case. Perhaps more useful are models that consider the combination of both evolution mechanisms which is the approach taken, for example, in Suzuki et al. (2016) and Chambers (2019). While our approach in chapters 2-4 considers the pure turbulent-viscosity case, along with a photoevaporation-driven outflow (see description in next paragraph), we incorporate the effects of the MHD wind in this manner in chapter 5. We refer the reader to section 2.3.1 for a detailed description of our viscous disk evolution model (the former case), and to chapter 5 for the model that incorporates disk winds.

We have related the third term in equation 1.6 to outflow from the MHD disk wind. However, this general outflow term also encompasses photoevaporation-driven outflows generated by X-ray and UV radiation from the host-star (i.e. Gorti et al. 2009; Owen et al. 2010). In this scenario, the high-energy photons heat upper layers of the disk, and can cause material to exceed the local escape speed, driving an outflow. While photoevaporation can drive outflows for the entire duration of disk evolution, models have shown that it becomes significant when the disk accretion rate decreases such that it becomes comparable to the mass-loss rate from photoevaporation, $\dot{M}_{\rm wind,pe} \simeq \dot{M}_{\rm disk}$. Once this criterion is satisfied, rapid clearing of the protoplanetary disk has been shown to take place on short timescales $\sim 10^4$ years (Owen et al., 2011).

These disk outflow mechanisms are paramount in disk evolution models as they are the means by which dissipation of protoplanetary disks takes place. Therefore, they physically set disk lifetimes which constrain the upper limit to timescales of planet formation and all processes taking place within disk material (i.e. dust evolution, chemistry, planet migration). As we have alluded to both photoevaporation and disk winds as driving outflows, it raises the question of when each is applicable to disk evolution and setting disk lifetimes. It has been shown that the simultaneous action of both outflow-generating processes are required to reproduce observed line profiles from disk outflows

(Weber et al., 2020), giving a good indication that the combined effect of both processes is important. However, the transition criteria between a wind-dominated and photoevaporation-dominated outflow was quantified in the disk wind models of Rodenkirch et al. (2020) using the plasma β parameter, a ratio of the gas to magnetic pressure ($\beta = \mathrm{P_{gas}}/\mathrm{P_B}$). They find that such a transition occurs at $\beta \sim 10^7$, with MHD wind outflows dominating at lower values of β or stronger magnetic fields, with weaker magnetic fields seeing the dominance of photoevaporative outflows.

Returning to the comparison between disk evolution via MRI and disk winds, a key consequence of angular momentum exchange via turbulent viscosity is the spreading of the disk as accretion takes place, which will result in the disk outer radius increasing with time (Chambers, 2009). Evolution via MHD winds will not result in disk spreading. Conversely, winds-driven evolution results in either the disk radius being roughly constant time, or in the disk contracting as evolution takes place, depending on the strength of the disk-wind torque and outflow rate (Suzuki et al., 2016; Shadmehri & Ghoreyshi, 2019). The evolution of the outer disk radius is an important consideration when comparing disk models to observed disk radii, for which systems have typically evolved over $\sim$ Myr timescales. If one assumes viscous evolution, then a model's initial disk radius needs to be less than a particular observed disk radius to achieve correspondence.

A protoplanetary disk's temperature profile can be derived by considering the two main heating sources it is subjected to: generalized viscous heating (i.e. dissipation of gravitational potential lost in accreting material), and radiation from the host star[1] (D'Alessio et al., 1998). In the former case, the turbulent viscosity responsible for angular momentum redistribution in the MRI has an associated heating term. Lynden-Bell & Pringle (1974) showed that this heating term leads to a characteristic midplane temperature profile of $T \sim r^{-3/4}$. As this mechanism relies on dissipating the gravitational potential lost by material accreting through the disk, it will be most prominent at large disk accretion rates $\dot{M} \sim \nu\Sigma$. Therefore, in the MRI turbulent viscosity scenario, viscous heating will be largest in the inner regions of the disk where Σ is large (since Σ is a decreasing function of radius r), and at early times in disk evolution (since $\dot{M}$ decreases with time t, as the disk surface density Σ decreases as accretion takes place).

In the alternate MHD disk winds scenario where there is no turbulent viscosity, the heating associated with dissipating gravitational potential has been shown to contribute minimally to the

[1]External background radiation can also contribute to generalized radiative heating, such as if the disk is embedded in a cluster environment. However, typically the host star's radiation dominates, with the external radiation providing a "minimum temperature" that only dominates over host-stellar radiation at large disk radii.

midplane temperature above that derived from host-star radiation (Mori et al., 2019). Therefore, in a pure disk winds-evolving model, one can expect minimal contributions to the midplane temperature profile from viscous heating. In this circumstance, the gravitational potential energy lost by accreting material is then carried off as kinetic energy of the outflow. There may be a non-ideal MHD heating term from gradients in the magnetic field throughout the disk, but similar to dissipation of gravitational potential, this non-ideal MHD heating is expected to contribute minimally beyond the heating provided by host-star radiation (Bai et al., 2016).

To derive the disk temperature achieved from radiative heating from the host star, the radiative flux received at the disk photosphere at radius r needs to be determined ($\sim L_* r^{-2}$, where L_* is the host-star's luminosity), which depends on the disk geometry. For example, assuming the disk has no vertical extent (the so-called *razor thin* case) leads to the *same* radial temperature dependence as in the MRI viscous heating case, $T \sim r^{-3/4}$. These heating sources can be tested in their ability to reproduce temperature profiles that achieve correspondence with those inferred from observed *spectral energy distributions* (SEDs) of protostars with disks. The temperature profiles derived from both MRI viscosity and flat disks give rise to SEDs $\nu F_\nu \sim \nu^n$ (where F_ν is the observed flux at frequency ν) with an index $n = 4/3$. This is steeper than observed SEDs which show flatter profiles $n \lesssim 3/4$ (Chiang & Goldreich, 1997). To resolve this discrepancy, one needs to consider a flared disk geometry, whereby the scale height H indicating the disk's vertical extent increases with radius r. A flared disk geometry results in a larger absorption cross section at the disk photosphere, leading to a flatter disk temperature profile of $T \sim r^{-1/2}$ (Kenyon & Hartmann, 1987), which achieves a better comparison to SED observations.

In reality, both disk heating sources are important to consider when determining the disk's temperature profile. This approach was taken in D'Alessio et al. (1998, 1999), to show that derived temperature profiles resulted in SEDs reflecting observations. As radiative heating depends only on the absorbed stellar flux $\sim L_*/r^2$, one finds that the resulting temperature profile is *time independent*, assuming a constant stellar luminosity and disk flaring angle. Combining this consideration with those outlined above for MRI turbulence heating (dominating at small radii and early times in disk evolution), one finds that MRI heating dominates the inner disk and radiative heating the outer disk. The transition point is the so-called *heat transition* which, for non-zero disk flaring angles, will be the location of an inhomogeneity in the slope of the disk's midplane temperature profile (Chambers, 2009). It turns out that this transition radius is also a dynamical trap for migrating planets ("planet

trap"), where the net torque upon them vanishes (see section 1.2.1). This is considered in our models. Additionally, one expects the heat transition to migrate inwards as disk evolution takes place, since MRI heating rates will decrease in time with disk accretion. In other words, the viscously-heated region of the disk will shrink in time. For instance, D'Alessio et al. (1998) find that for $\sim$ Myr-evolved disks, the viscous region covers on the innermost $\lesssim 2$ AU of the disk's extent.

1.1.1 Disk Chemistry

An understanding of the materials present in protoplanetary disks and their abundances is necessary for determining planet compositions arising from formation. The radial abundance profiles of gases and solids throughout the disk as computed with disk chemistry models are crucial in linking a planet's final composition to its formation history - i.e. the summed accretion rates over all disk radii, and therefore chemical abundances, planet formation takes place. The materials accreted throughout formation are an important consideration when computing planets' interior and atmospheric structure, necessary for determining their radii (see section 1.4).

Of particular interest are condensation fronts or ice lines, which are phase transitions between the solid and gas phases of a volatile occurring at a particular disk temperature. Ice lines not only define the phase of the material that is being accreted onto a planet (depending on the forming planet's location with respect to the ice line), but also affect the disk structure through a local transition in disk opacity (Ruden & Pollack, 1991). As we will discuss further in section 1.2.1, a local transition in disk opacity at an ice line will become an important factor affecting low-mass planet migration. The resulting gravitational torques between the forming planet and disk material depends on temperature and density gradients (Paardekooper et al., 2010), which can change sharply at radii where opacity transitions occur (Baillié et al., 2015; Coleman & Nelson, 2016b). Modelling of a disk's chemical structure is also useful in interpreting observations. For example, when a particular volatile's condensation front is observed, one can constrain disk properties such as the local temperature, gas density, or ionization (i.e. Qi et al. 2011; Cleeves et al. 2015; Favre et al. 2015; Schwarz et al. 2016).

Disk chemistry models can be broadly categorized based on their assumptions as to whether or not chemical equilibrium is attained. For these considerations, we recall protoplanetary disk formation occurs through the collapse of a protostellar core. In the first category of *equilibrium* models, the species provided by the collapsing core are assumed to be completely altered through

chemical processes taking place within the disk. The collapsing core's chemistry is therefore "reset", with disk chemistry taking place in situ, forming species out of the constituent materials transported to the disk via core collapse. The alternate scenario of *non-equilibrium* models applies when chemical equilibrium is not attained, and chemical abundances provided by the collapsing protostellar core are, at least to a degree, preserved (i.e. Visser et al. 2009). Thus, in this case, the disk's chemical abundances are said to be *inherited*. Due to the large range in timescales for chemical processes in disks, both the chemical "reset" and "inheritance" scenarios remain plausible (see, for example, review by Pontoppidan et al. 2014).

It is therefore likely that both of these processes apply within different regions in the disk. The inner disk ($\lesssim$10-20 AU) may favour the chemical reset scenario due to the higher density of material and closer proximity to the protostar, whereas at larger disk radii chemical inheritance becomes applicable (Aikawa & Herbst, 1999). As we will discuss in section 1.2, this inner disk region is most significant for planet formation in the core accretion scenario due to the higher midplane density of disk material. Thus, the disk chemistry model we use assumes a chemical reset scenario as we are focused on tracking forming planets' compositions. Conversely, when using disk chemistry models to understand observations a chemical reset scenario becomes more useful, as the majority of the observed disk's spatial extent (for which the observations are limited by spatial resolution) will be at radii $\gtrsim$ 10 AU.

In chemistry models assuming a chemical reset scenario, one can use a thermodynamic approach to determine the disk's chemical structure. The local disk temperature and pressure define conditions for a chemical system in local thermodynamic equilibrium. In this approach, the initially hot disk material composed of constituent elements in their gas-phase slowly cools to the local disk temperature and pressure, with materials condensing throughout the process, until the chemical system reaches thermodynamic equilibrium. The thermodynamic treatment, or equilibrium chemistry approach, can be used when the chemical equilibrium timescale is *shorter* than the disk's viscous timescale $\sim 10^6$ years. In other words, the disk needs to reach chemical equilibrium faster than disk evolution takes place, which changes the local disk temperature and pressure defining the chemical system. Equilibrium chemistry is particularly useful for solids, which have been shown to condense out of the gas phase on very short ($\sim 100 - 1000$ year) timescales (Toppani et al., 2006). We give a general overview of this method here, and refer the reader to chapter 4 Appendix A for further details.

Thermodynamic equilibrium is achieved when the Gibbs free energy, G, is minimized. The Gibbs free energy is a thermodynamic potential defined as,

$$G = H - TS \, , \tag{1.9}$$

where H is the system's enthalpy, T its temperature, and S its entropy. In a chemical system composed of N species, the total Gibbs free energy G_T is,

$$G_T = \sum_{i=1}^{N} X_i G_i = \sum_{i=1}^{N} X_i (G_i^o + RT \ln X_i) \, , \tag{1.10}$$

where X_i is the mole fraction of species i. The Gibbs free energy of a particular species, G_i, is related to its Gibbs free energy of formation G_i^o through $G_i = G_i^o + RT \ln X_i$ where R is the gas constant. An additional constraint is provided through conservation of mass considerations. Initial elemental abundances are provided as an initial condition to the calculation, and one must ensure that the equilibrium state $\{X_i\}$ has a summed molar amount of each element consistent with the initial condition. For instance, one can use Solar or a planet hosting star's abundances as the initial chemical condition, under the standard assumption that the abundances in the outer layers of the host star are reflective of abundances that were present throughout its disk.

In order to determine the system's equilibrium state, one must first define the set of possible species that can form out of the elements provided in the initial condition (i.e. those supplied by the collapsing core). The difficulty lies in determining this set of species prior to calculating disk chemistry. As each species has its own Gibbs free energy that is a function of the system's temperature and pressure (and in cases, can depend on other species' abundances), determining the set of abundances $\{X_i\}$ that minimize equation 1.10 can be challenging to calculate for even moderate lists of chemical species. As such, numerical techniques (equilibrium chemistry solvers) are used for this purpose.

Including every possible molecule and mineral that can form out of the elements included in the initial conditions will lead to unnecessarily long computation times, especially considering many species will have extremely low abundances throughout the disk's extent and evolution. Conversely, taking unnecessarily small species lists could result in neglecting species with non-negligible abundances. A technique used by Pignatale et al. (2011) that circumvents these issues is to first prescribe

a large species list and use a low temperature and pressure resolution equilibrium chemistry calculation to determine their abundances. Following this, the species list is reduced by removing the species whose abundances over all investigated temperatures and pressures are negligible. This reduced list can then be carried forward for higher-resolution calculations.

Equilibrium disk chemistry models have been used previously in studies of disk chemical abundances (i.e. Pasek et al. 2005; Pignatale et al. 2011). Additionally, as this approach is sufficient in predicting solid abundances, results of equilibrium chemistry calculations have been used to determine solid abundances on planets resulting from formation models. For example, several works have combined equilibrium disk chemistry with terrestrial planet formation, in which low-mass planets form after the disk phase through the dynamical assembly of solid planetesimals, whose compositions are prescribed following the chemistry calculation (Bond et al., 2010; Elser et al., 2012; Moriarty et al., 2014). Combining disk chemistry with the core accretion model, the approach taken here, has also been previously done to calculate super Earth solid compositions (Alessi et al., 2017).

In many cases, particularly at large disk radii with low temperatures, equilibrium timescales for gases can be comparable to the disk's viscous timescale. In these cases, using an equilibrium approach to predict gas abundances is not justified, and non-equilibrium chemistry needs to be used. We recall, additionally, that at larger disk radii, the chemical inheritance scenario also becomes applicable, and molecular abundances from the collapsing core will provide initial conditions for disk chemistry. In non-equilibrium models, chemical kinetics are used to calculate reaction rates and molecular abundances (Woodall et al., 2007). Of particular importance in their effect on rate coefficients are grain surface reactions, as they provide a surface for gaseous species to interact and act as a catalyst in reactions (Walsh et al., 2010). Photochemistry is another important inclusion in non-equilibrium models as it causes, for example, photodissociation of molecules. On this basis, calculating the radiation field throughout the disk through radiative transfer modelling is necessary in non-equilibrium chemistry approaches (Woitke et al., 2009; Cridland et al., 2016).

Ionization chemistry is another important consideration in non-equilibrium chemistry models, for example, in its role in ion-molecule and charge transfer reactions. We recall that understanding disk ionization was also necessary when determining the operation of the disk MRI and in determining the presence and/or existence of a dead zone (section 1.1). Both X-rays generated by accretion onto the host star and interstellar cosmic rays con contribute significantly to disk ionization, although the latter source may be effectively screened by disk outflows (Cleeves et al., 2013). Determining the

disk ionization rate involves radiative transfer modelling, as both ionizing sources are attenuated by outflows and/or disk material. Lastly, high energy radiation from decay of radioactive nuclei is a third source of disk ionization that can be considered.

1.1.2 Dust Evolution

Understanding the factors affecting dust evolution is important when interpreting disk observations (i.e. with *ALMA*) that probe the distribution of dust through mm-continuum observations. We recall that these observations indicate that solid disk radii are typically a factor of 1-3 times smaller than observed gas disk radii (Ansdell et al., 2018), with the more extreme discrepancies in radii indicating the influence of grain growth and/or radial dust drift that systematically transports solids inwards (Facchini et al., 2017).

In the core accretion scenario, planet formation takes place through a bottom-up process, whereby the solids dispersed throughout the protoplanetary disk will coalesce to form a planetary core sufficiently massive to accrete nebular gas. As dust is the smallest constituent solid material existing throughout the disk, its growth represents the earliest stage of this process. Dust evolution, both in terms of its growth (coagulation), and its motion throughout the disk (radial drift), is an important factor for planet formation studies as the distribution of solid material in the disk will affect the growth of planets that are accumulating mass through solid accretion. As we will see in the following section 1.2, the processes affecting dust dynamics are of key consideration in understanding the formation of metre-kilometre sized solid planetesimals.

We outline here the key physical considerations governing dust growth and radial drift. Dust evolution is a major component of our model, which is covered in further detail in section 3.2.2.

A key physical effect on dust throughout protoplanetary disks is the drag forces they experience due to a headwind caused by the disk gas. While the solids orbit at the local Keplerian velocity, the gas material orbits at a slightly sub-Keplerian rate due to the support related to the pressure gradient dP/dr existing throughout the disk. One can define a stopping time for dust grains (Testi et al., 2014),

$$t_{\rm stop} = \frac{mv}{|F_D|} \, , \tag{1.11}$$

where m and v are the grain's mass and velocity, and F_D is the drag force. The stopping time will depend on the size of the dust particle in question. Small dust grains up to $\sim$ cm sizes experience drag

forces in the so-called *Epstein* regime, whereby they are tightly coupled to the gas motion. Larger solids are within the *Stokes* drag regime, experiencing standard fluid-like drag forces (Armitage, 2010). It is useful to define a dimensionless stopping time, referred to as the Stokes number (Testi et al., 2014),

$$\mathrm{St} \equiv \mathrm{t_{stop}}\Omega_{\mathrm{K}} \ , \tag{1.12}$$

where Ω_K is the local Keplerian orbital frequency. While the Stokes number does scale with particle size a, it also depends on the local disk conditions. Stokes numbers near unity correspond to particles whose stopping times are comparable to their orbital periods.

In a typical disk setup with gas pressure decreasing radially outward, the drag forces exerted on solid particles reduce their angular momentum causing radial drift. A particle with a given Stokes number St will have a radial drift velocity (Weidenschilling, 1977b),

$$u_{\mathrm{D}} = \frac{1}{\mathrm{St} + \mathrm{St}^{-1}} \frac{1}{\rho_g \Omega_K} \frac{\partial P}{\partial r} \ , \tag{1.13}$$

where ρ_g is the gas density, and the pressure gradient $\partial P/\partial r < 0$ for typical disk temperature profiles correspond to inward radial drift velocities $u_{\mathrm{D}} < 0$. One finds that the most extreme radial drift velocities in equation 1.13 occur for particles with Stokes numbers near unity, corresponding to $\sim$ 10 cm for typical disk settings. This is an important factor when considering growth of solids, as the rapid radial drift timescales over this size range lead to a theoretical challenge in planetesimal formation (discussed further in section 1.2).

By equating a particle's growth timescale $\tau_{\mathrm{grow}} = a/\dot{a}$ with its radial drift timescale $\tau_{\mathrm{drift}} = r/u_{\mathrm{D}}$, Birnstiel et al. (2012) obtain an estimate for the maximum grain size or Stokes number that can be achieved before radial drift transports the solid inwards. The growth timescale is derived to be,

$$\tau_{\mathrm{grow}} \simeq \frac{1}{\Omega_K} \frac{\Sigma_g}{\Sigma_d} \ , \tag{1.14}$$

and is dependent on the inverse of the dust-to-gas ratio Σ_d/Σ_g. Equating these timescales leads to a maximum Stokes number in the drift-limited regime of (Birnstiel et al., 2012),

$$\mathrm{St_{drift}} \sim \frac{\mathrm{V_K^2}}{\mathrm{c_s^2}} \left| \frac{\mathrm{d\ ln\, P}}{\mathrm{d\ ln\, r}} \right|^{-1} \tag{1.15}$$

where V_K is the local Keplerian orbital velocity, c_s is the gas sound speed, and $\mathrm{St}_{\mathrm{drift}}$ scales with the inverse of the magnitude of the disk's pressure gradient. Therefore, steeper pressure gradients, resulting in stronger headwinds and more rapid radial drift, will give smaller maximum grain sizes in the drift-limited regime.

Dust particle growth occurs through the process of coagulation. An additional limiting factor on particle growth is fragmentation. As coagulation is a collisional process, net growth can only be achieved provided that the kinetic energy related to the particles' relative velocity Δu is less than the short-range binding energies between the particles (Ormel et al., 2009; Paszun & Dominik, 2009). If the converse is true, and the particles' relative velocity exceeds the *fragmentation velocity* u_f, the collision will result in the particles breaking up into multiple fragments with no net growth occurring. Fragmentation becomes an important factor limiting grain growth when particle sizes exceed $\sim$ the cm-scale. The fragmentation velocity u_f depends on grain properties and composition. When comparing dry grains to grains with an ice mantle, one finds higher fragmentation velocities in the case of icy grains as the mantle increases their tensile strength (Wada et al., 2009). This consideration indicates that outside the snow line, particles will be able to grow to larger sizes before being limited by fragmentation.

Assuming that relative velocities Δu of dust grains are driven by coupling to the turbulent motions in the gas disk, Ormel & Cuzzi (2007) give the following Δu for two grains of comparable sizes,

$$\Delta u \sim \sqrt{\alpha_{\mathrm{turb}} \mathrm{St}} c_s \ . \tag{1.16}$$

This can be equated to the fragmentation threshold velocity u_f to obtain the maximum grain size or Stokes number that can be achieved in the fragmentation-limited regime (Birnstiel et al., 2009),

$$\mathrm{St}_{\mathrm{frag}} \simeq \frac{\mathrm{u_f^2}}{\alpha_{\mathrm{turb}} \mathrm{c_s^2}} \ , \tag{1.17}$$

At a particular disk radius, the relevant limiting factor of grain growth is the lesser of the fragmentation and radial drift size limits. We notice in equations 1.15 and 1.17, that both have a factor of $1/c_s^2 \sim 1/T$ with disk temperature T being a decreasing function of radius r. However, there is an additional factor of Keplerian velocity $V_K^2 \sim r^{-1}$ only present in the drift limited grain size. The fragmentation-limit has a factor of u_f^2 which, for our purposes here, can be approximated to be constant in radius (neglecting variations with grain composition). Therefore, the drift-limit

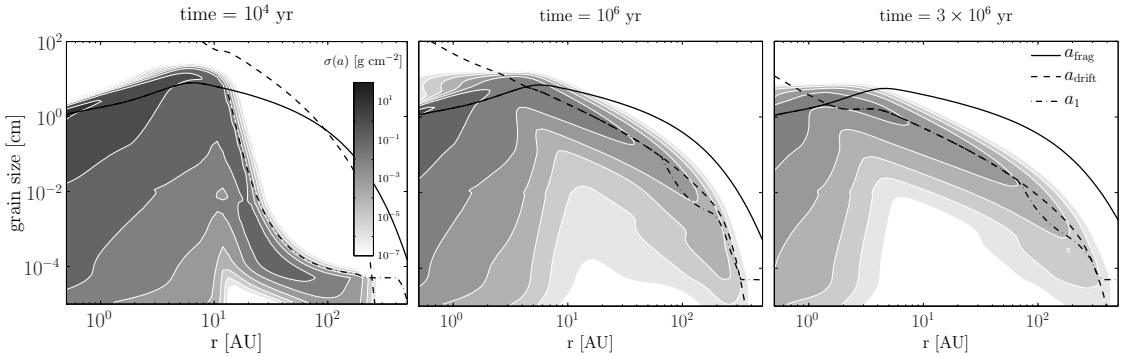

Figure 1.7: Results of a numerical dust evolution treatment are shown, plotting σ, defined as the dust surface density per unit grain size a, as a function of grain size and disk radius at three snapshots during disk evolution. The solid and dashed lines indicate the fragmentation-limited and drift-limited grain sizes, respectively. The dash-dotted line shows the radius profile of the maximum grain size at each snapshot, roughly corresponding with that of the growth-limiting factor at later times. This simulation assumes a turbulence strength of $\alpha_{\rm turb} = 10^{-3}$. Reproduced with permission from Birnstiel T., Klahr H., Ercolano B., 2012, A&A, 539, A148. DOI:10.1051/0004-6361/201118136, figure 1, ©ESO.

decreases more steeply with disk radius than the fragmentation-limited size, indicating that radial drift will limit grain growth in the outer disk, and fragmentation will limit growth in the inner disk.

In figure 1.7, we show the results of a numerical treatment of dust evolution calculated in Birnstiel et al. (2012). The dust surface density per unit grain size is plotted as a function of grain size and disk radius at three times during disk evolution. We see that large surface densities are achieved at small disk radii and large grain sizes as a consequence of radial dust drift. The dust distribution does extend to large disk radii, but is composed of smaller sized grains. Figure 1.7 also shows fragmentation and drift-limited maximum grain sizes. Comparing these two grain size limits confirms that radial drift is the limiting factor in the outer disk, and fragmentation is relevant in the inner disk. Each snapshot shows the radial profile of the maximum grain size. At later times > 1 Myr in disk evolution, the maximum grain size has a reasonable correspondence with the relevant grain size limit (estimated with equations 1.15 and 1.17) throughout the disk's extent.

Radial drift is a process that, particularly for large grain sizes, significantly affects the radial distribution of solids. The inward radial drift velocities $u_{\rm D}$ calculated with equation 1.13 were a result of the disk pressure profile decreasing with radius, $\partial_r P < 0$, which will be the case for typical disk surface density and temperature profiles. However, the interesting effect of *dust trapping* can occur if local pressure maxima are present within the disk. In this case, one can show using the direction of radial drift (i.e. the sign of $\partial_r P$) at radii near a pressure maximum that radial drift will

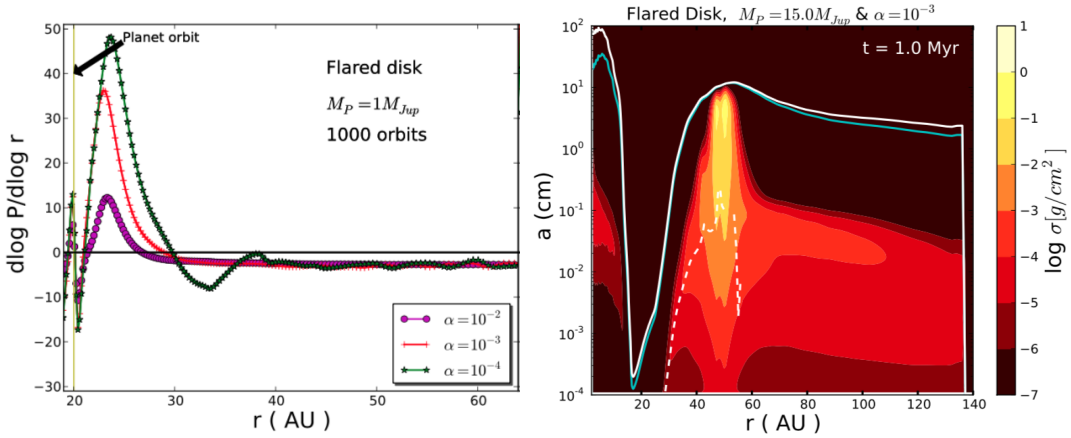

Figure 1.8: **Left:** Radial profile of the disk pressure gradient $\partial_r P$ is shown at three different settings of disk α, computed in a disk model subjected to the gravitational perturbation of a Jupiter-mass planet at 20 AU. In addition to opening a gap, the planet also causes a dust trap, physically corresponding to a maximum in the disk pressure (or Σ) just outside the gap. The sign of $\partial_r P$ shows that radial drift will concentrate dust towards the dust trap at $\sim$ 30 AU, where $\partial_r P$=0. Reproduced with permission from Pinilla P., Benisty M., Birnstiel T., 2012, A&A, 545, A81. DOI:10.1051/0004-6361/201219315, figure 2 (left panel), ©ESO.
Right: The result of numerical dust evolution modelling is shown for the same set up described for figure 1.8 left panel, but with a 15 Jupiter-mass planet at 20 AU creating a gap in the gas surface density, and a disk α=10^{-3}. Dust surface density per unit grain size σ is plotted on the colour scale as a function of disk radius and grain size. The dust distribution shows an increased density at the dust trap at $\sim$ 50 AU (note that the pressure maximum shifts *outwards* for a more massive planet). The white and blue lines correspond to particles with St = 1 (equation 1.12) and at the fragmentation barrier (equation 1.17), respectively. The dashed white line indicates the grain size where radial drift occurs faster than gas drag (i.e. drift-dominated, or trapped particles). Reproduced with permission from Pinilla P., Benisty M., Birnstiel T., 2012, A&A, 545, A81. DOI:10.1051/0004-6361/201219315, figure 9 (top panel), ©ESO.

transport solids *towards* the pressure enhancement, creating a dust trap.

Dust trapping is illustrated in figure 1.8 by showing the consequence of a pressure maximum existing within the disk on the overall dust distribution. In this numerical treatment from Pinilla et al. (2012b), the presence of a massive gas giant in the disk at 20 AU creates an annular gap with reduced surface density (see also section 1.2.2), which in turn results in a pressure maximum existing just outside the gap's radial extent (i.e. Dong et al. 2015a; Bae et al. 2016). The left panel of figure 1.8 plots the radial pressure gradient $\partial_r P$, which directs dust towards the pressure maximum at $\sim$ 30 AU where $\partial_r P = 0$. Therefore, locations of pressure maxima in the disk are dust traps. On this physical basis, large dust concentrations can arise at disk pressure maxima from radial drift. We notice the important role that α plays in how sharp the gradient $\partial_r P$ becomes, which will directly translate to the prominence of the resulting dust trap. As α decreases, the turbulence-induced

diffusion (that removes dust from the trap) is reduced, making the features sharper (e.g. Dullemond et al. 2018).

This process of dust trapping is shown in the right panel of figure 1.8 where the dust surface density per unit grain size σ (same definition as in figure 1.7) is greatly enhanced at the pressure maximum near 50 AU, existing outside of the gap created by the massive planet at 20 AU in the Pinilla et al. (2012b) configuration. We note that the positions of the dust traps differ between the two panels of figure 1.8 due to different planet masses creating the gaps, with the more massive planet (right panel) creating a wider gap, and a larger separation between the planet's orbit and the dust trap.

Through this process, dust trapping is considered as the physical means by which bright rings that have been observed in dust continuum observations arise (recall figure 1.5 from Andrews et al. 2018, see also van der Marel et al. 2015; Dullemond et al. 2018; Cazzoletti et al. 2018). Dust trapping also has significant implications for planet formation. The large dust concentrations at these traps becomes an important factor to consider in planetesimal formation as they give rise to the appropriate conditions for the *streaming instability*, which is a solution to the problem of rapid inward radial drift of solids in the cm-m size range (Johansen et al., 2007). Additionally, dust trapping can be an important effect to maintain extended dust distributions, particularly for large grain sizes (Pinilla et al., 2012a; Rosotti et al., 2020). We discuss these important issues further in section 1.2.3.

1.2 Planet Formation & Migration

Here we outline the main physical considerations in understanding planet formation throughout the protoplanetary disk phase. We consider the standard core accretion model (Pollack et al., 1996), which is a bottom-up approach to forming planets wherein small solids throughout the disk are assembled into a planetary core massive enough to accrete nebular gas. The core accretion model can be contrasted with the top-down approach of forming planets through gravitational collapse of large, Toomre-unstable regions of the disk (i.e. Boss 1997; Meru & Bate 2010; see also review by Kratter & Lodato 2016). We recall that the disk properties set planet formation timescales and will play a significant role in their effect on the range of planet formation outcomes. Furthermore, the disk's dust distribution will affect early stages of the core accretion model where growth occurs through accretion of solid material. Regions of the disk that are partially cleared of solids by radial

drift, for example, will have reduced solid growth timescales.

Another key consideration for planet formation studies the link it provides between disk chemistry and final planet compositions. A planet's final composition reflects its accretion throughout the disk, sampling the local disk's composition as it forms. On this basis, it is important to not only understand planet accretion rates, but also where accretion is taking place in the disk (given the temperature, and therefore disk radius-dependence of material abundances; see section 1.1.1).

Gaps and asymmetries observed in disks' dust continuum emission provide evidence for planet-disk gravitational interactions. The related torque on a forming planet will cause the planet to migrate throughout the disk (changing its orbital radius with time), as opposed to forming in situ (stationary). Migration is an interesting and necessary consideration in planet formation, as it represents a means of transporting planets to regions of the disk that may have substantially different densities and/or compositions. We start by outlining the physics of planet migration in sections 1.2.1 and 1.2.2 before giving an overview of the core accretion model in section 1.2.3.

1.2.1 Type-I Migration & Planet Traps

Type-I migration theory pertains to relatively low-mass planets $\lesssim$ 15-30 $M_\oplus$ whose gravitational interaction with disk material does not greatly disrupt the overall disk structure. Rather, its effect on the disk can be regarded as a gravitational perturbation, altering the disk structure in two ways. The first is through its interaction with disk material at both larger and smaller orbits, at *Lindblad resonances*, defined to have orbital frequencies that scale with the planet's Ω_p,

$$\Omega = \Omega_p(1 \pm 1/m) \,, \tag{1.18}$$

for non-zero integer values of m. The planet's perturbation at the Lindblad-resonant locations throughout the disk will raise a spiral density wave extending to both smaller and larger orbits. The second effect applies to disk material near the planet's orbit $\Omega \simeq \Omega_p$ that will undergo horseshoe orbits, being "kicked" to larger and smaller orbits through the gravitational interaction with the planet. This occurs over the horseshoe, or corotation region, that has a width x_s scaling as (Masset et al., 2006b),

$$x_s \sim a_p\sqrt{q/h} \,, \tag{1.19}$$

where q is the planet to star mass ratio, and $h = H/r$ is the disk aspect ratio between the scale height H and disk radius r. The gravitational back-reaction of the disk material at Lindblad resonances and the corotation region exerts the net type-I torque on the planet causing migration,

$$\Gamma_{\rm I} = \Gamma_{\rm Lindblad} + \Gamma_{\rm Corotation} \ . \tag{1.20}$$

Calculating the Lindblad torque involves a summation of the torque contributions at all Lindblad resonances. The torque from disk material in the outer resonances will *reduce* the planet's angular momentum, while that from material at inner resonances increases the planet's angular momentum. Using equation 1.18, and assuming a Keplerian disk, their radii r_L scale with the planet's radius r_p as,

$$r_L = r_p \left(\frac{m}{m \pm 1} \right)^{2/3} \ . \tag{1.21}$$

However, it must be noted that, due to the pressure support of disk material which causes gas to orbit at sub-Keplerian speeds, these resonant locations will be shifted. Provided the disk pressure decreases with radius (which will typically be the case), the outer Lindblad resonances will be shifted *closer* to the planet than the inner resonances. As a result, for typical disk structures, the net contribution from the outer Lindblad resonances will be larger than the inner resonances, leading to a total $\Gamma_{\rm Lindblad} < 0$ causing inward migration.

In complex 3D disk models, closed-form solutions of the Lindblad torque (found through summing over the contribution at all Lindblad resonances) cannot be obtained. However, significant insight to the effect of the Lindblad torque can be gained from models that linearize the planet's equations of motion. For example, Tanaka et al. (2002) use 2D linear analysis to obtain the following Lindblad torque assuming an isothermal disk,

$$\frac{\Gamma_{\rm Lindblad}}{\Gamma_0} = -3.2 - 1.468\alpha \ , \tag{1.22}$$

where α is the absolute value of the index of the radial disk surface density profile $\Sigma \sim r^{-\alpha}$, and the torque normalization is (Tanaka et al., 2002),

$$\Gamma_0 = \left(\frac{q}{h} \right)^2 \Sigma_p r_p^4 \Omega_p^2 \ , \tag{1.23}$$

with each of the above quantities determined at the planet's location.

Equation 1.22 illustrates that, for typical disk structures with $d\Sigma/dr < 0$, and $\alpha > 0$ (for example, a MMSN[2] with surface density index α=1.5), the Lindblad resonances' contribution to the type-I torque is negative and, if acting alone, gives rise to inward migration. Additionally, linear analysis of Lindblad torques predict quite extreme migration timescales, such as a $\sim 10^5$ year timescale for a 1 $M_\oplus$ core embedded in the MMSN disk. Furthermore, the migration timescale becomes even shorter for more massive planets due to the torque normalization's scaling with planet mass (equation 1.23). This short migration timescale of $\sim 10^5$ years has a significant discrepancy with observationally-inferred disk lifetimes of ~ 3 Myr, and is at least a factor of ten shorter than typical planet formation timescales in the core accretion scenario (Pollack et al., 1996). With these restrictions, the short migration timescale due to the Lindblad torque has become known as the *type-I migration problem*, as it can cause forming planetary cores to migrate into their host star much faster than they are able to accrete substantial disk material.

One can then consider the corotation torque in its ability to reduce the rapid inward migration rates caused by the Lindblad resonances' contribution. We recall that disk material in the corotation region will undergo horseshoe orbits induced by the planet's perturbation, during which half the orbit occurs at a slightly larger orbital radius than the planet, and the other half at slightly smaller orbit. One finds that, if the disk material properties in the corotation region are conserved throughout the horseshoe orbit, then the orbit-averaged corotation torque will be zero (Kley & Nelson, 2012). In this case, the positive and negative torque contributions (from the lower and higher portions of the horseshoe orbit respectively) will cancel since the disk material's properties are the same, thus exerting the same torque on the planet in both instances. In this case, the corotation torque is said to *saturate*, as it contributes no net torque on the forming planet.

The potential saturation of the corotation torque is therefore a significant consideration when determining type-I torques. If saturated, the corotation torque will not be able to slow or reverse the rapid inward Lindblad-driven migration. In the above case the saturation of the orbit-averaged corotation torque was caused by the disk material conserving its properties (i.e. temperature) throughout the horseshoe orbit. If the converse is true, and the material elements change throughout the horseshoe orbit, the orbit-averaged corotation torque will be non-zero. In this circumstance, the torque

[2]Minimum-Mass Solar Nebula, a disk model which considers the smallest amount of material required to form the Solar system planets (Weidenschilling, 1977a).

contributions from each fluid element in the lower and higher portions of their horseshoe orbits will not sum to zero.

Whether or not the corotation torque operates is therefore dependent on how quickly the disk material undergoing horseshoe orbits can mix with surrounding fluid elements and change properties. This mixing occurs on the disk's viscous timescale $\tau_{\rm vis}$. If $\tau_{\rm vis}$ is *shorter* than the horseshoe libration timescale $\tau_{\rm lib}$, then the material will change properties within the horseshoe orbits, exerting a non-zero orbit averaged torque. Conversely, if $\tau_{\rm lib} < \tau_{\rm vis}$, then the material will not change properties throughout the horseshoe orbit and the corotation torque will saturate (Masset, 2002; Dittkrist et al., 2014). These timescales, and thus the operation of the corotation torque itself, are set by the planet and local disk properties.

Calculating the effect of the corotation torque involves integrating over the contributions from disk material within the horseshoe region. Even in complex models, the comparison between $\tau_{\rm vis}$ and $\tau_{\rm lib}$ is relevant when determining whether or not the corotation torque saturates (McNally et al., 2017). For insight on the effect of the corotation torque, we return to the simplification of linear analysis of the planet's equations of motion from Tanaka et al. (2002), who obtain the following corotation torque in an isothermal disk,

$$\frac{\Gamma_{\rm corotation}}{\Gamma_0} = 1.36(1.5 - \alpha) \ , \tag{1.24}$$

where the torque normalization is listed in equation 1.23. One obtains a corotation torque of zero in a MMSN disk structure with $\alpha = 1.5$. While equation 1.24 shows that, for shallower surface density profiles, positive corotation torques (contributing to outward planet migration) can be obtained, the corotation torque's magnitude will often be smaller than that of the Lindblad torque (equation 1.22) for typical disk structures, resulting in net inward migration. Furthermore, due to the torque scaling (equation 1.23), even with the corotation torque's positive contribution, the overall negative type-I migration torque can still predict rapid inward migration timescales. We again note, however, that the Lindblad and corotation torques listed in equations 1.22 and 1.24, respectively, correspond to an isothermal disk, and the effect of the disk's temperature gradients have not yet been accounted for.

By combining linear estimates of the Lindblad torque with a non-linear adiabatic corotation

torque model, Paardekooper et al. (2010) obtain the following total type-I torque,

$$\gamma\frac{\Gamma_{\rm I}}{\Gamma_0} = -2.5 - 1.7\beta + 0.1\alpha + 1.1(1.5-\alpha) + 7.9\frac{\xi}{\gamma}\ , \tag{1.25}$$

where the torque normalization is the same as in previous cases (equation 1.23), γ is the adiabatic index, and α and β are the negative indices of the disk surface density $\Sigma \sim r^{-\alpha}$ (as previously) and temperature profiles, $T \sim r^{-\beta}$, respectively. Lastly, ξ is the disk entropy gradient,

$$\xi = \beta - (\gamma - 1)\alpha\ . \tag{1.26}$$

By relaxing the isothermal assumption and including the temperature gradient's effect on the type-I migration torque, Paardekooper et al. (2010) find a large reduction from the large, negative Lindblad-driven torques arising under the isothermal assumption. In particular, this reduction is due to the positive adiabatic corotation torque contribution. However, even with the above corrections, typical disk structures can still result in large inward migration rates.

Equation 1.25 shows that the total type-I migration torque is sensitive to the local disk surface density and temperature gradients. Locations of zero net type-I torque can arise at disk inhomogeneities, where there are sharp gradients in the disk surface density and/or temperature. Null-torque locations at disk inhomogeneities provide the physical basis for *planet traps*, as these regions of the disk provide local barriers against the typical inward, rapid type-I migration (Masset et al., 2006a; Sándor et al., 2011). Given that inward migration is expected to occur over the majority of disks' extents, these null torque locations can therefore be regarded as the most likely locations for planet formation to occur, indicating that planet traps play a key role in formation.

Examples of planet traps, or local inhomegeneities in the disk structure, are volatile transitions and their effect on the disk opacity (Lyra et al., 2010; Baillié et al., 2015), the heat transition between disk heating through accretion and radiation (Hasegawa & Pudritz, 2011), and the inner and outer edges of the dead zone where the local transition in $\alpha_{\rm turb}$ causes a local surface density transition (Matsumura et al., 2007). This set of traps has been shown to exist and migrate with disk evolution through the main planet forming ($\lesssim$ 30AU) region of the disk (Hasegawa & Pudritz, 2011), forming planets that correspond well with the observed M-a diagram (Hasegawa & Pudritz, 2012, 2013). We give a detailed description of our approach to planet migration and trapping beyond this section's

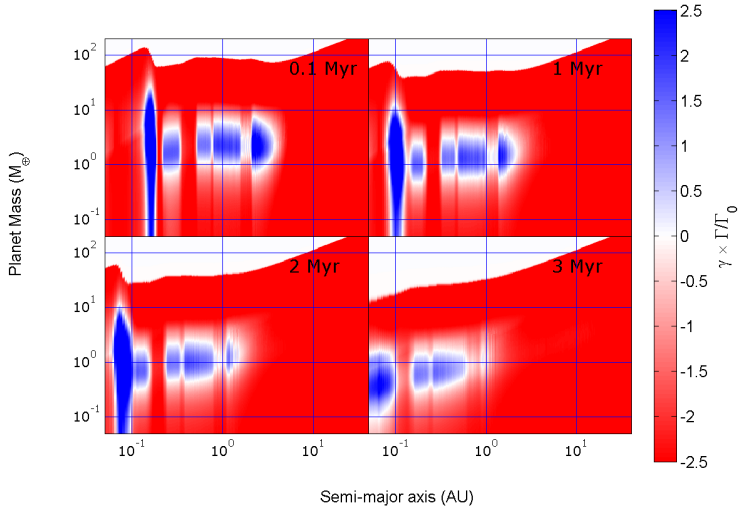

Figure 1.9: Type-I migration contour plots are shown throughout the evolution of an MMSN disk, as determined through numerical modelling. The colour indicates the direction of migration (red = inwards; blue = outwards) as dependent on planet mass and orbital radius. The white regions indicate null-torque locations or planet traps, which are shown to be mass-dependent in this model. Reproduced with permission from Coleman G.A.L., Nelson R.P., 2016, MNRAS, 460, 2779. DOI:10.1093/mnras/stw1177, figure 3 (left panel).

physical overview in section 2.3.2.

In figure 1.9, we show the result of a numerical calculation of type-I torques, that plots torque contours within the M-a space throughout the evolution of a MMSN disk as calculated in Coleman & Nelson (2016b). The colour scale indicates the direction of planet migration, with white regions corresponding to locations of zero net torque, or planet traps. Of particular interest is that many of the planet traps are *mass-dependent*, as the null torque regions pertain to only a finite range of planet masses. The mass-dependence of traps is an important result that arises when calculating corotation torque saturation, and has been shown in several other numerical type-I torque calculations (Hellary & Nelson, 2012; Dittkrist et al., 2014; Baillié et al., 2016; Coleman & Nelson, 2016b; Cridland et al., 2019a).

It is important to note that numerical calculations of type-I planet migration depend sensitively on the assumptions related to the underlying disk model, which can change the shape of migration contours and planet traps' locations. Furthermore, as these type-I migration models have been studied in the viscous framework, significant changes can be expected when they are applied within models of laminar disks that evolve via MHD-winds. For example, the positions and time evolution of

planet traps will change due to their dependence on the disk's Σ and T profiles that, in a disk-winds scenario, will evolve over different timescales and under a different mechanism (i.e. a wind-driven outflow). Additionally, in a pure laminar disk, the dead zone will not be present, as there will be no transition between turbulent and laminar regions within the disk. Recent models have investigated planet migration in winds-evolving, laminar disks, finding that resulting planet migration can be significantly changed compared to the viscous scenario (Ogihara et al., 2015; McNally et al., 2017, 2018, 2020). However, since investigations of planet formation in winds-evolving disks (for which, we recall there is recent observational and numerical evidence) are in relatively early phases of development, we may expect significant advances in our understanding of planet formation in the disk-winds framework in coming years.

1.2.2 Gap Opening & Type-II Migration

The type-II migration regime applies to planets massive enough to disrupt the overall disk structure through opening an annular gap at the planet's radius. Gaps have been observed in many protoplanetary disk's *dust* distributions through mm dust continuum observations (i.e. ALMA Partnership et al. 2015; Andrews et al. 2018; Long et al. 2018). While these observations probe the dust component of protoplanetary disks, they do not necessarily indicate the presence of a gap in the more massive gaseous component. However, taking the common assumption that the dust, to a degree, traces the overall gas distribution, observations of gaps in disks' dust distributions do allude to the presence of gaps in their gas distributions. Yen et al. (2016) & Yen et al. (2019) have recently used HCO^+ observations in HL Tau, a well-studied system revealed to have several gaps in its dust distribution (ALMA Partnership et al., 2015), to show correspondence between certain gaps revealed in both the dust and gas distributions (although, they did not find a match between all detected gaps in both components).

Once gap-opening has occurred, the planet's inward migration is governed by the disk's viscous timescale $\tau_{\rm vis} \simeq r^2/\nu$, as the planet's torque becomes an intermediary in accreting material between the gap outer and inner edge. An exception is very massive planets that well exceed their gap-opening mass, in which the planets' inertiae resist the disk's viscous evolution, and migrate at a slower rate than $\tau_{\rm vis}$ (Ivanov et al., 1999). The disk's viscous timescale is $\sim 10^6$ years, and predicts much less extreme migration rates than, for example, Lindblad-driven type-I torques. It therefore does not pose significant restrictions on planet formation considerations. We outline below the physical

criteria that must be met to transition into the type-II migration regime through gap-opening. In the case of trapped type-I migration, this transition to type-II migration also indicates the mass at which the planet will be able to migrate away from the trap it was forming within.

For a planet to open an annular gap, there are two physical criteria that must be met. First, the planet's Hill-radius,

$$R_H = a_p \left(\frac{M_p}{3M_*} \right)^{1/3} , \tag{1.27}$$

dependent on the planet (M_p) to star (M_*) mass ratio and orbital radius a_p, which signifies the planet's region of gravitational dominance in the disk, must be larger than the disk pressure scale height H. Otherwise, the gas pressure of the disk will prevent gap-opening. The second criteria is that the torque exerted by the planet must be sufficiently large to overcome disk viscosity, in that it must be able to clear out a gap within the disk viscous timescale. Otherwise disk viscosity will fill in the gap and will prevent gap-opening (Lin & Papaloizou, 1993).

While both of these effects can be individually considered to estimate the gap-opening mass, the semi-analytic model of Crida et al. (2006) combines both in the following gap-opening criterion, which will be satisfied by planets massive enough to overcome both the gas-pressure and viscosity gap-suppressing effects,

$$\frac{3}{4}\frac{H_p}{R_H} + \frac{50\nu_p}{q\Omega_p a_p^2} \leq 1 , \tag{1.28}$$

where q is the planet to star mass ratio, ν is the disk viscosity, and each of the above quantities are evaluated at the planet's location. Equation 1.28 predicts gap-opening masses of $\sim 25 - 30$ $M_\oplus$, whereas considering the pressure or viscous gap-opening processes individually predict slightly lower masses $\sim$ 15-20 $M_\oplus$. As the viscous gap suppression depends on the strength of disk viscosity and therefore MRI-turbulence, it will be small in laminar disks whose evolution is driven via MHD-winds with small ν. In this case, the pressure criterion will remain, leading to slightly lower gap-opening masses $\sim$ 15-20 $M_\oplus$ than the summed criteria with a nonzero viscosity contribution (equation 1.28).

Once this criterion has been met, the disk surface density will indeed be reduced within the gap. However, it has been shown that a portion of disk material can remain in the gap for planets that just exceed their gap-opening mass (Duffell, 2015). Additionally, it has been shown that significant disk material can flow through the gap (Lubow & D'Angelo, 2006). Since substantial material can remain in, and flow through the gap, the planet may be only partially detached from the disk material. This result is an important consideration for late stages of planet formation as discussed in the next

section 1.2.3. As planet mass increases beyond the gap-opening mass, both the gap width - scaling as $M_p^{1/3}$ following the Hill radius (equation 1.27) - and gap depth (the difference in surface density inside and outside the gap) have been shown to increase, thereby increasing the planet's detachment from the disk material (Fung & Chiang, 2016).

1.2.3 Core Accretion Model of Planet Formation

The core accretion model is a standard bottom-up approach to planet formation, whereby solids dispersed throughout the protoplanetary disk coalesce into a larger planetary core that is $\sim$ a few $M_\oplus$ capable of accreting disk gas. This model was introduced in Pollack et al. (1996) as a means of forming Jovian planets on several Myr timescales, which is comparable to observed disk lifetimes.

In figure 1.10, we show the formation of a gas giant calculated with the core accretion model. The time-evolution of the planet's total mass is plotted throughout formation, along with its accreted mass in solids and gas. This process can be broken up into three stages: planetary core growth through accretion of solids over several 10^5 years; slow, hydrostatic gas accretion spanning several Myrs; and lastly rapid runaway gas accretion wherein the planet accretes most of its gaseous envelope in a short 0.1 Myr timescale. Accretion rates in the core accretion model are dependent on the local density of material, set by the disk mass, radius, and in the case of solids, metallicity.

The disk lifetime sets the upper limit to the time in which planets can accrete disk material. Only in the case where the planet formation timescale is shorter than the disk lifetime will the full process (i.e. formation through the end of runaway growth) shown in figure 1.10 occur. Conversely, it can often be the case where the planet formation timescale exceeds the disk lifetime, which will result in the stranding of growing planets at an intermediate phase in the core accretion process. This scenario typically results in formation being terminated during the slow gas accretion phase, since its timescale of a few Myr is comparable to the disk lifetime. Through this process, low-mass planets - super Earths and Neptunes - can form, and are regarded as "failed cores" in the core accretion scenario, in the sense that they were not able to accrete a substantial atmosphere to form a gas giant (Alibert et al., 2006; Rogers et al., 2011; Hasegawa & Pudritz, 2012). In this regard, the core accretion model is not only useful in predicting the formation of gas giants, but can be used to understand the formation of the full observed range of planet masses.

Core accretion calculations usually begin by considering the growth of a planetary core that is a fraction $\sim 0.1\%$ $M_\oplus$. However, achieving growth over the many orders of magnitude in size from

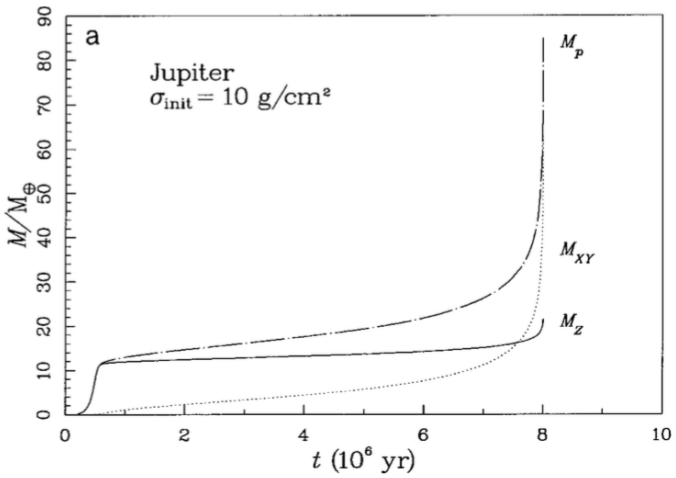

Figure 1.10: The formation of a gas giant planet in the core accretion model is shown. The time evolution of the planet's overall mass (M_p) is plotted, along with its accreted mass in solids M_Z and gas M_{XY}. The model is dependent on the disk surface density (labelled here as $\sigma_{\rm init}$), set by the disk's mass and radius. The core accretion model can form gas giants on timescales comparable to observed disk lifetimes. Reproduced with permission from Pollack J.B., Hubickyj O., Bodenheimer P., et al., 1996, Icarus, 124, 62. DOI:10.1006/icar.1996.0190, figure 1 (top, left panel), ©Elsevier.

the smallest solids in the disk, being dust that is up to mm-cm scales, to such a planetary core that is ∼km already presents theoretical challenges. Growth of solids past 10-100 cm is limited by both fragmentation and radial drift (recall section 1.1.2). Collisions between objects in this size range are unlikely to result in net growth due to their sufficiently large relative velocities that can overcome the grains' binding energy, resulting in fragmentation (Benz, 2000). Additionally, the short ∼100-1000 yr radial drift timescale of solids in this size range presents another theoretical barrier (Weidenschilling, 1977b). Combining these two considerations leads to the *metre-barrier problem*.

Overcoming the metre-barrier problem can be achieved by considering solid growth in regions of the disk that are locally enhanced in solids, such as at dust traps arising at disk pressure maxima, wherein radial dust drift attracts solids to its location. Such overdensities in solids have been observed in disk dust continuum observations (Dullemond et al., 2018). Streaming instability models (i.e. Youdin & Goodman 2005) can achieve a runaway growth process at such dust overdensities, as the local solid density enhancement increases the overall disk pressure maximum, which further funnels solids into the region. Solid growth in this region is able to overcome the metre-barrier, as it occurs in a region with no inward radial drift (i.e. at a pressure trap) and with large solid densities that enhance the collisional growth rate. Streaming instability models result in the formation of

planetesimals ($\sim$ m-km objects) over short (100-1000 yr) timescales (Johansen et al., 2007). When applied over the entire disk's extent, the streaming instability can provide a "sea" of planetesimals that are available for further collisional-accretion.

When considering the growth of a planetesimal or planetary core by the collisional accretion of solids, its effective accretion cross-section, $\Gamma_{\rm acc}$, is (Armitage, 2010),

$$\Gamma_{\rm acc} = \pi R_p^2 F_g^2 = \pi R_p^2 \left(1 + \frac{v_{\rm esc}^2}{v_{\rm rel}^2}\right) , \tag{1.29}$$

where the planet's physical cross-section πR_p^2 is enhanced by gravitational focusing, whose factor F_g^2 depends on the escape velocity from the planetesimal's surface $v_{\rm esc}$ and the relative velocity $v_{\rm rel}$ it has with solid material in the disk. Assuming all solid material swept by this cross-section throughout an orbit is accreted, the solid growth rate scales as,

$$\frac{dM}{dt} \sim \Sigma_p \Omega \pi R_p^2 \left(1 + \frac{v_{\rm esc}^2}{v_{\rm rel}^2}\right) , \tag{1.30}$$

where Σ_p is the local density of solids at the planet's location, and Ω is its orbital frequency.

Depending on the mass of the accreting object, one can define two distinct growth regimes with equation 1.30. In the first case, we consider a relatively low-mass object such as a planetesimal that will not affect the velocity of nearby solids. In this circumstance, using $v_{\rm esc}^2 \sim M_p/R_p$ and $R_p \sim M_p^{1/3}$, an accretion rate scaling of $\dot{M} \sim \Sigma_p M_p^{4/3}$ and growth timescale $\tau \sim M/\dot{M} \sim M_p^{-1/3}$ results. As the growth-timescale has an inverse scaling with mass, more massive planetesimals will grow faster, and initial differences in the masses of multiple growing planetesimals will be amplified in time. Solid accretion in this regime is therefore a runaway process that will lead to the formation of planetary cores $\sim 0.1\%$ $M_\oplus$ that dominate their respective regions of the disk.

At such planet core masses, the second growth regime applies, whereby the core is massive enough to affect the velocity dispersion of nearby solids. In this case, one can apply a scaling of the relative velocities of nearby solids of $v_{\rm rel} \sim M_p^{1/3}$ (Chambers, 2010). Similar scaling relations as the previous case can be used to infer an accretion rate of $\dot{M} \sim \Sigma_p M_p^{2/3}$, leading to a growth timescale $\tau \sim M_p^{1/3}$. This second so-called *oligarchic growth* regime is therefore convergent in nature, as more massive cores will accrete slower than less massive cores due to the increased velocity dispersion they cause in nearby solids.

Models of core growth via solid accretion can be categorized based on the assumed size range of accreted solids, with growth taking place through either the accretion of $\sim$ m-km sized *planetesimals* or through the accretion of 1-10 cm *pebbles*. While the above considerations and scalings can apply directly to planetesimal accretion, the accretion cross-section presented in equation 1.29 will be altered in the case of pebble accretion. In addition to gravitational focusing, atmospheric focusing from drag on incoming pebbles will enhance the forming core's cross section (Lambrechts & Johansen, 2012; Chambers, 2014). Even at low masses, the gravitational field of the growing core will cause an enhancement in the surrounding gas density, applying a drag force on pebbles. This effect is negligible in the case of planetesimals due to their larger inertias.

In the traditional case of planetesimal accretion, a so-called "planet-forming" region at disk radii $\lesssim$ 30 AU can arise, as accretion rates at larger separations are small leading to large solid growth timescales comparable to the disk lifetime. Small solid accretion rates in the outer disk arise due to a decrease in both orbital frequency and planetesimal surface density Σ_p with disk radius (the latter following, to some degree, the overall gas surface density decrease). Additionally, planetesimal accretion rates are typically lower than those predicted through pebble accretion due to the lack of atmospheric focusing.

Pebble accretion models predict quite large solid accretion rates, suggesting rapid solid growth (Lambrechts & Johansen, 2012; Levison et al., 2015). Furthermore, these models may not be restricted to small orbital radii as extended distributions of pebbles (i.e. larger Σ_p beyond 30 AU) can be maintained, following the disk's dust distribution. However, a significant theoretical restriction in pebble accretion theory arises as incoming pebbles have been shown to ablate or vaporize as they pass through the envelope of the forming planetary core when the core mass exceeds $\sim$ 0.6 $M_\oplus$ (Alibert, 2017; Brouwers et al., 2018). In this case, the incoming material would not contribute mass to the planetary core, but rather becomes dispersed through the envelope which may be recycled back into the disk at these low planet masses (Ormel et al., 2015). Recently, Brouwers & Ormel (2020) have shown that ablated pebbles can contribute to the overall planet mass through enriching the envelope's metallicity, which can sustain growth until the point of non-negligible gas accretion rates. This result can circumvent the issue of a maximum core mass that arises when considering pebble ablation, but requires that the metallicity-enriched envelope is sufficiently retained, and not entirely recycled back into the disk.

Such a theoretical constraint does not apply to planetesimals, as Alibert (2017) show that plan-

etesimals are not disrupted as they pass through envelopes of up to 3 $M_\oplus$. An atmosphere this massive would not be acquired until significant gas accretion has occurred at a later stage in formation, and thus does not pose a restriction on solid core growth in the oligarchic phase. However, when combining these two approaches, the high predicted accretion rates may suggest that growth quickly takes place via accretion of pebbles up to this theoretical limit of several 0.1 $M_\oplus$, with planetesimal accretion being applicable for growth through to higher masses. However, the convergent nature of the oligarchic growth timescale gives a theoretical indication that such a change in initial planetesimal accretion mass (i.e. supplied by the outcome of pebble accretion) would not drastically change the result of oligarchic growth.

The core accretion model transitions to a gas accretion regime when the hydrostatic balance of gas surrounding the forming planet can no longer be maintained. Throughout solid accretion, the heat released from accretion of incoming solids acts to maintain the envelope's equilibrium, preventing gas accretion. As the core becomes more massive, and/or the solid accretion rate decreases, this equilibrium is no longer sustained, allowing inflow, or accretion, of surrounding gas. This *critical core mass* $M_{\rm crit}$ represents the onset of gas accretion, and is presented in Ikoma et al. (2000) as,

$$M_{\rm crit} \simeq 7 \left(\frac{\dot{M}_{\rm core}}{10^{-7}\,{\rm M}_\oplus\,{\rm yr}^{-1}} \right)^q \left(\frac{\kappa_{\rm env}}{1\,{\rm cm}^2\,{\rm g}^{-1}} \right)^s {\rm M}_\oplus \ , \tag{1.31}$$

where $\kappa_{\rm env}$ represents the Rosseland-mean opacity of the surrounding envelope, and the values of both parameters q and s are 0.2-0.3. Typical values of $M_{\rm crit}$ are $\sim$ 3-10 $M_\oplus$, depending on the setting of envelope opacity.

At masses just above $M_{\rm crit}$, gas accretion takes place slowly. Recalling figure 1.10, this slow gas accretion phase occurs over a few Myr, where the planet slowly grows up to $\sim$30 $M_\oplus$. A full treatment of gas accretion involves modelling the forming planet's atmosphere. As growth is slow in this regime, and the atmosphere is in quasi-hydrostatic balance, one can use the stellar structure equations to do so. Accretion of gas in this regime is limited by the atmosphere's ability to cool and contract, which is physically set by the envelope opacity $\kappa_{\rm env}$. The slow gas accretion timescale is then defined by the Kelvin-Helmholtz timescale (Ikoma et al., 2000),

$$\tau_{\rm kh} \simeq 10^c \left(\frac{M_p}{M_\oplus} \right)^{-d} {\rm yr} \ , \tag{1.32}$$

where the Kelvin-Helmholtz parameters $c \simeq 7 - 9$ and $d \simeq 2 - 3$ are dependent on the envelope opacity.

In this regard, the results of gas accretion in the core accretion model are dependent on the value of the forming planets' envelope opacities, as it is a key factor in the mass at which gas accretion initiates, and in determining the rate of gas accretion (equations 1.31 & 1.32, respectively). On this basis, we perform a detailed analysis of this physical quantity in its effect on outcomes of the core accretion model in chapter 2.

Due to the Kevin-Helmholtz timescale's inverse scaling with planet mass, gas accretion will become a runaway process at large masses ~ 30 $M_\oplus$. In this final stage of the core accretion model, a forming gas giant accretes a significant amount ($\gtrsim 50\%$) of its final mass in a short $\sim 10^5$ year timescale. However, as this is a runaway process, it raises the question of how gas accretion onto planets is terminated. The most massive observed exoplanets are $\lesssim 10^4$ $M_\oplus$, so what determines how massive planets can become? The overall amount of remaining disk material sets an upper limit, but other physical considerations can provide a better constraint. Due to the rapid nature of runaway growth which occurs on timescales orders of magnitude shorter than the disk lifetime, disk dissipation is unlikely to occur during this final phase and therefore does not provide an explanation.

Recalling section 1.2.2, massive planets will become detached from the disk as their gravitational torque will disrupt the disk structure through opening an annular gap. Gap width and depth also scales with planet mass, so as a planet grows beyond its gap opening mass (equation 1.28) it will become further detached from the disk material. It has been shown that significant accretion can be sustained after gap opening (Kley, 1999), and that substantial disk material flows through the gap that can supply this accretion onto the planet (Morbidelli et al., 2014). These results justify the application of the Kelvin-Helmholtz timescale (equation 1.32) to determine gas accretion rates throughout the runaway growth stage. While uncertainties remain in the process of terminating gas accretion, it is likely linked to gap-opening. Following this argument, Hasegawa & Pudritz (2013) relate a planet's maximum mass with its gap opening mass through the parameter $f_{\rm max}$, setting $M_{\rm max} = f_{\rm max} M_{\rm gap}$.

A competing theory to late stages of planet formation is the disk-limited accretion approach (Tanigawa & Tanaka, 2016). In this model, the maximum accretion rate onto a planet that has opened a gap is set by the disk accretion rate, as opposed to being limited only by the planet's envelope opacity as is the case when applying the Kelvin-Helmholtz timescale. With this approach,

one needs to use a parameter relating the fraction of the disk accretion rate to the accretion rate onto the planet. An advantage of this approach is that one does not have to manually set an upper limit (i.e. through the use of the $f_{\rm max}$ parameter above) to the planet's mass as the disk accretion rate is a decreasing function of time, and the gas accretion rate will therefore also decay. However, the necessary parameter relating disk to planet accretion serves a similar purpose as $f_{\rm max}$ in that it ultimately determines how massive a planet can grow in the disk-limited approach.

Finally, we highlight another physical means of truncating gas accretion, through the interaction of a forming planet's magnetic field and the disk material (Batygin, 2018). In this mechanism, the accretion cross-section that results from disk material flowing towards the planet following its magnetic field lines has an inverse scaling with planet mass. Cridland (2018) used this model of gas accretion termination to show that it produces final planet masses comparable to observed gas giants. However, one can obtain different final planet masses with this approach by considering different magnetic field strengths produced by the forming planet. Ultimately, all three models of gas accretion termination rely on a parameter that plays a significant role in determining the maximum masses planets can achieve.

1.3 Post-Disk Evolution

Typical observed exoplanets or exoplanetary systems will have evolved over ∼Gyr timescales past the protoplanetary disk phase. It is thus important to account for means through which their observed properties can change between formation (i.e. what follows immediately from the disk phase) and the time they are observed. The results of planet formation during the disk phase provide necessary initial conditions for any post-disk evolutionary scenario, and in this regard observed planets' properties indeed remain linked to their formation.

Post-disk evolutionary mechanisms encompass a wide range of physical effects. Most importantly for our considerations are mechanisms that change planets' masses and orbital radii from what forms out of the disk phase, thereby directly affecting the M-a and M-R distributions. For example, the wide range of dynamics effects between objects that form out of the disk (perhaps multiple planets that may have a range of masses, and leftover solid planetesimals) can contribute to *both* accretion and migration. Additionally, there are several mechanisms that can contribute to atmospheric mass loss, which will significantly affect planet masses and radii.

In this section, we focus on these two key post-disk evolution mechanisms and their effect on observed planet distributions, first covering atmospheric mass loss in section 1.3.1, and planet gravitational dynamics in section 1.3.2. We consider atmospheric mass-loss through photoevaporation in our approach, described in section 4.2.4. While we do not include gravitational dynamics between multiple forming planets, we recognize this as an important extension of our model and prospective future work. We also recognize that there are additional post-disk evolution effects that can alter planets' physical and/or chemical structures that are not discussed here. However, our focus in this section is to cover these two basic mechanisms that directly affect the M-a and M-R distributions, and likely play an important role in the evolution of the majority of planetary systems.

1.3.1 Atmospheric Mass-Loss

Following the disk phase, planet atmospheres will be puffy as planets release their acquired heats of formation. During this phase, coupled with the loss of external pressure that was provided from the protoplanetary disk gas, substantial atmospheric loss can occur. Atmospheric mass-loss will be an important consideration for low-mass super Earths and Neptunes, whereas atmospheric loss on massive gas giants may be insignificant due to their larger surface gravities. As an atmosphere is the lightest material out of which a planet forms, it has the largest effect on a planet's overall transit radius - the location in the atmosphere where the optical depth $\tau = 2/3$ (we simply refer to a planet's *transit radius* as its radius, as this is what is being measured in transit surveys). For example, Lopez & Fortney (2013) show that only a small amount of planet atmosphere ($\sim 1\%$) can double a planet's radius. Therefore, it is important to not only account for gas that is accreted onto planets, but also the amount of this gas that is retained following the disk phase when understanding the M-R relation. Here we will discuss two mechanisms that have been shown to be effective in driving atmospheric mass-loss on low-mass planets.

In photoevaporative mass-loss, the high energy X-ray and UV radiation from the host star imparts energy into the upper layers of a planet atmosphere, driving escape from the planet's gravitational potential (Owen & Jackson, 2012; Owen & Wu, 2013). As this mechanism is driven via radiation, its effectiveness will depend on the flux received by the planet scaling with orbital radius as a_p^{-2}. Therefore, photoevaporation will be more effective in driving mass loss on planets with small orbital radii. Photoevaporative mass-loss will also be dependent upon the host-star's age, as the FUV luminosity will decrease as the star evolves towards the main sequence (Ribas et al., 2005).

The core-driven mass loss offers an alternative scenario, whereby atmospheric mass loss occurs through the upper layers of a planet's atmosphere as a planet releases its heat of formation, with luminosity generated by the planet core (Ginzburg et al., 2018). The result of core-powered mass loss depends on the comparison between the cooling and mass loss timescales, as planets that are able to cool quickly (faster than the mass-loss timescale) are able to retain their accreted atmospheres (Gupta & Schlichting, 2019).

Both models (Owen & Wu, 2017; Gupta & Schlichting, 2019) have been shown to reproduce the observed valley in planet occurrence rate at $\sim$1.5-2 $R_\oplus$, as observed with the California-Kepler survey (Fulton et al., 2017). Physically, this radius valley can be understood as a separation between low-mass super Earths whose gravitational potentials are insufficient to retain accreted gas, and more massive sub-Neptunes that do retain their atmospheres (Rogers, 2015).

Lastly, we mention collisional impacts as an additional atmospheric mass-loss mechanism (Schlichting et al., 2015). In this circumstance, energy imparted through impacts, such as with planetesimals present as leftover debris from the disk phase, can drive atmospheric loss. Depending on a planet's collisional history, energy imparted via impacts may be sufficient to remove its entire accreted atmosphere.

1.3.2 Planet Dynamics & Scattering

Gravitational dynamics will play a significant role in shaping the evolution of planetary systems. Following protoplanetary disk dissipation, there will be a substantial amount of leftover solid material (so-called debris) as indicated through debris-disk observations (i.e. Hughes et al., 2018). Through gravitational interaction with formed planets, this debris will need to be accreted or scattered (ejected from the system) in order to achieve a dynamically evolved planetary system architecture. Additionally, the gravitational influence between multiple formed planets needs to be accounted for when considering the stability of a newly-formed planetary system over long timescales. When present, the protoplanetary disk material damps any induced eccentricities on short timescales (Kley & Nelson, 2012). Therefore, gravitational interactions between multiple formed planets following the disk phase are necessary to achieve the wide range of orbital eccentricities seen in observations (recalling the eccentricity-orbital radius diagram, figure 1.3).

When such a planetary system forms that is closely-packed, in the sense that mutual gravitational interactions will be significant, eccentricities in one or more planets can be induced (Chatterjee et al.,

2008; Ford & Rasio, 2008). Over time, these induced orbital eccentricities can lead to orbit crossings or overlap of the planets' Hill spheres, defining their regions of gravitational influence in the planetary system. This circumstance will lead to a collision or scattering event, whereby a planet is ejected from the system. Such scattering events can be significant in driving high orbital eccentricities in the remaining planet's orbit. As an additional consequence for planetary orbits, a scattering event can reduce the remaining planet's semi-major axis by up to a factor of two, which would be the case for scattering between two equal-mass planets. In this regard, planet scattering can also effect the overall M-a distribution. Planet scattering has been shown to generate large orbital eccentricities comparable to observations in a population synthesis framework in Ida et al. (2013).

Additionally, the dynamical assembly of planetesimals and/or planetary cores leftover from the disk phase offers an additional means of forming low-mass terrestrial planets (see review by Raymond et al. 2014). In this scenario, these objects will be under the dynamical influence of any massive planets (i.e. warm Jupiters, or super Earths) that form during the disk phase, which can perturb planetesimal orbits to induce collisions.

1.4 Planet Interior & Atmospheric Structure

Planetary structure calculations are a necessary inclusion in our approach as they determine planets' overall radii, allowing for comparisons between synthetic and observed planetary distributions on the M-R diagram. Planet formation models that include disk chemistry result in the determination of planets' solid core and atmospheric masses, solid and gas chemical abundances, as well as semi-major axes - all of which are inputs to planetary structure models that determine each planet's density profile $\rho(r)$ and overall radius R_p. We recall that a main observational result of the planetary M-R diagram is that, particularly super Earths and Neptunes show a range of radii or mean densities at any given planetary mass. In terms of the two main planetary components - a solid core and gaseous envelope - a range in density can be achieved through differences in solid compositions and atmospheric masses, respectively, and planetary structure is needed to translate these results of planet formation onto the M-R distribution in order to compare with observations.

A standard approach in the structure modelling of a solid planetary core is assuming a spherical, differentiated planet composed of three bulk materials: an innermost iron core, a rocky, silicate (enstatite $MgSiO_3$) mantle, and an upper water/ice layer (Valencia et al., 2006; Seager et al., 2007).

The mass fractions of each of these three components, as well as the total solid mass of each planet, are established in our planet formation calculations. Modelling the planet's solid component consists of solving the standard (stellar) structure equations of mass continuity and hydrostatic equilibrium that we list in chapter 4, Appendix B. These structure equations can be integrated when combined with equations of state $\rho(T, P)$ for each component.

For the iron and silicate components of the planetary core, the high pressures (~ 100 GPa) in the planet's interior cause pressure effects to dominate over those of temperature, and their equations of state can be accurately approximated as temperature-independent $\rho \simeq \rho(P)$. The standard approach is to adopt the perovskite phase of $MgSiO_3$ in the silicate layer, and the hexagonal closely-packed phase of iron (Seager et al., 2007; Zeng & Sasselov, 2013).

Modelling of water's equation of state is more involved, as it undergoes a number of phase transitions throughout the temperature and pressure regime of the upper layers of a planetary core (Thomas & Madhusudhan, 2016). The relevant water phases, however, can be tracked throughout the temperatures and pressures of this upper layer, having the equation of state updated for each shell (radius 'step') in the integration (Zeng & Sasselov, 2013). With water being the lightest of the three solid components, and least compressed as it exists on the upper layers of the solid core, accurate modelling of its equation of state is important as its treatment has the largest influence on a planet's radius among the three solid components.

Before incorporating planetary atmospheres and considering, for example, planets composed entirely of solid material, structure models can already demonstrate how a range in planetary compositions can be achieved. The ternary diagrams of Valencia et al. (2007), for instance, show that at a given mass, different planetary radii are attained depending on composition (ie. mass fractions among each of the three components). Furthermore, their results nicely illustrate the *degeneracy* of this problem, in that the same core radius can result from different compositions at a given mass. In other words, if a planet's mass and radius is known, its composition is constrained but not entirely determined. Our approach combines models of planet formation and disk chemistry to track planet compositions and lift this degeneracy, as it determines the masses and abundances of each planet that are then used to calculate planet radii.

As a gaseous envelope is the lightest material contributing to a planet's overall mass, it will have the largest influence on a planet's radius. A solid planet's transit radius can be greatly increased by only a small amount of atmospheric mass. For example, a factor of 2 increase in R_p results

from only a 1% mass addition of atmosphere (Lopez & Fortney, 2013). A planet's transit depth, defining its radius, is set at the point in its atmosphere where the optical depth to transmitting stellar radiation is $\tau = 2/3$. This point in the planet's atmosphere will depend on the amount of gas it has accreted and its overall temperature-pressure profile, and careful modelling of atmospheric structure is important as it has a significant effect on a planet's overall radius.

Modelling structure of planetary atmospheres also involves solving the equations of mass continuity and hydrostatic balance in addition to the structure equation of energy transport (also listed in chapter 4, Appendix B). As in standard stellar structure calculations, solving the energy transport equation involves determining the local radiative and adiabatic temperature gradients, with the steeper temperature gradient establishing the energy transport mechanism at a given radius. In the temperature and pressure regime associated with super Earth atmospheres, this comparison yields a lower convective region (closer to the planetary surface), and an upper more tenuous radiative region (Piso & Youdin, 2014).

A planet's atmospheric temperature structure is affected by two heating sources: external heating from the host star, and internal heating from radioactive decay of isotopes. Gravitational contraction is another important source of internal heating for gas giants, but is expected to be minimal for super Earths. The above sources of atmospheric heating are again set by formation conditions, as the temperature from host-star radiation is set by the planet's semi-major axis, and the amount of radioactive isotopes scales with the planet's overall mass in rocky silicate material (Mordasini et al., 2012c). These factors, in addition to the amount of accreted gas that is also determined during formation and post-disk evolution, shows that atmospheric structure and therefore a planet's overall radius is very much linked to its formation history.

A common approach for the atmospheric equation of state is to consider a Solar mix of hydrogen and helium, as these are the two most abundant gases throughout the Solar nebula. Assuming a complete hydrogen and helium atmosphere can be justified as secondary gas abundances (i.e. H_2O, CO, CH_4, N_2, NH_3) are factors of $\sim$ 1000 less than those of H_2 and He (Asplund et al., 2009; Pignatale et al., 2011). We note however, that this assumed composition pertains to modelling the atmospheric structure of gas directly accreted from the protoplanetary disk, and applies to planets that retain their accreted atmospheres. Secondary atmospheres on Solar system terrestrial planets, for example, will have very different compositions dominated by secondary gases.

Another common assumption in atmospheric modelling is to use a grey, or wavelength-independent

Rosseland-mean opacity. We take this approach, for instance, in Chapter 4, using opacity tables of Freedman et al. (2008) corresponding to Solar-metallicity gas. A limitation of this assumption is that it does not allow for different opacities in the optical and infrared wavelength ranges, which are crucial in their effect on planetary heating and cooling, respectively, as the former is the main waveband of incoming stellar radiation, and the latter the waveband of thermal emission from the planet's surface. Atmospheric composition has an important effect on (particularly optical and infrared) atmospheric opacities, as greenhouse gases such as water vapour or methane, for instance, will significantly increase a planet's infrared opacity and inhibit cooling. A semi-grey (or two-stream) model, such as that used in Guillot (2010), allows for unique optical and infrared opacities and incorporates their effect on heating and cooling when determining the atmospheric temperature-pressure profiles. A full wavelength-dependent atmospheric opacity can be achieved through detailed modelling that is self-consistently linked to planet composition (i.e. Mollière et al. 2015), by considering all molecular transitions of gases present in the atmosphere in a given wavelength range.

1.5 Planet Population Synthesis

Throughout this thesis, we use the technique of planet population synthesis in order to make the connection between planet formation theory and observed planetary populations. Most generally, this technique involves the statistical variation of intrinsic and/or extrinsic model parameters in a Monte-Carlo calculation, computing large numbers of planet formation models and obtaining a final synthetic planet population. The variation in outcomes of the planet formation models can then be attributed to the ranges of these varied parameters, whether they are constrained observationally, physically, or are unconstrained. In semi-analytic planet formation theory, there can be many intrinsic model parameters owing to the fact that there can be several combined sub-models (ie. disk evolution, planet formation, migration, etc.). Population synthesis, for example, can be used to investigate model parameter(s), or an entire sub-model in its effect on the resulting planet populations.

A powerful advantage of planet population synthesis, is to rather use it to explore the effects of protoplanetary disk parameters set during protostellar collapse, which are extrinsic parameters to a planet formation model. These parameters play a crucial role in the outcome of planet formation calculations. Disk mass, for instance, sets the density of material throughout the disk, and metallicity

sets the overall dust-to-gas ratio, each affecting solid accretion or overall planet formation timescales (Pollack et al., 1996). The disk lifetime is another key disk parameter as it sets the upper limit to the time for which planets can accrete disk material. Comparing planet formation timescales to the disk lifetime illustrates the formation criteria for different planet classes, with super Earths for instance being planets whose formation timescales exceed their disk lifetimes in the failed core scenario (Hasegawa & Pudritz, 2012; Alessi et al., 2017).

Examining the effects of disk properties on planet formation is precisely our approach in using population synthesis models throughout this thesis, as it allows us to link the observed variability in protoplanetary disks to resulting planet populations. The final synthetic populations' distributions on the M-a or M-R diagram can then be compared to observations. These comparisons can be used to constrain model parameters, for example, by finding the best correspondence between the two distributions. One can also readily see the effect of model assumptions by comparing resulting planet populations with and without a particular physical process included. We therefore emphasize that this approach allows our understanding of planet formation to be shaped both by our understanding of disk properties, as their observationally-constrained distributions are input as priors to the our calculations, as well as by exoplanet distributions, as we constrain our model in its comparisons with the observed M-a and M-R relations.

In this framework, distributions of protoplanetary disk mass and lifetime are typically modelled using log-normal distributions (Benz et al. (2014); see also section 2.2). A log-normal distribution is a natural fit for the disk mass as a protoplanetary disk's origins is the turbulent collapse of molecular cloud core. Our observational constraint on disk lifetimes comes from measuring the fraction of stars in young clusters that display infrared excesses (indicating presence of dusty, high infrared opacity disks), and considering this fraction as a function of the cluster's age (Hernández et al., 2007; Ribas et al., 2014). These observations give a range of possible disk lifetimes of $\sim$ 1-10 Myr, with a mean of 3 Myr and a standard deviation in the log-normal function covering this range being a standard approach.

Observationally constraining disk masses involves dust continuum observations combined with an assumed dust-to-gas ratio, typically 1:100 (Isella et al., 2009; Andrews et al., 2010). A difficulty in this approach, when modelling evolving disks, is that observed disks have evolved over $\sim$ Myr timescales. As a time-decreasing disk mass is a standard result in disk evolution models (i.e. Hueso & Guillot, 2005; Chambers, 2009; Shadmehri & Ghoreyshi, 2019), observationally-estimated disk

masses (which may be close to a standard Minimum Mass Solar Nebula) may be factors of $\gtrsim$100 reduced from their initial mass at the time of formation. Protostellar collapse models can also offer constraints on this parameter (i.e. Bate 2018). While collapse models show that a wide range of initial disk masses are plausible, 0.1 $M_\odot$ is an acceptable average of these results. This mass is commonly used for a mean initial disk mass in the log-normal function, with spread covering the $\sim \pm$ 1 dex uncertainty (Benz et al., 2014). Another means of characterizing the variability in disk mass is through a scaling factor in a surface density distribution, as ultimately the disk mass's effect on planet formation is through the disk surface density (i.e. Ida & Lin 2004a).

For the observationally-constrained disk metallicity distribution, a Gaussian function with average near Solar metallicity and spread in [Fe/H] of $\sim$ 0.2 is used (Mordasini et al., 2009a; Benz et al., 2014). This average and standard deviation achieve a metallicity distribution that compares well with G- and K-type stars in the Solar neighbourhood found with the CORALIE survey (Queloz et al., 2000; Udry et al., 2000; Santos et al., 2003). More recently, the sample of stars in the California-Kepler Survey (Kepler objects of interest) show a similar metallicity distribution (Petigura et al., 2018). We constrain the disk metallicity distribution by plotting planet-hosting stellar metallicities (using data from exoplanets.org, Han et al. 2014), and fitting a Gaussian distribution, for which we find a comparable average and standard deviation as above (see section 2.2). We note that random samples of field stars have been found to have $\sim$ 0.1-0.2 dex lower metallicities than planet-hosting stars (Santos et al., 2003; Nordström et al., 2004; Fischer & Valenti, 2005; Petigura et al., 2018), and fitting only to planet-hosting stars may bias a model to over-produce massive gas giants.

This approach assumes these disk parameters to be statistically independent, however from a physical standpoint this likely is not the case. Disk dissipation, which sets disk lifetime, is driven at least in part through photoevaporation from the host-star's XUV flux, and the disk's column density and metallicity will affect its rate of dissipation (Ercolano & Clarke, 2010; Nakatani et al., 2017). One could in principle correlate these quantities in the population synthesis framework, however this may be unjustified as disk lifetimes and masses remain loosely observationally-constrained.

This correlation among host-star and disk properties also alludes to the difficulty in self-consistently including stellar mass as an additional parameter in the population synthesis approach, which has been done in previous works (Ida & Lin, 2005; Alibert et al., 2011). It remains unclear how the disk parameters' distributions scale with host-stellar mass or spectral class. Including stellar mass in population synthesis is an interesting consideration for future work, for example in modelling planet

formation around M-dwarf stars to compare with data coming from the TESS mission. However, due to this uncertainty in disk parameters and how they may scale with stellar mass, we restrict our focus to a Sun-like host star. In doing so, we are still able to compare to the wealth of Kepler data which has detected the majority of known exoplanets around G-type stars.

The method of planet population synthesis has been used in many previous works (i.e. Ida & Lin 2004a; Mordasini et al. 2009a), with the effect of type-I migration rates highlighted in Ida & Lin (2008). Population synthesis has been considered in a planet formation framework including planet traps in Hasegawa & Pudritz (2012) and Hasegawa & Pudritz (2013), which our approach in this thesis builds upon. The effect of disk metallicity on solid accretion timescales and planet populations was previously considered in Ida & Lin (2004b); Mordasini et al. (2012a); Hasegawa & Pudritz (2014). Lastly, population synthesis has been used in a pebble accretion (as opposed to planetesimal) framework in works such as Bitsch et al. (2015) and Ali-Dib (2017).

1.6 Overview of Strategy & Results

The following chapters of this thesis present our model's theoretical framework and our main findings. We investigate various mechanisms in the planet formation process in how they shape synthetic planet distributions, constraining associated quantities through comparing with observations. Our goal with this strategy is to develop a complete theoretical planet formation framework that links the observed variability in protoplanetary disk conditions to the distribution of observed exoplanets on the M-a and M-R diagrams. In this section we now present an outline of the remaining thesis chapters, giving an overview of our approach to this problem and our main findings.

We first consider (in results chapters 2-4) protoplanetary disk evolution in a generalized viscous framework. As recent observations have found low-levels of turbulence in disks (Flaherty et al., 2018), we adopt an $\alpha_{\rm turb} = 10^{-3}$ that is within current measured constraints. We model planet formation in the standard core accretion framework (Pollack et al., 1996), considering solid core growth to take place via accretion of planetesimals, and modelling subsequent gas accretion through the Kelvin-Helmholtz timescale whose rate is determined by the forming planets' atmospheric opacities.

Planet traps, or zero-torque locations in the disk associated with inhomogeneities, play a key role in our approach, as they provide barriers to otherwise rapid type-I migration. They are therefore crucial in determining the orbital radius-evolution of low mass forming cores, and play a significant

role in shaping our synthetic planet distributions. The traps we include (described in detail in section 2.3.3) are the water ice line, the transition between laminar and turbulent regions at the outer edge of the dead zone, and the heat transition between generalized viscous heating and heating through radiation from the host star. We consider these traps as they are the disk inhomogeneities that exist and evolve throughout the main planet forming ($\lesssim$ 10-20 AU) region of the disk, as planetesimal accretion rates are negligibly small outside of this extent.

As we have discussed in section 1.1, MHD simulations have shown that non-ideal MHD effects can suppress MRI-turbulence over large regions of disks' vertical and radial extents (i.e. Bai & Stone, 2013). As a result, disk evolution will not take place under the traditionally-studied viscous framework that we consider in chapters 2-4, but rather under the effects of MHD disk winds. Accordingly, we incorporate a simple model of winds-driven disk evolution into our framework in chapter 5. The positions of planet traps will be affected in this alternate disk evolution picture - most directly the dead zone's outer edge since it requires a transition between laminar and turbulent regions of the disk, with the latter not present in a pure winds-driven disk. Our strategy in chapters 2-4 is to first undergo a comprehensive investigation of a viscous evolution framework before considering the alternate picture of evolution via disk winds (for which, recent observational and numerical advancements lend supporting evidence).

All of our calculations utilize the method of planet population synthesis, through which we recall that protoplanetary disk parameters' distributions - mass, lifetime, and metallicity - are sampled as inputs to thousands of planet formation models. We regard these disk parameters as external to the calculation, as they are set during disk formation through protostellar collapse. Among all of our sub-models (disk, migration, planet formation, etc.), there is only one true model parameter that is stochastically varied in the population synthesis framework, being a parameter $f_{\rm max}$ that pre-determines the maximum mass a planet can attain through gas accretion, related to the mass at which it opens an annular gap in the disk (this is discussed in section 2.3.3). We find that variation of this parameter is necessary to obtain a range in masses of gas giants that match observations.

While this treatment of prescribing planets' maximum masses simplifies the complex problem of terminating gas accretion onto massive gas giants, it does relate their final masses to their gap-opening mass which likely has a significant physical role in the gas-accretion termination process. Furthermore, hydrodynamic models of gas flow within annular gaps have shown that planets who exceed their gap opening mass are only partially detached from the disk, and that substantial material

can flow through the gap that can supply the Kelvin-Helmholtz accretion rate (Morbidelli et al., 2014; Lambrechts et al., 2019). Lastly, our prescribed range of $f_{\max}$ leads to a range of maximum planet masses that has good correspondence with the gas-giant mass range seen on the M-a diagram. Additionally, the range of maximum masses we obtain with this parameterization are comparable to other, parameter-dependent models of terminating massive planets' gas accretion (i.e. disk-limited accretion, or magnetic termination; see section 2.3.3).

Our use of the population synthesis technique is therefore not an exercise in the variation of many unconstrained model parameters to discern their combined effect on synthetic planet distributions. Rather, we vary a single model parameter, combined with three that characterize protoplanetary disks to link final planet distributions to the observed variation in their formation environments. Other model parameters are either constrained observationally (i.e. the turbulent disk α), or are individually investigated in their effect on our populations' distributions and constrained based on their correspondence with observations, which we outline below.

The following chapters present original research that was performed in this thesis, with chapters 2 and 3 being published papers (Alessi & Pudritz (2018), and Alessi, Pudritz & Cridland (2020), respectively; both published in MNRAS). At the time of writing, chapter 4 has been accepted for publication in MNRAS, and chapter 5 consists of research that is in preparation for submission.

In chapter 2 (Paper 1; Alessi & Pudritz 2018), we first explore the effects of forming planets' envelope opacities $\kappa_{\rm env}$ and disk metallicity on resulting planet populations. While the overall disk dust-to-gas ratio is linked to disk metallicity, we otherwise use a simplified dust treatment by assuming a globally constant, time-independent dust-to-gas ratio, using a standard value of 0.01 in a Solar-metallicity disk. As the envelope opacity affects the gas accretion rate onto planets, it significantly shapes the planet distribution on the M-a diagram. In particular, the orbital radius distribution of gas giants is very sensitive to the setting of $\kappa_{\rm env}$. Occurrence rate studies show the a_p distribution of gas giants to be maximal between 3-10 AU (Bryan et al., 2016). We find that a low setting of $\kappa_{\rm env} \simeq 0.001$ cm^{2}g^{-1} is required in order to produce a large warm gas giant population at $a_p \sim$ 2-3 AU, with larger settings of $\kappa_{\rm env}$ (increased by a factor of order unity) resulting in a reduced warm gas giant population and an increased production of hot Jupiters. This optimal setting of $\kappa_{\rm env}$ is a factor 100-1000 lower than typical disk opacities, which could indicate significant and rapid grain growth in forming planets' atmospheres in order to reduce their opacities.

In chapter 2, we also compare dead zone locations and their evolution resulting from different

sources of disk ionization: external cosmic rays and X-rays generated from host-star accretion. We find that, in order to achieve a separation between the hot and warm Jupiter populations, X-ray disk ionization and its related dead zone trap must be considered. Such a reduction in the occurrence rate in gas giants is seen at orbital radii near 0.1 AU (i.e. Santerne et al. 2016; Petigura et al. 2018). Other works have shown that disk outflows can screen cosmic rays from reaching the disk (Matt & Pudritz, 2005; Cleeves et al., 2013), and that X-ray disk ionization results in chemical profiles that better match observations (Cleeves et al., 2015).

In chapter 3 (Paper 2; Alessi et al. 2020), we continue with the best-fit model found in paper 1 ($\kappa_{\rm env}$ =0.001 cm^{2}g^{-1} and X-ray ionization) to investigate the role of radial dust drift and the initial disk size in shaping the M-a distribution. We relax our constant dust-to-gas ratio assumption from paper 1, and consider a full dust treatment that includes coagulation, fragmentation, and radial drift. We find that radial drift efficiently removes solids from the outer disk, transporting them inwards to the ice line. While radial drift greatly reduces solid accretion rates in the outer disk, the water ice line becomes the most important trap for planet formation through this enhancement in solids.

We find that the initial disk radius affects the ratio of super Earths to warm gas giants formed in the ice line trap. An intermediate setting of initial disk radius $\simeq$ 50 AU results in the largest super Earth population, while both smaller and larger disk radius models produce more warm gas giants. In the case of small disks, planets forming in the ice line have larger gap-opening masses, causing gas-accretion termination to have a smaller effect, thereby producing more gas giants. In large disks, there is a larger region outside the ice line whereby solids are removed through radial drift. As a result, there is higher solid surface densities at the ice line, leading to an increased rate of planet formation and producing more gas giants. As observations show super Earths to be the largest population of planets, our results indicate intermediate disk radii of $\simeq$ 50 AU to be optimal. From a disk formation perspective, disk radii near 50 AU correspond to an intermediate amount of magnetic braking during protostellar collapse. Our results confirm that the ranges of disk radii, shown both from an observational (Ansdell et al., 2018) and numerical (Bate, 2018) perspective, play a crucial role in affecting planet formation.

Papers 1 & 2, considering no radial drift and (very) efficient radial drift, respectively, can be regarded as a means of bracketing the true effect of radial dust drift on planet populations. As we discuss in chapter 3 the dust model that we use does not maintain extended dust distributions as are seen in evolved disks, and therefore likely over-estimates radial drift rates. In contrast, by

considering a constant dust-to-gas ratio in paper 1, we are effectively setting the radial drift rate to zero. Papers 1 & 2 can therefore be considered the two extremes of radial drift and its effect on the solid distribution in disks.

Next, in chapter 4, we use the best-fit model of paper 2 - that of an intermediate initial disk radius of 50 AU - and incorporate disk chemistry and planetary structure in order to calculate our populations' M-R distributions and compare with observations. We use an equilibrium disk chemistry model to calculate evolving abundance profiles of minerals, and track their accretion onto forming planets to compute solid compositions. We include the observed variance in C/O and Mg/Si ratios and their correlation with host-star metallicity among G-type stars in our approach (Suárez-Andrés et al., 2018). We also consider the crucial effect of atmospheric mass loss through photoevaporation following disk-dissipation. Photoevaporation strips the accreted gas from small $a_p \lesssim 0.1$ AU Neptunes and sub-Saturns, and plays a key role in shaping the M-R distribution. Atmospheric mass-loss also becomes a means of forming short-period super Earths, as planets can first form as Neptunes or sub-Saturns (ie. accreting substantial gas) at small orbital radii, with subsequent photevaporative stripping reducing their masses to 1-10 $M_\oplus$.

Our disk chemistry model produces a range of planet solid compositions from dry, Earth-like planets to those with substantial ice abundances (up to 50% by mass). This difference in solid compositions translates to different radii on the M-R diagram in the case of planets with no accreted/retained atmospheres, with ice-rich planets having larger radii than dry, rocky planets at a given mass. Atmospheres, however, play a dominant role on planet radii. We find that planets with quite different compositions (ice abundances) occupy similar regions of the M-R space if they retain their atmospheres.

Recent protoplanetary disk observations and disk MHD simulations are revealing lower-levels of turbulence than previously expected. As disk winds are the other main mechanism through which disk evolution can occur, they are becoming increasingly important in understanding disk observations. On this basis, in chapter 5, we explore a protoplanetary disk model that incorporates the combined effects of turbulence and disk winds in driving evolution, with a particular emphasis on models in which disk wind stresses dominate over viscous stresses. Lastly, in chapter 6, we list our main findings, discuss their implications, and future work.

Chapter 2

Formation of Planetary Populations I: Metallicity & Envelope Opacity Effects

Matthew Alessi & Ralph Pudritz

What follows has been published in Monthly Notices of the Royal Astronomical Society (MNRAS). See: Alessi & Pudritz (2018), MNRAS **478**: 2599.

Abstract

We present a comprehensive body of simulations of the formation of exoplanetary populations that incorporate the role of disk inhomogeneities in slowing planetary migration. We reduce our model parameter set to two physical parameters: the opacity of the accreting planetary atmospheres ($\kappa_{\rm env}$) and a measure of the efficiency of planetary accretion after gap opening ($f_{\rm max}$). We perform planet population synthesis calculations based on the initial observed distributions of host star and disk properties - their disk masses, lifetimes, and stellar metallicities. We find that the frequency of giant planet formation scales with disk metallicity, a result in agreement with the observed Jovian planet frequency-metallicity relation. We consider both X-ray and cosmic ray disk ionization models, whose

differing ionization rates lead to different dead zone trap locations. In both cases, Jovian planets form in our model out to 2-3 AU, with a distribution at smaller orbital radii dependent on the disk ionization source and the setting of envelope opacity. We find that low values of $\kappa_{\rm env}$ (0.001-0.002 cm^2 g^{-1}) and X-ray disk ionization are necessary to obtain a separation between hot Jupiters near 0.1 AU, and warm Jupiters outside 0.6 AU, a feature present in the data. Our model also produces a large number of super Earths, but the majority are outside of 2 AU. As our model assumes a constant dust to gas ratio, we suggest that radial dust evolution must be taken into account to reproduce the observed super Earth population.

2.1 Introduction

With the ever-growing sample of nearly 3000 confirmed exoplanets and over 2300 unconfirmed planetary candidates, we are gaining a statistical understanding of the outcomes of planet formation (Borucki et al., 2011b; Mayor et al., 2011; Cassan et al., 2012; Batalha et al., 2013; Burke et al., 2014; Fischer et al., 2014; Rowe et al., 2014; Morton et al., 2016). The mass semi-major axis distribution contains a tremendous amount of information revealed by observations that can strongly constrain planet formation theories. As was first suggested by Chiang & Laughlin (2013), and also discussed in Hasegawa & Pudritz (2013, 2014), & Hasegawa (2016), the diagram can be divided into zones that define sub-populations that appear within the distribution. The frequencies by which planets populate different zones offers strong constraints and insight into the process of planet formation.

We summarize the observations in figure 2.1, where we show the most current m-a diagram for exoplanetary data. The vast majority of observed planets are comprised of super Earths (masses 1 - 10 $M_\oplus$) and hot Neptunes (masses 10 - 30 $M_\oplus$) orbiting within 2 AU of their host stars, which lie in zone 5 on the distribution. In the Jovian zones, the hot Jupiters (zone 1 planets), whose semi-major axes are within 0.1 AU of their host stars, comprise nearly an equal fraction of observed planets as Jupiters orbiting near or outside 1 AU (zone 3 planets). Conversely, at orbital radii between 0.6-1 AU (zone 2), there is a reduction in the number of Jovian planets compared to the adjacent zones. Lastly, zone 4 contains distant planets, a region of the diagram that is observationally incomplete (Cumming et al., 2008; Bryan et al., 2016).

In this paper, we use the features and trends in the observed mass semi-major axis distribution

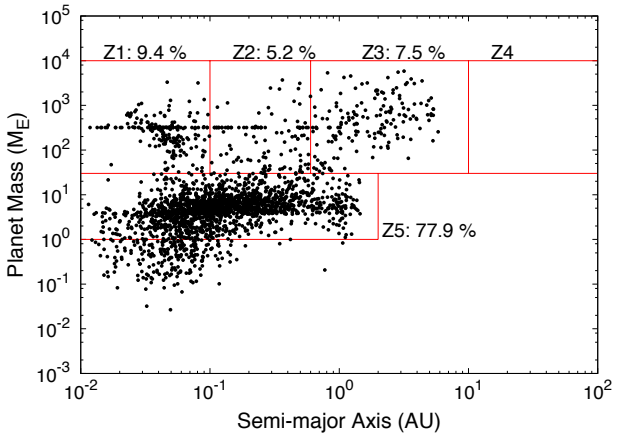

Figure 2.1: The observed planetary mass semi-major axis distribution is shown for G-type host stars, including both confirmed planets and unconfirmed *Kepler* candidates. The diagram can be divided into five zones defining populations seen in the data (first suggested by Chiang & Laughlin (2013)). Zone 1 contains hot Jupiters. Zone 2 has warm Jupiters. Zone 3 contains the largest population of gas giants orbiting near or outside 1 AU. Zone 4 contains distant planets. Lastly, zone 5 contains the largest population of planets, super Earths and Neptune-mass planets. This data was retrieved from http://exoplanets.org on October 16, 2017 (Han et al., 2014).

to constrain the core accretion model of planet formation. The core accretion model predicts Jovian planets to form in a bottom-up manner, starting with planetary cores that are a fraction of an Earth mass accreting solids before becoming massive enough to directly accrete gas from the surrounding protoplanetary disk. This model has been shown to successfully form Jupiter-mass planets in disks with average to long lifetimes of $\gtrsim 3$ Myr (Alibert et al., 2005; Lissauer et al., 2009; Hasegawa & Pudritz, 2012).

As was shown in Ida & Lin (2008); Mordasini, Alibert & Benz (2009a); Hasegawa & Pudritz (2011, 2013); Alessi, Pudritz & Cridland (2017), the natal disk's mass and lifetime are two key parameters that strongly affect the outcome of core accretion calculations. For example, super Earths or hot Neptunes have been shown to arise in cases where the planet's formation timescale greatly exceeds the disk's lifetime, so that it does not have sufficient time to build a massive core that can quickly accrete gas (Alessi et al., 2017). This situation is encountered in low-mass disks whose lower densities give rise to long planet formation timescales, or in disks with short lifetimes.

Disk metallicity has also been shown to greatly affect outcomes of core accretion models (Ida & Lin, 2004b; Mordasini et al., 2012c; Hasegawa & Pudritz, 2014). Disk metallicity affects the global

disk dust to gas ratio, and therefore the solid accretion timescale throughout planet formation. This is particularly important for setting the timescale for early stages of core accretion prior to gas accretion. Stellar metallicities range from -0.6 $\leq$ [Fe/H] $\leq$ 0.6 among the sample of G-type stars hosting observed planets (Han et al., 2014). The metallicities of the gaseous disks reflect those of their parent stars, which formed out of this material. The observed planet-metallicity relation shows that the detected gas giant frequency scales with host star metallicity (Fischer & Valenti, 2005; Valenti & Fischer, 2008; Wang & Fischer, 2015), highlighting the importance of disk metallicity in the framework of planet formation.

The technique of planet population synthesis is a useful method for calculating the outcomes of a core accretion model while considering a range of several input and model parameters. In particular, one can consider the observed distributions of disk lifetimes, masses, and metallicities as priors in a population synthesis calculation and determine the corresponding statistical distribution of planet properties. Planet population synthesis has been used in this manner in many previous works, considering either planetesimal accretion (e.g. Ida & Lin (2004a, 2008); Mordasini et al. (2009a,b) & Hasegawa & Pudritz (2013)) or pebble accretion (e.g. Bitsch, Lambrechts & Johansen (2015); Ali-Dib (2017); Ndugu, Bitsch & Jurua (2018)). We will take a similar approach here to account for the observationally constrained ranges of disk parameters on the outcomes of our core accretion model that considers planetesimal accretion.

A central feature of any theory of planet formation is how to prevent the rapid loss of planetary embryos to the central star due to rapid Type I migration (Alibert et al., 2004; Ida & Lin, 2008; Mordasini et al., 2009a). A robust solution to this problem is the existence of regions of zero net torque - or planet traps - that arise at various kinds of disk inhomogeneities and transitions. This could arise at the inner edge of a dead zone (Masset et al., 2006a). More generally, planet traps arise in a number of regions throughout the body of protoplanetary disks.

Planet traps have been previously considered in population synthesis models in Matsumura, Pudritz & Thommes (2007); Hasegawa & Pudritz (2013, 2014) and Hasegawa (2016), who found that including multiple traps originating at a range of orbital radii resulted in the formation of different classes of observed planets. The planet traps considered in this model are the water ice line, the heat transition that exists at the boundary between an inner, viscously-heated region of disks and an outer region heated via direct radiation from the host star, and lastly the dead zone's outer edge which separates turbulently active and inactive regions of disks(Hasegawa & Pudritz,

2011).

The outcomes of core accretion models are sensitive to the calculated gas accretion rates. Gas accretion onto forming planets is set by the Kelvin-Helmholtz timescale, which describes how quickly a forming planet's envelope can cool and contract (Pollack et al., 1996). In semi-analytic core accretion models, the Kelvin-Helmholtz timescale is often written in terms of two poorly constrained parameters which are physically linked to the forming planet's envelope opacity Ikoma, Nakazawa & Emori (2000); Ida & Lin (2004a).

To track a forming planet's envelope opacity throughout its formation self-consistently, one would need to consider the size distribution of grains in the atmosphere as well as the compositions of those grains as they are accreted from the disk onto the planet (Mordasini, 2014; Ormel, 2014; Venturini et al., 2016). Due to the difficulty of such a calculation, the envelope opacity of a forming planet is a somewhat poorly constrained parameter, and results of core accretion calculations are sensitive to the related Kelvin-Helmholtz parameters (Ikoma et al., 2000).

The goal of this paper is to connect the statistical distribution of planets on the mass semi-major axis diagram to observed properties of host stars and protoplanetary disks. We will consider observationally constrained distributions of disk masses, metallicities, and lifetimes in population synthesis calculations. This will allow us to determine if the core accretion model, including the effects of trapped type-I migration, can reproduce features of the observed mass semi-major axis diagram.

We also greatly improve the physical model of the accretion process onto planets by reducing earlier highly parameterized treatments to only one - the envelope opacity - which plays the central role in controlling the accretion rate onto the planetary atmospheres. As was previously considered in Mordasini et al. (2014), we aim to constrain envelope opacity values by including the parameter in our population synthesis calculations.

The remainder of this paper is organized as follows. In section 2.2, we summarize the observational constraints on host star and disk properties, motivating the chosen distribution functions for our population synthesis calculations. In section 2.3 we outline our model, describing our calculation of physical disk conditions, the time-dependent locations of planet traps, our core accretion model, and lastly the methods used in our population synthesis approach. In section 2.4, we show the planet populations resulting from our calculations that consider a range of envelope opacities and disk metallicities. We discuss our results and contrast them with other models in section 2.5. Lastly,

in section 2.6, we summarize our key findings.

2.2 Distributions of Disk Properties

In our planet population synthesis approach we connect the mass-semimajor axis distribution of planets to the range of protoplanetary disk properties. The distributions of disk lifetimes, initial masses, and metallicities are therefore external inputs to our population synthesis model as they depend on processes external to planet formation. Initial disk masses and metallicities are set during the star formation process, and disk lifetimes are linked to the ongoing process of disk photoevaporation driven by ionizing radiation fields from the host stars.

The rate at which disk photoevaporation takes place is dependent on the UV and X-ray luminosity of the host star. Disks surrounding stars with high X-ray and/or UV luminosities will have high photoevaporation rates and correspondingly short disk lifetimes (Gorti, Dullemond & Hollenbach, 2009; Owen, Ercolano & Clarke, 2011; Gorti, Hollenbach & Dullemond, 2015). In this sense, the disk lifetime distribution shares a physical link with the distribution of X-ray and UV luminosities for disk-hosting stars. Additionally, photoevaporation rates have been shown to depend on disk metallicity (Ercolano & Clarke, 2010; Nakatani et al., 2017) since metallicity affects the disk structure, and therefore the optical depth to photoevaporating radiation. In particular, these works have shown disk lifetimes resulting from photoevaporation to be longer when disk metallicity is increased. Therefore, the relation between disk lifetime and UV/X-ray luminosity of the host star is more complex than one-to-one. In addition to radiation from the host star, the external radiation field can also affect photoevaporative rates and disk lifetimes of a disk within a star cluster (Clarke, 2007).

For the distributions of disk lifetimes, $t_{\rm LT}$, and initial masses f_M, we use a log-normal distribution,

$$P(X|\mu_x, \sigma_x) \sim \exp\left(-\frac{(\log(X) - \log(\mu_x))^2}{2\sigma_x^2}\right) . \tag{2.1}$$

In the case of the disk lifetime, we use an average $\mu_{\rm lt} = 3$ Myr and standard deviation $\sigma_{\rm lt} = 0.222$, which results in 1.8 Myr - 5 Myr corresponding to the $\pm\sigma_{\rm lt}$ range of the distribution. For initial disk masses, we use $\mu_{\rm m} = 0.1$ and $\sigma_{\rm m} = 0.138$, whereby $f_M = 0.073 - 0.137$ are within one sigma of the mean. We note that this range of initial disk masses corresponds to a 1-σ range of ~ 0.037 - 0.065 $M_\odot$ after 1 Myr of disk evolution. We choose these parameters to correspond with lifetime and initial

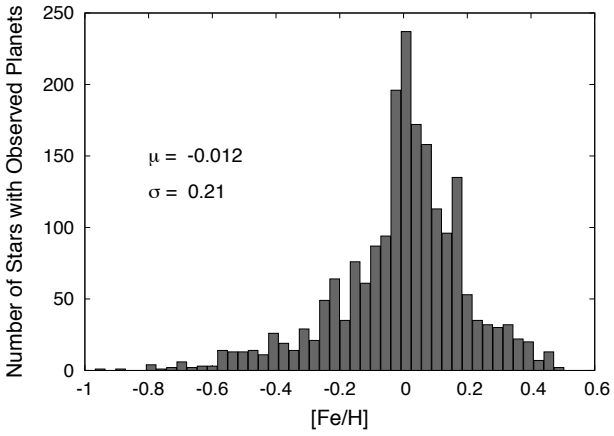

Figure 2.2: The metallicity distribution for G-type stars hosting planets is shown. The mean and standard deviation of this distribution are used to define the parameters in our population synthesis metallicity distribution (see equation 2.2). This data was retrieved from http://exoplanets.org on October 16, 2017 (Han et al., 2014).

disk accretion rate distributions used in Hasegawa & Pudritz (2013). Our resulting disk lifetime and initial mass distributions correspond reasonably well with those used in previous population synthesis works such as Ida & Lin (2008) and Mordasini et al. (2009a).

In figure 2.2, we show the distribution of metallicities ([Fe/H]) among G-type stars hosting observed planets. We consider the initial disk metallicity distribution to follow that of the observed host stars, and model the observed data using a normal distribution,

$$P(X|\mu_x, \sigma_x) \sim \exp\left(-\frac{(X-\mu_x)^2}{2\sigma_x^2}\right) , \tag{2.2}$$

with mean $\mu_z = -0.012$ and $\sigma_z = 0.21$.

In figure 2.3, we plot the distributions of disk parameters stochastically varied in our population synthesis models. The lifetime and initial mass distribution (left and centre panels, respectively) correspond to the distributions described in equation 2.1 while the metallicity distribution is described by equation 2.2.

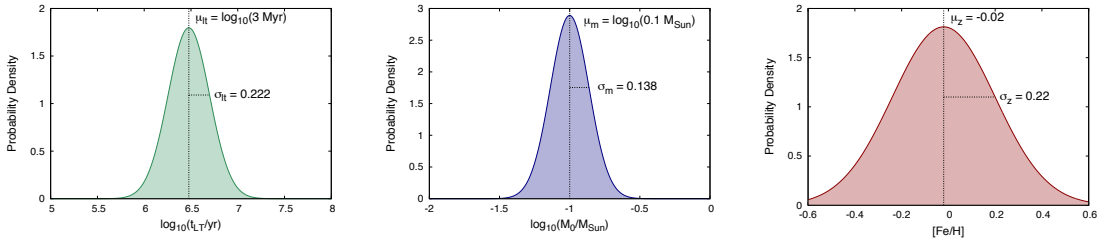

Figure 2.3: Distributions of the varied quantities in our population synthesis calculations are shown. We use log-normal distributions for disk lifetimes and masses, and a normal distribution for disk metallicities.

2.3 Planet Formation Model

Our model combines a calculation of the evolving physical conditions within a protoplanetary disk with a core accretion model of planet formation that includes a prescription for planet formation. For a complete, detailed description of the model used in this work, we refer the reader to Alessi et al. (2017). In this section, we summarize its key features as well as our implementation of population synthesis, and note any updates to the model presented in Alessi et al. (2017).

2.3.1 Disk Evolution Model

To calculate disk structure and evolution, we use the 1+1D semi-analytic model presented in Chambers (2009). An analytic disk model is advantageous for our purposes as it allows for efficient calculation of disk conditions in population synthesis calculations that model the formation of thousands of planets. The Chambers (2009) model provides a self-similar solution to the viscous evolution equation describing the evolving surface density profile $\Sigma(r,t)$ of a protoplanetary disk,

$$\frac{\partial \Sigma}{\partial t} = \frac{3}{r}\frac{\partial}{\partial r}\left[r^{1/2}\frac{\partial}{\partial r}\left(r^{1/2}\nu\Sigma\right)\right] , \tag{2.3}$$

where $\nu(r,t)$ is the disk's viscosity. Self-similar solutions to this equation can be obtained for α-disk models, where the disk viscosity is written in terms of an effective viscosity coefficient, α, defined as (Shakura & Sunyaev, 1973; Lynden-Bell & Pringle, 1974),

$$\nu = \alpha c_s H , \tag{2.4}$$

where c_s is the local sound speed and H is the disk scale height.

We recall that self-similar solutions for disk evolution require a constant α throughout the disk and we take that value to be $\alpha = 10^{-3}$. However, there are two mechanisms for angular momentum transport throughout the disk corresponding to angular momentum transport through MRI generated turbulence and torques exerted by MHD disk winds,

$$\alpha = \alpha_{\rm turb} + \alpha_{\rm wind} \, . \tag{2.5}$$

Models considering angular momentum transport to occur solely via MRI turbulence predict an outer, turbulently active region that has a larger $\alpha_{\rm turb} \sim 10^{-3} - 10^{-2}$ value than an inner, turbulently inactive regions (the so-called *dead zone*), with $\alpha_{\rm turb} \sim 10^{-5} - 10^{-4}$ (Gammie, 1996; Matsumura & Pudritz, 2003). However, disk winds have been shown to sustain accretion rates within dead zones (Bai & Stone, 2013; Gressel et al., 2015; Gressel & Pessah, 2015; Bai, 2016), motivating our assumption of a globally constant disk α in spite of a radially dependent $\alpha_{\rm turb}$ component.

Our model accounts for disk evolution to occur through both the generalized "viscous" accretion and photoevaporation, whereby UV and X-ray radiation from the protostar disperses disk material throughout its evolution (Pascucci & Sterzik, 2009; Owen, Ercolano & Clarke, 2011). The time-dependent disk accretion rate used in this work,

$$\dot{M}(t) = \frac{\dot{M}_0}{(1 + t/\tau_{\rm vis})^{19/16}} \exp\left(-\frac{t - \tau_{\rm int}}{t_{\rm LT}}\right) \, , \tag{2.6}$$

includes a viscous evolution term multiplied by an exponentially-decreasing factor that models the effect of photoevaporation on our disk's viscous evolution. In equation 2.6, $\tau_{\rm vis}$ is the disk's viscous timescale, $\dot{M}_0$ is the accretion rate at the initial time $\tau_{\rm int} = 10^5$ years, and $t_{\rm LT}$ is the disk's lifetime.

We note that equation 2.6 is an improvement of the model presented in Alessi et al. (2017), as we now set the e-folding timescale of disks equal to their disk lifetimes, thereby reducing our set of parameters by one. With this change all of the disks in our populations have accretion rates that are reduced by a factor of e at the end of their lifetimes as driven by photoevaporation in addition to their viscous evolution that is handled by the Chambers (2009) model. Following our discussion in section 2.2, disk lifetimes are linked to photoevaporation driven by UV and X-ray luminosities of their host stars, and with this change to equation 2.6 every disk considered in our model undergoes

Table 2.1: Surface density (Σ) and temperature (T) dependencies on disk accretion rate and radius in both the viscous region ($r < r_t$) and the region heated by radiation from the host star ($r > r_t$).

$r < r_t$	$r > r_t$
$\Sigma(r,t) \sim \dot{M}^{3/5} r^{-3/5}$	$\Sigma(r,t) \sim \dot{M} r^{-15/14}$
$T(r,t) \sim \dot{M}^{2/5} r^{-9/10}$	$T(r,t) \sim r^{-3/7}$

the same photoevaporative evolution albeit over different timescales set by $t_{\rm LT}$.

When the disk evolution time $t = t_{\rm LT}$ we assume the disk rapidly clears, terminating planet formation and migration. This is motivated by photoevaporation models that show disks to rapidly clear once the photoevaporative mass-loss rate exceeds the disk accretion rate (Owen et al., 2010; Haworth et al., 2016). We emphasize that disk lifetimes are physically linked to the amount of UV and X-ray emission from the protostar, as stars with higher UV-excesses will have higher photoevaporative mass-loss rates, and correspondingly shorter disk lifetimes (Owen et al., 2011). This motivates our inclusion of $t_{\rm LT}$ in the photoevaporation factor in equation 2.6.

The Chambers (2009) disk model is divided into two regions: an inner region heated through viscous dissipation, and an outer region where radiative heating from the protostar dominates any other heating mechanism. We note that within the dead zone where disk winds dominate angular momentum transport, the effective "viscous" dissipation is, in reality, due to non-ideal MHD heating effects (eg. Ohmic heating at the disk midplane). The heat transition (r_t), a planet trap in our model, exists at the boundary between the inner region heated through viscous dissipation or non-ideal MHD heating and the outer region heated via radiation from the protostar.

In figure 2.4, we show the evolution of the disk accretion rate, as well as radial profiles of surface density and midplane temperature at several times throughout a fiducial disk's evolution. In table 2.1, we show the radius and accretion rate scalings of surface density and temperature profiles in both regions computed with our disk model. We refer the reader to section 2.1 of (Alessi et al., 2017) for a complete description of our disk evolution model.

We calculate the dust to gas ratio throughout the disk as a function of disk metallicity [Fe/H] using,

$$f_{\rm dtg} \equiv \frac{\Sigma_d}{\Sigma_g} = f_{\rm dtg,0} 10^{\rm [Fe/H]} \ , \tag{2.7}$$

where $f_{\rm dtg,0} = 0.01$ is the fiducial dust to gas ratio for a Solar-metallicity disk, and $\Sigma_g \simeq \Sigma(r,t)$ calculated with our disk model. This simplified constant dust-to-gas ratio has no radial or time dependence, and thus does not include the effects of condensation fronts or dust evolution through

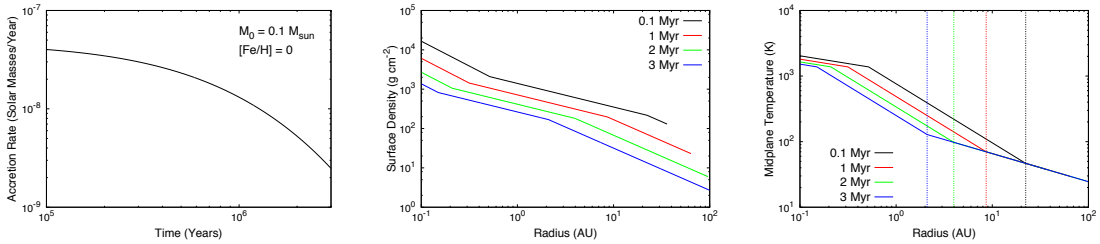

Figure 2.4: The time evolution of the disk accretion rate, and radial profiles of surface density and midplane temperature are shown for a fiducial disk model. The vertical dashed lines in the right panel denote the location of the disk heat transition, existing at the boundary of the two different power law profiles pertaining to viscous and radiative heating. The innermost power law in the Σ and T plots within a few tenths of an AU corresponds to the region where the disk opacity is reduced to due evaporation of dust grains.

radial drift, coagulation and fragmentation (which are considered, for example, in Birnstiel, Klahr & Ercolano (2012) and Cridland, Pudritz & Birnstiel (2017)). Models that include these effects have shown the dust-to-gas ratio has an abrupt increase across the ice line, and that the ionization structure of the disk is altered by including dust evolution effects, shifting the dead zone inward (Cridland, Pudritz & Birnstiel, 2017). By assuming a constant dust-to-gas ratio throughout the disk, we are neglecting the variations in the quantity that would arise across planet traps, and its affect on the solid accretion rates in our planet formation calculations. In a future paper (Alessi, Pudritz, & Cridland, in prep.), we will include these effects in our population synthesis model.

Following Chambers (2009), our disk model assumes a constant opacity of $\kappa_0 = 3$ cm^2 g^{-1} for Solar metallicity disks, except in a small (~ 0.1 AU) inner region with temperatures exceeding 1380 K, where dust grains evaporate. We scale our assumed average disk opacity with metallicity as (Rémy-Ruyer et al., 2014),

$$\kappa = \kappa_0 10^{[\mathrm{Fe/H}]} \ , \tag{2.8}$$

where the disk opacity is dominated by grain opacities over the disk temperature and metallicity range considered, -0.6 $\leq$ [Fe/H] $\leq$ 0.6. By assuming a constant disk opacity, we are neglecting the variation that would occur across ice lines. This transition in disk opacity is the physical cause for the ice line planet trap in our model, however this variation in κ is not necessary for our model as we do not directly compute the planet-disk torques. Including a detailed opacity structure, as was done in Stepinski (1998) would also affect the disk surface density and temperature profiles. However, this would be a small effect as the Chambers (2009) disk model is only weakly sensitive to disk opacity,

so variations in κ would not greatly alter the global disk structure.

2.3.2 Planet Migration & Traps

The local density and composition of material in protoplanetary disks are heavily dependent on disk radius. Therefore, including the effects of planetary migration in core accretion scenarios is crucial to properly track a planet's time-dependent accretion rate and composition (e.g. Cridland, Pudritz & Alessi (2016)). Migration of forming planets occurs due to the gravitational interaction, and resulting angular momentum exchange, between a forming planet and the surrounding disk material.

Trapped Type-I Migration

The theory of type-I migration applies to low-mass ($\lesssim 10$ $M_\oplus$) forming planets that have only a small influence on surrounding disk material. To determine type-I migration rates, one must account for the Lindblad and corotation torques exerted on the planet, which depend on the planet and local disk conditions (Lyra et al., 2010; Hellary & Nelson, 2012; Dittkrist et al., 2014; Baillié et al., 2016; Coleman & Nelson, 2016b). In the absence of a corotation torque, Lindblad torques exerted on a forming planet lead to rapid inward migration timescales of $\sim 10^5$ years (Goldreich & Tremaine, 1980). The discrepancy between this inward Lindblad migration timescale and the $\gtrsim 10^6$ year core accretion timescales (i.e. Pollack et al. (1996)) is known as the *type-I migration problem.*

The corotation torque, which often increases the planet's angular momentum, is a means for slowing the rapid inward migration caused by Lindblad torques and offers a solution to the type-I migration problem. The caveat with this mechanism is that the corotation torque's operation depends sensitively on the local disk conditions. In many cases, the corotation torque will saturate, exerting no positive torque on the planet which will then only be subjected to the strong negative Lindblad torques (Masset, 2001, 2002). The corotation torque has been shown to be sustained in disks when there is sufficient thermal and viscous diffusion within the corotation region (Paardekooper, Baruteau & Kley, 2011).

Near planet traps, or inhomogeneities in disk surface density and temperature profiles, the corotation torque has been shown to remain unsaturated (Masset et al., 2006a; Hasegawa & Pudritz, 2011). Planet traps are zero torque equilibrium radii resulting from the summed contributions from the negative Lindblad torque and strong corotation torque operating locally near the planet trap. Moreover, planet traps are stable equilibria as planets on nearby orbits migrate into the trap due

to the planet-disk torque, as has been demonstrated in numerical simulations (Lyra et al., 2010; Coleman & Nelson, 2016b). In trapped type-I migration, the planets thus form while migrating inwards following their host trap's evolution with the disk (Paardekooper et al., 2010). The planet's migration timescale is therefore comparable to the disk's viscous evolution timescale of a few Myr, which is comparable to the core accretion timescale (Hasegawa & Pudritz, 2012).

Other authors, such as Hellary & Nelson (2012) and Dittkrist et al. (2014) have included multiple type-I migration regimes during early stages of planet formation. In this work, we only consider the trapped type-I migration regime. It remains possible, however, for corotation torques to saturate prior to the planet entering the type-II migration regime (see equation 2.17). As discussed in Hasegawa (2016), the mass at which the corotation torque saturates ($M_{\rm sat}$) is similar to the gap-opening mass ($M_{\rm gap}$) where type-II migration begins. Moreover, we have shown in Alessi et al. (2017) that planets enter type-II migration prior to corotation torque saturation for a wide range of model parameters. We therefore include trapped type-I migration and type-II migration as the only migration regimes in our model.

The planet traps we include are the water ice line, the heat transition, and the outer edge of the dead zone. Determining the locations of the traps within disks is a key component of our model, as we assume planets to form within traps for the entirety of their type-I migration mass-regime, and do not directly calculate the planet-disk torques. There are additional inhomogeneities and transitions that can lead to trapping present in disks that we do not include. One example is the dead zone inner edge, which is located at ~ 0.1 AU (Gammie, 1996). Since this trap is restricted to the inner regions of the disk, it is unclear if such high temperatures ($\gtrsim 1000$ K) will allow forming planets to accrete substantial amounts of gas.

There are also volatile ice lines in addition to water whose ability to act as traps has not yet been established and are not included here. An example of a prominent volatile in disks with an observed ice line is carbon monoxide (Qi et al., 2013). The CO condensation front will lie in the outer portion of the disk (roughly 30 AU), within the radiatively-heated region where the temperature is determined by the flux from the star, and not heat generated by the disk. Therefore, the temperature in this region has no time (or $\dot{M}$) dependence (see table 2.1). Thus, the trap will not evolve inward if included in our model, and planet formation at this condensation front would be confined to large orbital radii where the planetesimal accretion rate would be exceedingly low. For this reason, we do not include the CO ice line as a trap in our model, as it will not contribute to the planet populations

seen in the data. We rather follow Hasegawa & Pudritz (2012, 2013), who showed that the three traps we do include in our model are sufficient to reproduce observed classes of planets. We note that the traps we do include are the general type of possibilities for traps within the body of the disk.

The location of the water ice line along the disk's midplane, r_{il}, is determined using an equilibrium chemistry calculation over the corresponding range of temperatures and pressures of the disk midplane throughout its evolution. We use the equilibrium chemistry software ChemApp to perform these calculations (distributed by GTT Technologies; http://www.gtt-technologies.de/newsletter) over the full range of metallicities considered in this work. We find that the location of the water ice line scales with the disk accretion rate as $r_{il} \sim \dot{M}^{4/9}$. This is the same scaling as was found in Hasegawa & Pudritz (2011) who tracked the position of the water condensation temperature, 170 K, through the disk's evolution.

The heat transition represents the midplane boundary between the region of the disk heated through viscous dissipation and the outer region heated via irradiation from the central star. Its location is defined in the Chambers (2009) model at the disk radius where the midplane temperature due to viscous heating is equal to the temperature caused by radiation from the host star (i.e. equating the two temperature power laws whose scalings are shown in table 2.1). Its location scales with disk accretion rate as $r_t \sim \dot{M}^{28/33}$.

Within the dead zone, the disk ionization fraction will be too low for the MRI to drive turbulence. The outer edge of the dead zone, r_{dz}, thus separates an inner, turbulently inactive region from an outer, turbulent region. This location has been shown to be a planet trap due to the abrupt increase in scale height of the dust, whose radiation creates a thermal barrier to planet migration (Hasegawa & Pudritz, 2010). In Alessi et al. (2017) (section 2.3.3) we describe our calculation of r_{dz} in detail, which we summarize below.

To determine whether MRI-turbulence will be generated at a particular disk radius, we equate the MRI growth timescale to the Ohmic diffusion damping timescale over all vertical scales in the disk, the largest being the disk scale height Gammie (1996). This results in a condition for the MRI to be inactive, and for the disk radius in question to be within the disk dead zone, written in terms of the magnetic Elsasser number (Blaes & Balbus, 1994; Simon et al., 2013),

$$\Lambda_0 = \frac{V_A^2}{\eta \Omega_K} \lesssim 1 \, , \tag{2.9}$$

where $V_A \simeq \alpha_{\rm turb}^{1/2} c_{\rm s}$ is the Alfvén speed and,

$$\eta = \frac{234}{x_e} T^{1/2} \,{\rm cm}^2\,{\rm s}^{-1} \,, \tag{2.10}$$

is the magnetic diffusivity, which depends on the electron fraction x_e.

The equilibrium electron fraction at a particular disk radius results from a balance between ionization and recombination rates. We calculate this electron fraction to be the solution of the following equation (Oppenheimer & Dalgarno, 1974),

$$x_{\rm e}^3 + \frac{\beta_{\rm t}}{\beta_{\rm d}} x_{\rm M} x_{\rm e} - \frac{\zeta}{\beta_{\rm d} n} x_{\rm e} \frac{\zeta \beta_{\rm t}}{\beta_{\rm d} \beta_{\rm r} n} x_{\rm M} = 0 \,, \tag{2.11}$$

where ζ is the ionization rate, n is the local number density of disk material, and $x_{\rm M}$ is the metal fraction. There are three recombination processes accounted for with associated rate coefficients in equation 2.11: dissociative recombination of electrons with molecular ions ($\beta_{\rm d} = 2 \times 10^{-6} T^{-1/2}\,{\rm cm}^3\,{\rm s}^{-1}$), radiative recombination of electrons with metal ions ($\beta_{\rm r} = 3 \times 10^{-11} T^{-1/2}\,{\rm cm}^3\,{\rm s}^{-1}$), and charge transfer from molecular ions to metal ions ($\beta_{\rm t} = 3 \times 10^{-9} {\rm cm}^3\,{\rm s}^{-1}$) (Matsumura & Pudritz, 2003).

We separately consider X-rays generated through magnetospheric accretion and interstellar cosmic rays as ionizing sources. Following (Sano et al., 2000), we calculate the cosmic ray ionization rate at the disk midplane by considering the interstellar cosmic ray ionization rate, $10^{-17}\,{\rm s}^{-1}$, attenuated over a length of 96 g cm^{-2} (Umebayashi & Nakano, 1981),

$$\zeta_{CR} = \frac{10^{-17}\,{\rm s}^{-1}}{2} \exp\left(-\frac{\Sigma}{96\,{\rm g\,cm}^{-2}}\right). \tag{2.12}$$

Following Matsumura & Pudritz (2003), the X-ray ionization rate is calculated using,

$$\zeta_X = \left[\left(\frac{L_X}{E_X 4\pi d^2}\right)\sigma(E_X)\right]\left(\frac{E_X}{\Delta\epsilon}\right) J(\tau, x_0) \,, \tag{2.13}$$

where $L_X \simeq 10^{30}$ ergs s^{-1} is the X-ray luminosity of the protostar, $E_X = 4$ keV is the X-ray energy considered, d is the distance between the X-ray source and the midplane radius considered, and $\Delta\epsilon$ is the energy required to make an ion pair. The absorption cross section for X-rays of energy E is (Glassgold et al., 1997),

$$\sigma(E) = 8.5 \times 10^{-23}\,{\rm cm}^2 \left(\frac{E}{\rm keV}\right)^{-2.81} \,, \tag{2.14}$$

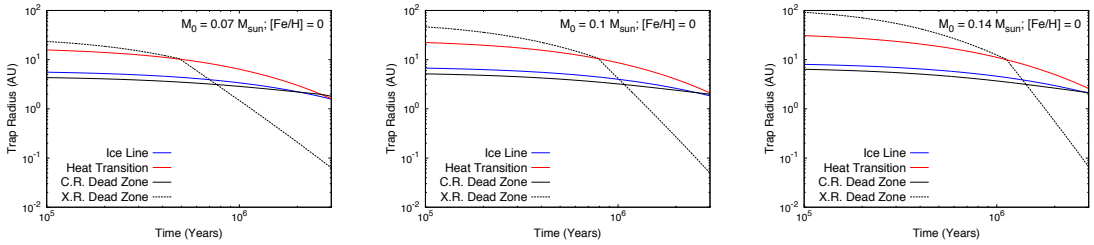

Figure 2.5: Time evolution of planet trap locations is shown for disks of initial masses 0.07 $M_\oplus$, 0.1 $M_\oplus$ (a fiducial disk mass), and 0.14 $M_\oplus$. The fiducial disk mass corresponds to the average value μ_m from the disk mass distribution used in our population synthesis model, while the light and heavy disk masses correspond to $\pm 1\sigma_m$ variation from the mean.

and the optical depth is,

$$\tau(E) = N_H \sigma(E) \,, \tag{2.15}$$

where N_H is the number density measured over the X-ray's path through the disk to the midplane radius considered. Lastly the X-ray attenuation factor in equation 2.13 is,

$$J(\tau, x_0) = \int_{x_0}^{\infty} x^{-n} \exp(-x - \tau(E_X) x^{-n}) dx \,, \tag{2.16}$$

written in terms of a dimensionless photon energy $x \equiv E/E_X$.

To calculate the location of the outer edge of the dead zone, we input the ionization rate corresponding to cosmic rays or X-rays (equation 2.12 or 2.13) into equation 2.11 to determine the electron fraction along the disk midplane. We then use equation 2.9 to determine the midplane radius where the critical magnetic Elsasser number condition is met, corresponding to the boundary between the MRI active and inactive regions of the disk.

In figure 2.5, we plot the time-dependent locations of planet traps in our model for three different initial disk masses, otherwise using fiducial disk parameters. For a range of disk masses corresponding to $\pm\sigma_m$ in our population synthesis calculations, the heat transition lies outside of the ice line for the entirety of a typical disk's lifetime of 3 Myr, while the cosmic ray dead zone exists $\lesssim 1$ AU inside of the ice line.

We note that the ice line, heat transition, and cosmic ray dead zone all evolve to $\simeq 1$ AU at the end of a typical disk lifetime, as was found in Hasegawa (2016). Conversely, the X-ray dead zone exists outside of the ice line for the first $\sim$ Myr of disk evolution before evolving to within 0.1

AU after 3 Myr. This comparatively rapid evolution is a result of the X-ray ionization along the midplane being extremely sensitive to the disk surface density.

We emphasize that the results of our planet formation models are connected to the location and evolution of the planet traps, since planets form within the traps throughout their type-I migration regime. For example, a planet forming within the heat transition forms outside ~ 5 AU during oligarchic growth, accreting solids from a lower surface density region than the inner $\sim 0.1 - 0.5$ AU regions encountered by planets forming in the X-ray dead zone. The effects of the traps on our planet population synthesis models will be discussed in detail in section 2.4.1.

Type-II Migration

Type-II migration applies to planets that are massive enough to alter the local disk structure through the formation of an annular gap. Gap formation, and resulting type-II migration, allows planets to migrate away from the traps they were forming within during type-I migration. The gap-opening mass is reached when the planet's torque on the local disk material exceeds that of disk viscosity, or when the planet's Hill radius exceeds the disk's pressure scale height H. The gap-opening mass is written as (Matsumura & Pudritz, 2006),

$$M_{\rm gap} = M_* \, \min \left[3h^2(r_p), \sqrt{40\alpha h^5(r_p)} \right] , \tag{2.17}$$

where r_p is the planet's radius, and $h = H/r_p$ is the disk aspect ratio at the planet's location. We note that, when calculated this way, we are predicting the planet to open a gap in the disk when it overcomes the suppressing effects of either the disk viscosity *or* the disk pressure (which are considered simultaneously, for example, in Crida et al. (2006)).

During type-II migration, the planet migrates following the disk viscous timescale of $\sim 10^6$ years, having a migration speed of,

$$v_{\rm mig,II} \simeq -\nu/r_p \, . \tag{2.18}$$

When the planet's mass becomes comparable to the total disk mass within the planet's orbit, exceeding a critical mass of $M_{\rm crit} = \pi r_p^2 \Sigma$, it will resist migrating with the disk evolution (Ivanov et al., 1999). In this case, the slowed type-II migration speed becomes (Hasegawa & Pudritz, 2012),

$$v_{\rm mig,slowII} \simeq -\frac{\nu}{r(1 + M_p/M_{\rm crit})} \, . \tag{2.19}$$

2.3.3 Core Accretion Model

We consider planet formation to take place through the core accretion scenario in this work, whereby an initially small planetary core accretes solids from the disk, building up its mass before accreting large amounts of gas. Our model considers an initial condition of a 0.01 $M_\oplus$ oligarch forming at an early stage of 10^5 years into disk evolution.

The first stage of planet formation in our model is oligarchic growth, whereby growth of the planetary core takes place via accretion of planetesimals. The accretion rate in this regime is Kokubo & Ida (2002),

$$\begin{aligned}\tau_{\rm c,acc} \simeq & 1.2\times10^5 \text{ yr } \left(\frac{\Sigma_d}{10 \text{ g cm}^{-2}}\right)^{-1} \\ & \times \left(\frac{r}{r_0}\right)^{1/2} \left(\frac{M_p}{M_\oplus}\right)^{1/3} \left(\frac{M_*}{M_\odot}\right)^{-1/6} \\ & \times \left[\left(\frac{b}{10}\right)^{-1/5} \left(\frac{\Sigma_g}{2.4\times10^3 \text{ g cm}^{-2}}\right)^{-1/5} \right. \\ & \left. \times \left(\frac{r}{r_0}\right)^{1/20} \left(\frac{m}{10^{18} \text{ g}}\right)\right]^2 ,\end{aligned} \tag{2.20}$$

where $m \simeq 10^{18}$ g is the mass of accreted planetesimals and $b \simeq 10$ is a parameter that defines the core's feeding zone. The corresponding accretion rate is $\dot{M} = M_p/\tau_{\rm c,acc}$.

During the oligarchic growth phase, accreted planetesimals heats gas surrounding the planet, keeping it in hydrostatic balance. The transition from the oligarchic growth phase to gas accretion phases takes place when the planetesimal accretion decreases to the point that the heat released is insufficient to maintain pressure support of the surrounding gas, which then accretes onto the planet. The critical core mass, $M_{\rm c,crit}$ that separates these stages of formation depends on the planetesimal accretion rate and the envelope opacity $\kappa_{\rm env}$ as (Ikoma et al., 2000; Ida & Lin, 2004a; Hasegawa & Pudritz, 2014),

$$\begin{aligned}M_{\rm c,crit} &\simeq f_{\rm c,crit} \left(\frac{1}{10^{-6} M_\oplus \text{ yr}^{-1}} \frac{dM_p}{dt}\right)^{1/4} M_\oplus \\ &\simeq 10\, M_\oplus \left(\frac{1}{10^{-6} M_\oplus \text{ yr}^{-1}} \frac{dM_p}{dt}\right)^{1/4} \left(\frac{\kappa_{\rm env}}{1 \text{ cm}^2 \text{ g}^{-1}}\right)^{0.3} .\end{aligned} \tag{2.21}$$

We note that this scaling is an update on the model presented in Alessi et al. (2017), which ignored the dependence of the parameter $f_{\rm c,crit}$ on envelope opacity. We include the dependence of $M_{\rm c,crit}$ on $\kappa_{\rm env}$ in equation 2.21 and we fully explore the role of envelope opacity in our core accretion model.

For masses $M_p > M_{\rm c,crit}$ planet formation occurs via gas accretion, which takes place on the

Kelvin-Helmholtz timescale (Ikoma et al., 2000),

$$\tau_{KH} \simeq 10^{c}\,\mathrm{yr}\left(\frac{M_p}{M_\oplus}\right)^{-d} . \tag{2.22}$$

The values of parameters c and d in the Kelvin-Helmholtz timescale are physically linked to $\kappa_{\rm env}$. We include this effect in our model by using the fits shown in Mordasini et al. (2014), that relate results of a numerical model of gas accretion to the Kelvin-Helmholtz parameters for a range of envelope opacities of $10^{-3} - 10^{-1}$ cm^2 g^{-1}. The fit given for the Kelvin-Helmholtz c parameter is,

$$c = 10.7 + \log_{10}\left(\frac{\kappa_{\rm env}}{1\,\mathrm{cm^2\,g^{-1}}}\right) . \tag{2.23}$$

The Kevlin-Helmholtz d parameter has a more complicated dependence on envelope opacity, ranging from ≈1.8-2.4 over the range of $\kappa_{\rm env}$ considered. The following piecewise-linear function reproduces the outputs shown in Mordasini et al. (2014),

$$d = \begin{cases} 0.994 - 0.335\log\left(\frac{\kappa_{\rm env}}{\mathrm{cm^2\,g^{-1}}}\right) & 0.001 \leq \frac{\kappa_{\rm env}}{\mathrm{cm^2\,g^{-1}}} < 0.003 \\ 1.954 + 0.045\log\left(\frac{\kappa_{\rm env}}{\mathrm{cm^2\,g^{-1}}}\right) & 0.003 \leq \frac{\kappa_{\rm env}}{\mathrm{cm^2\,g^{-1}}} < 0.005 \\ 3.093 + 0.54\log\left(\frac{\kappa_{\rm env}}{\mathrm{cm^2\,g^{-1}}}\right) & 0.005 \leq \frac{\kappa_{\rm env}}{\mathrm{cm^2\,g^{-1}}} < 0.05 \end{cases} \tag{2.24}$$

We do not consider envelope opacity values greater than 0.05 cm^2 g^{-1} in this work. Our approach here is an updated treatment of the gas accretion model presented in Alessi et al. (2017), that considered the Kelvin-Helmholtz c and d as separate parameters, ignoring their dependence on envelope opacities.

Hence, we have reduced our model's parameter set ($f_{\rm c,crit}$ and the Kelvin-Helmholtz c and d parameters) to just one; $\kappa_{\rm env}$.

The disk lifetime plays a crucial role in core accretion calculations, setting an upper limit to the amount of time planets have to form and hence to the amount of material that they can accrete. In our model, planets can accrete up until the point where the disk is photoevaporated, but at the disk lifetime when the disk is dissipated, their formation is truncated. We find that oligarchic growth typically takes place on a $\lesssim$ Myr timescale. Conversely, gas accretion initially takes place on a long $>$ Myr timescale, which is comparable to the disk lifetime, before reaching $\sim$ 30 M$_\oplus$ necessary to undergo runaway growth. The comparable timescale of the initially slow gas accretion phase and

the disk lifetime reveals why super Earths form in the core accretion model; these are planets whose natal disks photoevaporate during their slow gas accretion phase.

During all stages of gas accretion, including the runaway growth phase, we only consider the Kelvin Helmholtz timescale, modified to include its $\kappa_{\rm env}$ dependence. We choose our treatment following Hasegawa & Pudritz (2012, 2013), as these models also consider a trapped type-I migration phase and showed that such a gas accretion model can reproduce observed planet populations.

Other works such as Machida et al. (2010); Dittkrist et al. (2014), and Bitsch et al. (2015) have considered a disk limited accretion phase during late stages of planet formation which is in agreement with hydrostatic simulations (e.g. Lubow et al. (1999). Both approaches are sensitive to $\kappa_{\rm env}$, and can produce similar results depending on the envelope opacities considered.

Termination of gas accretion is related to gap opening, which depletes material in the planet's feeding zone (Lissauer et al., 2009). It is, however, unclear how soon a planet's accretion will terminate after opening a gap, with previous models finding that a substantial amount of material can flow through the gap and be accreted by the planet (Lubow & D'Angelo, 2006; Morbidelli et al., 2014). We therefore parameterize the maximum masses of planets in our model in terms of their gap-opening masses, truncating formation when planets reach a mass of,

$$M_{\rm max} = f_{\rm max} M_{\rm gap} \ , \tag{2.25}$$

where $f_{\rm max}$ is a parameter in our model. We consider a range of values of 1-500 for $f_{\rm max}$, where a value of 1 corresponds to a planet whose accretion is terminated abruptly after opening a gap. Conversely, larger values of $f_{\rm max}$ correspond to planets that are able to continue accreting well beyond reaching their gap-opening masses (e.g. Kley (1999)). Hasegawa & Pudritz (2013) considered the same method of terminating planet growth, and found that Jovian planet formation frequencies were insensitive to the parameter's setting when $f_{\rm max} \gtrsim 5$, while super Earth formation frequencies were sensitive to $f_{\rm max}$. We find that a range of $f_{\rm max}$ values is necessary in our population synthesis approach to obtain a range of Jovian masses seen in the M-a diagram.

In figure 2.6, we show planet formation tracks resulting from each of the traps in our model within a disk with 4 Myr lifetime, fiducial mass and metallicity. We initialize our calculations with a 0.01 $M_\oplus$ core beginning to form at $\tau_{\rm int} = 10^5$ years into the disk's lifetime, situated at an orbital radius coinciding with a planet trap. We place our embryos on traps because rapid typeI migration will

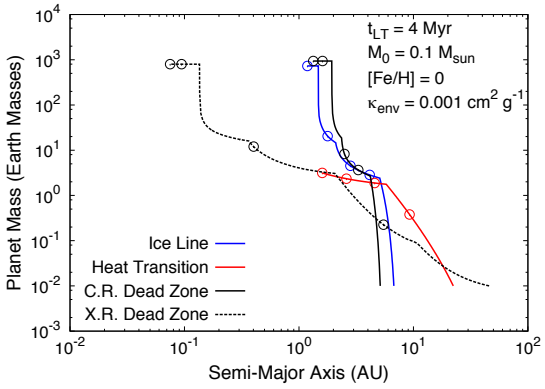

Figure 2.6: Planet formation tracks are shown corresponding to each of the planet traps in our model within a disk with 4 Myr lifetime, 0.1 $M_\odot$ initial mass, and Solar metallicity. Open circles along the tracks denote the location of the planets at 1 Myr intervals. The ice line and cosmic ray dead zone each produce $\sim$ 10^3 $M_\oplus$ Jupiters near 2 AU, while the X-ray dead zone produces a hot Jupiter orbiting within 0.1 AU. Lastly, the heat transition forms a $\sim$ 3 $M_\oplus$ super Earth orbiting near 2 AU.

quickly bring embryos from other initial locations into the traps[1]. With this set of disk parameters, both the ice line and cosmic ray dead zone produce Jupiters orbiting near 2 AU, while the X-ray dead zone forms a hot Jupiter, and the heat transition forms a super Earth.

2.3.4 Population Synthesis

We employ the technique of planet population synthesis to account for the range of disk conditions suggested by observations and their effect on planet formation. Three of the four parameters we vary, being properties of the host star and disk, are external parameters - namely the disk lifetime, mass, and metallicity, whose distributions are discussed in section 2.2. Core accretion results depend sensitively on these quantities which are set by the results of star formation in turbulent molecular clouds. Through varying these quantities, we aim to connect the observed ranges of host star and disk properties (which are vital to the planet formation process) with resulting planet populations.

In addition to the disk lifetime, initial mass, and metallicity, the fourth parameter we stochastically vary is the $f_{\rm max}$ parameter discussed in section 2.3.3 that sets the mass at which planet formation is terminated. For this parameter, we consider a log-uniform distribution with minimum 1 and maximum 500. We emphasize that this is the only parameter intrinsic in our model that is

[1]Our approach is different than Mordasini et al. (2009a) who assume an initial distribution of starting positions distributed between 0.1-20 AU.

stochastically varied.

In our population synthesis calculations, we employ a Monte-Carlo routine whereby we stochastically sample each of the four varied parameters' distributions prior to each individual planet formation calculation. In each run, we calculate formation tracks for 1000 planets within each planet trap, for a total of 3000 planets in each population[2]. For each population, we apply a synthetic observation described in Appendix A that allows us to filter out planets that have low probabilities of being observed with current technologies. This allows for a better comparison with the observed distributions.

For a subset of the population runs, we do not vary the disk metallicity, but rather choose a constant [Fe/H] value over the entire population. In these cases (specified in section 2.4) the remaining three parameters' distributions are sampled to compute the population. For all populations, we consider a central star mass of 1 $M_{\odot}$, stellar radius 3 $R_{\odot}$, and effective temperature 4200 K that correspond with pre-main sequence tracks for a G-type star as shown in Siess et al. (2000). In doing so, we are neglecting any consequences of deviating host-star masses from the Solar value on our resulting populations, as was investigated in Ida & Lin (2005) and Alibert et al. (2011). Lastly, we consider an effective disk $\alpha = 0.001$ for all populations in this work. This setting of α is consistent with the recently observed upper limits of the TW-Hya disk's $\alpha_{\rm turb}$ of 0.007 (Flaherty et al., 2018).

In each population run, we specify the chosen $\kappa_{\rm env}$ value, which remains constant over the entire population. In this work, we do not consider the connection between the disk metallicity and $\kappa_{\rm env}$ and treat these as independent parameters. Envelope opacities of forming planets will depend on the time-dependent size distribution and composition of dust grains in the planet's envelope, and it is currently unknown how these are related to disk metallicity - if at all (Mordasini, 2014).

2.4 Results

We perform three separate sets of population synthesis calculations. First, in section 2.4.1, we consider only Solar metallicity disks and vary the values of $\kappa_{\rm env}$ to determine its effect on population structure. Next, in section 2.4.2, we compute populations with constant disk metallicities at non-Solar values. Lastly, in section 2.4.3, we compute populations with stochastically varied disk metallicities. In all populations, the disk lifetime and initial masses are stochastically sampled using

[2]We separately consider the cosmic ray and X-ray dead zone in each population run.

the log-normal distributions for external parameters summarized in equation 2.1, unless otherwise specified. In all of these sections, two separate sets of populations are run: one that considers cosmic ray-ionized disks, and one considering X-ray ionized disks.

2.4.1 Solar Metallicity Populations

In figure 2.7a, we plot the outcomes of our population synthesis calculation for Solar metallicity disks, while considering different values of $\kappa_{\rm env}$. Populations generated in cosmic ray ionized disks are shown in the left column, and those for X-ray ionized disks in the right column. Each point on the diagrams represents the mass and orbital radius of a planet at the end of its natal disk's lifetime. The percentage included for each zone corresponds to the fraction of remaining planets that populate that region of the diagram. All populations shown have been observationally filtered using our method described in Appendix A, and planets with low estimated observation probabilities are shown in figure 2.7a as small grey points. These planets are not included when calculating the percentage of planets populating zones in the diagram.

Populations Arising From Planet Traps

The Jovian planets formed in our populations with the largest semi-major axes typically form within the cosmic ray dead zone or ice line traps. These are the two innermost traps in our model for the first $\sim 10^6$ years of disk evolution, each situated within 8 AU for typical disk masses (see figure 2.5) and evolving inwards. Compared to the outer traps, planets forming within the C.R. dead zone and the ice line therefore accrete from higher surface density regions of the disk, and have correspondingly lower accretion timescales during oligarchic growth.

In contrast, Jovian planets with the smallest orbital radii tend to arise from formation within the X-ray dead zone or heat transition traps. In the case of the heat transition, the large orbital radii ($\gtrsim 10$ AU for the first 2 Myr of disk evolution) of the trap leads to planets accreting from lower surface density regions, leading to longer oligarchic growth timescales. This causes planets forming within this trap to have slightly lower critical core masses at the onset of gas accretion, and migrating within ~ 2 AU before reaching this stage of formation (see equation 2.21). The lower $M_{\rm c,crit}$ values in turn lead to subsequent gas accretion to take place on longer timescales, causing heat transition planets to migrate in further prior to reaching runaway growth (which only takes place in long-lived disks, with lifetimes $\gtrsim 5-6$ Myr).

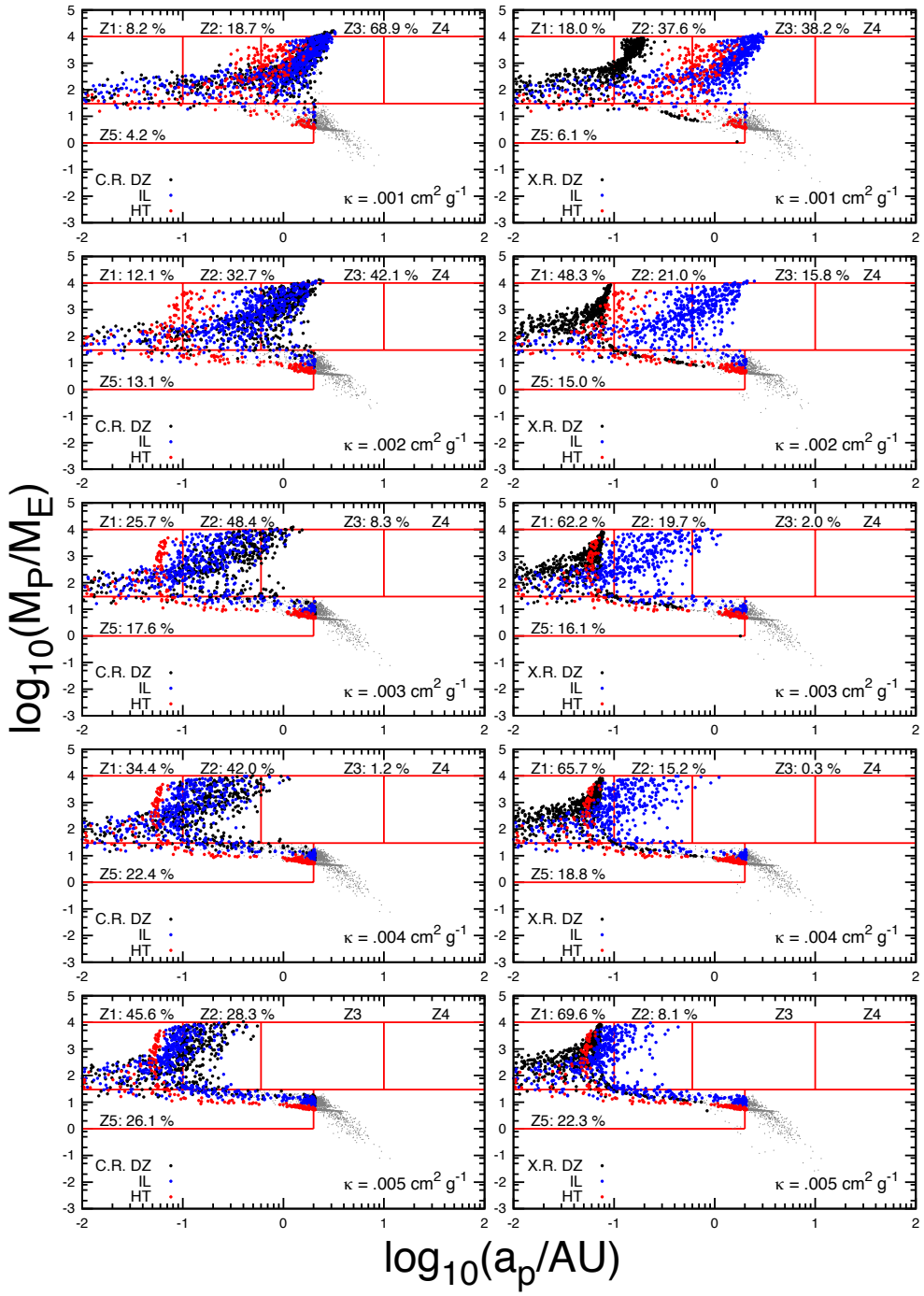

Figure 2.7a: Mass semi-major axis distributions of computed planet populations in Solar metallicity disks are shown. The left column of panels shows populations where cosmic ray ionization is considered to calculate the dead zone trap, and the right column corresponds to X-ray dead zone models. We increase the envelope opacity $\kappa_{\rm env}$ values from 0.001 cm^2 g^{-1} to 0.005 cm^2 g^{-1} from the top to bottom row of panels. Planets with low observation probabilities have been removed from the population and shown as small grey points. The remaining planets are coloured based on the trap they formed in.

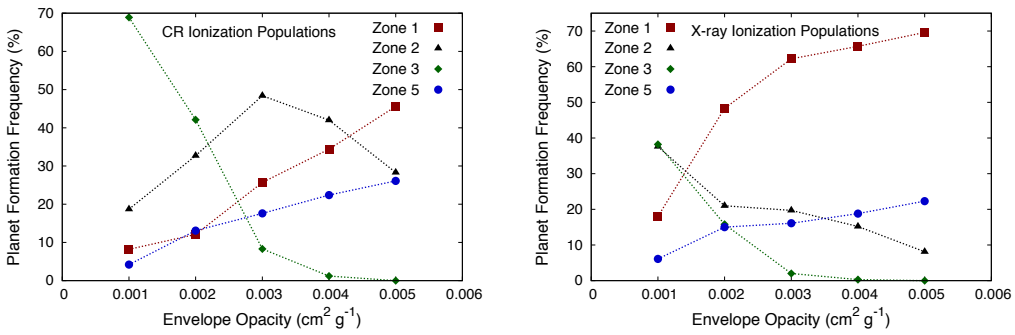

Figure 2.7b: Planet population frequencies for each zone are plotted for each envelope opacity considered in figure 2.7a. The left panel corresponds to the cosmic ray dead zone runs, and the right panel to X-ray dead zone runs. Planets with low observation probabilities (the small grey points in figure 2.7a) are not included when calculating zone frequencies.

The X-ray dead zone trap is initially the outermost trap in our model having orbital radii of $\gtrsim$ 20 AU. However, this trap evolves inwards the fastest, and is located at $\sim$ 1-2 AU after 1 Myr of disk evolution, and is within 0.1 AU after 3 Myr, which is an average disk lifetime in our population synthesis models. Once the trap has quickly evolved to small orbital radii, planets forming within the trap accrete from high-density regions, and have low formation timescales (typically the shortest out of all the traps in our model). The trap's rapid evolution to small orbital radii leads to Jovians population zones 1 or 2 in our population runs.

Our model produces a vast number of cores that fail to reach Jovian masses within their disks' lifetimes. In all of our population runs, more than $\sim$ half of our 3000 individual runs result in planets whose formation is terminated during the slow gas accretion phase or the oligarchic growth phase. However, the fraction of these failed cores that end up as super Earths or Neptunes within the observed zone 5 region of the M-a diagram remains low. Many of them are situated just outside the outer boundary of the zone (where our estimated observable limit is defined). Additionally, a large portion of the planets that do end up within zone 5 have low observation probabilities and are filtered out of the population. Our zone 5 population fractions are therefore substantially lower ($\sim 5\% - 25\%$) than what is found in observations (78%). We believe that this is a consequence of our constant dust to gas model, and discuss this further in section 2.5.

Planet formation within each zone contributes to each zone 5 population. However, the heat transition forms most of the super Earths and Neptunes due to planet formation in this trap having

the longest timescale. There is a large region of zone 5 that our planet formation model fails to populate; specifically the low-mass, low-period region of the diagram. At 1-2 AU, our lowest mass super Earths in zone 5 are ~ 5 $M_\oplus$, and within 0.1 AU all zone 5 planets are Neptunes with masses exceeding 10 or 20 $M_\oplus$. This "zone of avoidance" within zone 5 in our model can be attributed to the inward migration of our formed planets being restricted to the rate at which the traps themselves migrate. The ice line, heat transition, and cosmic ray dead zone traps all converge near 1-2 AU after 3 Myr of disk evolution, so planets forming within these traps that have not reached their gap-opening masses will not be found at smaller orbital radii. The X-ray dead zone, having the most rapid inward migration, results in efficient planet formation. By the time the trap has evolved to 0.1 AU, a planet forming within the trap will exceed 10 $M_\oplus$.

Effects of Envelope Opacities; Cosmic Ray vs. X-Ray Dead Zone

In figure 2.7a, we consider a range of $\kappa_{\rm env}$ values between 0.001-0.005 cm^2 g^{-1}, the population pertaining to each value in a different row. The main effect of increasing envelope opacity is that it increases gas accretion timescales, as planet envelopes take longer to cool and contract. This causes the Jovian planet distribution in each population to shift to smaller orbital radii, as planets take longer to reach their runaway growth phase and in turn have more time to migrate inwards throughout their formation. The longer gas accretion timescales also favour the formation of zone 5 planets as the slow gas accretion phase takes longer, causing more planets' accretion to be terminated in this phase. In the case of the largest $\kappa_{\rm env}$ shown in figure 2.7a, the resulting population has the largest frequency of zone 5 planets, and the gas giants are all within 0.6 AU.

Based on these conclusions, if we were to extend our investigated $\kappa_{\rm env}$ values towards unity, our populations would consist entirely of hot Jupiters (zone 1) and super Earths (zone 5). The increased formation timescales would result in a larger population of zone 5 planets, while also causing planets that do undergo runaway growth to migrate to even smaller orbital radii before doing so.

Comparing the left- and right-columns of figure 2.7a, we find that the main difference between the CR and X-ray ionized disk models is that the CR models never result in a clear separation between the hot Jupiter and warm Jupiter populations. In contrast, the X-ray ionized disks have a distinct separation of these populations for low opacity models ($\kappa_{\rm env}$ = .001 - .002 cm^2 g^{-1}). Since this separation is a clear property of the observations we can conclude that based on our model that considers planetesimal accretion, (i) X-ray ionization dominates CR ionization effects in disks,

a point supported by disk astrochemistry calculations (Cleeves et al., 2013, 2015), and that (ii) population separation between the hot Jupiter and warm Jupiter populations demands low envelope opacities (in agreement with results found in Mordasini et al. (2014)). Ali-Dib, Johansen & Huang (2017) also obtained such a separation between the hot and warm Jupiter population using a pebble accretion planet formation model without considering a disk ionization model.

In figure 2.7b, we summarize these results by plotting each zone's frequency as a function of the envelope opacity considered in each population. For both cosmic ray dead zone and X-ray dead zone populations, zone 3 represents a reasonably large fraction of the population only for the lowest $\kappa_{\rm env}$ settings. At higher settings, this zone's frequency diminishes due to planet migration having a larger effect due to planets forming over longer timescales. For the same reason, the hot Jupiter population increases with envelope opacity. As was previously discussed, higher $\kappa_{\rm env}$ settings favour zone 5 planet formation as well, which is shown in figure 2.7b.

2.4.2 Effects of Disk Metallicity

In figure 2.8a, we show the results of our calculations that consider different disk metallicities while stochastically varying disk lifetimes and masses using equation 2.1. For all populations, we only consider an envelope opacity value of $\kappa_{\rm env} = 0.001$ cm^2 g^{-1} for the reasons outlined in the previous subsection. Each population shown has filtered out planets with low probabilities of being observed using our method discussed in Appendix A. The populations shown in figure 2.8a reproduce the basic trends shown in section 2.4.1 (i.e. the zones typically populated by the different traps), but highlight the effects of the setting of disk metallicity on our population results.

Disk metallicity affects the global dust to gas ratio throughout the disk (equation 2.7) and impacts each planet formation track during the oligarchic growth stage. Lower disk metallicities and dust-to-gas ratios result in longer oligarchic growth timescales. This causes planets to migrate further inward during this first phase of their formation following the evolution of the planet trap they are forming within. Additionally, critical core masses (equation 2.21) are lower for planets forming in low-metallicity disks as well. This mass is the boundary between the oligarchic growth and slow gas accretion phases of formation. The low $M_{\rm c,crit}$ values achieved in low-metallicity disks result in longer gas accretion timescales, and in turn further inward migration.

Due to the resulting low critical core masses, and the long formation timescales exposing planets to migration for the longest, the low-metallicity populations are particularly important for populating

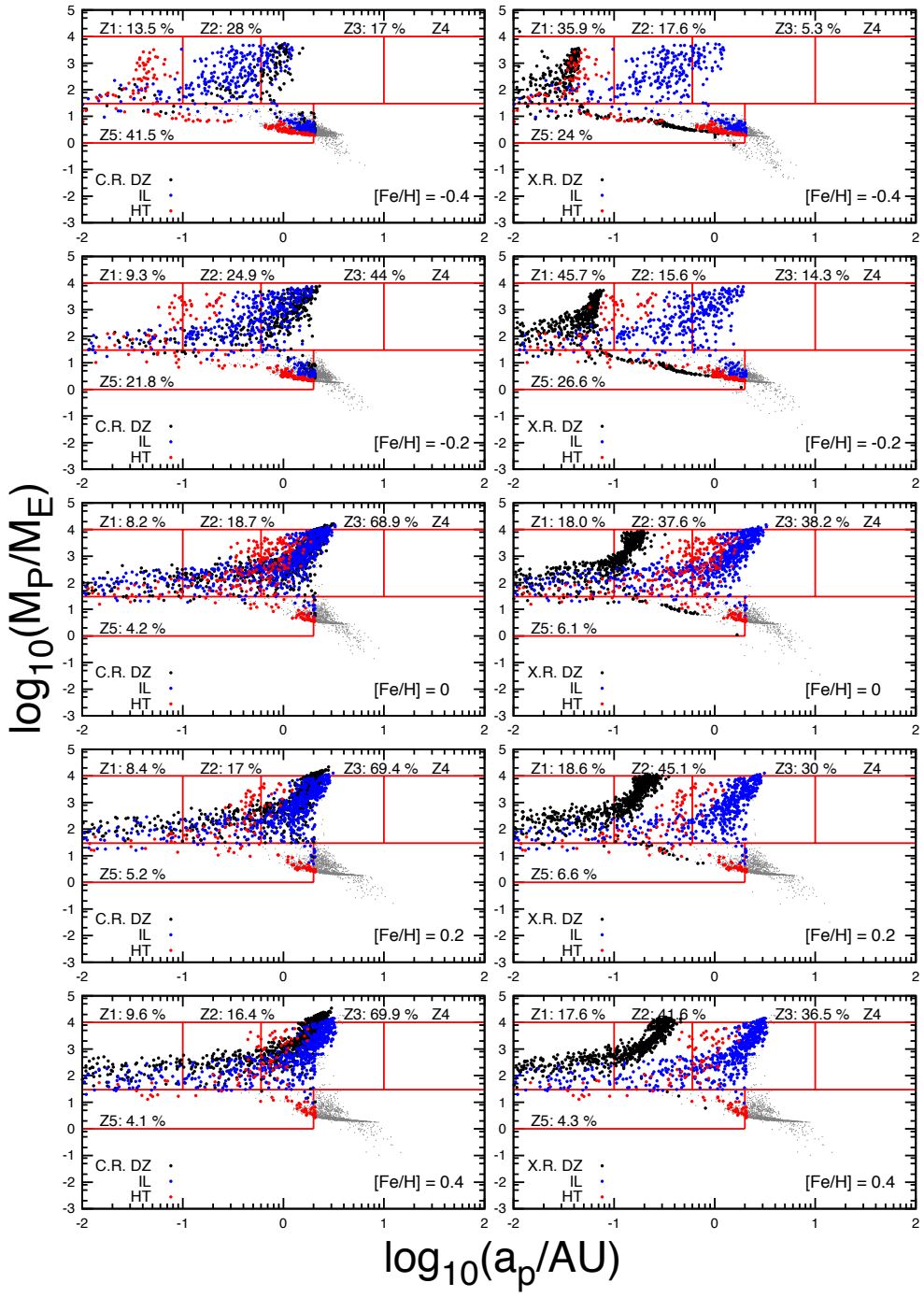

Figure 2.8a: Planet populations for constant disk metallicities are shown. The value of [Fe/H] is indicated for each population. In all runs, we consider an envelope opacity $\kappa_{\rm env} = 0.001$ cm^2 g^{-1}. Cosmic ray dead zone populations are shown in the left columns, and X-ray dead zone populations in the right. The plotted populations have been observationally filtered with small grey points indicating planets with low observation probabilities.

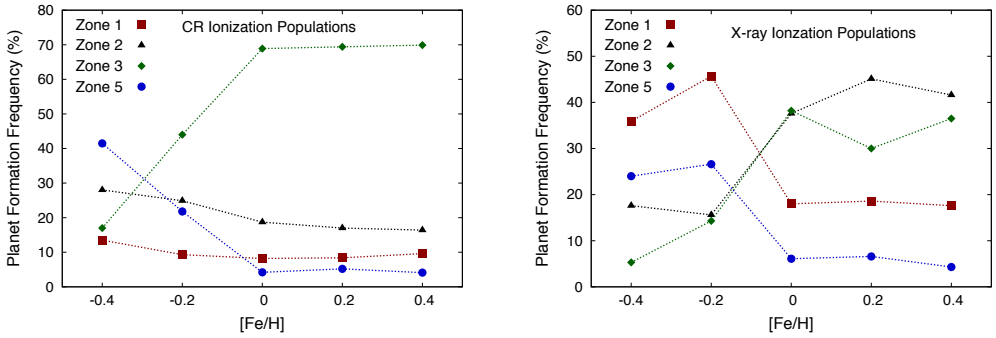

Figure 2.8b: Planet population frequencies from figure 2.8a are plotted for each zone as a function of disk metallicity.

the zone of avoidance within zone 5 discussed in section 2.4.1. In the case of Solar metallicity, quite a large region of zone 5, corresponding to super Earths within 1 AU, remains unpopulated. Low metallicity settings do aid in populating this region, but only act to decrease the region's size, and there still remains a substantial region of zone 5 that our model is not able to populate.

In the upper panels of figure 2.8a where a metallicity of [Fe/H] = -0.4 is considered, the lowest mass planet that forms near 0.01 AU is roughly 10 $M_{\oplus}$, and at 0.1 AU is roughly 6 $M_{\oplus}$. Even with the optimal set-up to form low-mass zone 5 planets, our model cannot produce planets at these orbital radii with smaller masses, which are seen abundantly in the observed distribution.

The increased formation timescales resulting from low disk metallicities favours the formation of super Earths and Neptunes, as was shown in previous metallicity studies such as Fischer & Valenti (2005) and Valenti & Fischer (2008). In our low-metallicity populations, Jovian planets often require longer disk lifetimes than the average 3 Myr lifetimes considered in the $t_{\rm LT}$ distribution, and therefore form less frequently. The Jovian planets that do form are subject to migration for longer due to their increased formation timescale, which favours the formation of zone 1 and zone 2 Jupiters as opposed to zone 3.

We note also that a variation of disk metallicity does not affect the double peaked structure of the Jovian populations, indicating that the low value of $\kappa_{\rm env}$ is still the key parameter (along with X-ray ionization), that controls this.

In figure 2.8b, we show the frequencies by which planets populate various zones in figure 2.8a and their trends with disk metallicity. For both the cosmic ray and X-ray ionized models, the expected trend of low-metallicity disks favouring the formation of zone 5 planets is found. As disk metallicity is

increased, the frequency of zone 5 planets decreases to less than 10 % while the frequency of Jovian planets (sum of zones 1, 2, and 3) increases, in agreement with the observed planet-metallicity relation (Fischer & Valenti, 2005). The distribution of Jovian planets in the populations in 2.8a is seen to shift outwards as disk metallicity is increased due to the shorter formation timescales.

For the case of cosmic ray populations, the majority of the Jovian population consists of zone 3 planets for metallicities [Fe/H] ≥ 0. The zone 1 and zone 2 frequencies decrease as metallicity is increased due to the distribution of Jovian planets shifting outwards.

The X-ray populations are capable of forming hot Jupiters even at the lowest metallicity settings considered. Since the X-ray dead zone trap evolves to small orbital radii early in the disk's evolution, planets forming within this trap accrete from higher surface density regions and have correspondingly lower formation timescales. Thus, the X-ray dead zone is the trap in our model that forms Jovian planets the most efficiently in low-metallicity disks. In figure 2.8b, the hot Jupiter and the failed core populations (zone 1 and 5) comprise the majority of the sub-Solar metallicity populations, and their frequencies decrease as the metallicity increases beyond Solar. In the high metallicity cases, zones 2 and 3 are the highest frequency zones as the ice line and heat transition are able to form Jovians more often, and the distribution of Jovian planets shifts outwards due to shorter formation timescales.

2.4.3 Stochastically Varied Disk Metallicity

In figure 2.9, we show populations resulting from a stochastic variation of disk metallicity, lifetime, and initial mass corresponding to their observationally constrained distributions. In the upper three rows of this figure, we consider different envelope opacities; the fiducial value of 0.001 cm^2 g^{-1} (top row), as well as a higher setting of $\kappa_{\rm env} = 0.002$ cm^2 g^{-1} (second row), and a lower setting of 5×10^{-4} cm^2 g^{-1} (third row).

Similar to section 2.4.1, we find that the best setting of $\kappa_{\rm env}$ is 0.002 cm^2 g^{-1} for models using a cosmic ray dead zone. Lower settings of $\kappa_{\rm env}$ result in a very high fraction of zone 3 planets as well as a reduced amount of zone 5 planets due to shorter gas accretion timescales. In all cases, our model forms a significantly smaller fraction of zone 5 planets than are present in the observed distribution.

In our populations that stochastically vary the disk metallicity, we again find that low settings of envelope opacity produce the best results when we consider an X-ray ionized disk. In the case

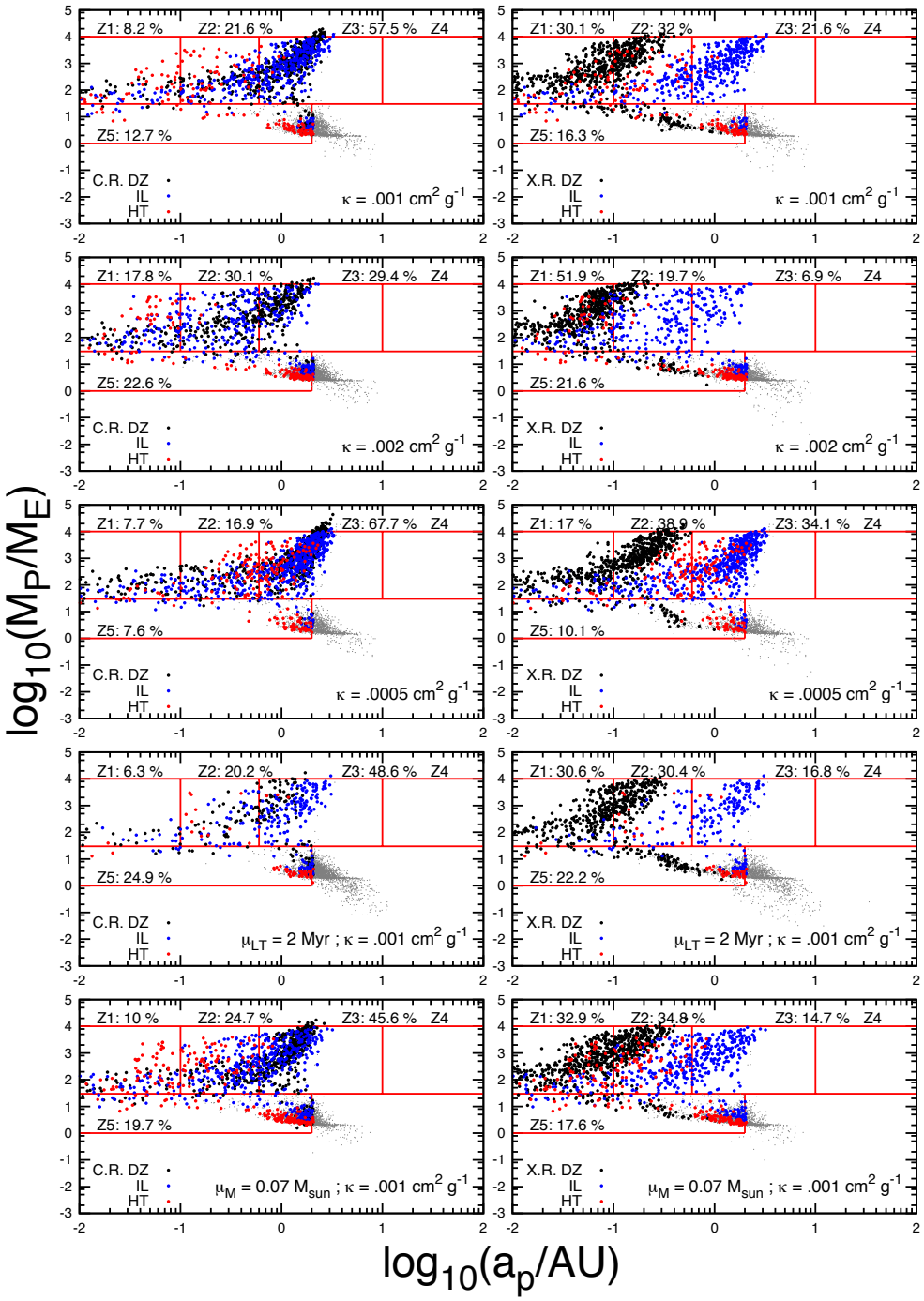

Figure 2.9: Observationally-filtered planet populations are shown whereby disk metallicity is stochastically selected, along with disk lifetime and initial mass. In the top three rows, we consider different envelope opacity values of 0.001, 0.002, and 5×10^{-4} cm^2 g^{-1} as indicated in each panel. In the bottom two rows, we shift the mean of the disk lifetime and initial mass distribution, respectively, to -1σ of the mean.

of $\kappa_{\rm env} = 0.002$ cm^2 g^{-1}, our model produces too few zone 3 Jupiters. Lower opacity settings are more optimal for X-ray dead zone populations as they result in a larger fraction of the Jupiter-mass planets having orbital radii larger than 1 AU.

However, as was the case for the cosmic ray dead zone models, our populations form a much smaller fraction of super Earths and Neptunes compared to the observations. In the case of our best-fit $\kappa_{\rm env} = 0.001$ cm^2 g^{-1} setting for X-ray dead zone models from section 2.4.1, we only obtain a zone 5 fraction of 16.1 %. For the lowest opacity setting considered, $\kappa_{\rm env} = 5 \times 10^{-4}$ cm^2 g^{-1}, the fraction of zone 5 planets further diminishes to roughly 10 % due to short gas accretion timescales that favour the formation of Jupiters. We therefore consider $\kappa_{\rm env} = 0.001$ cm^2 g^{-1} to remain our optimal setting for X-ray dead zone populations that stochastically vary the disk metallicity.

In the bottom two rows of figure 2.9, we show populations resulting from stochastically sampling modified disk lifetime and mass distributions. In the fourth row, we change the mean disk lifetime to 2 Myr, and in the bottom row, we reduce the mean initial disk mass to 0.07 M$_\odot$ (corresponding to -1σ in its distribution). In both cases, we consider an envelope opacity of 0.001 cm^2 g^{-1}, and make no modification to the disk metallicity distribution we consider.

Our motivation for modifying the disk lifetime and mass distributions is two-fold. First, since these distributions are somewhat poorly constrained observationally, we want to determine how robust our population results are to $\sim 1\sigma$ changes in the distributions' means which may result from future observations. Second, both these changes favour the formation of zone 5 planets (see discussion below), and we want to determine if such changes improve the fraction of zone 5 planets our model is able to form.

In the case of a reduced mean disk lifetime of 2 Myr (figure 2.9, fourth row), the planets on average have less time to form, and this favours the formation of zone 5 planets. Comparing with the top row, we see that the zone 5 frequency has increased by roughly 6 % which is not a drastic change. The frequencies within all of the zones do not change significantly, the total number of planets that populate zones has reduced. Decreasing the mean disk lifetime to 2 Myr results in an even more significant pile-up of planets just outside of zone 5 - masses between 1 and 20 M$_\oplus$ orbiting between 2 and 5 AU. Since these planets have low observation probabilities, they get filtered out of the population.

When considering a reduced mean initial disk mass of 0.07 M$_\odot$ (figure 2.9, bottom row), the resulting populations do have a slightly larger fraction of zone 5 planets. However, as was the

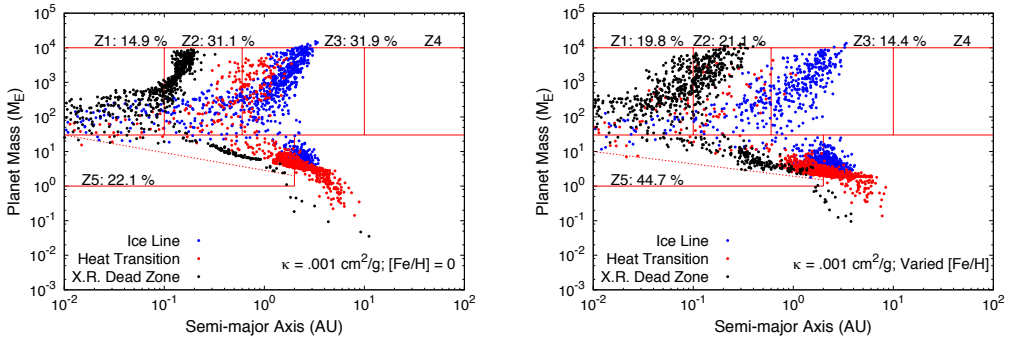

Figure 2.10: Our populations that best correspond to the data are shown, without any observational filtering. Both populations use an X-ray ionization model and resulting dead zone structure, as well as a low envelope opacity of 0.001 cm^2 g^{-1}. The left panel corresponds to a Solar-metallicity disk for the entire population, and the right panel corresponds to stochastically-sampled disk metallicities. In both cases, our model does not populate a low-mass, low period region of zone 5 that we have identified for each population. The corresponding populations that have been corrected for observational biases are shown in figure 2.7a, top right panel, and figure 2.9, top right panel, respectively.

case with a reduced mean disk lifetime, the fraction of planets within all of the zones does not change drastically when compared to the fiducial distributions. This shows that the results of our calculations, in terms of formation frequencies among the various zones, are robust to $\sim 1\sigma$ changes in the mean of the disk lifetime and initial disk mass distributions.

In figure 2.10, we highlight results that best approximate the planetary populations in the observed M-a diagram. Specifically, we show two populations that have no corrections for observational biases, and are direct outputs from our planet population synthesis model. The populations chosen give the best comparison to observations, and both use the X-ray dead zone, and an envelope opacity of 0.001 cm^2 g^{-1}. The left panel considers a Solar metallicity, while the right panel stochastically varies the disk metallicity within the population in accordance with equation 2.2.

These populations show that, before correcting our populations for observational biases, our model is capable of forming a significant fraction of zone 5 planets. The majority of our failed cores are situated between 1 and 5 AU and typically have low observation probabilities and are therefore likely to get filtered out. These fractions are still lower than the observed distribution's zone 5 fraction, but are much greater than the fractions that are obtained for populations that are corrected for observational biases.

In the case of a Solar metallicity disk (figure 2.10, left panel), all zone 5 planets formed within

$\sim$ 0.3 AU are $\gtrsim$ 20 $M_\oplus$, and are typically $\gtrsim$ 3 $M_\oplus$ near 1-2 AU. These represent the lowest mass planets our model can form that populate zone 5 using a Solar-metallicity disk.

When considering the observed disk metallicity distribution (figure 2.10, right panel), the resulting planet population appears less clustered and more scattered. In this case, we can form slightly lower-mass planets due to the sub-Solar metallicity portion of this distribution resulting in planets with lower critical core masses during their formation. The low-metallicity portion of the distribution results in planets that are $\gtrsim$ 8 $M_\oplus$ within 0.3 AU and $\gtrsim$ 2 $M_\oplus$ between 1-2 AU. In either case, there remains a large portion of zone 5 that is a zone of avoidance for super Earths in our core accretion - planet trap picture. We address this and other general results below.

2.5 Discussion

Our population synthesis results show that the planet formation model used in this work is able to form the range of different planetary classes seen in observations. There are, however, regions of the planet mass semi-major axis diagram where our model does not produce planets.

Our models are capable of forming Jovian planets for semi-major axes $\lesssim$ 2-3 AU, but do not produce any at larger orbital radii. The observed radial frequency distribution of Jovian planets, which peaks at roughly 3-10 AU, indicates that gas giants are less common at larger orbital radii (Cumming et al., 2008; Bryan et al., 2016). Thus, our populations agree with this result, as our model produces Jovian planets with $a_p \lesssim 3$ AU, but does not produce longer period gas giants.

We separately consider X-rays (originating due to magnetospheric accretion) and interstellar cosmic rays as disk ionization sources. The different corresponding ionization rates result in notably different dead zone radii and evolution, leading to significantly different planet populations. The gas giants produced in the cosmic ray dead zone trap display a continuously increasing frequency with orbital radius out to 2 or 3 AU. The X-ray dead zone populations, conversely, show a double-peaked period distribution of gas giants as the X-ray dead zone tends to form hot Jupiters while the ice line forms gas giants at larger orbital radii near 1 AU. These models that include an X-ray dead zone offer an explanation to the observed reduction in frequency of gas giants between 0.1-0.6 AU (Cumming et al., 2008).

As discussed, for example, in Matt & Pudritz (2005) and Frank et al. (2014), young stars are associated with both disk and stellar (accretion powered) MHD winds that produce shocks that

scatter cosmic rays and prevent them from reaching the disk (Cleeves, Adams & Bergin, 2013). Moreover, Cleeves et al. (2015) show that reduced cosmic ray ionization (a consequence of exclusion by disk winds) produce disk chemistry features in agreement with TW Hya observations. Our population results showing that X-ray ionized models produce populations that better reproduce observational features are in agreement with these results.

One key difference in our super Earth populations and the observations is that our model produces fewer close-in super Earths. When comparing the direct population outputs (figure 2.10) with the populations that account for observational biases (figure 2.9), we see that a portion of the zone 5 planets our model are filtered out as they have low observation probabilities. Additionally, our model does produce a large number of failed cores, but a significant fraction of these orbit just outside the defined outer observable limit of 2 AU, and are situated on orbits out to 5 AU. The range of radii between 1-5 AU is the most common region for super Earths to form in our model as this is the region where the ice line, heat transition, and cosmic ray dead zone traps converge to. Thus, our model predicts there to be a significant population of super Earths with orbital radii of 1-5 AU.

Our planet formation model does not produce low mass super Earths that migrate into short-period orbits. We noted this several times throughout section 2.4 and refer to this as a zone of avoidance of our model within zone 5 of the mass-semimajor axis diagram. The lowest mass super Earths formed in our model that populate zone 5 are ~ 3 $M_\oplus$ and orbit outside of 1 AU. This feature of our populations is tied to the evolution of the traps, that evolve from orbital radii outside ~ 8 AU to within ~ 1 AU on disk evolution timescales. This prevents $\sim$ Earth-mass planets from migrating to short period orbits in our model as they evolve with the trap they are forming within.

Planets can, however, become liberated from their host planet traps at the onset of type-II migration. In this case, planets must exceed their gap opening mass (equation 2.17) of ~ 10 $M_\oplus$ to type-II migrate separately from their trap. Initially, type-II migration takes place on shorter timescales than trapped type-I migration, so these planets can, in some cases migrate to short period orbits during their slow gas accretion phase before their accretion is terminated at the disk lifetime. Thus, the lowest mass zone 5 planets orbiting between 0.01-0.1 AU formed in our model have masses $\gtrsim 10$ $M_\oplus$.

Hasegawa (2016) also found that a core accretion model involving trapped type-I migration could not form a failed core population consistent with observations. In particular, this model could only form super Earths more massive than $\sim 4-5$ $M_\oplus$, similar to the results found in this work.

Based on the results of our constant dust-to-gas ratio model, one might suggest that formation scenarios in addition to the failed core scenario are necessary to explain the observed super Earth population. In particular, Hasegawa (2016) suggested that embryo assembly (similar to the mechanism by which the Solar System terrestrials formed) may produce super Earth populations that, in combination with the failed core scenario, compare well with observations.

We emphasize, however, that we have not included the effects that radial drift of dust may have on our populations. Birnstiel et al. (2012) and Cridland et al. (2017) have shown that dust evolution models result in depleted dust-to-gas ratios outside of the ice line. Based on these results, we predict that planet formation in the outer disk (for example, in the heat transition trap) will result in longer oligarchic growth timescales and correspondingly smaller $M_{\rm c,crit}$ values (see equation 2.21). As discussed in section 2.4.2, this will in turn result in longer gas accretion timescales allowing migration to transport these planets to smaller orbital radii prior to disk dissipation. We expect that including the effects of radial drift and dust evolution will populate the zone of avoidance by moving the region of planet formation inward. We will fully explore these effects in an upcoming publication.

In this work, we only consider two migration regimes: trapped type-I migration and type-II migration. However, it is possible that there is an additional migration regime for which the corotation torque saturates prior to the onset of type-II migration (Dittkrist et al., 2014). In this case, the planet would no longer be trapped in the disk inhomogeneity, and would type-I migrate to inner regions of the disk on short timescales before reaching its gap opening mass. If this phase were applicable to planets in our model, it would greatly affect our population results.

In Alessi et al. (2017), we perform an analysis to confirm that planets reach their gap-opening masses prior to their saturation-masses in our model, thereby confirming that the trapped phase is applicable throughout the entirety of the type-I migration regime in our model. There is however, a notable similarity in the gap-opening masses of planets in our model and typical saturation masses. As both of these quantities depend sensitively on the planet and local disk conditions, a model that considers in detail the planet-disk interactions is a prospect for future work (which is considered, for example, in Hellary & Nelson (2012), and Cridland, Pudritz, & Alessi (2018), in prep.).

We restrict our model to consider only the case of planet formation in isolation, and do not account for the dynamical interaction between planetary cores. We do this to provide a clear bench mark against which we can compare future calculations that include the effects of planet-planet

interaction. We note that the traps in our model converge and intersect throughout disk evolution, and thus dynamic interactions would take place between forming planets. Planet-planet dynamics during planet formation (as was previously considered, for example, by Hellary & Nelson (2012) and Ida, Lin & Nagasawa (2013)) is another prospect for future work to determine the effects of resonances and scattering on our computed planet populations.

An additional parameter we have not varied that could affect our results is the disk α, which we held to a constant value of 10^{-3}. If we were to consider larger estimates of α up to 10^{-2}, the following effects would take place: (i) disk evolution would take place on a shorter timescale, reducing the surface density quicker, causing planet formation to be less efficient; and (ii) inward migration rates would be faster. Hasegawa & Pudritz (2013) included a parameter study of α in their population synthesis work including planet traps. This work indeed showed that gas giants formed less efficiently when larger α values were considered. Additionally, zone 3 Jovians formed less frequently in populations when higher values of α were considered, while the zone 1 hot Jupiter population frequency increased with α - both as a result of the increased migration rates. Notably, the zone 5 population frequency was found to be insensitive to the particular setting of α within its estimated range of $10^{-3} - 10^{-2}$.

We obtained the best comparison between computed populations and the observed distribution when considering low envelope opacities $\sim 10^{-3}$ cm^2 g^{-1}. Our focus in this paper has not been to calculate $\kappa_{\rm env}$ values as they are acquired from the disk and processed in the forming planet's envelope, but rather to constrain its value by comparing resulting planet populations with the observed distribution. Calculating this directly would require one to track the dust grain sizes and compositions as they are accreted onto a planet, as well as how they are processed in the forming planet's envelope, which is beyond the scope of this paper. We note that one value of $\kappa_{\rm env}$ will not describe a planet's atmosphere throughout the entirety of its formation (as its opacity will change as a result of its accretion history), let alone describe an entire population of planets. However, by comparing our computed populations to observations we have constrained this parameter that sets gas accretion timescales.

The earliest core accretion models found that an envelope opacity ~ 1 % of the ISM opacity was necessary to achieve reasonable planet formation timescales (Pollack et al., 1996). Our results indicate that an even further reduced envelope opacity of ~ 0.1 % the ISM opacity produces the best results, which is similar to the more recent result of Mordasini et al. (2014), who found a reduction

factor of 0.3 % of the ISM opacity gave the best comparison of their computed populations with observations. It is notable that this result indicates that the best fit $\kappa_{\rm env}$ value is a factor of 1000 lower than the typical opacity assumed in our disk model for the case of Solar metallicity, which assumes a κ_0 of 3 cm^2 g^{-1} (Chambers, 2009). One possible explanation is that significant grain growth takes place within envelopes of forming planets to achieve a much lower opacity than the surrounding disk material. This was shown to be the case in Mordasini (2014), who found that efficient grain growth takes place over a significant portion of a planet atmosphere, leading to low optical depths consistent of a low $\kappa_{\rm env}$ value of 0.3 % of the ISM opacity.

2.6 Conclusions

In this paper, we have computed a comprehensive suite of planet population synthesis calculations, each involving three thousand model evolutionary tracks, that incorporate the observationally constrained distributions of disk lifetimes, masses, and metallicities in outcomes of a core accretion model with trapped type-I migration. Planets formed in our model are not free to migrate into the inner disk, but are rather tied to the radial locations of the planet traps they form within for all stages prior to type-II migration. The main focus of this paper has been to study the effects of forming planets' envelope opacities, as well as disk metallicities, on our results. We list our main conclusions here:

- We separately considered X-ray and cosmic ray disk ionization and resulting dead zones in our populations. These two traps produce significantly different populations as the X-ray dead zone tends to form massive planets within 0.5 AU while the cosmic ray dead zone forms Jovian planets near or outside 1 AU. When combined with the planets formed in the ice line and heat transition, populations involving a cosmic ray dead zone form a distribution of Jovian planets whose frequency increases with orbital radii out to $\sim$ 2 AU. Conversely, populations including an X-ray dead zone features a double-peaked distribution of Jupiters, with an inner peak within 0.3 AU consisting mainly of planets formed in the X-ray dead zone and an outer peak near 1 AU corresponding to planets formed within the ice line. Populations using an X-ray dead zone are the only ones that produce such a double-peaked feature in the Jovian planets' radial distribution that is seen in observations.

- We find that Jovian planets form less frequently in disks with sub-Solar metallicity. In such

disks, failed cores (super Earths or Neptunes) are much more common. Our populations show that the formation frequency of Jovian planets is correlated with disk metallicity, in agreement with the planet-metallicity relation (Fischer & Valenti, 2005).

- Our planet formation model does not produce low-mass, low-period super Earths. The lowest mass planets formed in our model orbiting near 0.01 AU are ~ 10 $M_\oplus$, and the lowest mass planets orbiting near 0.1 AU are ~ 6 $M_\oplus$. The traps are located outside of 5 AU in the earliest stages of disk evolution, and converge to ~ 1 AU within a typical 3 Myr disk lifetime, with the exception of the X-ray dead zone which evolves to ~ 0.05 AU. We suggest that this is a consequence of our assumption of a constant dust to gas ratio.

- Since planet migration to small orbital radii are limited to large, disk evolution timescales, accretion throughout this process prevents our model from forming low-mass and low-period super Earths that have been observed. Based on the results of our constant dust-to-gas ratio model, we suggest these planets to have formed via a different process such as collisional growth, similar to the process that formed the Solar System's terrestrial planets. However, the radial drift of dust grains may result in a super Earth population that is much more concentrated towards small disk radii. We defer this analysis to our next paper.

- We find that low envelope opacities of $\sim 10^{-3}$ cm^2 g^{-1} are necessary Jovian planets with orbital radii ≥ 1 AU in our populations. Higher envelope opacities (greater than 0.003 cm^2 g^{-1}) cause for longer formation timescales, whereby Jovian planets typically migrate within 0.6 AU prior to undergoing runaway growth. In populations considering an X-ray dead zone, we find an optimal setting of 0.001 cm^2 g^{-1}.

In our next paper in this series, we will examine the effect of radial drift of dust in the disk on planet formation and on the structure of planetary populations.

Appendix A: Observationally Filtering Computed Populations

In this section, we describe our method of correction our computed populations for observational biases by estimating their observation probabilities. We obtain separate estimations for transit and radial velocity detection probabilities and assume that planets with high transit detection probabilities *or* high radial velocity detection probabilities are observable and are therefore included in

the populations. Planets that have low detection probabilities corresponding to both methods are filtered out of the populations.

To estimate detection probabilities for each computed planet, we use signal to noise ratios (SNR). We assume that cases where S/N $\geq$ 10 correspond to successful observations of a planet. This is a conservative estimate as a SNR of 10 corresponds to a detection at the 10σ confidence level. For each population of 3000 planets this results in a false positive probability of 10^{-18}. This is the same SNR threshold used in Howard et al. (2012) to confirm detections of hot Jupiters in *Kepler*'s first quarter.

In the case of a transit detection, the SNR ratio is (Howard et al., 2012),

$$\mathrm{S/N}_{\mathrm{transit}} = \frac{R_p^2/R_*^2}{\sigma_{\mathrm{CDPP}}}\sqrt{\frac{n_{\mathrm{tr}}t_{rmdur}}{3\,\mathrm{hr}}}\,, \tag{2.26}$$

where R_p is the planet's radius, $R_* = R_\odot$ is the radius of the star, here n_{tr} is the number of detected transits during the observation time, t_{dur} is the transit duration, and σ_{CDPP} is the differential photometric precision measured over a duration of 3 hours. The "noise" factor in equation 2.26 is σ_{cdpp} is related to errors associated with telescope stability, transit light curve, and stellar activity. As reported in Howard et al. (2012), typical 3 hour σ_{cdpp} values range from 30-300 ppm.

Our model does not directly calculate planet radii as we do not consider interior structure models. To estimate the radii of low mass planets $M_p < 30$ $\mathrm{M}_\oplus$, where we compute solid abundances using our disk equilibrium chemistry model, we interpolate over results presented in Zeng & Sasselov (2013) who performed an interior model of solid planets in order to calculate their radii as a function of planet mass and composition. For higher mass planets, we use the empirical relation from Bashi et al. (2017) to estimate planet radii.

Since this model does not consider dynamical effects during or after planet formation, we do not have an estimate of orbital eccentricities or inclinations of planets in our computed populations. We therefore make the simplifying assumption that both of these quantities are zero when calculating the transit durations t_{dur}. To estimate the number of transits n_{tr}, the total "observation time" needs to be defined, which we assume to be 3 years to roughly correspond to the *Kepler* mission (prior to the *K2* mission).

The radial velocity amplitude corresponding to a planet of mass M_p orbiting a star M_s with

period P is (Cumming, 2004),

$$K = \frac{28.4\,\mathrm{m/s}}{\sqrt{1-e^2}} \frac{M_p \sin i}{M_{\mathrm{Jup}}} \left(\frac{M_s + M_p}{M_\odot}\right)^{-2/3} \left(\frac{P}{1\,\mathrm{year}}\right)^{-1/3} . \tag{2.27}$$

In this work, $M_s = M_\odot$, and we assume $e = 0$ for all planets for the reasons discussed previously. The corresponding SNR for a radial velocity detection is,

$$\mathrm{S/N_{RV}} = \frac{K}{\sigma_{\mathrm{RV}}} \sqrt{n_{\mathrm{orb}}}\,, \tag{2.28}$$

where n_{orb} are the number of orbits during the observation time and σ_{RV} is the noise associated with a radial velocity detection. Sources of error related to the RV method are caused by a combination of measurement error and stellar "jitter" (pulsation and/or surface convection that adds noise to an RV signal). These two sources of error are reported in Cumming (2004) to be 3-5 m/s each. Taking into account addition in quadrature, we estimate σ_{RV} to range from 4-10 m/s. We consider a longer observation time of 6 years for transit detections when estimating n_{orb}.

We assume uniform distributions for both σ_{cdpp} and σ_{RV} over the ranges previously mentioned and calculate the corresponding SNR distribution for each planet formed in the population. To estimate a detection probability associated with each method, we calculate the fraction of the SNR distributions that are ≥ 10, which we chose as our threshold. We then performed a simple Monte Carlo routine using each planet's detection probabilities to determine if each planet was observed or not. We note that the majority of planets in each population have detection probabilities calculated with this method of or 1 or 0, and in these cases this is a binary problem. However, there is always a portion of planets who have a non-binary detection probability, which correspond to planets that would be observed around stars with low noise values, or unlikely to be observed around stars with high noise values. It is these cases that necessitate the Monte Carlo calculation.

Acknowledgements

The authors thank Alex J. Cridland for fruitful discussions regarding this work. We also thank the anonymous referee for their helpful and insightful comments. M.A. acknowledges funding from the National Sciences and engineering Research Council (NSERC) through the Alexander Graham Bell CGS/PGS Doctoral Scholarship. R.E.P. is supported by an NSERC Discovery Grant. This research

has made use of the Exoplanet Orbit Database and the Exoplanet Data Explorer at exoplanets.org.

Chapter 3

Formation of Planetary Populations II: Effects of Initial Disk Size & Radial Dust Drift

Matthew Alessi, Ralph Pudritz, & Alex Cridland

What follows has been published in Monthly Notices of the Royal Astronomical Society (MNRAS). See: Alessi, Pudritz, & Cridland (2020), MNRAS **493**: 1013. We include minor additional justification for a model assumption in the addendum at the end of this chapter.

Abstract

Recent ALMA observations indicate that while a range of disk sizes exist, typical disk radii are small, and that radial dust drift affects the distribution of solids in disks. Here we explore the consequences of these features in planet population synthesis models. A key feature of our model is planet traps - barriers to otherwise rapid type-I migration of forming planets - for which we include the ice line, heat transition, and outer edge of the dead zone. We find that the ice line plays a fundamental role in the formation of warm Jupiters. In particular, the ratio of super Earths to warm Jupiters formed at the ice line depend sensitively on the initial disk radius. Initial gas disk radii of $\sim$50 AU results

in the largest super Earth populations, while both larger and smaller disk sizes result in the ice line producing more gas giants near 1 AU. This transition between typical planet class formed at the ice line at various disk radii confirms that planet formation is fundamentally linked to disk properties (in this case, disk size), and is a result that is only seen when dust evolution effects are included in our models. Additionally, we find that including radial dust drift results in the formation of more super Earths between 0.1 - 1 AU, having shorter orbital radii than those produced in models where dust evolution effects are not included.

3.1 Introduction

The current wealth of exoplanetary data provides crucial constraints on the potential outcomes of planet formation. The current sample of nearly 4000 confirmed exoplanets (Borucki et al., 2011b; Batalha et al., 2013; Burke et al., 2014; Rowe et al., 2014; Morton et al., 2016) is consistently increasing as the *K2* mission (Crossfield et al., 2016; Livingston et al., 2018a,b) and *TESS* (Gandolfi et al., 2018; Huang et al., 2018a; Vanderspek et al., 2019) continue to discover and confirm even more exoplanets. The distribution of planets on the mass-semimajor axis (hereafter M-a) diagram reveals an immense amount of information that can significantly constrain planet formation theories. For example, exoplanet populations can be discerned from the structure in the planet distribution on the M-a diagram, and the diagram can be divided into zones that broadly define these various planet populations (Chiang & Laughlin, 2013; Hasegawa & Pudritz, 2013). A key question that arises from this data is, how do planets populate these regions of the M-a diagram?

In figure 3.1, we show the current distribution of confirmed exoplanets on the M-a digram. In terms of frequency, the dominant planet population consists of Earth-Neptune mass planets (1-30 $M_{\oplus}$) orbiting within 2 AU of their host stars, lying within zone 5 on the diagram (comprising 65.1% of the total exoplanet population). Zones 1-4 define the various classes of gas giants: hot Jupiters (zone 1; 12.7%), period-valley giants (zone 2; 4.5%), warm Jupiters (zone 3; 11.9%), and long-period giants (zone 4; 0.16%).

While the M-a diagram is useful in revealing the outcomes of planet formation, the distribution is shaped, in part, by the inherent biases present in exoplanet detection techniques. For example, the frequency of hot Jupiters on the M-a diagram exceeds the frequency of zone 3 planets, even though warm Jupiters have been shown to be the most common type of gas giant (Cumming et al.,

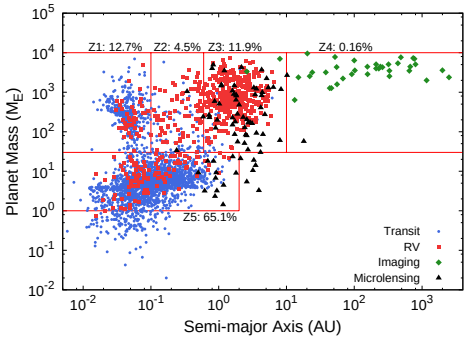

Figure 3.1: The observed mass-semimajor axis distribution of confirmed exoplanets. As was first suggested by Chiang & Laughlin (2013), the diagram is divided into zones that define planet populations: hot Jupiters (zone 1), period-valley giants (zone 2), warm Jupiters (zone 3), long-period giants (zone 4), and lastly super Earths and Neptunes (zone 5). The individual planets are colour-coded based on their initial detection technique. These data were compiled using the NASA Exoplanet Archive, current as of May 31, 2019.

2008). Occurrence rate studies, such as Santerne et al. (2016); Petigura et al. (2018), account for detection biases to reveal the true underlying distribution of exoplanets. Results from these studies are extremely useful in constraining planet formation theories, offering the best means to compare theory to observations.

In this paper, we consider planet formation in the framework of the core accretion scenario (Pollack et al., 1996). Outcomes of the core accretion model have been shown to sensitively depend on host star and disk properties (Ida & Lin, 2008; Mordasini et al., 2009a; Hasegawa & Pudritz, 2011; Alessi et al., 2017).

We utilize the technique of planet population synthesis to link the range of outcomes of planet formation, as contained in the M-a diagram, to the variance of disk properties. Planet population synthesis allows one to explore the effects of ranges of input parameters on planet formation results, and the parameters we consider in this work are the disk's mass, lifetime, and metallicity. The technique has been used in many previous works, such as Ida & Lin (2004a, 2008); Mordasini et al. (2009a); Hasegawa & Pudritz (2013); Bitsch et al. (2015); Ali-Dib (2017); Alessi & Pudritz (2018).

Recent observations by *ALMA* (e.g. ALMA Partnership et al. (2015); Andrews et al. (2018)) and *SPHERE* (e.g. Avenhaus et al. (2018)) have revolutionized our understanding of protoplanetary disks. In particular, observations that aim to measure disk masses and radii continue to inform planet formation models, as these quantities set the midplane densities throughout the disk, thereby

affecting planet formation timescales.

For example, Ansdell et al. (2016, 2018) measured dust and gas disk masses[1] and radii of protoplanetary disks in Lupus with *ALMA*. These observed disks surrounding a range of host-stellar masses have gas radii in the range of 63-500 AU at an age of $\sim$ 1-3 Myr. We emphasize, however, that these large, extended disks are the exception and are not indicative of typical disks that are much more compact, as indicated by numerous observations showing dust radii of $\lesssim 20 - 30$ AU (Barenfeld et al., 2016, 2017; Cox et al., 2017; Hendler et al., 2017; Tazzari et al., 2017; Cieza et al., 2019; Long et al., 2019).

The compact dust-distribution resulting from radial drift models predict that (sub-) mm emission from disks will be more compact than measurements of CO isotopologues that trace the gas distribution (Facchini et al., 2017; Trapman et al., 2019). The Ansdell et al. (2018) survey of the Lupus disks found that gas disk radii were typically between 1.5 and 3 times larger than dust disk radii. This offset can be explained by the differences in optical depths of gas and dust without the need to consider effects of radial drift (Facchini et al., 2017). Radial drift, however, is indicated in cases where there is a more severe discrepancy between the gas and dust disk radii (i.e. Facchini et al. (2019)).

Quantifying disk properties has also been approached numerically in Bate (2018), who used radiative hydrodynamic calculations to compute distributions of disk masses and radii resulting from protostellar collapse. This work shows that initial disk radii significantly larger than $\sim$ 70 AU are uncommon. Constraints on distributions of disk properties, revealed either observationally or from simulations of disk formation, improve population synthesis models and the predicted outcomes of planet formation.

In Alessi & Pudritz (2018), we performed a suite of population synthesis calculations that assumed a constant disk dust-to-gas ratio of 1:100 while exploring the effects of planet envelope opacity and disk metallicity. In these calculations, we found that our models were unable to produce low-mass, short-period super Earths. While our models did produce many low-mass planets in the super-Earth - Neptune mass range, the majority of these had orbital radii exceeding 2 AU, situated outside of the observable limit for planets of these masses. This result was insensitive to model parameters.

Here, we incorporate a more realistic dust treatment by directly modelling the radial drift of solid

[1]Recent work has shown that dust masses may not be accurately estimated from sub-mm observations of disks due to optical depth or dust scattering effects (Zhu et al., 2019).

dust particles throughout to the disk's evolution. We account for dust evolution through coagulation, fragmentation, and most importantly, radial drift. Radial drift of solids throughout the disk can drastically change the disk's dust density profile, depleting outer regions of large grains (Brauer, Dullemond & Henning, 2008; Birnstiel, Dullemond & Brauer, 2010a). The resulting distribution of solids affects solid accretion rates onto planets, in turn affecting planet formation outcomes in this work. Including dust evolution, therefore, will have a particularly large effect on the formation of super-Earths and Neptunes (whose masses are dominated by solids), and their resulting period distribution.

A crucial feature of planet formation theories is a physical means to prevent the loss of forming planetary cores by rapid type-I migration (Alibert, Mordasini & Benz, 2004; Ida & Lin, 2008; Mordasini, Alibert & Benz, 2009a). A solution to this "type-I migration problem" is planet traps - locations of zero net-torque on forming planetary cores that arise at inhomogeneities or transitions in disks (Masset et al., 2006a; Hasegawa & Pudritz, 2011). As these are locations of zero net-torque on planetary cores that would otherwise experience rapid inward migration, planet traps are the most likely locations of planet formation within the protoplanetary disk.

The planet traps that we consider in this model are the water ice line (the location of an opacity transition), the outer edge of the dead zone (a transition in disk turbulence), and the heat transition (separating an inner viscously heated region from an outer region heated through stellar radiation). While there are other disk features that can result in planet traps, such as the inner edge of the dead zone (Masset et al., 2006a), the dust sublimation front (Flock et al., 2019), or other volatile ice lines (such as CO_2 - see Cridland, Pudritz & Alessi (2019a)), the three we include are the traps in the main planet-forming region of the disk. Planet traps have been previously used in population synthesis calculations, such as Matsumura et al. (2007); Hasegawa & Pudritz (2013, 2014); Hasegawa (2016); Alessi & Pudritz (2018), who show that including this set of traps and their range of radii can result in the formation of the various observed exoplanet classes.

The goal of this work is to study the effects of dust evolution and radial drift on the resulting distribution of planets. By including dust evolution effects, we compare how important dust drift is to planet formation by comparing the period distribution of resulting super Earth and Neptune planets to our previous work (Alessi & Pudritz, 2018) that assumed a constant 1:100 dust-to-gas ratio. Additionally, we will explore the link between disk properties and the statistical distribution of planets on the M-a diagram. In particular, since the dust distribution in disks will depend on

their initial sizes, we will explore the effect of the characteristic radius of initial protoplanetary disks upon the resulting planet populations.

We have discovered an intriguing result, namely, that the ratio of warm Jupiters and super Earths formed at the ice line trap is physically linked to the initial disk radius. Warm Jupiters are produced in excess of super Earths in both small and large disks, with the largest super Earth population formed at intermediate disk sizes of roughly 50 AU. This result is only encountered when dust evolution and radial drift effects are included in our models. Since the exoplanet data clearly indicates low-mass planets to be the dominant planet population, intermediate disk sizes (producing the largest number of super Earths) provide us with the best populations to compare with observations. This result is supported by MHD-simulations of disk formation during protostellar collapse that produce disks comparable to this size, depending on the mass-to-magnetic flux rato of the collapsing region (Masson et al., 2016). Additionally, we find our models are able to produce super Earths with small orbital radii (~ 0.03 AU) due to radial drift and the resulting delayed growth at the dead zone trap. This is a region of the M-a diagram that the constant dust-to-gas ratio models of our previous work, Alessi & Pudritz (2018), was unable to populate.

The remainder of this paper is arranged as follows. In section 3.2, we give an overview of our model, first describing our calculation of the disk's physical conditions and its evolution in 3.2.1. We then outline the evolution and resulting distribution of dust in 3.2.2. In 3.2.3, we describe our model of planet formation and migration - notably the trapped type-I migration phase. In 3.2.4 we outline our population synthesis method. Our planet population results are shown in section 3.3. In section 3.4, we discuss our results and summarize this work's key findings.

3.2 Model

This section summarizes the model used in this work, that combines models of the structure of an evolving protoplanetary disk, growth and radial drift of dust particles, the core accretion model of planet formation, and planet migration in a population synthesis calculation. We stochastically vary four parameters in our population synthesis approach, three of which describe properties of protoplanetary disks whose distributions are observationally constrained. The fourth parameter that we vary in our population synthesis framework is the only intrinsic model parameter stochastically varied.

For a detailed description of our disk, planet formation, and migration models, we refer the reader to Alessi et al. (2017); Alessi & Pudritz (2018). The dust evolution model, as a new inclusion to our calculations, is covered in detail in section 3.2.2.

3.2.1 Disk Model

We compute protoplanetary disk structure and evolution using the Chambers (2009) model. We briefly mention the key assumptions of this model in this section, and refer the reader to Appendix A for a more complete description.

The Chambers (2009) model is a 1+1D model that evolves with time due to viscous accretion and photoevaporation. While, generally, disk evolution takes place due to a combination of MRI-turbulence and MHD-driven disk winds, the Chambers (2009) model inherently assumes the former. As a result of this assumption, disks will spread as they evolve according to,

$$\frac{R}{R_0} = \left(\frac{\dot{M}}{\dot{M}_0}\right)^{-6/19} , \tag{3.1}$$

with R being the disk's size, which depends on the disk's changing accretion rate $\dot{M}$ throughout its evolution.

We emphasize that the Chambers (2009) disk models the evolution of the total (gas + dust) surface density, so the disk size R best corresponds to a gas disk radius. Our fiducial setting for the initial disk radius R_0 is 50 AU. We highlight this feature of the disk model as the setting of the initial disk radius and its affect on planet populations will be explored in detail in this work. The fiducial setting for the initial disk mass is $M_0 = 0.1$ $M_\odot$. This is a stochastically-varied parameter in our population synthesis models - see equation 3.7.

The disk midplane is heated through a generalized viscous accretion (dominant in the inner region) and radiative heating from the host-star (dominant in the outer region). These two different heating mechanisms lead to different surface density and temperature power-law indices depending on the dominant heating mechanism at the radius in question. The heat transition, a planet trap in our model, separates these two regimes.

We refer the reader to figure 3.11 for the disk's accretion rate evolution, and radial profiles of the surface density and midplane temperature throughout the disk's evolution.

3.2.2 Dust Evolution

The main addition to our model in this work is the inclusion of dust evolution, as the disk dust-to-gas ratio was assumed to be 1:100 in previous works (Alessi et al. 2017; Alessi & Pudritz 2018). We use the Birnstiel, Klahr & Ercolano (2012) two-population dust model that accounts for dust evolution through coagulation, fragmentation, and radial drift. These effects are crucial for interpreting modern disk images (i.e. Birnstiel et al. (2018)).

The Birnstiel et al. (2012) model is itself a simplified version of a full dust simulation over a distribution of grain sizes, as it only considers two grain sizes (a small, monomer grain size and a large grain near the upper limit of the grain size distribution), yet is able to reproduce the full simulation results of Birnstiel, Dullemond & Brauer (2010a). The two-population model is thus advantageous as our population synthesis calculations benefit from its reduced computational cost. We have modified the Birnstiel et al. (2012) dust model such that the gas evolves according to the Chambers (2009) disk model (section 3.2.1). The initial global dust-to-gas ratio input into the Birnstiel et al. (2012) dust model scales with metallicity as,

$$\frac{\Sigma_d}{\Sigma_g} = f_{\rm dtg,0} 10^{\rm [Fe/H]}\,, \tag{3.2}$$

where $f_{\rm dtg,0} = 0.01$ is the often-assumed setting for Solar metallicity. In Alessi & Pudritz (2018), the dust-to-gas ratio was assumed to be radially and temporally constant, and dust evolution was not considered.

Fragmentation (i.e. Blum & Wurm 2000) and radial drift (i.e. Weidenschilling 1977b) are barriers to the maximum size that grains can grow. By equating the relative velocity of grains to their fragmentation velocity, u_f, Birnstiel, Dullemond & Brauer (2009) show the maximum grain size in the *fragmentation-limited* case to be,

$$a_{\rm frag} = f_f \frac{2}{3\pi} \frac{\Sigma_g}{\rho_s \alpha_{\rm turb}} \frac{u_f^2}{c_s^2}\,, \tag{3.3}$$

where f_f is an order-unity parameter, Σ_g is the gas surface density, and ρ_s is the volume-density of solids. Analytical models of grain size distributions in Birnstiel, Ormel & Dullemond (2011) find that most of the mass in large grains is contained in sizes slightly below the maximum fragmentation-limited grain size. The fragmentation parameter f_f in equation 3.3 is used to correct this offset. By

comparing to their detailed simulations (Birnstiel et al., 2010a), a best-fit setting of $f_f = 0.37$ was found in Birnstiel et al. (2012).

We follow Birnstiel et al. (2010a) for settings of the fragmentation velocity u_f. Within the ice line, grains have a fragmentation threshold velocity of 1 m s^{-1}, while outside the ice line, grains are enshrouded in an icy layer that strengthens the grains, increasing the fragmentation velocity threshold to 10 m s^{-1}. The region of the disk where water undergoes its phase transition spans of order a few tenths of an AU in our model (Cridland et al., 2016; Alessi et al., 2017). We follow Cridland, Pudritz & Birnstiel (2017), who model the transition in u_f across the width of the ice line with an arctan function, fit to the radial ice distributions of Cridland et al. (2016).

Radial drift is a result of the drag forces experienced by dust grains due to the sub-Keplerian orbit of gas in the disk. While fragmentation does not change the radial distribution of dust surface density, Σ_d (only redistributes dust mass among smaller grain sizes), radial drift affects the orbits of large grains which in turn affects Σ_d. The difference between the two effects is apparent when comparing dust evolution models, and resulting Σ_d distributions, that include radial drift (i.e. Brauer et al. (2008)) to those that do not (i.e. Dullemond & Dominik (2005)).

By equating growth and radial drift timescales, Birnstiel et al. (2012) derive the maximum grain size in the *drift-limited* case to be,

$$a_{\rm drift} = f_d \frac{2\Sigma_d}{\pi \rho_s} \frac{V_K^2}{c_s^2} \gamma^{-1} \,, \tag{3.4}$$

where f_d is an order-unity parameter, V_K is the local Keplerian velocity, and γ is the absolute value of the power-law index of the gas pressure profile,

$$\gamma = \left| \frac{\mathrm{d} \ln \mathrm{P}}{\mathrm{d} \ln \mathrm{r}} \right| . \tag{3.5}$$

The parameter f_d is calibrated in Birnstiel et al. (2012) by comparing to detailed numerical simulations (Birnstiel et al., 2010a), who find a best-fit value of $f_d = 0.55$. We note that we have explored a range of settings $f_d = 0.1 - 1$ and find results of the Birnstiel et al. (2012) model to be insensitive to this parameter.

The grain size distribution up to the maximum grain size can be reasonably fit with a power law

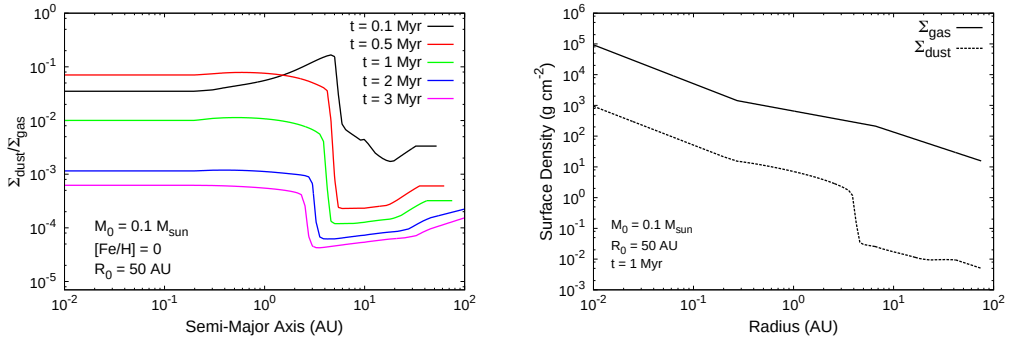

Figure 3.2: **Left**: Dust-to-gas ratios computed using the Birnstiel et al. (2012) model are plotted for various stages our fiducial disk's evolution. The drift-limited region of the disk exterior to the snow line is apparent from these profiles. **Right**: The gas and dust surface densities at 1 Myr are shown.

(i.e. Birnstiel et al. (2011)),

$$n(m)\,\mathrm{dm} = \mathrm{A}\mathrm{m}^{-\delta}\,\mathrm{dm}\,, \tag{3.6}$$

where A and δ are positive constants. These constants depend on the maximum grain size, therefore depending on whether fragmentation or radial drift limits the growth (i.e. the smaller of a_{frag} and a_{drift}). After computing the evolution of the two grain sizes in the two-population model, Birnstiel et al. (2012) reconstruct the full distribution, calibrated by Birnstiel et al. (2010a), throughout the disk.

In figure 3.2 (left), we plot radial profiles of the dust-to-gas ratio, Σ_d/Σ_g, computed using the Birnstiel et al. (2012) dust model at various stages throughout our fiducial disk's evolution. The disk can be divided into three regions: (1) interior to the ice line, the grains have a lower fragmentation velocity, and their growth is *fragmentation limited*; (2) outside the ice line, the grains' larger fragmentation velocity allows growth to larger sizes, and growth is therefore *drift limited*; and lastly (3) the small region across the ice line where the fragmentation velocity transitions. In the right panel of figure 3.2, we show the gas and dust surface density profiles after 1 Myr of disk evolution.

The effects of radial drift are apparent in figure 3.2, as the regions of the disk outside the ice line (the drift-limited regime) are depleted in solids compared to within the ice line. At early times, the dust-to-gas ratio is enhanced near the ice line as radial drift efficiently moves solids from the outer disk inwards. The global dust-to-gas ratio decreases in time as stellar accretion takes place, and dust is removed without being replenished. After $\sim$ 1 Myr, the dust-to-gas ratio falls beneath

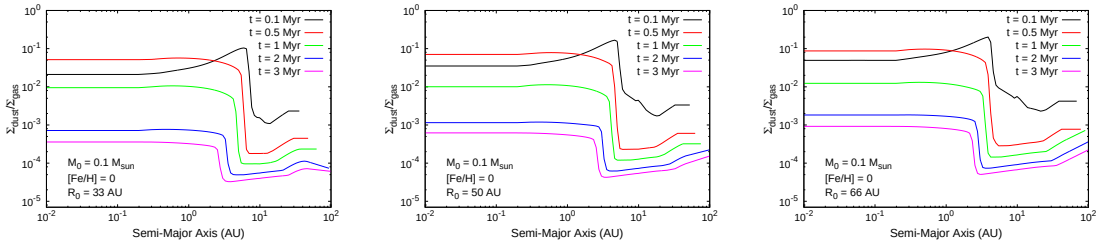

Figure 3.3: Evolution of dust-to-gas ratio profiles are shown for disks of different initial radii: R_0 = 33 AU (left), the fiducial R_0 = 50 AU (middle), and R_0 = 66 AU (right). The dust-to-gas ratio in the inner regions (at the ice line and fragmentation-limited regime) is higher in disks with larger R_0 settings. Profiles otherwise show the same qualitative behaviour regardless of R_0 setting (fragmentation and drift-limited regimes with the ice line physically separating the two).

the often-assumed 1:100 value at all radii, even in the fragmentation limited inner disk.

From the results of the dust model, one can infer two imposed restrictions on our planet formation calculations, and in particular the solid accretion phase. First, and most crucially, solid accretion from regions of the disk outside the ice line will be inefficient as this region is depleted in solids by radial drift. The second is that solid accretion timescales will increase after $\sim$ 1 Myr as the dust-to-gas ratio has decreased beneath 0.01 across all radii.

In figure 3.3, we show how the initial disk radius affects dust-to-gas ratio profiles by comparing smaller (33 AU) and larger (66 AU) settings of the initial disk radius to the fiducial 50 AU case. Regardless of the initial disk radius setting, the computed dust-to-gas ratio profiles show the same qualitative behaviour. All profiles display a dust-depleted outer (drift-limited) region and an inner fragmentation-limited region with higher dust surface densities, with the ice line physically separating the two due to the changing fragmentation velocity.

In figure 3.4, we summarize a key trend seen in figure 3.3 by plotting the dust-to-gas ratios at the ice line at various evolution times in disks with different initial radii. We see that the dust-to-gas ratios in the inner regions of the disk (namely at the ice line and the fragmentation-limited region) are systematically higher in disks with larger initial disk radii settings.

While the ice line does shift inwards slightly in larger disks due to the lower surface density, the change in the ice line's location between the three disk radius settings is small, with the difference being less than 1 AU between the 33 AU and 66 AU initial disk radii. Since, in the three models there is the same dust mass spread across the entire disk initially, larger disk radii settings will have more dust existing outside of the ice line simply because the disks themselves are more extended.

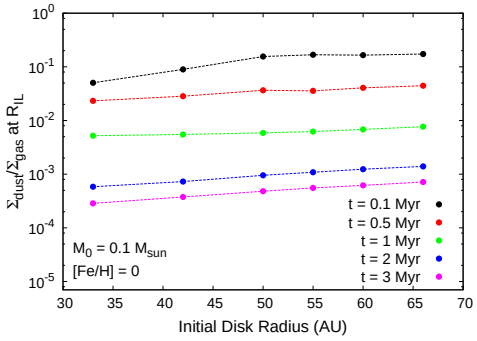

Figure 3.4: The dust-to-gas ratio at the ice line is plotted at various times throughout fiducial mass and metallicity disks' evolutions with different settings of the initial disk radius. At all disk evolution times, the dust-to-gas ratio at the ice line is larger for disks with larger R_0 values.

The biggest effect of radial drift in these models is to remove dust from the outer disk, efficiently migrating it inwards to the ice line. Therefore, in more extended disks (bigger R_0), radial drift will have more material to transport inwards to the ice line, resulting in the trend of increasing dust-to-gas ratios in the inner disk with increasing initial disk radius.

A potential limitation of the Birnstiel et al. (2010a, 2012) models is that radial drift is too efficient, and the corresponding discrepancy between the dust and gas distributions in disks are too extreme. When comparing the spectral energy distribution indices resulting from the Birnstiel et al. (2010a) simulation's dust distribution to observed indices of the Ophiucus disks, Birnstiel et al., (2010b) found that radial drift needed to be suppressed in order to fit to the observations. Dust trapping by local pressure maxima in disks is a physical means by which radial drift can be halted and extended dust distributions be maintained (Pinilla et al., 2012a). Recent disk observations have revealed dust substructures consistent with confinement to dust traps (Casassus et al., 2015; van der Marel et al., 2015; Dullemond et al., 2018), supporting this theory.

Dust trapping is not included in this work, as it is not present in the Birnstiel et al. (2012) model. We do, however, include the effects of a changing fragmentation velocity across the ice line, which mimics the effects of a dust trap through local enhancement in solid density. While radial drift may be too efficient in this calculation, one of the main goals in this paper is to explore its unhindered effect on our planet populations. We also highlight that the combination of our previous work (Alessi & Pudritz, 2018) where radial drift was not included, and this paper's high setting of radial drift explore the two extreme ends of radial drift's effects.

3.2.3 Planet Migration & Formation

Our treatment of planet migration and formation is unchanged from our previous work, Alessi & Pudritz (2018), and we refer the reader to Appendix B for a complete description.

The planet traps we include in our model are the water ice line, the heat transition, and the outer edge of the dead zone. The ice line's location is determined using an equilibrium chemistry calculation. The heat transition separates the inner portion of the disk where heating at the midplane takes place due to a generalized viscous accretion, and the outer portion of the disk heated via host-star radiation. The heat transition's location is determined within the framework of the Chambers (2009) disk model. We compute the location of the dead zone's outer edge using the radiative transfer model presented in Matsumura & Pudritz (2003). In this work, we only consider X-ray ionization caused by magnetospheric accretion and the resulting dead zone location, as our previous work (Alessi & Pudritz (2018)) showed X-ray ionized disks (as opposed to galactic cosmic rays) to produce features in the resulting M-a distribution that better resembled the data.

We consider the core accretion model of planet formation. We use the Birnstiel et al. (2012) dust model to compute the solid surface density distribution throughout the disk, thereby influencing solid accretion rates onto planetary cores. We use our best-fit envelope opacity models of Alessi & Pudritz (2018) to set gas accretion parameters in equations for the critical core mass (equation 3.21) and the Kelvin-Helmholtz timescale (equation 3.22). Termination of gas accretion is handled by a parameter, $f_{\max}$, in our models (equation 3.23) that relates a planet's final mass to its gap-opening mass (equation 3.17).

In figure 3.5, left panel, we plot planet formation tracks resulting from a 5 Myr-lived disk that incorporate the dust model's effects on the solid distribution. We choose a long-lived disk to illustrate types of gas giants arising from various traps in our model. In figure 3.5, right panel, we show planet formation tracks that assume a constant dust-to-gas ratio (the approach of Alessi & Pudritz (2018)) for comparison.

Planet formation at the ice line benefits from the early enhancement of solids caused by radial drift in the outer disk. This planet completes its solid accretion phase within 1 Myr and formation in this trap results in a warm Jupiter. The effects of radial drift on our planet formation model are apparent in the case of the heat transition track. The solid accretion rates onto this planet are extremely low, due to the trap being outside the ice line (see figure 3.12), in the radial-drift limited

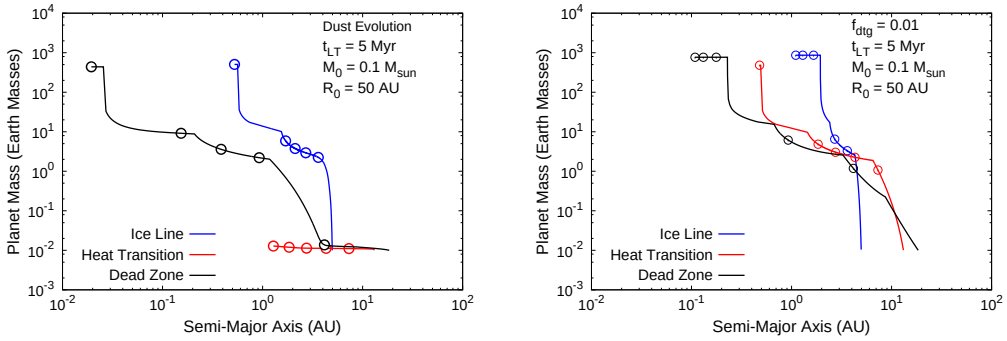

Figure 3.5: **Left**: Planet formation tracks that include the effects of dust evolution on the solid surface density are shown for a long-lived, 5 Myr disk. Open circles along the tracks mark the location of the planets at 1 Myr intervals. The effects of the dust evolution model, namely low solid accretion rates outside the ice line, are apparent in the heat transition and dead zone tracks. **Right**: Planet formation tracks that assume a global, time-independent dust-to-gas ratio as was done in Alessi & Pudritz (2018), for comparison. The model set up is otherwise the same.

region of the disk that is depleted in solids.

The dead zone trap is initially situated outside the ice line as well, until a $\sim$ 1 Myr when it migrates within the ice line. Thus, the solid accretion rate is initially low for the planet forming in the dead zone trap as it is accreting from the radial-drift depleted region. After 1 Myr, the planet enters the fragmentation-limited region interior to the ice line with higher solid surface densities, and its accretion rate therefore increases. The result of planet formation in this trap is a hot Jupiter, whose mass is somewhat below that of the warm Jupiter near 1 AU

We emphasize that in the ice line and dead zone planet formation tracks, the slow gas accretion phase takes 2-3 Myr which is comparable to a typical disk lifetime. This highlights the way in which super Earths and Neptunes form in our model - these are planets whose disks photoevaporate during their slow gas accretion phases. Namely, if we were to use an average disk lifetime of 3 Myr in our example calculation (figure 3.5), the ice line and dead zone would both have formed a Neptune mass planet at different orbital radii. The comparable slow gas accretion timescales to typical disk lifetimes suggest that this outcome should be common in our calculations.

3.2.4 Population Synthesis

We use a planet population synthesis approach to account for the spread in disk properties in the outcomes of planet formation models and distribution of computed populations on the M-a diagram.

We stochastically vary four parameters in our population synthesis calculations, three of which are disk properties resulting from protostellar collapse that are external to our calculation - the disk lifetime, initial mass, and metallicity. The fourth stochastically varied parameter is the $f_{\rm max}$ parameter that determines the mass where gas accretion terminates (see equation 3.23 and related discussion). This is the only parameter intrinsic to our model that is varied. We use a log-uniform distribution for $f_{\rm max}$ ranging from 1 to 500.

We use the same disk mass, lifetime, and metallicity distributions as Alessi & Pudritz (2018). In the cases of disk mass and lifetime, we use a log-normal distribution,

$$P(X|\mu_x, \sigma_x) \sim \exp\left(-\frac{(\log(X) - \log(\mu_x))^2}{2\sigma_x^2}\right), \tag{3.7}$$

with $\mu_{\rm lt} = 3$ Myr and $\sigma_{\rm lt} = 0.222$ as mean and standard deviation for the disk lifetime distribution, and $\mu_{\rm m} = 0.1$ $M_\odot$ and $\sigma_{\rm m} = 0.138$ for the initial disk mass distribution. A normal distribution is used for disk metallicities,

$$P(X|\mu_x, \sigma_x) \sim \exp\left(-\frac{(X - \mu_x)^2}{2\sigma_x^2}\right), \tag{3.8}$$

with $\mu_{\rm Z}$ = -0.012 and $\sigma_{\rm Z} = 0.21$ providing a fit the metallicity distribution of G-type planet-hosting stars.

In this work, we explore the effects of initial disk radius on resulting planet populations. We do this by keeping the initial disk radius constant within each population, rather than choosing a distribution of disk radii to stochastically sample over. We do so to highlight the differences comparing populations with different initial disk radii. Including this as an additional stochastically varied parameter in the populations would 'wash out' the parameter's effects. We note that we assume the distribution of disk masses to be unchanged regardless of the choice of initial disk radius in each individual population. While observations do indicate a correlation between disk masses and radii (Tazzari et al., 2017; Tripathi et al., 2017; Ansdell et al., 2018), we treat these as separate, uncorrelated parameters to isolate the effects of varying the initial disk radius on our resulting planet populations, independent of changes in the disk mass distribution.

In the more massive disks considered in our population synthesis framework, and particularly with smaller settings of the disk's initial radius, disks in our model can be gravitationally unstable at early times ($\lesssim$ several 10^5 years), but only at large radii ($\gtrsim$ 25-30 AU). The region where planet formation takes place ($\lesssim$ 10 AU, outside of which solid accretion rates are negligible) lies well within

Table 3.1: Summary of model parameters

Symbol	Meaning	Fiducial Value
	Population Synthesis Parameters	
$t_{\rm LT}$	Disk lifetime	3 Myr[a]
M_0	Initial disk mass	0.1 $M_\odot$[b]
[Fe/H]	Disk metallicity	0[c]
$f_{\rm max}$	Maximum planet mass parameter (equation 3.23)	50[d]
	Disk Parameters	
R_0	Initial gas disk radius	50 AU
α	Effective viscosity coefficient (equations 3.10 & 3.11)	0.001
$\tau_{\rm int}$	Initial time (equation 3.12)	10^5 years
	Stellar Parameters[e]	
M_*	Stellar mass	1 $M_\odot$
R_*	Stellar radius	3 $R_\odot$
T_*	Stellar effective temperature	4200 K
	Dust Model Parameters	
$f_{\rm dtg,0}$	Initial global dust-to-gas ratio at [Fe/H] = 0 (equation 3.2)	0.01
f_f	Fragmentation parameter (equation 3.3)	0.37[f]
f_d	Drift parameter (equation 3.4)	0.55[f]
	Planet Formation Parameters[g]	
$f_{\rm c,crit}$	Critical core mass parameter (equation 3.21)	1.26
c	Kelvin-Helmholtz c parameter (equation 3.22)	7.7
d	Kelvin-Helmholtz d parameter (equation 3.22)	2

Notes: *a.* Log-normal distribution (equation 3.7) with $\mu_{\rm lt} = 3$ Myr and $\sigma_{\rm lt} = 0.222$.
b. Log-normal distribution (equation 3.7 with $\mu_{\rm m} = 0.1$ $M_\odot$ and $\sigma_{\rm m} = 0.138$.
c. Normal distribution (equation 3.8) with $\mu_{\rm Z}$ = -0.012 and $\sigma_{\rm Z} = 0.21$.
d. Log-uniform distribution ranging from 1-500.
e. Chosen to model a pre-main sequence solar type star (Siess et al., 2000).
f. Parameters of Birnstiel et al. (2012) two-population dust model calibrated by fitting to full simulation of Birnstiel et al. (2010a).
g. Determined using best-fit envelope opacity from Alessi & Pudritz (2018).

the gravitationally stable region for all disks considered.

The most extreme case for gravitational instability that can be encountered in our populations is an initial disk mass of 0.2 $M_\odot$ and initial radius of 33 AU, for which the disk is initially stable out to 25 AU. The gravitationally unstable inner boundary shifts outwards as the disk evolves until the disk is entirely stable by 0.8 Myr. However, due to the log-normal distribution of initial disk masses (equation 3.7), sampling such a large disk mass as considered in this example is rare, and typical disk masses encountered in our populations will have gravitationally unstable regions confined to even larger radii and earlier times.

We include a summary of parameters used in our calculations and their fiducial settings in

table 3.1. Our population synthesis calculations consist of a Monte Carlo method whereby the four varied parameters' distributions are stochastically sampled before computing a planet formation track (as listed in table 3.1, the disk lifetime, initial disk mass, metallicity, and maximum planet mass parameter $f_{\rm max}$). To compute a population, we iterate this process 1000 times in each trap, for a total of 3000 planets in each population.

3.3 Results

3.3.1 Fiducial Population

In figure 3.6, we show the population resulting from the full dust evolution treatment and the fiducial setting of the initial disk radius, $R_0 = 50$ AU. The data points show the final masses and semi-major axes of the planets at the disk lifetime of the disk in which they form - a varied parameter in our population synthesis calculation. The dust evolution model plays a key role in shaping this distribution, with the outer disk being depleted in solids by radial drift towards the ice line. The resulting planet formation within each trap can be understood by considering where the traps exist with respect to the ice line.

Planet formation at the ice line in the fiducial model produces a mix of super Earths and Neptune-mass planets, as well as gas giants, primarily in the warm Jupiter (zone 3) region of the M-a diagram. At early stages in the disk's evolution, inward radial drift of solids from the outer disk results in a local enhancement of solids at the ice line (see figure 3.2), and solid accretion at this trap is therefore efficient. Short solid accretion timescales in turn will result in short gas accretion timescales, making the ice line a main producer of warm gas giants.

In the case of planet formation at the heat transition, very few planets with masses exceeding only 1 $M_\oplus$ are formed. The majority of planets formed in this trap accrete very little mass, and have final planet masses near the initial condition mass of 0.01 $M_\oplus$. The heat transition lies outside the ice line for nearly all planet masses and metallicities encountered in the population synthesis calculations. Since the region of the disk outside of the ice line is depleted in solids by efficient radial drift, planets forming in the heat transition have extremely long solid accretion timescales due to the low solid surface densities, resulting in inefficient overall growth.

Planets formed in the dead zone trap result in a range of planet masses: low mass (< 1 $M_\oplus$) planets, super Earths and Neptunes, as well as gas giants spread over a range of orbital radii,

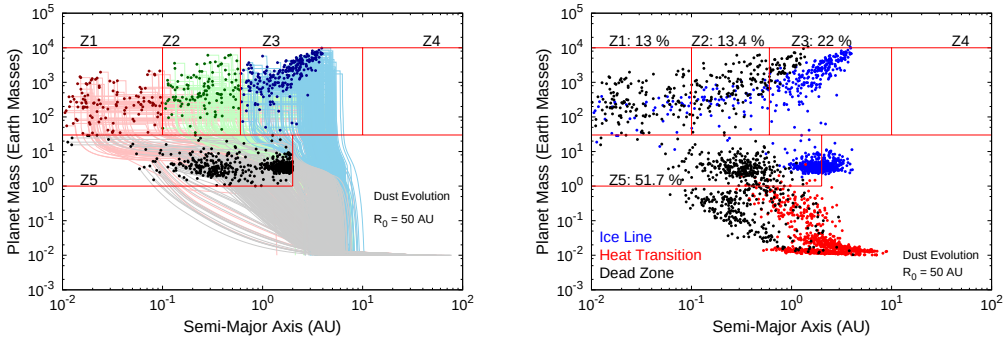

Figure 3.6: The planet population resulting from the full dust evolution model and fiducial initial disk radius ($R_0 = 50$ AU) is shown. **Left:** Planet formation tracks leading to the final population are shown only for planets that populate zones. End points of the tracks represent the final masses and semi-major axes of planets at the end of each of their disks' lifetimes. Colours of tracks and data points distinguish planets populating different zones of the diagram. **Right:** Resulting M-a distribution of the full population (including planets lying outside of the zones), with colour denoting the planet trap they formed in. We include the frequencies by which planets populate various zones.

but typically shorter periods than gas giants formed in the ice line. The dead zone trap initially lies outside the ice line but quickly migrates inwards, intersecting the ice line at ~ 1 Myr and ending up in the inner disk towards the end of disk evolution. Solid accretion is therefore inefficient initially while the dead zone exists outside the ice line, as was the case for planets forming in the heat transition. Solid accretion becomes efficient once the dead zone migrates within the ice line and planets forming within the dead zone encounter the high solid surface densities in the fragmentation-limited regime of the disk.

The relatively fast migration of the dead zone trap and the delayed solid accretion caused by the dead zone's migration inside the ice line result in the three cases of planet classes: (1) Low-mass planets (< 1 M$_\oplus$) are produced in the case of the shortest disk lifetimes where the planets primarily accrete from outside of the ice line where solids are depleted; (2) Zone 5 planets result from intermediate disk lifetimes where the dead zone has migrated inside the ice line and the solid accretion stage has taken place, but gas accretion has insufficient time to produce gas giants; Lastly (3), gas giants are formed from the dead zone in the longest-lived disks.

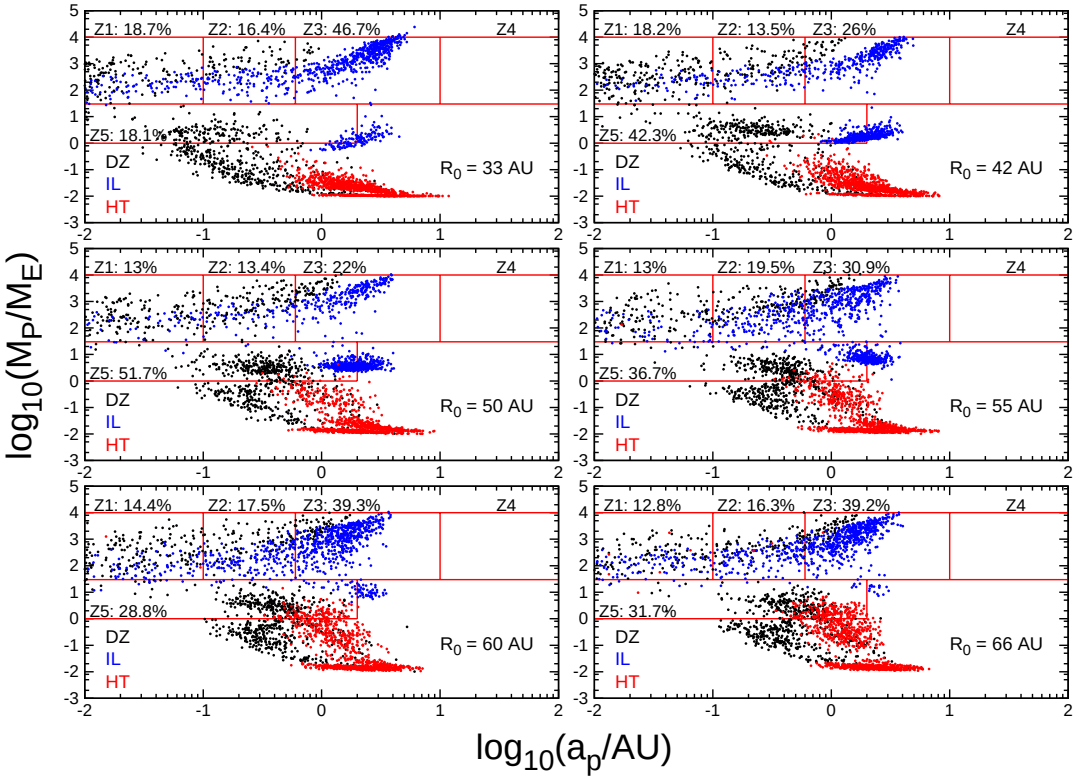

Figure 3.7: M-a distributions of computed planet populations are shown for a range of initial disk radii, spanning from 33 AU to 66 AU. The largest super Earth and Neptune population is formed when considering intermediate disk sizes ($R_0 = 50$ AU), with smaller and larger initial disk sizes producing more warm gas giants.

3.3.2 Effects of Initial Disk Radius

In figure 3.7, we explore the effects of initial disk radius on our population results. We consider a range of initial disk radii spanning from 33 AU to 66 AU. This range was chosen to encompass the range of disk radii predicted by models of disk formation in protostellar collapse simulations, with the small disk radius end corresponding to a somewhat strong setting of the mass-to-magnetic flux parameter (Masson et al., 2016), and the large disk radius end corresponding to the pure hydrostatic case (Bate, 2018). Since our disk model is assumed to evolve via viscous evolution, disk spreading occurs. After 1 Myr of disk evolution, the corresponding range of disk sizes becomes 63 - 90 AU, and after 3 Myr of evolution (a typical disk lifetime), this range corresponds to 125-140 AU. As discussed in section 3.2.4, the range of disk masses that we consider remains the same in each population run, despite the initial disk radius changing. The changes in population outcomes between runs with different initial disk radii is therefore physically caused by changes in the disk's surface density.

The initial disk radius affects planet formation outcomes in each trap in our models, with the ice line being the most sensitive to the setting of R_0. The planets that form in the ice line trap can be divided into two groups: those in the super Earth - Neptune mass range, and gas giant planets, the majority of which populate the warm Jupiter region of the M-a diagram. In the cases of the smallest and largest disks considered in figure 3.7, the ice line produces many more gas giants than zone 5 planets. The population of super Earths and Neptunes formed in the ice line reaches a maximum at intermediate disk radii near 50 AU. Additionally, the mass of the zone 5 planets that are produced in the ice line systematically increases as larger disk sizes are considered. In the case of the largest disk size, the population of ice line super Earths nearly washes out entirely, with the ice line producing gas giants almost exclusively.

The dead zone produces a combination of gas giants, zone 5 planets, and sub-Earth mass planets in each population regardless of the setting of initial disk radius. However, planet formation becomes slightly more efficient as the disk radius increases, for the same reason as it does in the heat transition. Thus, more gas giants are formed in the dead zone at larger R_0 settings. The minimum orbital radii of super Earths formed in the dead zone also increases with initial disk radius. In the smallest disk radius run, the dead zone produced super Earths with orbital radii as small as ~ 0.03 AU, whereas in the case of the largest disk radius run, super Earths formed in the dead zone all had orbital radii larger than 0.1 AU.

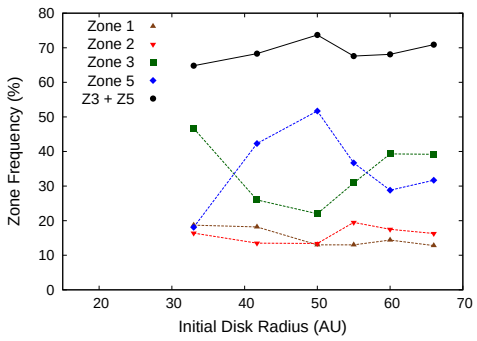

Figure 3.8: We summarize the grid of computed populations in figure 3.7 by plotting the frequency by which planets populate zones as a function of initial disk radius. We also show a summed total of zones 3 & 5 which remains relatively constant across the range of R_0 settings considered, showing that there is a trade-off between super Earths and warm Jupiter populations that each individually vary significantly as R_0 changes. The zone 1 and zone 2 populations show little variation with initial disk radius.

The heat transition primarily produces sub-Earth mass planets in all but the largest initial disk radius runs. As larger disk sizes are considered, the upper end of the mass distribution of planets formed in the heat transition increases, and begins to substantially populate zone 5. In the $R_0 =$ 60 AU and 66 AU runs, the heat transition forms a significant number of super Earths at larger orbital radii than those produced in the dead zone. Recalling that substantial solid accretion only takes place near or within the ice line, these results for the heat transition planets can be explained by noting that the heat transition trap converges with the ice line at systematically earlier times when lower surface density disks are considered. Therefore, it becomes increasingly likely for the heat transition to migrate to the high solid surface density regions of the disk at a given disk mass as the initial disk radius is increased. The subset of planets formed in the heat transition that incur some solid accretion thereby increase as the setting of R_0 increases.

In figure 3.8, we present the key plot of the paper, which summarizes the results of figure 3.7 by plotting the frequencies by which planets populate the different zones of the M-a diagram as a function of initial disk radius.

We highlight the drastic variation among warm Jupiters (zone 3) and super Earths (zone 5) as the initial disk radius is changed. For both small and large settings of R_0, warm Jupiters form more frequently than super Earths, with super Earth formation frequency maximized at intermediate settings of initial disk radius near 50 AU. Moreover, there is a striking trade-off between these two

planet populations, with the increasing super Earth population at intermediate disk radii coupled with a corresponding decreasing warm Jupiter population.

We show this in figure 3.8 by including a summed zone 3 and zone 5 population frequency that remains relatively constant across the range of explored R_0 settings. This disk radius-dependent exchange between super Earths and warm Jupiters is driven exclusively by planet formation at the ice line where the relative formation frequencies of super Earth and Neptune-massed planets and gas giants are sensitive to the setting of R_0. Our results show that planet formation is fundamentally linked to disk properties, as the formation frequency of super Earths is linked to the disk's radius.

Additionally, we find that the populations of hot Jupiters (zone 1) and period-valley giants (zone 2) are insensitive to the setting of R_0, with the corresponding frequencies having minimal variation across the span of R_0 investigated. We find no disk radius-dependent interplay between hot Jupiters and super Earths comparable to that seen with the warm Jupiter population. Since the warm Jupiter population is to a large extent formed from the ice line and the hot Jupiters through the dead zone, we conclude that planet formation at the ice line is sensitive to the initial disk radius setting, while formation at the dead zone is not.

In figure 3.9 (left panel), we consider a series of individual planet formation tracks that consider different initial disk radii, holding other parameters (disk mass, metallicity, and lifetime) constant. This is done to investigate the results we see regarding the formation frequency of gas giants and super Earths at the ice line, and their dependence on the initial disk radius. We highlight that all initial radii settings result in tracks that efficiently form zone 3 gas giants, with the exception of the $R_0 = 50$ AU case that undergoes significant inward migration during its formation. We also note that the initial position of the cores (i.e. the initial position of the ice line) shifts inwards as the disk radius is increased, due to the lower disk surface density.

In figure 3.9, right panel, we show the solid accretion timescale for the series of ice line planet formation tracks computed using equation 3.20. The solid accretion rate scaling is $\tau_{\rm c,acc} \sim r_p^{3/5}\Sigma_d^{-1}\Sigma_g^{-2/5}$, with the dust and gas surface densities being calculated at the location of the planet (i.e. the ice line). As was discussed in section 3.2.2, the dust surface density at the ice line increases as the disk radius is increased. The ice line's position does shift inward for larger R_0, however this change is small compared to the variations in the disks' extents that we have explored. The dust surface density is larger at the ice line for bigger disk radii settings simply because the drift-limited region is larger and there is more dust from the outer disk that is transported into the ice line. Therefore,

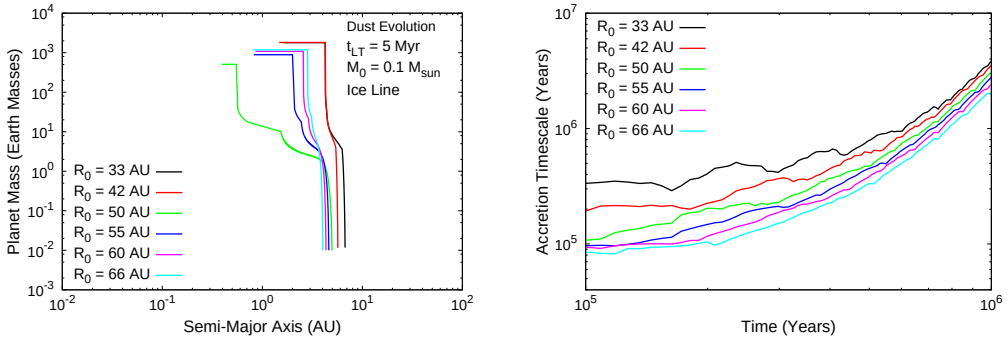

Figure 3.9: **Left:** Planet formation tracks at the ice line are shown for a series of initial disk radii. The disk mass and metallicity are set at their fiducial values ($M_0 = 0.1$ M$_\odot$, [Fe/H] $= 0$). The initial position of the planetary cores (the position of the ice line) shifts slightly inwards for larger R_0 settings due to the lower column densities. **Right:** Solid accretion timescale, computed using equation 3.20 is plotted for the ice line planet formation tracks. The accretion timescales systematically decrease as the initial disk radius is increased.

both the smaller r_p and larger Σ_d contribute to a shorter solid accretion timescale in larger disks. The gas surface density, however, is larger for the smaller disk settings due to the initial disk mass being held constant with the radius changing.

Combining these three effects, the right panel of figure 3.9 clearly shows that the solid accretion timescale at the ice line is shorter as the disk radius is increased. The difference between the $\tau_{\rm c,acc}$ values is largest at early times, and when comparing more compact disks (i.e. the difference is smaller when comparing two large R_0 settings). This shows that solid accretion is most efficient at the ice line in large disks. Since subsequent gas accretion is dependent upon the solid accretion stage, this indicates that the ice line should be more efficient at forming gas giants in disks with larger initial radii. We also note that the solid accretion timescales converge within 1 Myr, and by that time the difference in timescales is small across the range of R_0 values considered.

This trend is shown in our population results for disks with initial radii 50 AU and larger (see figure 3.8). The super Earth formation frequency is maximized at 50 AU, mainly due to formation of this class of planets at the ice line. Beyond 50 AU, the frequency of zone 3 gas giants increases due to faster solid accretion caused by radial drift transporting more solids to the ice line in bigger disks. However, our population results also show the gas giant formation frequency to be large in disks smaller than 50 AU, namely the 33 AU and 42 AU cases.

This begs an interesting question because as we have seen, more massive planets are expected for

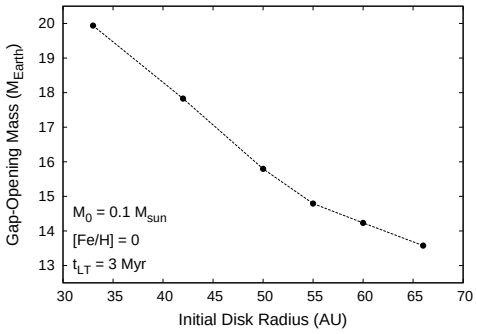

Figure 3.10: We plot gap-opening masses for planets forming at the ice line in disks with different initial radius settings, and otherwise fiducial parameters. The gap-opening mass is systematically larger in more compact disks.

large disks based on the amount of solid material is available at the ice line. Therefore a different aspect of our planet formation model must be causing gas giants to form more frequently than super Earths within the ice line in disks with small initial radii.

Another important aspect of giant planet formation is the amount of gas that will accrete onto them. We note that this is controlled by the gap opening mass. Accordingly, in figure 3.10, we plot the gap-opening masses of planets forming at the ice line in disks with different initial radii, computed using equation 3.17. We see immediately that the gap-opening masses for these planets are larger in more compact disks. This trend can be simply explained by considering the gap-opening mass' dependence on the disk aspect ratio, with $M_{\rm GAP} \sim h^3$ or $h^{5/2}$, depending on whether the viscous or thermal gap-opening criterion is met.

The disk aspect ratio scales as $h \sim T^{1/2} r_p^{1/2}$ and we note that, since we are considering planet formation to take place at the ice line, the local disk temperature will be the same (the sublimation temperature of water) regardless of the initial disk radius setting. This simplifies the above gap-opening mass scaling to $M_{\rm GAP} \sim r_p^{3/2}$ or $r_p^{5/4}$. Since the initial masses of the disks we are comparing are the same, the column density in more compact disks will be higher, and in turn the ice line trap (which sets the planets' radii, r_p) will exist at a larger radius.

Thus, larger ice line planet radii r_p in smaller disks leads to the trend seen in figure 3.10, whereby the gap opening masses of planets forming at the ice line are larger in disks with smaller initial radii. As previously mentioned (see initial position of planets in figure 3.9, left panel), the position of the ice line does not vary drastically with initial disk radius, but the sensitive scaling of the gap-opening

mass with planet radius causes the somewhat large range of gap-opening masses encountered across the investigated range of R_0.

Planets forming at the ice line in more compact disks (the 33 and 42 AU cases) are less impacted by gas accretion termination due to their larger gap-opening masses, and we attribute the high gas giant formation frequency in these smaller R_0 disks to this. We recall that termination of gas accretion is set by our $f_{\rm max}$ parameter (see equation 3.23), with low $f_{\rm max}$ settings of order unity corresponding to planets whose gas accretion is terminated shortly after they exceed their gap-opening masses. In these cases, low $f_{\rm max}$ settings of order unity can terminate gas accretion at an intermediate super Earth - Neptune mass that results in a planet population zone 5. Due to the larger gap-opening mass in smaller disks, these planets have a smaller $f_{\rm max}$ range that can lead to planets populating zone 5. This outcome is therefore less likely for smaller settings of R_0, but has a larger effect on planets forming in disks with larger R_0 settings.

To summarize, the large formation frequency of gas giants at the ice line in small disks is a result of the larger gap-opening masses, and the planets therefore being less subjected to the effects of gas accretion termination. On the large disk radius end of explored R_0 range, the high formation frequency of gas giants at the ice line is a result of the higher solid surface densities at the trap, and the correspondingly shorter solid accretion timescales. The $R_0 = 50$ AU setting, as an intermediate disk radius case, is the least optimal setting for formation of gas giants at the ice line (as it does not benefit from either of the effects that help produce gas giants in the small or large disk cases), but is the optimal condition for forming the largest observed planetary population - the Super Earths and Neptunes.

3.3.3 Comparison to Constant Dust-to-Gas Ratio Models

In Appendix C, we do a full comparison between M-a distributions resulting from this paper's models that include dust evolution to models of our previous work (Alessi & Pudritz (2018)) that assume a constant dust-to-gas ratio of $f_{\rm dtg} = 0.01$.

We find that the trade-off between warm Jupiters and super Earths formed at the ice line, depending on the setting of the initial disk radius, is a result only seen when dust evolution is included. Constant dust-to-gas ratio models show significantly less sensitivity to the initial disk radius.

We also find that, when dust evolution is included, our models can produce super Earths with

smaller orbital radii (down to ~ 0.03 AU) than when a constant dust-to-gas ratio is assumed. This is caused by radial dust drift and the resulting delayed formation at the X-ray dead zone, whereby solid accretion rates are negligibly small until the trap migrates near or within the ice line.

3.4 Discussion

3.4.1 Population synthesis: Host-star and disk parameters

The initial disk radius

The main result from our initial disk radius parameter study is that the largest super Earth population is formed at an initial disk size of 50 AU. This, in addition with the sensitivity of the ratio of warm Jupiters and super Earths formed at the ice line to the initial disk radius, shows that planet formation is fundamentally linked to protoplanetary disk properties. The population synthesis technique itself assumes this link between the scatter in the planet M-a distribution and disk properties; however, we have built upon results of previous works through a separate parameter study of the initial disk radius. By keeping the initial disk radius constant within each population run while varying the disk's mass, lifetime, and metallicity stochastically in our calculations, we have isolated the effect of R_0 by changing it between each population run.

As observations indicate low-mass planets to dominate the M-a diagram in terms of frequency, our conclusion is that intermediate disk sizes (~ 50 AU) produce best-fit populations, as these models produce the largest super Earth population. This is nicely in accord with MHD simulations of disk formation during protostellar collapse which show that, depending on the setting of the mass-to-magnetic flux ratio (μ) of the collapsing region, comparable disk sizes are produced, supporting our results (Masson et al., 2016). Additionally, this result is supported by the recent observations that show small to intermediate disk sizes to be common (i.e. Barenfeld et al. (2017); Cox et al. (2017); Long et al. (2019)).

As the distribution of protoplanetary disk radii becomes better constrained by observations, this can be incorporated into our population synthesis models as an additional parameter that is stochastically varied in each population run. In this work, we did not include any correlation between disk masses and radii to isolate the effect of changing the disk radius on outcomes of our planet formation model. Such a correlation has been shown to exist, indicated by the correlation

between dust continuum fluxes and either dust disk radii (Tazzari et al., 2017; Tripathi et al., 2017) or gas disk radii (Ansdell et al., 2018). Again, as observations better constrain these disk properties, changes in these disk parameters' distributions, and any correlations among them, can be readily incorporated in our population synthesis models. Updating these distributions as more data becomes available will be important, since the resulting M-a planet distributions are to a large degree shaped by disk properties.

We note that, while the investigated range of initial disk radii clearly has a large effect on the outcomes of planet formation, it is unlikely that the observed range of dust disk radii can be reproduced with the dust model considered in this work. After $\gtrsim 1$ Myr of evolution (a typical age of an observed disk), the dust distribution exists entirely within the ice line due to the dust model's efficient radial drift. Thus, the range of solid disk radii (spanning the relatively small range in ice line radii) will not reflect the range of initial disk radii investigated. We expect that a means of maintaining a more extended dust distribution, either through reducing the efficiency of radial drift or with the inclusion of dust traps, would lead to a larger range of dust disk radii in evolved disks (see also section 3.4.6).

However, we emphasize that the earliest stages of disk evolution, where differences in disk conditions for different initial radii are most pronounced, are most crucial for planet formation. This is particularly true for the ice line, where planet formation is seen to depend on R_0 most sensitively (see timestamps in figure 3.5, left panel).

Host-star mass

In this work, we modelled our disks to exist around pre-main sequence G-type stars, and did not explore other spectral classes. In doing so, we were focusing on effects that the disk itself has on outcomes of planet formation as opposed to the host-stellar mass and luminosity. Additionally, by restricting our models to Solar-type stars we are comparing with the majority of the exoplanetary data.

Previous works have shown that the stellar mass also plays an important role in the outcomes of planet formation. Ida & Lin (2005) showed that the stellar mass affects the ratio of short-period gas giants to Neptune-mass planets. Additionally, the results of Alibert et al. (2011) show that the scaling of disk properties (lifetime and mass) with stellar mass is an important inclusion and greatly influences the final outcomes of population synthesis calculations. Including variation in host-stellar

mass is a prospect for future work, and building off of the results of Alibert et al. (2011), including host-stellar mass-dependent distributions of disk lifetimes, masses, metallicities, *and disk radii* will be important to fully explore the effects of stellar mass on outcomes of our population synthesis models. It is currently unlikely that sufficient observational data exists to correlate all of these disk properties' distributions with host-stellar mass.

3.4.2 Implications for super Earth compositions

This work's optimized model of $R_0 = 50$ AU resulted in the largest population of zone 5 planets. In this model, the super Earth population consists almost entirely of planets formed at the ice line and at the dead zone. This has implications for these planets' compositions. Planets formed at the ice line will have a significant fraction of their solid mass in ice, while planets formed in the dead zone trap will have nearly no ice accreted, since all of their solid accretion takes place within the ice line. Super Earth compositions are therefore bimodal in these models. Additionally, we find that the super Earths with larger orbital radii ($\gtrsim 1$ AU) are predominantly ice line planets, and those at smaller orbits were formed at the dead zone. Our best-fit model therefore predicts a jump in the mean density of super Earth solid cores at ~ 1 AU, transitioning from dry, dense planets formed at the dead zone to those with a substantial ice fraction formed at the ice line. We will follow up on this issue in considerable detail in our next paper.

At larger initial disk radii ($R_0 = 66$ AU), we find that zone 5 is nearly entirely populated by planets formed at the dead zone and heat transition, with the ice line mainly forming warm Jupiters. In this case, the bimodality of the super Earth compositions will be lost, since in both cases of planets forming in the dead zone and heat transition traps, solid accretion will be restricted to take place within the ice line. This is due to radial drift efficiently depleting the outer disk of solids, and therefore it is not until the traps migrate within the ice line that planets forming at either the heat transition or dead zone are able to accrete significant amounts of solids. In this case there would be no transition among the core compositions (or densities) in super Earths, despite there being a clear transition between short period super Earths formed mostly in the dead zone, with super Earth on longer orbits being formed in the heat transition.

3.4.3 Low solid accretion in outer disk & additional planet traps

An additional implication of low solid accretion rates in the outer disk due to radial drift is that outer planet traps not included in our model would contribute planets in the observable region of the M-a diagram. Traps such as additional condensation fronts (such as CO_2 (Cridland et al., 2019a)), or resonances of traps we include in our model would exist outside of the ice line for the entirety of disk evolution. Since planets forming in these traps would be accreting from the drift limited region of the disk, there would be minimal solid accretion, and minimal growth of planetary cores. Planet formation at these traps would therefore only result in very low mass failed cores (comparable to planet formation in the heat transition in the $R_0 = 33$ AU case), and would not contribute even to the zone 5 population. Our results remain unaffected regardless of whether or not additional traps in the outer disk are included, justifying their omission.

3.4.4 Increasing the short-period super Earth population

While the best-fit model produced the largest super Earth population, the formation frequencies of zone 5 planets in our models is still not large enough to compare with the data. The inclusion of the dust model results in more short-period super Earths being produced (down to orbits of ~ 0.03 AU), with the majority of super Earths formed in our model having orbits between $\sim$ 0.1-3 AU. Similar to our previous work (Alessi & Pudritz, 2018), we again find that our models produce many super Earths between 1-3 AU, and thus predict many low-mass planets to exist just outside the ~ 1 AU outer limit where super Earths have been detected via transits.

The observed M-a diagram shows the existence of more super Earths between 0.01-0.1 AU than our model produces. However, with observational biases accounted for, the occurrence rate study of Petigura et al. (2018) shows that super Earth and Neptune-mass planets' frequencies peak just within 0.1 AU, with occurrence rates decreasing at smaller orbital radii. Our results compare well with this data as the low orbital radius end of the bulk of our super Earth populations lie at ~ 0.1 AU.

At yet smaller orbital radii, our populations do not compare well with the observed M-a diagram or occurrence rate studies due to the lack of super Earths at orbits < 0.1 AU in the cases of our best-fit model with $R_0 = 50$ AU or larger. An exception is the smallest initial disk radius case of $R_0 = 33$ AU where the low orbital radius end of the super Earth population extends down to 0.05 AU.

With the inclusion of dust evolution, our models show the core accretion model is capable of producing short-period super Earths reliably down to 0.05 AU. Nonetheless, we identify three mechanisms by which the very short-period super Earth population (0.01-0.1 AU) could be increased in our calculations to better compare with the data.

Planet-planet dynamics

Firstly, we assume our planetary cores form in isolation and neglect any dynamics effects. Post-disk dynamics can have an effect on the final orbits of planets formed during the disk phase in our calculations, as was shown in Ida et al. (2013). Planet-planet scattering can reduce the orbital radius of the remaining planet by up to a factor of two - the case for scattering between two equally massive planets. We therefore do not expect this to have a drastic effect on our planet populations, although we do note this as a means by which planets' orbital radii can be reduced. Investigating the ways in which dynamics can affect our calculations during and after the disk phase remains a prospect for future work. We highlight that our models form many low-mass (< 1 $M_\oplus$) planets that can take place in accretion or scattering if dynamics was included during the post-disk phase.

Corotation torque saturation

As discussed in Appendix B, saturation of the corotation torque prior to gap opening and type-II migration is another method by which more short-period planets could be formed. Here, we only include the trapped type-I migration phase following the results of Alessi et al. (2017), using the timescale approach of Dittkrist et al. (2014) to determine if a saturated type-I migration phase applies. We note that the gap-opening mass and the mass at which the corotation torque saturates are comparable and sensitive to model parameters.

As was noted in Hasegawa (2016), if the corotation torque saturates prior to gap-opening, a saturated type-I migration regime would apply as an intermediate step between trapped type-I migration and type-II migration (the two regimes included in this work). This would remove planets from their traps prior to them reaching their gap-opening masses, and planet-induced gaps observed in disk dust distributions may not have to align with planet traps (or condensation fronts). If a saturated corotation torque phase applied prior to the onset of type-II migration in our model, then the orbital radii of planets would indeed be smaller, and could lead to a reduction in the orbital radii of formed super Earths. This would also, however, lead to more planets being accreted onto the host

star.

The embryo assembly mechanism

Lastly, as suggested in Hasegawa (2016), the embryo assembly method of forming super Earths could lead to more short-period super Earths beyond what our models are capable of producing. This is an alternate scenario to the core accretion mechanism, whereby planetary embryos migrate to the inner edge of the disk but do not accrete gas (due to their low masses), and undergo collisions after the disk phase to build up a super Earth. With the inclusion of dust evolution, however, the core accretion model is better able to produce short-period super Earths, so we speculate that a change in a model detail within the core accretion approach could lead to more super Earths in the 0.01-0.1 AU range as opposed to requiring a different formation mechanism entirely.

3.4.5 Zone 1 & Zone 2 Populations

Our populations produce too large a fraction of gas giants, particularly in zones 1 & 2, when compared with data from occurrence rate studies (Santerne et al., 2016; Petigura et al., 2018). Many of the planets in zones 1 & 2 are formed within the dead zone trap. We recall that dead zone planets only begin accreting appreciable amounts of solids once they have migrated within the ice line, a consequence of radial drift removing solids from the outer disk. Thus, the over-production of short-period gas giants from the dead zone is another result that can be attributed to the efficiency of radial drift in the dust model. The resulting high surface densities of solids in the inner disk lead to efficient solid accretion onto dead zone planets once they have migrated within the ice line, leading to many short-period gas giants. Additionally, an increased super Earth population (discussed in the previous subsection 3.4.4) would result in a comparatively smaller frequency across all gas giant zones, so the over-production of gas giants is related to the under-production of super Earths.

Our models do not show a separation between hot Jupiter and warm Jupiter populations, regardless of the setting of the initial disk radius. We therefore do not reproduce the reduced frequency of period-valley giants at orbital periods $\sim$ 10 days seen in occurrence rate studies (Santerne et al., 2016; Petigura et al., 2018). We note that this range of reduced occurrence rates for the period-valley giants is much smaller than the raw exoplanet data on the M-a diagram would indicate (across the extent of zone 2 as indicated by Chiang & Laughlin (2013)).

The best fit model from our previous paper in this series (Alessi & Pudritz, 2018) resulted in a large population of warm Jupiters as well as a clear separation between warm Jupiters and shorter period hot Jupiters (see figure 3.13, top right panel), reproducing this feature of the data. However, we recall that our previous work did not account for any dust evolution effects. Additionally, this separation is only seen in constant dust-to-gas ratio models when an initial disk radius of $R_0 = 33$ AU is used.

3.4.6 Efficiency of radial drift & dust trapping

The planet formation results of this paper are influenced to a large degree by the dust evolution model, and particularly the efficient radial drift that transports solids outside of the ice line inwards. We note that radial drift in the Birnstiel et al. (2010a) (for which the dust model used in this work (Birnstiel et al., 2012) is a numerical fit) was found to be too efficient when compared with spectral energy indices of observed disks (Birnstiel et al., 2010b). Additionally, the offset in gas and dust dust radii can by explained by differences in optical depths for the majority of cases, and only require invoking radial drift for the most extreme discrepancies (Facchini et al., 2017, 2019). In our calculations, high dust-to-gas ratios are maintained only within the ice line (~ 5 AU) even at early stages in the disk's evolution due to efficient radial drift in the outer disk. Comparing the ice line radius to the extent of the disk (~ 50 AU), there is indeed an extreme discrepancy between the dust and gas disk radii in our models as a result of radial drift in the Birnstiel et al. (2012) model being too efficient. We found the dust model to be largely insensitive to the fragmentation and drift parameters (f_f and f_d; see section 3.2.2) used to fit the Birnstiel et al. (2012) simplified two-population model to the full numerical calculation of Birnstiel et al. (2010a). The dust-to-gas ratio profiles and the rates of radial drift remained mostly unaffected through a large variation in each parameter.

As discussed in Pinilla et al. (2012a), dust trapping at local pressure maxima is a means of maintaining extended dust distributions despite efficient radial drift elsewhere in the disk. This mechanism is consistent with disk observations that show local structures in dust (i.e. Casassus et al. (2015)) indicating dust trapping. Including dust traps in our model as a physical means of slowing radial drift would likely affect our results, as the solid accretion phase is sensitive to the distribution of solids throughout the disk. If dust traps were able to maintain high solid surface densities in the outer disk, and prevent solids from quickly radially drifting towards the ice line, planet formation

timescales at all the traps (particularly the heat transition and the ice line) would be impacted. Additionally, if the dust traps were also a location of a planet trap, the local enhancement of solids would lead to efficient planet formation at the dust trap. This is similar to the behaviour at the ice line in our models. Although it is not modelled as a dust trap, there is a local enhancement of solids at the ice line during early stages of disk evolution due to the changing fragmentation velocity across the ice line's radial extent, leading to efficient solid accretion and planet formation at the ice line.

Prior to planet formation taking place, it is unlikely that dust traps could exist at arbitrary locations in the disk as opposed to existing at inhomogeneities and local disk structures - namely planet traps. At early times in the disk's evolution, both the heat transition and outer dead zone radii exist outside the ice line, as do condensation fronts of volatiles other than water, such as CO_2. If these, in addition to the water ice line, were all treated as dust traps in the model, the dust surface density would be larger over a more extended range of radii, and there would be a smaller discrepancy between the gas and dust radii despite radial drift being present in the calculations. Dust traps were not included in this work as one of our main goals was to explore the unhindered effects of radial drift on our planet formation models.

It is interesting to consider the populations computed in this work that include radial drift, and those resulting from the constant dust-to-gas ratio assumption of Alessi & Pudritz (2018) as two extremes in treatment of radial drift. In this work's case, radial drift is too efficient, while it is "turned off" when neglecting radial drift effects. Therefore, the populations of this work and our last can be thought of as bracketing the true effects of radial drift on planet formation (in which dust trapping would need to be accounted for). We thus identify dust trapping as an important inclusion in models that include dust evolution and radial drift, and incorporating this into our dust treatment is a prospect for future work.

3.4.7 MHD disk winds vs. turbulent alpha

While the turbulent $\alpha_{\rm turb}$ setting used in this work is within the accepted range based on observed line widths in disks (Flaherty et al., 2018), it remains possible that the low levels of turbulence observed in disks can be attributed to them evolving through MHD-driven disk winds as opposed to MRI-turbulence, as the Chambers (2009) model used in our calculations assumes. A key difference between the two mechanisms of angular momentum exchange is the disks evolving via MRI-turbulence spread to conserve angular momentum, while winds-driven models do not as their angular momentum is

carried in the wind-driven material (Pudritz & Ray, 2019).

Changing the disk model to one that evolves through MHD winds could certainly affect our results, but most crucially within the region of the disk where planet formation takes place, which is confined to occur within the ice line with the current treatment of radial drift, but is generally $\lesssim$ 10 AU in planetesimal accretion models. While the surface density evolution in the outer disk would be different between the two mechanisms of disk evolution due to spreading in the case of MRI-turbulence, this alone would not greatly influence planet formation results.

If an MHD winds-driven model were used, the different surface density profile in the inner disk would, however, affect various stages of our planet formation model. The lower level of turbulence throughout the disk despite similar overall α settings would affect dust growth and radial drift rates. The set of planet traps we include would also change, as winds-evolving disk models show local maxima in surface density profiles (i.e. Ogihara et al. (2018)). Conversely, the outer edge of the dead zone may be removed as a trap due to the overall lower levels of $\alpha_{\rm turb}$. It has additionally been shown that the co-rotation torque works very differently in inviscid MHD wind-driven disks (McNally et al., 2017, 2018; Kimmig et al., 2019). Ultimately, all of these aspects combined might affect our population synthesis results, and incorporating a winds-evolving disk model will be the focus of our future work in this series.

3.4.8 Gas accretion termination

Our treatment of the late stages of planet formation only considers gas accretion to proceed at the Kelvin-Helmholtz rate prior to being terminated artificially when planet's reach their maximum mass, set by the $f_{\rm max}$ parameter that is varied in our population synthesis models. While terminating accretion in such a manner is a simplified approach, stochastically varying the $f_{\rm max}$ parameter in our populations results in a range of gas giant masses that is comparable with the data.

Lambrechts et al. (2019) find that even massive planets can maintain high accretion rates and there is no self-driven mechanism to halt planetary accretion. They found their results were unaffected by gap-formation due to the large amount of material flowing through the gap available for accretion onto the planet (Morbidelli et al., 2014). This result supports our treatment of late stages of gas accretion, in the sense that gas accretion is unhindered prior to the planet reaching its maximum mass.

There are two alternate treatments of truncating accretion for high mass planets. The first is the

disk-limited accretion mechanism (i.e. Tanigawa & Tanaka (2016)) whereby the reduced accretion rate through the disk itself truncates accretion onto the planet. Second is the magnetic termination of gas accretion (Batygin, 2018; Cridland, 2018) whereby the interaction of the planet's magnetic field and the disk results in an accretion cross-section that inversely scales with planet mass, leading to termination of accretion at high masses.

In both of these alternate treatments, we argue that the planet's final mass is still ultimately set by a model parameter[2], and in that regard do not improve over our $f_{\rm max}$ approach. If we instead were to use an alternate approach of terminating accretion, we do not expect our final populations to be affected, as a suitable range of model parameters would need to be chosen (as is the case with $f_{\rm max}$) to obtain a reasonable range of gas giant masses.

We note that during the runaway growth phase the Kelvin-Helmholtz accretion rate is systematically higher than the disk-limited accretion rate that has been used in many previous works (i.e. Machida et al. (2010); Dittkrist et al. (2014); Bitsch et al. (2015)). Additionally, Hasegawa et al. (2019) found that including a disk-limited accretion phase is necessary to reproduce the exoplanetary heavy-element content trend. If we were to include the disk-limited accretion phase, we expect that our giant planet populations would systematically lie at smaller orbital radii. However, we do not expect this shift to be extreme, and depending on model parameters (such as the planet's envelope opacity, and the fraction of material accreted through the disk that accretes onto the planet), both methods can lead to quite similar results.

3.5 Conclusions

In this work, we have examined the role of the initial disk radius in core accretion models through a comprehensive set of planet population synthesis calculations. We have also updated our calculations in their treatment of dust to a physical model that combines dust growth, fragmentation, and radial drift. Including dust evolution effects has shown a drastic change in the population results shown in Alessi & Pudritz (2018) that assumed a constant dust-to-gas ratio of $f_{\rm dtg} = 0.01$.

Our major finding - that intermediate disk radii of the order of 50 AU drives the appearance of the observed M-a diagram - indicates that planet formation and star formation processes are intimately

[2]In disk-limited accretion, the fraction of the disk accretion rate that accretes onto the planet is parameterized, setting the planet's final mass. In the case of magnetic termination, the forming planet's magnetic field strength is a parameter that sets the final mass of the planet.

linked. The characteristic disk radius is determined by a combination of gravitational collapse of turbulent regions and their angular momentum evolution due to magnetic braking and outflows.

We list our main conclusions below:

- *The ice line is the most important location for warm Jupiter formation.* The trap becomes locally enhanced in solids early in the disk's evolution due to radial drift removing solids from the outer disk and transporting them towards the ice line. This effect restricts the region of the disk where solid accretion can take place at an appreciable rate to within the ice line, as solid accretion in the outer disk is inefficient due to the low solid surface densities. This has the largest affect on planet formation in the heat transition trap in our models.

- *Planet formation is fundamentally linked to the characteristic initial radius of the protoplanetary disk population.* The ratio of super Earths to warm Jupiters formed at the ice line is sensitive to the setting of the initial disk radius. The smallest (33 AU) and largest (66 AU) initial disk sizes (which would form in collapsing regions with strong magnetic fields, and pure hydrodynamics collapse, respectively) resulted in the ice line producing many more warm Jupiters than super Earths

- *An initial gas disk size of 50 AU produces the largest super Earth population.* This is a feature of planet formation at the ice line, for which we find that super Earth formation is optimized for intermediate disk radii settings (that would form from collapsing regions with moderate magnetic field strengths). Gas giant formation at the ice line is more efficient (1) at smaller disk radii due to larger gap-opening masses and planets being less effected by related gas accretion termination; and (2) at larger disk radii due to larger solid surface densities at the ice line trap and correspondingly shorter solid accretion timescales. These effects minimize at the intermediate disk radius of 50 AU.

- *Inclusion of radial drift is essential to form short period super Earths.* Notably, planet formation at the dead zone trap, which is delayed until the dead zone migrates to within the ice line, results in super Earth formation with orbital radii as small as 0.03 AU. Our previous treatment (Alessi & Pudritz, 2018) that neglected dust evolution effects and assumed a constant dust-to-gas ratio throughout the disk was unable to form super Earths with orbital radii significantly less than 1 AU.

In our upcoming work in this series, we will investigate the chemical compositions of these various populations using planets produced in our populations and the disk chemistry model of Alessi et al. (2017). We will combine our computed planet compositions with an interior structure model to examine our populations' distributions on the mass-radius diagram. In future work, we will consider the effects of a MHD-winds driven disk model on our populations, as an alternative to the MRI-turbulence driven model we have thus far considered.

Appendix A: Protoplanetary Disk Model

We use the Chambers (2009) 1+1D semi-analytic model to calculate disk structure and evolution. This model calculates self-similar solutions to the disk evolution equation,

$$\frac{\partial \Sigma}{\partial t} = \frac{3}{r}\frac{\partial}{\partial r}\left[r^{1/2}\frac{\partial}{\partial r}\left(r^{1/2}\nu\Sigma\right)\right] , \tag{3.9}$$

where $\Sigma(r,t)$ is the disk's evolving surface density profile, and $\nu(r,t)$ is the disk's viscosity. Self-similar solutions to equation 3.9 can be obtained by parameterizing the disk's viscosity using an effective viscosity coefficient α (Shakura & Sunyaev, 1973; Lynden-Bell & Pringle, 1974),

$$\nu = \alpha c_s H , \tag{3.10}$$

where c_s is the disk sound speed and H is the disk scale height.

A globally-constant value of α is required in order to obtain self-similar solutions to equation 3.9. Angular momentum transport in protoplanetary disks can take place through either MRI-turbulence or MHD-driven disk winds. Thus, α can be written as a sum of the effective viscosities of each source of angular momentum transport ($\alpha_{\rm turb}$ and $\alpha_{\rm wind}$, respectively),

$$\alpha = \alpha_{\rm turb} + \alpha_{\rm wind} . \tag{3.11}$$

In this work, we set $\alpha = 10^{-3}$ in all calculations. This setting is consistent with the upper limit of $\alpha_{\rm turb} < 0.007$ measured in the TW-Hya disk (Flaherty et al., 2018).

MRI-driven turbulence requires the disk to have a critical ionization fraction in order to operate. The high-density inner region of a disk prevents ionizing radiation from reaching the midplane, pre-

venting MRI-turbulence (the disk's *dead zone*). Previous works considering only the MRI-turbulence contribution to angular momentum transport, such as Gammie (1996) and Matsumura & Pudritz (2003) have shown that within the disk's dead zone, $\alpha_{\rm turb} \sim 10^{-5} - 10^{-4}$, while in the outer, turbulently active region of the disk, $\alpha_{\rm turb} \sim 10^{-3} - 10^{-2}$. However, MHD-driven disk winds have been shown to maintain accretion rates within the disk's dead zone (Bai & Stone, 2013; Gressel et al., 2015; Gressel & Pessah, 2015; Bai, 2016). Our assumption of a globally constant effective α, despite a radially changing $\alpha_{\rm turb}$, is consistent with these results - requiring an $\alpha_{\rm wind}$ contribution to maintain a radially constant accretion rate.

In all calculations, we consider a pre-main sequence G-type host star, with mass 1 $M_{\odot}$, radius 3 $R_{\odot}$, and an effective temperature of 4200 K. Therefore, any variations in planet populations that would result from different stellar properties (i.e. Ida & Lin (2005); Alibert, Mordasini & Benz (2011)) are not included in this work. Instead, we focus on the effects that disk properties have on the planetary M-a distribution. We use a fiducial initial disk radius of $R_0 = 50$ AU, and recall that disks will viscously spread as they evolve via MRI-turbulence.

Disk evolution takes place in our model through the combined effects of viscous accretion and photoevaporation. The latter effect is caused by high-energy radiation from the host star (UV and X-rays) that continuously disperse disk material (Pascucci & Sterzik, 2009). We model the time-evolution of the disk accretion rate to be,

$$\dot{M}(t) = \frac{\dot{M}_0}{(1 + t/\tau_{\rm vis})^{19/16}} \exp\left(-\frac{t - t_{\rm int}}{t_{\rm LT}}\right) , \tag{3.12}$$

where $\tau_{\rm vis}$ is the viscous timescale, $\dot{M}_0$ is the initial accretion rate at $t_{\rm int} = 10^5$ years, and $t_{\rm LT}$ is the disk's lifetime. Equation 3.12 includes an exponential photoevaporation factor multiplying the viscous accretion rate evolution of Chambers (2009). At early stages of the disk's evolution, photoevaporation is a small modification on viscous accretion, but rapidly disperses the disk (on 10^4 year timescales, short compared to the $\sim 10^6$ year viscous timescale) once the photoevaporative rate becomes comparable to the viscous accretion rate (Owen, Ercolano & Clarke, 2011; Haworth, Clarke & Owen, 2016). We therefore assume the disk to rapidly clear at $t = t_{\rm LT}$, ceasing planet formation and migration.

We assume a constant disk opacity, with metallicity scaling, of (Chambers, 2009; Rémy-Ruyer

Table 3.2: The accretion rate and radius scalings of surface density (Σ) and midplane temperature (T) in the three regions in the disk model.

$r < r_e$	$r_e < r < r_t$	$r > r_t$
$\Sigma \sim \dot{M}^{17/19} r^{-24/19}$	$\Sigma \sim \dot{M}^{3/5} r^{-3/5}$	$\Sigma \sim \dot{M} r^{-15/14}$
$T \sim \dot{M}^{2/19} r^{-9/38}$	$T \sim \dot{M}^{2/5} r^{-9/10}$	$T \sim r^{-3/7}$

et al., 2014),

$$\kappa = 10^{[\mathrm{Fe/H}]} (3\,\mathrm{cm}^2\,\mathrm{g}^{-1})\,. \tag{3.13}$$

That is, the disk opacity has no radial or temporal variations. The exception to this is in the innermost 'evaporative' region, $r_e \lesssim 0.3$ AU, of the disk where the temperature exceeds 1380 K and dust grains sublimate. Here the opacity is modified to (Stepinski, 1998),

$$\kappa = 10^{[\mathrm{Fe/H}]} \left(\frac{T}{1380\,\mathrm{K}}\right)^{-14} (3\,\mathrm{cm}^2\,\mathrm{g}^{-1})\,, \tag{3.14}$$

where T is the midplane temperature.

By assuming a radially-constant opacity over the majority of the disk's extent, we are neglecting the opacity variation that would arise at condensation fronts - the physical cause for planet trapping at the ice line. This is not a necessary inclusion in our model, however, as we do not directly compute planet-disk torques when modelling planet migration in this work.

Our disk model can be divided into three regions: an outer region heated by radiation from the host star, an inner region heated by the generalized viscous heating, and the innermost 'evaporative' region, within the viscously-heated regime where the dust opacity is modified due to grains sublimating. The heat transition, r_t, separates the two heating regimes and is a planet trap in our model. We note that within the disk's dead zone (where angular momentum is transported via disk winds), the generalized viscous heating is due to Ohmic dissipation at the midplane (a non-ideal MHD heating effect).

In figure 3.11, we plot the evolution of the disk accretion rate, as well as radial surface density and midplane temperature profiles at various times throughout the evolution of our fiducial disk model. The heat transition trap is seen to shift inwards as the disk evolves. In table 3.2, we show the radial and accretion rate scalings of surface density and midplane temperature in the three regions of the disk model.

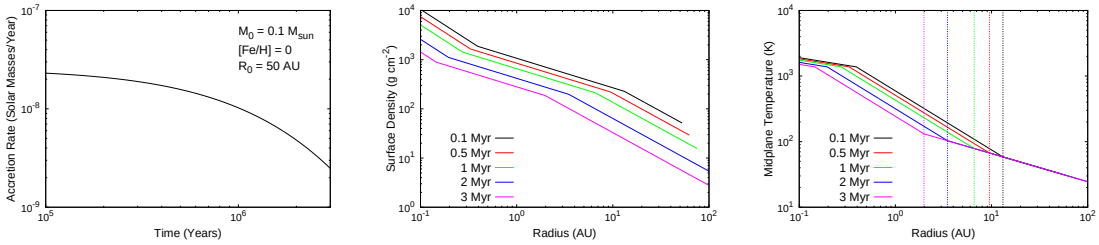

Figure 3.11: The time evolution of the accretion rate (left) and radial profiles of surface density (middle) and midplane temperature (right) are plotted for a fiducial disk. The vertical dashed lines in the right panel mark the location of the heat transition at the boundary of the viscously- and radiatively-heated regimes.

Appendix B: Planet Migration & Formation

In the type-I migration regime, applying to low-mass planets ($\lesssim$ 10 $M_\oplus$), the summed contributions of torques arising at the Lindblad resonances and the planet's corotation region need to be accounted for to compute the resulting planet migration rate. The Lindblad and corotation torques are dependent on the planet's mass and the local disk conditions - namely the power law index of the local surface density and temperature profiles (Paardekooper et al., 2010). For typical disk surface density and temperature profiles, the Lindblad torque on forming planets is negative, and can lead to planetary cores migrating into their host stars on short $\sim 10^5$ year timescales if not counteracted. The corotation torque, a positive torque for typical disk structures, can slow or reverse the migration rate resulting from the Lindblad torque.

However, in addition to the magnitude of the corotation torque, its *operation* is also sensitive to the disk's local structure (Masset, 2001, 2002). The libration timescale of material within the corotation region undergoing horseshoe orbits must be shorter than the disk's local viscous timescale in order for the corotation torque to operate (Hellary & Nelson, 2012; Dittkrist et al., 2014). If the reverse is true, the librating disk material in the corotation region will not produce a net torque on the planet. In this case, the Lindblad torque (and resulting short inward migration timescale) will operate unopposed.

The corotation torque remains unsaturated and counteracts the Lindblad torque near inhomogeneities and transitions in disks (Masset et al., 2006a; Sándor et al., 2011). These regions, where the positive corotation torque balances the negative Lindblad torque, are radii of net torque equilibrium, referred to as *planet traps*. Numerical works, such as Lyra et al. (2010) and Coleman & Nelson

(2016a) have calculated the sense of migration of orbits near planet traps and have shown traps to be stable equilibria, and as such nearby orbits will migrate towards planet traps. Inhomogeneities and transitions in disks are therefore likely sites of planet formation. Trapped planets will form within planet traps, which themselves migrate inwards on timescales comparable to the disk's evolution time.

Other works that have computed type-I torques on a range of planet masses and disk radii for various disk models (so-called migration maps) have shown zero net torque locations to be common (Hellary & Nelson, 2012; Baillié et al., 2016; Coleman & Nelson, 2016a; Cridland et al., 2019a). However, these works find that the locations of the equilibrium points have mass dependences. In particular, it has been shown that torque equilibrium points do not exist for low mass planets ($\lesssim 1$ $M_\oplus$). We do not account for mass-dependence of planet traps in our model, and assume planets to be trapped for the entirety of the type-I migration phase - from an initial mass of 0.01 $M_\oplus$ up until the planet opens a gap and transitions to the type-II migration regime. While we note the discrepancy between our treatment of the migration of low-mass planetary cores with these other works, Coleman & Nelson (2016b) showed traps related to disk inhomogeneities to be mass-independent, which is consistent with our model's treatment.

Dittkrist et al. (2014) considered multiple type-I migration regimes, and found that in many cases, the corotation torque would saturate prior to planets entering the type-II migration phase. This is also in contrast with our assumed mass-independent traps, since we assume the traps (and therefore corotation torque) operate until the planets reach their gap opening masses. If corotation torques were to saturate prior to gap-opening, this would have a large effect on results of our planet formation runs, since the migration rates would be large for planets on the more massive end of the type-I migration regime acted upon solely by the Lindblad torque. However, Hasegawa (2016) showed that the mass at which the corotation torque saturates is comparable to the gap-opening mass. This result was also found in Alessi et al. (2017), where we additionally show that planets in our model enter the type-II migration regime prior to the corotation torque saturating.

Since planets remain trapped for the entirety of the type-I migration phase, our treatment of type-I migration involves determining the location of the planet traps themselves as these are the locations of planet formation in our model. The traps we include in our model are the ice line, heat transition, and outer edge of the dead zone. This is not an exhaustive list, as planet traps may exist in the inner regions of the disk such as at the inner edge of the dead zone (Gammie, 1996),

near the silicate sublimation front (Flock et al., 2019), or at the inner edge of the disk itself. It is unclear if the high temperatures ($\gtrsim$ 1000 K) of the inner disk would favour planet formation, as solid surface densities would be low due to dust evaporation, and high gas temperatures would hinder gas accretion onto planet cores. These traps may, however, be important to prevent cores that have already formed from being accreted onto the host stars.

Volatile transitions in the cooler regions of the outer disk (i.e. CO_2) are an additional set of traps that are not included in our model. We note that Cridland et al. (2019a) showed that the CO ice line does not trap planets due to the shallow temperature (and thus, opacity) gradient in the outer disk. This work did show that the CO_2 ice line can trap planets at larger radii ($\gtrsim$ 20 AU). However, since it exists in the radiatively heated regime of the disk, the trap will not migrate inwards, and will remain at large radii where solid surface densities and accretion rates are small. It is therefore unlikely to form planets that are comparable to even the low-mass end of observed planet masses. The traps we include are therefore the main traps across the body of the disk that are most likely to play a key role in forming the observed classes of planets.

We determine the ice line's location using an equilibrium chemistry solver, CHEMAPP (distributed by GTT Technologies; http://www.gtt-technologies.de/newsletter), over the range of temperatures and pressures encountered across the disk midplane throughout its evolution. The chemistry calculations are done assuming Solar elemental abundances, and considering the range of metallicities used in our population synthesis calculations. The ice line radius, r_{il} is determined to be the disk radius where the midplane abundances of ice and water vapour are equal. We find the ice line evolves as $r_{il} \sim \dot{M}^{4/9}$, which is the same scaling found in Hasegawa & Pudritz (2011) who tracked the location in the disk with a midplane temperature of 170 K to determine the ice line's location.

The heat transition, r_t, separates the inner region of the disk heated via generalized viscous heating and the outer region of the disk heated through radiation, as discussed in section 3.2.1. Its location is determined directly in the Chambers (2009) model by equating the midplane temperatures arising from both heating mechanisms. Figure 3.11 shows that both the disk surface density and temperature profile power laws change at the heat transition.

The dead zone outer edge r_{dz}, separates an inner laminar region from an outer, turbulent region of the disk (Gammie, 1996). MRI-driven turbulence requires a low-level of disk ionization, and within the disk dead zone the surface density is sufficiently high such that ionizing photons are attenuated prior to reaching the disk midplane. Hasegawa & Pudritz (2010) showed that the outer edge of

the dead zone can trap planets due to a sharp increase in dust scale height, with resulting thermal radiation producing an abrupt temperature change leading to planet trapping.

We refer the reader to Alessi et al. (2017) and Alessi & Pudritz (2018) for detailed descriptions on calculating r_{dz}, which closely follows the model presented in Matsumura & Pudritz (2003). In summary, to determine if MRI-turbulence can be generated at a particular location in the disk, one can equate the MRI growth and damping timescales. This results in a condition for the MRI to be inactive, written in terms of magnetic Elsasser number (Blaes & Balbus, 1994; Simon et al., 2013),

$$\Lambda_0 = \frac{V_A^2}{\eta \Omega_K} \lesssim 1 \, , \tag{3.15}$$

where the Alfvén speed is $V_A \simeq \alpha_{\rm turb} c_s$, and η is the magnetic diffusivity, which depends on the electron fraction x_e as follows,

$$\eta = \frac{234}{x_e} T^{1/2} \, {\rm cm}^2 \, {\rm s}^{-1} \, . \tag{3.16}$$

This can be re-written to obtain a critical electron fraction along the midplane, separating the MRI-active and inactive regions (r_{dz}).

The remainder of the calculation of the dead zone's location involves balancing sources and sinks of ionization to determine the electron fraction throughout the disk. We consider ionizing X-rays generated through magnetospheric accretion as the source of ionization in our calculation. This is an update from Alessi & Pudritz (2018), where in addition to X-rays, interstellar cosmic rays were also considered. X-rays are only considered here since our population results in Alessi & Pudritz (2018) were more consistent with the data when considering X-ray ionization. X-rays being a dominant ionizing source in disks is also supported in astrochemistry calculations that show X-ray ionized models to better reproduce observations (Cleeves et al., 2015), as well as by cosmic ray scattering produced by accretion-generated star and disk winds that can prevent cosmic rays from reaching the disk (Matt & Pudritz, 2005; Cleeves et al., 2013; Frank et al., 2014).

We note that the heat transition is the only trap in our model that has a corresponding transition accounted for in the disk model. We rather use the Chambers (2009) disk model to determine where in the disk the ice line and dead zone are, but there are no transitions in the overall disk surface density or temperature profiles. There is, however, a transition in the surface density of solids, Σ_d at the ice line due to the change in fragmentation velocity from the dust evolution model. Including changes in disk surface density and temperature at the ice line and dead zone are not necessary in

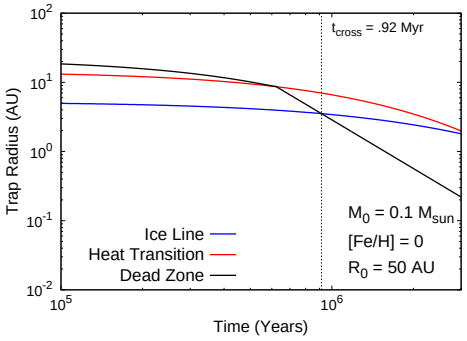

Figure 3.12: The evolution of planet trap radii is shown for a fiducial disk model. The dead zone is initially the outer-most trap in our model, but migrates within the ice line early in the disk's evolution at $t_{\rm cross} = 0.92$ Myr labelled in the figure. The heat transition is location outside of the ice line for the entirety of the disk's evolution. Both the the heat transition and ice line traps converge to ~ 1 AU at the disk's 3 Myr lifetime.

our calculation as we are not directly computing the type-I migration torques, but rather assume the planets are trapped at the features for the entirety of the type-I migration phase.

In figure 3.12, we plot the evolution of the three traps in our model for a fiducial disk setup. The ice line and heat transition both converge to ~ 1 AU at the end of the disk's 3 Myr-lifetime, with the heat transition lying outside of the ice line for the entirety of the disk's evolution. The dead zone radius is initially ~ 20 AU, but the trap quickly evolves to the inner disk, crossing the ice line within 1 Myr, and continuing to ~ 0.02 AU at the disk's lifetime. The dead zone's evolution is the most drastic of the three because of the nearly horizontal path the magnetospheric accretion-generated X-rays take through the disk, and the resulting attenuation rates being very sensitive to the disk's surface density. Recalling the large change in solid surface density at the ice line and the outer disk depleted of solids by radial drift, the locations of the traps and their evolution will greatly affect the solid accretion stage of planet formation in each of the three traps.

Type-II migration applies to planets that are sufficiently massive to open a gap in the disk structure through gravitational torques. An annular gap is opened if the planet's gravitational torque on disk material exceeds the disk's viscous torque, or if the planet's hill sphere exceeds the disk's pressure scale height (Matsumura & Pudritz, 2006),

$$M_{\rm GAP} = M_* \min\left[3{\rm h}^3({\rm r_p}), \sqrt{40\alpha {\rm h}^5({\rm r_p})}\right] . \tag{3.17}$$

Here, r_p denotes the planet's radius and $h = H/r$ is the disk aspect ratio.

Planets undergo type-II migration once exceeding the local gap-opening mass, proceeding at a rate determined by the disk's viscous-timescale,

$$v_{\rm mig,II} = -\nu/r_p\,. \tag{3.18}$$

When the planet greatly exceeds its gap-opening mass, achieving masses comparable to the remaining disk mass interior to its orbit ($M_p > M_{\rm crit} = \pi r_p^2 \Sigma$), the planet's inertia will slow its migration beneath the disk's viscous rate (Ivanov, Papaloizou & Polnarev, 1999; Hasegawa & Pudritz, 2012),

$$v_{\rm mig,II,slow} = -\frac{\nu}{r_p\,(1 + M_p/M_{\rm crit})}\,. \tag{3.19}$$

This migration phase applies to planets that undergo runaway gas accretion. During the type-II migration phases, planets migrate away from the trap they were forming in during the trapped type-I migration regime, and planet orbital radii are not solely determined by the location of the traps.

We initialize our planet formation runs with a 0.01 $M_\oplus$ core situated at the orbital radius of the trap it is forming within. Here we are assuming that type-I migration will quickly migrate planets into a trap within the disk if a distribution of initial orbital radii were instead used. The first growth stage in the core accretion scenario is solid accretion, whereby we model the core's growth to take place via planetesimal accretion or oligarchic growth. The accretion timescale in this phase is (Kokubo & Ida, 2002),

$$\begin{aligned}\tau_{\rm c,acc} \simeq & 1.2\times10^5\ {\rm yr}\left(\frac{\Sigma_d}{10\ {\rm g\ cm^{-2}}}\right)^{-1} \\ & \times\left(\frac{r}{r_0}\right)^{1/2}\left(\frac{M_p}{M_\oplus}\right)^{1/3}\left(\frac{M_*}{M_\odot}\right)^{-1/6} \\ & \times\left[\left(\frac{b}{10}\right)^{-1/5}\left(\frac{\Sigma_g}{2.4\times10^3\ {\rm g\ cm^{-2}}}\right)^{-1/5}\right. \\ & \left.\times\left(\frac{r}{r_0}\right)^{1/20}\left(\frac{m}{10^{18}\ {\rm g}}\right)\right]^2\,,\end{aligned} \tag{3.20}$$

where $m \simeq 10^{18}$ g is the mass of accreted planetesimals and $b \simeq 10$ is a parameter defining the core's feeding zone. The corresponding accretion rate is $\dot{M}_p = M_p/\tau_{\rm c,acc}$.

Including the dust evolution model affects our planet formation model in equation 3.20, as we take the local solid surface density Σ_d from the dust-to-gas ratio distribution calculated using the Birnstiel et al. (2012) model. In doing so, we are assuming that the distribution of planetesimals will match the disk's dust distribution. This assumption can be justified as streaming instability models have shown planetesimal assembly from dust takes place on short ($\lesssim 10^3$ year) timescales (Johansen et al., 2007). Gravitational dynamics may yet change the planetesimal distribution, however the oligarchic growth phase is short ($\sim 10^5 - 10^6$ years) and we do not consider these effects here.

The second, slow gas accretion phase of the core accretion model begins when the planetesimal accretion rate, and resulting core heating, becomes insufficient to maintain hydrostatic balance in gas surrounding the forming core. The critical core mass where a forming planet transitions from oligarchic growth to slow gas accretion is (Ikoma et al., 2000; Ida & Lin, 2008; Hasegawa & Pudritz, 2014),

$$M_{\rm c,crit} \simeq f_{\rm c,crit} \left(\frac{1}{10^{-6} M_\oplus \ {\rm yr}^{-1}} \frac{dM_p}{dt} \right)^{1/4} M_\oplus \ . \tag{3.21}$$

We set $f_{\rm c,crit} = 1.26$, which results from the best-fit envelope opacity of 0.001 cm^2 g^{-1} determined in Alessi & Pudritz (2018), where we explored the full dependence of equation 3.21 on the envelope opacities of forming planets.

The slow gas accretion timescale proceeds at the Kelvin-Helmholtz rate (Ikoma et al., 2000),

$$\tau_{KH} \simeq 10^c \ {\rm yr} \left(\frac{M_p}{M_\oplus} \right)^{-d} \ . \tag{3.22}$$

We take $c = 7.7$ and $d = 2$, as determined by the best-fit envelope opacity from Alessi & Pudritz (2018), where fits from Mordasini et al. (2014) were used to link the Kelvin-Helmholtz c and d parameters to envelope opacity. The associated gas accretion rate is $\dot{M} = M_p / \tau_{KH}$.

As gas accretion proceeds, the planetary envelope may become sufficiently massive to lose pressure support, whereby the planet will transition into a runaway growth phase. We only consider the Kelvin-Helmholtz timescale in calculating gas accretion rates, and the runaway growth phase is a consequence of τ_{KH} decreasing as the planet's mass increases. Other works have instead considered the disk-limited accretion phase when determining the gas accretion rate on massive planets (e.g. Machida et al. (2010); Tanigawa & Tanaka (2016); Hasegawa et al. (2018, 2019)). Both approaches can produce similar results depending on the settings of the planet's envelope opacity (or Kelvin-Helmholtz parameters).

The termination of gas accretion onto massive planets is expected physically linked to gap-opening as the local surface density of gas within the planet's feeding zone decreases. We therefore parameterize the maximum mass of a forming planet, following Hasegawa & Pudritz (2013), as,

$$M_{\rm max} = f_{\rm max} M_{\rm gap} \, . \tag{3.23}$$

Accretion onto planets whose masses exceed $M_{\rm max}$ is artificially truncated. The settings of the parameter $f_{\rm max}$ range from 1-500, with low values corresponding to planets whose accretion is terminated shortly after gap-opening. It has been shown, however, that substantial gas accretion can be sustained after gap-opening takes place, corresponding to larger $f_{\rm max}$ values (Kley, 1999; Lubow & D'Angelo, 2006; Morbidelli et al., 2014). We highlight that this parameter is the only intrinsic model parameter that we vary in our population synthesis calculations. It is a necessary inclusion to obtain a range of final planet masses corresponding to the data[3].

Tanigawa & Tanaka (2016) show that disk accretion rate limits a planet's gas supply, providing a physical means of terminating gas accretion. This is further explored in Lee (2019), who consider both disk accretion rate and local hydrodynamic flows to terminate the accretion onto short-period sub-Saturns. Another physical means of terminating gas accretion is through the interaction of the accreting planet's magnetic field and in-falling disk material, resulting in an accretion cross-section that inversely scales with planet mass (Batygin, 2018; Cridland, 2018). Our method of terminating gas accretion simplifies the late stages of planet formation for the purposes of population synthesis calculations.

Appendix C: Comparing M-a distributions to constant dust-to-gas ratio models

In figure 3.13, we plot M-a distributions of planet populations resulting from two sets of models with different treatments of dust evolution: those with a full dust evolution treatment of Birnstiel et al. (2012) (left column), and those that neglect dust evolution and assume a constant dust-to-gas ratio of 0.01 (right column). We include both models to compare this work's dust treatment to the

[3]We note that in models that assume a disk-limited final accretion stage to truncate gas accretion, the accretion rate onto the planet is parameterized as a fraction of the disk accretion rate. In such models, this parameter serves the same purpose as our $f_{\rm max}$ parameter, ultimately setting the final mass of the planet.

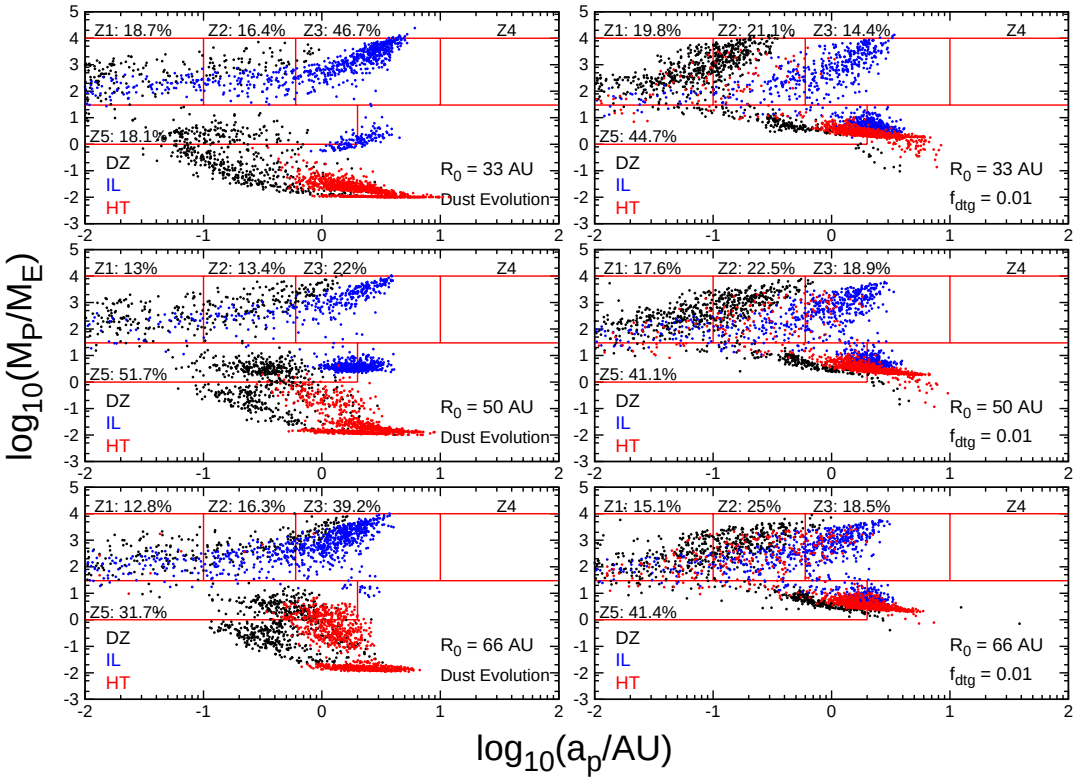

Figure 3.13: **Left Column:** Planet populations resulting from the full dust evolution model are shown. We consider a range of initial disk radii (R_0) between the top (33 AU), middle (the fiducial 50 AU setting), and bottom panels (66 AU). **Right Column:** Populations resulting from an assumed constant dust-to-gas ratio of 0.01 (neglecting dust evolution as in Alessi & Pudritz (2018)) are shown for comparison, using the same initial disk radii settings.

assumed constant $f_{\rm dtg}$ models from Alessi & Pudritz (2018), and to see the effects the dust evolution model has on our planet populations. For both sets of models, we include a small (33 AU) and large (66 AU) initial disk radius setting, in addition to the fiducial 50 AU models.

The effects of including the dust evolution model are readily seen when compared to the constant dust-to-gas ratio treatment of Alessi & Pudritz (2018). We first emphasize that the super Earth and warm Jupiter frequencies are insensitive to the initial disk radius setting when a constant dust-to-gas ratio is assumed. Therefore, the disk radius-dependent trade-off between the super Earth and warm Jupiter populations formed at the ice line is only encountered when the full dust evolution treatment is included.

Inclusion of the dust evolution model also results in more short-period super Earths being formed from the dead zone trap. This is largely a result of the delayed growth in the dead zone, whereby the trap itself needs to migrate to the inner region of the disk before solid accretion can take place. This work's populations that include dust evolution can form super Earths with orbital radii down to ~ 0.03 AU in the case of the smallest disk sizes, and down to ~ 0.08 AU for the fiducial $R_0 = 50$ AU case. The constant dust-to-gas ratios of Alessi & Pudritz (2018) were not able to form short-period, low mass super Earths. This is seen in figure 3.13 as the constant dust-to-gas ratio models all produce super Earths with orbital periods between ~ 0.8 - 2 AU. Including the dust evolution treatment therefore results in improved population results, as we are readily able to produce shorter-period super Earths, filling out a region of the M-a diagram that is densely populated with observed planets.

Including dust evolution also results in many sub-Earth mass planets, which were not encountered in the constant dust-to-gas ratio cases. This is due to the solid depletion of the outer disk due to radial drift, and corresponding inefficient solid accretion in a subset of the planet formation runs that does not take place when $f_{\rm dtg}$ is held constant. The constant dust-to-gas ratio models additionally have an overall larger gas giant formation frequency because of this.

In the case of a small disk (33 AU), the constant dust-to-gas ratio population shows a separation between the shorter period gas giants formed in the dead zone and the larger period gas giants formed in the ice line - one of the main results of Alessi & Pudritz (2018). This feature is not seen in any of the models that include dust evolution, nor is it seen in the constant dust-to-gas ratio models where a larger initial disk size is considered.

Acknowledgements

The authors thank Tilman Birnstiel and Yasuhiro Hasegawa for insightful discussions regarding this work. We also thank the anonymous referee for their helpful comments improving the quality of this paper. M.A. acknowledges funding from the National Sciences and engineering Research Council (NSERC) through the Alexander Graham Bell CGS/PGS Doctoral Scholarship and from an Ontario graduate scholarship. R.E.P. is supported by an NSERC Discovery Grant. A.J.C acknowledges financial support from the European Union A-ERC grant 291141 CHEMPLAN, by the Netherlands Research School for Astronomy (NOVA), and by a Royal Netherlands Academy of Arts and Science (KNAW) professor prize. This work made use of Compute/Caclul Canada. This research has made use of the NASA Exoplanet Archive, which is operated by the California Institute of Technology, under contract with the National Aeronautics and Space Administration under the Exoplanet Exploration Program.

Addendum for Formation of Planetary Populations II: Effects of Initial Disk Size & Radial Dust Drift

In this paper, we used the Birnstiel et al. (2012) model to determine the radial distribution of dust throughout disk evolution under the effects of coagulation, fragmentation, and radial drift. We assumed that the computed dust distributions would also correspond to the radial distribution of planetesimals which are accreted onto planetary cores during the oligarchic growth phase of our planet formation models. We justified our assumption of inferring the planetesimal distribution throughout disks directly from the radial dust distribution by noting that the growth from dust to planetesimals via the streaming instability occurs quickly ($\lesssim 10^4$ years, Johansen et al. (2007)).

While this consideration remains valid, it only justifies an *initial* planetesimal distribution following the dust distribution. Oligarchic growth timescales are longer ($10^5 - 10^6$ years) than planetesimal formation timescales via the streaming instability. A potential disconnection between the planetesimals' radial distribution and that which is predicted from the dust (i.e. the initial planetesimal distribution) arises due to the fact that planetesimal migration through the disk occurs on a longer timescale than radial dust drift. This potentially could change the radial planetesimal distribution significantly during the oligarchic growth phase to be quite different than the dust distribution.

However, a key consequence of the Birnstiel et al. (2012) dust evolution model is that the radial dust surface density distributions all have a similar step-function profile, transitioning from higher surface densities inside the ice line, to lower surface densities outside the ice line in the drift-limited region (see figure 3.2). This was a robust result seen at all disk parameters investigated. Additionally, the dust model predicts this radial distribution to arise quickly, after only the first 10^5 years of disk evolution. Because of this feature of the dust evolution model, the rate of change in the dust surface density at all locations other than the ice line is small (since locations within either the drift- or fragmentation-limited regions have quite steady dust surface densities). Additionally, the ice line itself moves slowly through the disk on the viscous timescale, which is comparable to the oligarchic growth timescale.

Because of these results of the dust evolution model (mainly, the robust step-function profile transitioning at the ice line for all investigated disk models) we expect that the radial dust profile will remain a good indicator of what the planetesimal distribution will be throughout the entirety of oligarchic growth, even though planetesimals migrate with longer timescales than radial dust drift.

Chapter 4

Formation of Planetary Populations III: Core Composition & Atmospheric Evaporation

Matthew Alessi, Julie Inglis, & Ralph Pudritz

What follows has been published in Monthly Notices of the Royal Astronomical Society (MNRAS). See: Alessi, Inglis, & Pudritz (2020), MNRAS **497**: 4814. We include a minor correction in the corrigendum at the end of this chapter.

Abstract

The exoplanet mass radius diagram reveals that super Earths display a wide range of radii, and therefore mean densities, at a given mass. Using planet population synthesis models, we explore the key physical factors that shape this distribution: planets' solid core compositions, and their atmospheric structure. For the former, we use equilibrium disk chemistry models to track accreted minerals onto planetary cores throughout formation. For the latter, we track gas accretion during formation, and consider photoevaporation-driven atmospheric mass loss to determine what portion of accreted gas escapes after the disk phase. We find that atmospheric stripping of Neptunes and

sub-Saturns at small orbital radii ($\lesssim$0.1AU) plays a key role in the formation of short-period super Earths. Core compositions are strongly influenced by the trap in which they formed. We also find a separation between Earth-like planet compositions at small orbital radii $\lesssim$0.5AU and ice-rich planets (up to 50% by mass) at larger orbits $\sim$1AU. This corresponds well with the Earth-like mean densities inferred from the observed position of the low-mass planet radius valley at small orbital periods. Our model produces planet radii comparable to observations at masses $\sim$1-3$M_\oplus$. At larger masses, planets' accreted gas significantly increases their radii to be larger than most of the observed data. While photoevaporation, affecting planets at small orbital radii $\lesssim$0.1AU, reduces a subset of these planets' radii and improves our comparison, most planets in our computed populations are unaffected due to low FUV fluxes as they form at larger separations.

4.1 Introduction

The wide range of outcomes of planet formation, as indicated through exoplanet observations, reveals a tremendous amount of information regarding the variability in planet formation processes between different host stars (Borucki et al., 2011b; Batalha et al., 2013; Rowe et al., 2014; Morton et al., 2016). Comparing with observed exoplanet properties offers the best constraints on models of planet formation, and we gain a better statistical understanding of outcomes of planet formation as the observed sample grows with new discoveries from *TESS* (Gandolfi et al., 2018; Huang et al., 2018a). Additionally, as we are in the era of highly-resolved disk images from *ALMA* and *SPHERE* (ALMA Partnership et al., 2015; Andrews et al., 2018; Avenhaus et al., 2018), we can better understand the conditions within which planet formation takes place.

The current state of observations therefore constrains both the initial conditions for planet formation (the disks) and the resulting planetary systems, bracketing each end of the timeline of planet formation. Only in very select systems has planet formation been observed "in action" within gaps in these highly-resolved disk images (Keppler et al., 2018; Ubeira-Gabellini et al., 2020). Rather, planet formation theories are used and can be tested by how well they connect these two endpoint categories of observational data.

In figure 4.1, we show the observed planet mass semi-major axis (hereafter *M-a*) diagram with colour indicating each planet's detection method. Following, Chiang & Laughlin (2013) and Hasegawa & Pudritz (2013), we divide the diagram into different zones outlining various planet populations or

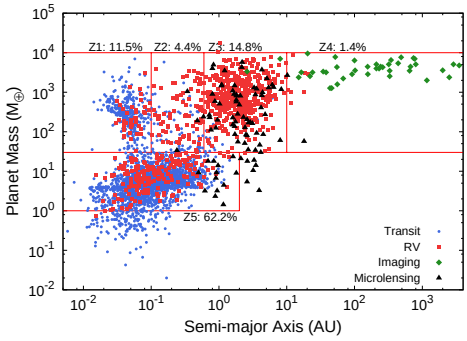

Figure 4.1: The observed planet mass semi-major axis distribution is shown. We divide the M-a space into zones separating various planet populations as suggested by Chiang & Laughlin (2013), and include frequencies by which planets populate each region. Zone 1 contains hot Jupiters; zone 2: period-valley giants; zone 3: warm Jupiters; zone 4: long-period giants; and the frequency-dominating zone 5 contains super Earths and Neptunes. Colours of data points indicate the planets' initial detection technique. These data were compiled using the NASA Exoplanet Archive, current as of March 2, 2020.

classes, with zones 1-5 corresponding to hot Jupiters, period-valley giants, warm Jupiters, long-period giants, and super Earths and Neptunes, respectively. In terms of frequency, the zone 5 planets (super Earths and Neptunes) dominate, indicating that planet formation mechanisms are overall much more efficient in forming low-mass planets than gas giants. The frequency of low mass planets relative to giant planets is even greater once observational biases are corrected for in occurrence rate studies (i.e. Santerne et al. (2016); Petigura et al. (2018)). These biases lead to higher observed rates of massive, close-in planets than their actual frequency in the underlying exoplanet distribution.

In figure 4.2, we show the observed planet mass-radius (hereafter *M-R*) distribution. The data is shown for low planetary masses, as we will be comparing our computed planet radii to the observed data over the super-Earth and Neptune mass range in this work. As has often been noted for all low mass planets, the observed distribution shows a range of planet radii for any given mass (Carter et al., 2012; Howard et al., 2012; Rogers, 2015). We therefore emphasize that super Earths and Neptunes in particular display a range of observed mean densities. We also include observational uncertainties for the low-mass M-R diagram, showing that planets typically have quite large mass uncertainties from their radial velocity measurement (due to the uncertain inclination angle of the observed system) and better-constrained radii from transit observations.

The observational data therefore shows that (1) super Earths form frequently, and (2) they display a range of mean densities. Earlier papers in this series centred on reproducing the first observational

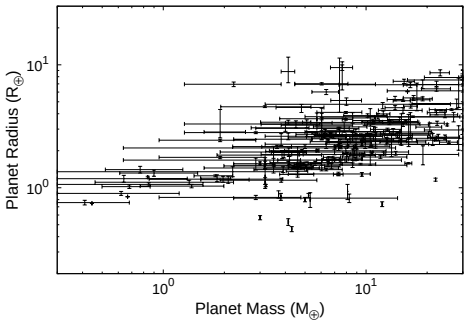

Figure 4.2: We show the low-mass portion of the M-R diagram pertaining to super Earths and Neptunes, plotted with observational uncertainties. Across the entire super Earth mass range, planets show a range of observed radii, and therefore have a range of mean densities. These data were compiled using the NASA Exoplanet Archive, current as of March 2, 2020.

result and comparing modelled planet populations to the observed M-a relation.

In Alessi & Pudritz (2018) (paper I), we studied the effect of forming planets' envelope opacities on gas accretion rates, and resulting ratio of super Earths to gas giants. We concluded that low settings of envelope opacities ~ 0.001 cm^2 g^{-1} were necessary to obtain a reasonable comparison to the observed gas giant occurrence rate - orbital radius relation.

Paper II in this series, Alessi et al. (2020), included dust evolution through radial drift, and focused on determining the effect of the initial disk size on the resulting M-a distribution. We found that, with planet formation at the water ice line, the produced ratio of warm gas giants to super Earths sensitively depends on the disk's initial radius as resulting from protostellar collapse. Intermediate disk sizes of roughly 50 AU resulted in the richest super Earth population, whereas formation in both smaller and larger disks resulted in more gas giants near 1 AU. In smaller disks ($\sim$ 30 AU), this was a result of larger gap-opening masses for planets forming at the ice line, leading to gas accretion termination having a smaller impact. In large disks ($\sim$ 65 AU), a larger reservoir of dust in the outer disk radially drifted into the ice line, leading to efficient planet formation.

In this work, we now focus on understanding the observed M-R relation, moving forward using the optimal model set up that resulted in the best fit to the M-a relation from papers I & II. A planet's radius is set by a combination of its solid core and atmosphere properties. A big question here is to what extent is the relation between properties of populations in the M-a diagram also reflected in the M-R diagram. In the M-a diagram, our previous papers have shown that orbital

radii and masses are a consequence of action of planet traps which also stamp a chemical signature on their forming planets. This signature is, to some degree, important in shaping the M-R diagram of the populations. Here we explore these links not only for planetary cores[1], but their atmospheres as well. We find two main compositions for super Earths: those formed at dead zones which achieve a dry, rocky composition, and those that have formed at the ice line which have much more ice in the cores (the same result as Alessi et al. (2017)). Atmospheres can mask the radius differences derived from core properties except for planets at small orbital radii such that photoevaporatiion strips their atmospheres.

An advantage to our approach is in achieving variation in both of these components within the super Earth population. In the case of planet cores, different densities indicate different compositions which are acquired during planet formation. For planets with atmospheres, their transit radii are measured at the optical depth $\tau = 2/3$ surface. Thus, the atmospheric scale height as set by the planet's proximity to its host star has a large effect on its transit radius[2]. However, this is contingent on planets accreting and retaining a significant amount of gas during formation.

Core compositions are usually grouped into three categories of materials; irons, silicates, and water ice; with their mass fractions used as inputs to structure calculations (i.e. Valencia et al. (2006); Zeng & Sasselov (2013); Thomas & Madhusudhan (2016)). Combining models of planet formation and protoplanetary disk chemistry is required for a complete picture of how planets acquire their composition, as this approach allows the composition of materials accreted onto planets to be tracked throughout formation. This type of approach that links planet composition to formation history has been used previously by many works, focusing on both low-mass planets' solid compositions (Bond et al., 2010; Elser et al., 2012; Moriarty et al., 2014; Alessi et al., 2017) and atmospheric signatures in gas giants (Öberg et al., 2011; Madhusudhan et al., 2014; Thiabaud et al., 2015; Cridland et al., 2016; Eistrup et al., 2018; Cridland et al., 2019b).

Outcomes of planet formation models are sensitive to disk and host star properties, such as disk lifetime, mass, and metallicity (Ida & Lin, 2004b; Mordasini et al., 2009a; Hasegawa & Pudritz, 2012; Alessi et al., 2017). We therefore use the technique of planet population synthesis in this series, where observationally-constrained distributions of these disk parameters are sampled as inputs to core accretion (Pollack et al., 1996) calculations of planet formation. This technique has been used

[1]We refer to a planet's entire solid component as the *planetary core*, following nomenclature of core accretion models. This is not to be confused with a planet's iron core, being the innermost region of a differentiated planet.

[2]We hereafter simply use *planet radius* when referring to a planet's transit radius

in previous works such as Ida & Lin (2008); Mordasini et al. (2009a); Hasegawa & Pudritz (2013); Bitsch et al. (2015), and Ali-Dib (2017). In using population synthesis, we account for the intrinsic variability in planet formation conditions on outcomes of planet formation. This method was used in previous entries in this series (Alessi & Pudritz, 2018; Alessi et al., 2020) to compare outcomes of planet formation with the observed M-a distribution.

We combine our population synthesis models with disk chemistry and planet structure calculations to produce an M-R distribution than can be compared with observations. We will therefore be connecting four planet properties- mass, semi-major axis, radius, and composition- with formation. Previously, Mordasini et al. (2012c) used a similar approach. We expand upon this by considering a full equilibrium chemistry model to compute mineral abundances throughout the disk. There are also differences in the planet formation models; particularly our use of planet traps as barriers to otherwise rapid type-I migration. Additionally, we will be using planet formation tracks from Alessi et al. (2020) that included a full treatment of dust evolution and radial drift, so those effects will be included here when computing planet compositions.

In our disk chemistry treatment, we include the ranges of C/O and Mg/Si ratios observed in nearby F, G, and K-type stars (Brewer & Fischer, 2016), as well as non-Solar metallicities. Disk abundances are sensitive to elemental ratios (Bond et al., 2010; Santos et al., 2017; Bitsch & Battistini, 2020), and this will therefore have an effect on planet compositions and radii. In addition, Suárez-Andrés et al. (2018) showed that correlations exist between both C/O and Mg/Si with disk metallicity, and we include this stellar data in our handling of elemental ratios as inputs to disk chemistry calculations. We are therefore further connecting our resulting M-R distribution to variability in planet-formation environments via the spread in observed elemental ratios affecting disk chemistry.

Lastly, we emphasize that the treatment of planet atmospheres is crucial when computing planet radii as this is the lightest component of a planet and therefore has a large effect on a planet's radius. Our planet formation model calculates the amount of gas that is accreted onto planets during the disk phase. As a new addition in this paper, here we also consider what fraction of that gas is retained after the disk has dissipated. Atmospheric mass-loss, or evaporation, can occur on super Earths after the disk has dissipated, driven either via photoevaporation due to high energy radiation from the host-star (Owen et al., 2011; Lopez & Fortney, 2013), or via the core-driven mass loss mechanism (Gupta & Schlichting, 2019, 2020).

Here we compute X-ray photoevaporation of planet atmospheres when computing planet radii. When calculating atmospheric mass loss, we use planet properties (orbital radii, core masses) as determined by our formation models, thereby linking outcomes of planet formation to post-disk phase photoevaporative evolution of atmospheres. Atmospheric evaporation has been previously included in population synthesis calculations, such as in Jin et al. (2014) and Mordasini (2020). The FUV flux that is output from the host star in photoevaporation models decreases with its age. We self-consistently use the disk lifetimes - a varied parameter in our population synthesis calculations - as inputs to this evaporation model, thereby including stellar variability in our treatment of atmospheric mass loss.

This paper is structured as follows: In section 2, we outline our model, emphasizing our treatment of disk chemistry, planet interior structures, and evaporation of super Earth atmospheres. In section 3, we show resulting planet compositions and mass-radius diagrams for our populations. Section 4 focuses on the individual effects of disk C/O and Mg/Si ratio on super Earth compositions. In section 5, we discuss our results and implications of model assumptions, and compare to other works. Lastly, we present our main conclusions in section 6.

4.2 Model

4.2.1 Planet Populations

Here we provide a brief summary of various needed components of our previous extensive work on planet formation and population synthesis models. We refer the reader to the previous entries in this series, Alessi & Pudritz (2018) and Alessi et al. (2020), for a complete model description.

Our planet formation model consists of several parts. We use the Chambers (2009) semi-analytic disk model to calculate evolving disk properties, including the midplane temperature and pressure that define the local conditions for our equilibrium chemistry model (see section 2.2). The model is useful for our purposes as it includes disk evolution, as well as heating through both generalized viscosity and host-star radiation. This is important in our approach as the boundary between these two heating regimes is a planet trap, namely the heat transition. This model assumes disk evolution to take place via MRI-turbulence, and we set the turbulent α parameter to 10^{-3} in our calculations. In Alessi et al. (2017), we also incorporated evolution via photoevaporation into this model, and this update is included in all papers in this series.

The Birnstiel et al. (2012) two-population dust model is used to determine the radial- and time-dependent dust surface densities, under the influence of radial drift, coagulation, and fragmentation, where the energy threshold for fragmentation depends on the grains' location in the disk with respect to the ice line. While only computing dust evolution at two sizes, this model achieves a good comparison with the full simulations of Birnstiel et al. (2010a) at a reduced computational cost. Radial drift is an important inclusion as it greatly affects the solid distribution in disks. However, following the conclusions of Birnstiel et al. (2010b); Pinilla et al. (2012a), we found in Alessi et al. (2020) that the radial drift rates of the Birnstiel et al. (2012) dust model are quite high, as they do not allow disks to maintain extended solid distributions over appreciable ($\sim$ 1 Myr) disk evolution timescales. Nonetheless, we achieved a better comparison with the M-a distribution when we included the effects of radial drift (Paper II), then when we did not (Paper I). In particular, radial drift resulted in a larger super Earth population forming at smaller orbital radii; the subset of the planet population we are focusing on in this paper.

We use the core accretion model of planet formation (Pollack et al., 1996), and include the effects of planet migration under the trapped type-I and type-II migration regimes, transitioning between the two at the gap-opening mass. Planet traps, or locations of zero-torque on low-mass forming planets from the summed planet-disk interaction, have been shown to exist in numerical simulations of inhomogeneous disks (Lyra et al., 2010; Baillié et al., 2015, 2016; Coleman & Nelson, 2016a). The semi-analytic approach of Hasegawa & Pudritz (2012, 2013) showed that, when incorporating planet traps, the core accretion model achieves a good correspondence with the observed M-a distribution.

Planet traps are central to our theory as they are barriers to otherwise rapid type-I migration. The traps we include are the water ice line, the heat transition (separating the inner, viscously heated region of the disk from the outer region heated through stellar radiation), and the outer edge of the dead zone (separating an inner, laminar disk midplane from an outer, turbulent region). Our model considers the *Ohmic* dead zone; the region in the disk midplane with no turbulence due to Ohmic dissipation dominating. When determining its location, we consider disk ionization to take place via X-rays generated from accretion onto the host star.

The three traps we include are present within the planet-forming region of the disk ($\lesssim$ 10-20 AU), and traps in the outer regions of the disk may slow core migration, but do not lead to appreciable accretion rates onto trapped cores. The location of the traps sets the regions in the disk where low-mass cores accrete, and thus play an important role in their final compositions. For typical disks,

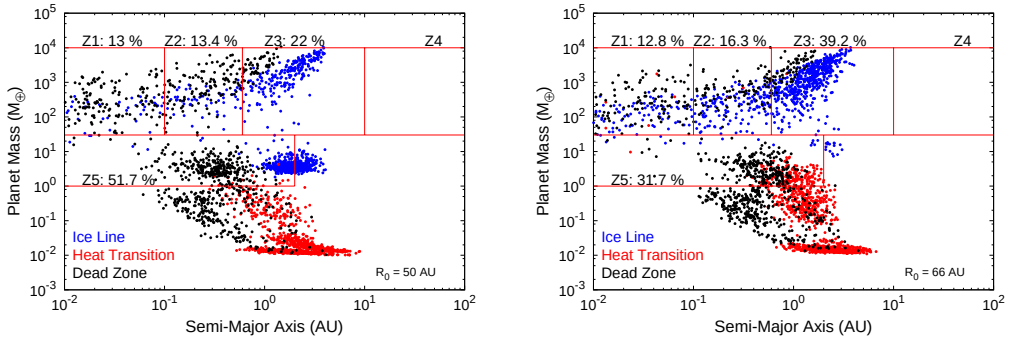

Figure 4.3: M-a distributions are shown for planet populations from Alessi et al. (2020) with different initial disk radii: $R_0 = 50$ AU (left) and $R_0 = 66$ AU (right). Zone 5 planets in the 50 AU population arise from formation in the ice line and dead zone traps, while those from the 66 AU population are formed in the heat transition and dead zone traps.

our models find that the dead zone is situated inside the ice line. By contrast, the heat transition typically is outside the ice line but, in sufficiently long-lived disks ($\gtrsim 3$ Myr) evolves to lie inside the ice line.

We use the population synthesis method to stochastically vary four parameters prior to each planet formation model. The first three are the disk lifetime, mass, and metallicity, for which observationally constrained distributions are used (see paper II, Alessi et al. (2020), for full description). By including these, we are accounting for the variability in formation environments on outcomes of planet formation. The fourth varied parameter sets the planets' maximum attainable masses (pertaining only to gas giant formation in sufficiently long-lived disks where runaway gas accretion takes place). We set the range of this parameter's settings such that the mass range of gas giants corresponds reasonably with the observed M-a distribution. Our populations consist of 3000 planet formation models, with 1000 per planet trap.

In figure 4.3, we show the main result of Alessi et al. (2020): M-a distributions corresponding to two values of the initial disk radius, R_0, highlighting the effect of this parameter on resulting planet populations. These distributions arise solely from our planet formation models and are not corrected for observational completeness limits. The $R_0 = 50$ AU model (left panel) resulted in the largest super Earth population, which is comprised of a mix of planets formed in the ice line and dead zone traps. We also show a larger disk size model, $R_0 = 66$ AU (right panel), whereby a smaller, but still appreciable super Earth population is formed in this case from the heat transition and dead zone

traps. At this disk radius, the ice line mainly contributes to the zone 3 (warm gas giant) population and does not form many super Earths. The larger disk size shifts the traps inwards (due to lower surface density), such that the accretion rates within the heat transition (situated furthest out in the disk among the traps) becomes high enough for super Earth formation.

Our strategy in considering fixed settings of R_0 in individual populations in paper II was to isolate the effect of the initial disk radius on resulting planet populations. The combination of a disk's initial mass f_M and radius R_0 fixes its initial surface density. For example the initial disk surface density at 1 AU, which can be referred to as Σ_0. By fixing R_0 and incorporating a full log-normal distribution of initial disk masses f_M, we are effectively setting a log-normal distribution of Σ_0 that is sampled in population runs. Different fixed R_0 values change the *average* of this Σ_0 distribution, which physically caused the changes in resulting populations we found in paper II, through its effect on disk evolution and planet accretion timescales. One could take an alternate strategy of incorporating a full distribution of R_0 values in a population, which, along with f_M, will contribute to the population's overall Σ_0 distribution. However, in this approach, it would be difficult to discern the effect of R_0 on the synthetic population. As this was a main focus of paper II (from which, populations are used to investigate their M-R distributions in this work), the alternate approach of investigating a fixed R_0 was instead taken.

The populations in figure 4.3, being from our previous work, do not include any effects of atmospheric mass-loss through photoevaporation. As we will show in section 4.3, atmospheric photoevaporation changes the resulting M-a distribution by reducing atmospheric masses of Neptunes and sub-Saturns at small orbital radii ($a_p \lesssim 0.1$ AU), ultimately producing super Earths at these small a_p.

4.2.2 Disk Chemistry

We include simulations of disk chemistry in order to track materials accreted onto planets formed in our populations. To do so, we use an equilibrium chemistry approach, best suited to calculating solid abundances as these materials condense from gas phase on short timescales (Toppani et al., 2006). Equilibrium chemistry is suitable for our purposes as we are mainly focused on tracking compositions of super Earths whose masses are predominantly comprised of a solid core. These compositions (along with mass, and semi-major axis provided from the planet formation model) become inputs for calculating planet structures as described in section 4.2.3.

We provide the details of our disk chemistry calculations in Appendix A, along with a complete list of the chemical species included in table 4.1. We also refer the reader to (Alessi et al., 2017) for a detailed description of our equilibrium chemistry approach that only considered Solar composition and metallicity, based off of Pignatale et al. (2011).

As an extension to the chemistry approach taken in Alessi et al. (2017), this work also considers non-Solar disk metallicity as well as non-Solar C/O and Mg/Si ratios. Brewer & Fischer (2016) showed that F, G, and K-type planet-hosting stars in the Solar neighbourhood display a range in these elemental ratios. The values of C/O and Mg/Si have a considerable effect on disk chemistry, as shown in Bond et al. (2010). For example, the C/O ratio has an impact on the water abundance throughout the disk, in addition to affecting water vs. methane abundances in atmospheric chemistry (Mollière et al., 2015; Molaverdikhani et al., 2019). The Mg/Si ratio sets the relative abundances of the most abundant silicate-bearing minerals - enstatite and forsterite (Carter-Bond et al., 2012).

When varying the disk C/O or Mg/Si ratio at a given metallicity, we do so by changing both the elements' abundances so as to not change the disk metallicity. For example, when increasing the disk C/O ratio at Solar metallicity, the molar abundance of carbon is increased in equal parts to a molar abundance decrease in oxygen, such that C/O is increased to the desired value while the total molar amount of carbon plus oxygen is kept the same. When varying the metallicity, we maintain the abundance ratio between hydrogen and helium, as well as the ratios between all metals. Thus at any metallicity, the molar ratios between metals are held at Solar value, with the exception being C, O, Mg, and Si when the relevant elemental ratio is set to a non-Solar value.

In our fiducial chemistry run, we vary the C/O and Mg/Si ratios with disk metallicity, in accordance with the data presented in Suárez-Andrés et al. (2018) for Solar-type stars. Based on data from this work, we use the following fits for the two elemental ratios,

$$\mathrm{C/O} = 0.4\,[\mathrm{Fe/H}] + 0.47\ ; \tag{4.1}$$

$$\mathrm{Mg/Si} = -0.2\,[\mathrm{Fe/H}] + 1.1\ . \tag{4.2}$$

We note that while these relations show the general trend of the elemental ratios with metallicity, the stellar data shows significant spread (in C/O & Mg/Si at a given metallicity) that the above one-to-one relations do not capture. Nonetheless, by changing the C/O and Mg/Si ratios with metallicity in this manner, we are accounting for their varying affects on disk chemistry throughout the explored

metallicity range in our planet populations. We recall that disk metallicity is a stochastically-varied parameter in our planet populations that is directly input into equations 4.1 & 4.2 when setting the disk elemental ratios.

For completeness, we also have considered disk chemistry models where the C/O and Mg/Si ratios were held constant (at both Solar and non-Solar values) with metallicity to see their individual effects on resulting abundances. Results of these chemistry runs are shown in appendices A and D.

The time-dependent disk abundances computed using the chemistry model are then used to calculate planet compositions throughout formation. This is done simply by tracking each planet's position and mass accretion rate throughout disk evolution, and using the disk abundances at that position to update the planet's composition. We assume that all solids accreted contribute mass to the planet's solid core, and do not consider any effects of ablation or vaporization that would cause incoming solid material to contribute to the planet's atmosphere.

This assumption is particularly important to consider in the case of water, where we assume all ice on accreted planetesimals gets added to the final water and ice budget of the planet - an input for the internal structure model. If vaporization of water ice during planetesimal accretion was considered, a portion of this would be lost to water vapour that either remains in the planet's atmosphere or is recycled back into the disk. Thus, the planet ice mass fractions we calculate are upper limits for our model.

However, it has been shown that that up to km-sized planetesimals can accrete directly onto a planetary core without mechanical/thermal disruption in its atmosphere for envelope masses up to 3 $M_{\oplus}$ (Alibert, 2017). This is well within the super Earth atmospheric-mass regime, and in this circumstance ice in accreted planetesimals can directly contribute to the ice budget of the core. While disruption of accreting solids can be an important factor affecting atmospheric composition and opacity (Thiabaud et al., 2015; Mordasini et al., 2015, 2016), based on the above result of Alibert (2017) we do not expect this to significantly affect our computed super Earth compositions. Additionally, while we do directly calculate the amount of gas accreted onto planets during their formation, we are not focused on accurately predicting their atmospheric compositions as we do not include non-equilibrium disk chemistry effects that are important for gas phase chemistry. Furthermore, our planet adiabatic atmosphere model assumes a hydrogen and helium envelope for which atmospheric composition has no effect.

4.2.3 Planetary Structure Model

Here we present a brief overview of our model of planetary structures. Our approach follows that of many previous works. The complete description is given in appendix B (Appendix B1 for the planetary core structure model, and appendix B2 for the atmospheric structure).

Core Structure Model

We take planet masses, orbital radii, and compositions as directly computed from the Alessi et al. (2020) planet formation model. Planet masses are a combination of all solids and gas accreted during formation, and here we first describe the former.

Taking the approach of many previous works, we model our planetary cores as differentiated spheres composed of three bulk materials: iron, silicate ($MgSiO_3$) and water ice (Valencia et al. (2006), Seager et al. (2007), Zeng & Sasselov (2013)). Since the pressures inside a planetary core are usually very high ($>10^{10}$ Pa), we assume that pressure effects dominate over temperature effects on the density of our materials, and therefore ignore temperature effects in our model. The exception to this is the water ice component that demands a temperature-dependent treatment, as it is well-known to undergo a complex series of phase transitions with changes in temperature and pressure resulting in sharp discontinuities in density that cannot be replicated by a polytropic equation of state (Zeng & Sasselov (2013), Thomas & Madhusudhan (2016)).

We therefore follow the approach of Zeng & Sasselov (2013) and assume a relationship between ice temperature and pressure by following the liquid-solid phase boundary of water. We consider only solid phases that occur along the melting curve, including Ice Ih, III, V, and VI (Choukroun & Grasset (2007)), Ice VII, (Frank et al. (2004)), Ice X and superionic ice (French et al. (2009)). This EOS employs a combination of high-pressure experimental results (diamond anvil cell testing, see Frank et al. (2004)) and theoretical calculations (Quantum Molecular Dynamics simulations, see French et al. (2009)).

For the solids in the core of our planets (irons and silicates), where the temperature-independent assumption is valid, we adopt the EOS used by Zeng & Sasselov (2013). We include minor corrections for high pressure regions from Fei et al. (2016).

Atmospheric Structure Model

We now briefly review our treatment of atmospheric structure, and refer the reader to appendix B2 for further details. We adopt the tabular Chabrier et al. (2019) hydrogen and helium EOS to model the atmospheres of our planets.

While, in principle, we could track the composition of accreted gas similar to our handling of solids, our disk chemistry model is not focused on accurately predicted abundances of gaseous species as it does not account for photochemistry or other non-equilibrium effects. Regardless, atmospheres acquired from the disk will be composed almost entirely of hydrogen and helium, with other secondary gases being substantially less abundant. We therefore treat our atmospheres as being composed entirely of a pure hydrogen-helium mix at the Solar-abundance ratio[3], and neglect other trace elements for simplicity.

We also assume grey (wavelength-independent) opacities when computing atmospheric structure. Following these assumptions, we use tables of Freedman et al. (2008) to determine Rosseland-mean opacities throughout planets' atmospheric temperature-pressure profiles. This opacity table corresponds to a Solar-metallicity star, which is suitable for our purposes as we assume atmospheres are composed entirely of hydrogen and helium at Solar abundance.

A more rigorous opacity treatment would be to use a semi-grey model (i.e. Guillot (2010)), which has been shown to systematically produce larger planetary radii than those computed resulting from our grey-opacity assumption (Jin et al., 2014). However, this difference in planetary radii resulting from different opacity treatments is significant only for planets on particularly small orbital radii $\lesssim 0.1$ AU (Mordasini et al., 2012b), and is generally a small difference ($\lesssim$1%) for larger planetary orbits. We comment on how our assumption of grey atmospheric opacities affects our results in section 4.4.3.

We recall that planetary (transit) radii R_p are defined at the $\tau = 2/3$ optical depth surface in the atmosphere. When modelling the atmosphere, thermal effects from stellar heating and internal luminosity become significant and we no longer use a zero-temperature approach as was done for planetary cores. We use a simple grey model for our atmosphere with both adiabatic and radiative zones.

The internal luminosity of our planets is generated entirely from radioactive decay of isotopes

[3]We note that the ratio of hydrogren:helium does not change regardless of the disk metallicity considered, as these abundances are always scaled with metallicity such that the ratio is preserved.

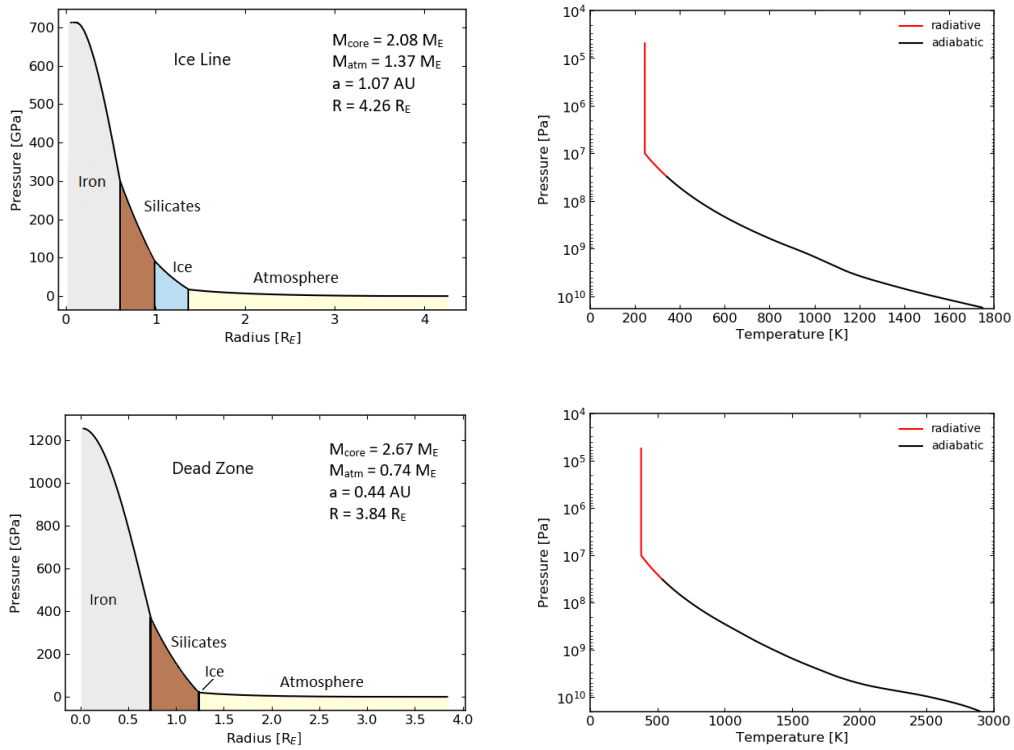

Figure 4.4: The computed structure for a sample ice line (top) and dead zone planet (bottom). On the left we show the pressure in each layer of the planet, and on the right the pressure-temperature profile of its atmosphere, with the radiative zone shown in red, and the convectively-stable region in black. Core masses, atmosphere masses, semi-major axes, and planet radii are listed in the figure. The ice line core composition is 27.1% iron, 37.9% silicate, and 35.0% water ice; much more ice-abundance than that of the dead zone planet: 43.5% iron, 56.1% silicate, and 0.4% water.

in the silicate layer, and assumes no gravitational contraction. Internal heating therefore scales with bulk silicate abundance as calculated directly from combining our planet formation and disk chemistry models.

In Figure 4.4 we present our first result of the paper, in which we contrast the computed structure for a sample ice line and dead zone planet. We compare the pressure profile of the two planets, as well as the pressure-temperature profile of their atmospheres. We highlight the two atmospheric zones (radiative and convective), and the vertical line in the atmosphere profiles corresponds to a radiatively stable, isothermal surface layer.

We note that despite the dead zone planet having a slightly lower total mass than the ice line planet, it has a higher core pressure. It also has a larger range of temperatures in its atmosphere.

This is due to a combination of its smaller semi-major axis, exposing it to a higher stellar flux, and also an effect of its higher core mass and core silicate content giving it a higher internal luminosity. Both planets also have a very similar core radius, despite the dead zone having a core that is 0.59 $M_\oplus$ more massive. This is because the ice line planet's core, while being less massive overall, has significantly more ice resulting in a lower average density.

4.2.4 Atmospheric Mass-Loss Model

As we are modelling planetary structure immediately after formation, they typically have accreted a gas envelope with mass determined in our planet formation model. It remains a question, however, what portion of the gas accreted from the disk will be retained by the planet as it cools. As gases are the lowest-density materials acquired during formation, they will have a much larger impact on planetary radii than materials contributing to the planet's core. Atmospheric loss, or *evaporation*, after the disk phase is therefore a crucial consideration when determining planet radii.

We model atmospheric mass loss to be driven through UV and X-ray photoevaporation from the host star, combining models of Murray-Clay et al. (2009) and Jackson et al. (2012), respectively. Power-law fits to measured integrated fluxes of young, Solar-type stars are used to determine the incident X-ray and EUV fluxes (Ribas et al., 2005). In this calculation, energy from the received EUV flux on each planet is converted into work that removes gas from the planet, driving mass loss. We initiate the atmospheric mass-loss model immediately after disk photoevaporation at each disk's lifetime which is a stochastically-varied parameter in our populations. We compute mass loss for each planet to a time of 1 Gyr as we find that after several 100 Myr, mass loss rates are negligible as planets have either become stripped, or will retain their remaining atmosphere. A complete description of our treatment that follows previous works is included in appendix C.

In figure 4.5 (left), we show the effect of our photoevaporation model on a sample of short-period planets selected from our $R_0 = 50$ AU population run. The planets were chosen to highlight the significant effect evaporation can have on planets with small semi-major axes. Immediately post-formation, prior to the effects of evaporation, super Earths in the 1-10 $M_\oplus$ mass range have larger radii than the observed data due to their inflated atmospheres. We see that evaporation acts to reduce these planets' radii, also slightly reducing their masses as the cores are stripped of gas, such that after the Gyr of calculated evolution, they compare well with the observed planets on the M-R diagram.

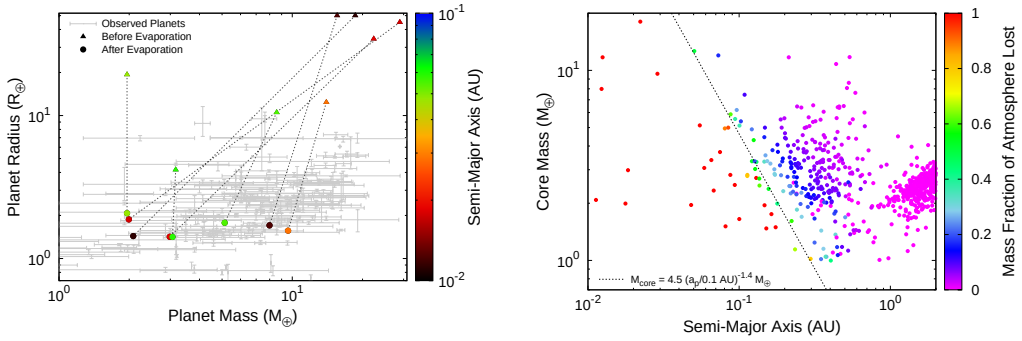

Figure 4.5: The effect of our atmosphere evaporation model is shown.
Left: A sample of short-period planets selected from the 50 AU population is used. Planets' initial and final masses and radii are shown, with colour indicating semi-major axes. The observed data is shown for comparison. Some of the chosen planets form as Neptunes with initial masses $\gtrsim$ 10 $M_\oplus$, but lose their atmospheric mass as they evolve to populate the super Earth region of the M-R diagram and compare well with observed data.
Right: Atmosphere mass loss fraction is plotted for the full $R_0 = 50$ AU run's super Earth and Neptune population. Effects of the two key input variables to the evaporation model are shown - core mass and orbital radius - with evaporation being most extreme at small core masses (low surface gravity) and small a_p (high XUV flux). We show a fit to the planets with roughly 60 % of their atmospheres stripped to show the dependence of the mass-loss model on core mass and orbital radius.

A subset of the planets shown in figure 4.5 form as Neptunes with initial masses of 10-30 $M_\oplus$. These planets have atmosphere masses $\gtrsim$ 50 % of the planet's total mass immediately after disk dissipation. Due to the close proximities to their host stars (with $a_p \simeq 0.01$ AU), evaporation has a substantial effect. In these cases, planets lose a significant fraction of their masses and radii from evaporation. This results in these planets, after evaporation, populating the super-Earth region of the M-R diagram, comparing well with the observed data.

We note that this sample of planets was chosen to be illustrative, and evaporation will generally have a less significant effect on planets orbiting well outside of a few 0.1 AU. This is particularly true in the case of Neptunes, where a significant amount of ongoing mass loss needs to be sustained to strip their cores, and the extreme effects shown in figure 4.5 will only apply to the shortest-period planets. Nonetheless, evaporation can indeed have a significant effect on planet masses and radii, even changing a planet's class from a Neptune immediately after formation to a super Earth after a Gyr of post-disk evolution. It is therefore an important inclusion when comparing to both the observed M-R and M-a diagrams.

In figure 4.5 (right), we show the effect of evaporation on the complete $R_0 = 50$ AU super

Earth and Neptune population. We plot the fraction as dependent on two key input parameters: the planets' orbital radii (which sets the XUV flux), and their core masses (which sets the surface gravities). As previously discussed, within $\sim$ 0.1 AU evaporation is extreme and typically results in total stripping. We find that evaporation typically has minimal effect outside $\sim$ 0.8 AU. In the intermediate range of orbital radii, $\sim$ 0.1-0.8 AU (between entirely stripped cores at small a_p and no stripping at larger a_p), the fraction of atmosphere lost due to photoevaporation depends upon both the core mass and orbital radius of the planet. Overall, most of the population loses less than 20 % of its accreted atmospheric mass.

To quantify the dependence of the atmospheric mass loss model on core mass and orbital radius, we obtain a core mass ($M_{\rm core}$) - orbital radius fit to planets with $\sim$ 60 % of their atmospheres stripped, resulting in,

$$M_{\rm core} = 4.5 \left(\frac{a_p}{0.1\,{\rm AU}}\right)^{-1.4} {\rm M}_\oplus \, . \tag{4.3}$$

We select and fit to planets with roughly 60 % of their accreted atmospheric mass stripped as this is an indicator of planets that are significantly impacted by the mass-loss model. A different choice of atmospheric mass loss fraction would not change the $M_{\rm core} \sim a_p^{-1.4}$ scaling, but would affect the factor 4.5 $\rm M_\oplus$ in equation 4.3.

Jin & Mordasini (2018) find a scaling of $M_{\rm core} \sim a_p^{-1}$ for their atmospheric mass-loss model[4]. We find that our fit has a steeper scaling of $M_{\rm core}$ with a_p, indicating that our mass-loss model strips planets of a given core mass over a smaller range of orbital radii. We identify different assumptions for the atmospheres' opacities as the reason for the different scalings and effectiveness of photoevaporative mass loss between the two models. Our model uses a grey atmospheric opacity, while Jin & Mordasini (2018) use a semi-grey opacity, resulting in larger planet radii (Jin et al., 2014). This causes atmospheric mass-loss to be more significant due to planet atmospheres filling out their Roche lobes over a larger range of orbital radii.

[4]The Jin & Mordasini (2018) fit indicates the most massive cores at a given a_p stripped of an atmosphere. It still serves a similar purpose to our fit, however, indicating how the mass-loss model depends on $M_{\rm core}$ and a_p.

4.3 Metallicity-Fit Disk C/O & Mg/Si Ratios: M-R Diagrams and Super Earth Abundances

We now turn our attention to planet compositions and mass-radius diagrams for the main disk chemistry run where the C/O and Mg/Si ratios are varied in accordance with fits obtained from Suárez-Andrés et al. (2018). We remind the reader that this disk chemistry run uses stellar data to correlate these chemical ratios with disk metallicity - a parameter incorporated into our population synthesis calculations. We separately discuss composition results for the 50 AU and 66 AU populations.

We refer the reader to appendix D for individual effects of both elemental ratios, held constant with metallicity, on planet populations.

4.3.1 50 AU Population

The $R_0 = 50$ AU population from Alessi et al. (2020) leads to the largest zone 5 planet population compared to other initial disk radii. We recall from figure 4.3 (left panel) that the super Earths from this population are predominantly formed in the ice line and dead zone traps, with only a small amount arising from the heat transition. Additionally, we note that the ice line typically forms super Earths with orbital radii outside 0.8 AU, while those formed in the dead zone have smaller orbits. There is a clear transition between super Earths formed in the dead zone to those formed in the ice line between 0.6-0.8 AU in this population.

In figure 4.6, we show the distributions of solid abundances for super Earths formed in the ice line and dead zone traps from the 50 AU population - the traps contributing the vast majority of zone 5 planets in this population. We do not show the corresponding distribution for the super Earths formed in the heat transition since they contribute very little to this population's zone 5 planets.

The ice line planets from this population accrete a significant portion of their solid mass as ice, as these planets form at the ice line for the entirety of their trapped type-I migration phase. Their average ice abundance is $\simeq 37.5$ %, with a spread of $\gtrsim 5$ % in ice content across all super Earths formed in this trap. The range of ice contents in the population's super Earths is primarily caused by the corresponding range in the disks' ice budgets, set by the C/O and Mg/Si ratios varied in correlation with disk metallicity within the population. As discussed in section 2.2, low values of the C/O ratio and high values of Mg/Si lead to larger water contents in the disk. The spread we see in

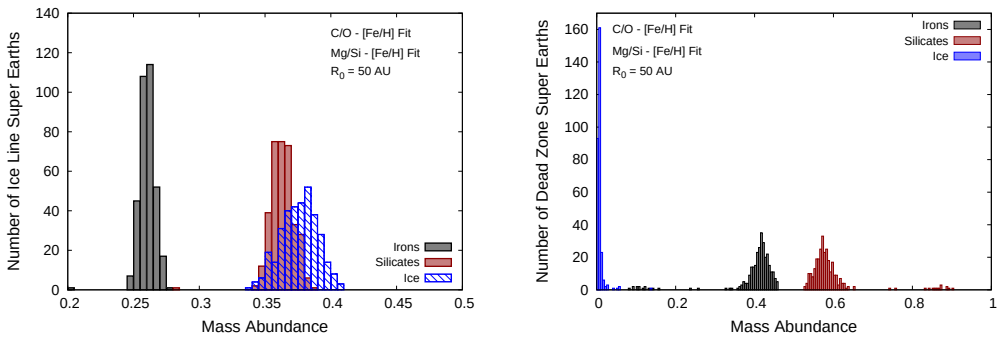

Figure 4.6: We show solid abundance distributions for super Earths formed in ice line (left) and dead zone (right) in the $R_0 = 50$ AU population using the disk chemistry run with metallicity-fit C/O and Mg/Si ratios. Ice line planets have a $\simeq 37.5$ % ice mass abundance, with a ~ 5 % spread in all three components' abundances. Dead zone planets are quite dry, with ice mass abundances $\lesssim 0.2$ %, and a ~ 5 % spread in irons and silicates with minimal variance in ice abundance.

the composition of ice line super Earths is therefore primarily due to the range of the disk elemental abundances explored.

Type-II migration is a secondary effect on the ice line planets' compositions. The more massive super Earths will have transitioned into the type-II migration regime, with a migration timescale that is initially faster than the migration rate of the ice line trap. These planets will no longer be confined to the ice line trap, and will therefore spend the last portion of their formation time accreting from within the ice line. Since this material will be less ice abundant than the local composition at the ice line, this secondary effect caused by type-II migration will extend the low ice-abundance portion of the distribution in figure 4.6 (left).

In the case of super Earths formed at the ice line, the range seen in iron and silicate percent mass-abundances within the population is *in response to* the range of ice abundances. As shown previously (section 2.2 and figure 4.14) the C/O and Mg/Si ratios do not affect the abundances of irons and silicates throughout the disk, but do result in changes to the disk's water abundance. This therefore causes a variation in the planets' ice mass fractions, and in response to this the mass fractions of irons and silicates change such that each planet's total solid composition sums to unity even though the local disk abundance of these two components is not affected by C/O or Mg/Si.

In figure 4.6, right, the solid abundance distribution for the dead zone super Earths from the $R_0 = 50$ AU population is shown. These planets typically are quite ice-poor compared to the ice line planets, with the majority of dead zone super Earths having $\lesssim 0.2$ % of their solid mass in ice. This

is a result of the location of the trap itself within the disk. While the dead zone is initially in the outer disk, it quickly migrates within the ice line, existing well within the ice line for the majority of the disk's evolution (times $\gtrsim$ a few 10^5 years). Planets forming at the dead zone therefore spend most of their formation accreting solids devoid of ice. There is a small amount variation here, with planets in very short-lived disks having larger ice abundances from solids accreted early in the disk evolution when the dead zone was outside the ice line. However, these planets can be seen as outliers, with the vast majority having quite small ice abundances and little variation across the population.

We also notice that there is a $\gtrsim$ 5 % range in iron and silicate mass abundances in the dead zone planets. Whereas in the case of the ice line planets, the variation in these components were in response to the different ice contents in the population's super Earths, there is no comparable range in ice contents for dead zone super Earths. Therefore, the range of iron and silicate abundances on these planets must be caused by variations in the disk abundances.

Shown in figure 4.14 (Appendix A), the iron and silicate abundance profiles are constant except for the innermost region of the disk, $\lesssim$ 1 AU, where variance is seen. This is indeed where the dead zone planets accrete due to the trap quickly evolving to exist in the innermost region of the disk. Planets forming in the dead zone are therefore accreting solids from the region of the disk where iron and silicate abundances have radial dependence, which results in the range of iron and silicate mass fractions seen in figure 4.6, despite the population of planets having minimal spread in ice fractions.

In figure 4.7, we show the M-R distribution for zone 5 planets in the 50 AU population both before and after atmospheric photoevaporation are accounted for. The colour scale indicates the planets' semi-major axes, so as to indicate the effect of atmospheric evaporation. We also include the observed distribution in this planet mass range for comparison. We again notice the difference in typical orbital radii of planets formed in the ice line and those formed in the dead zone. The former results in planets that typically orbit at $\sim$ 1-2 AU, and the latter in planets on smaller orbits $\lesssim$ 0.5 AU.

The three contours on the diagrams in figure 4.7 correspond to different core-only compositions: that of the mean ice line core composition, the mean dead zone core composition, and lastly a pure iron core. The contours have the following power-law form,

$$R_p \sim M_p^{\beta} \, , \tag{4.4}$$

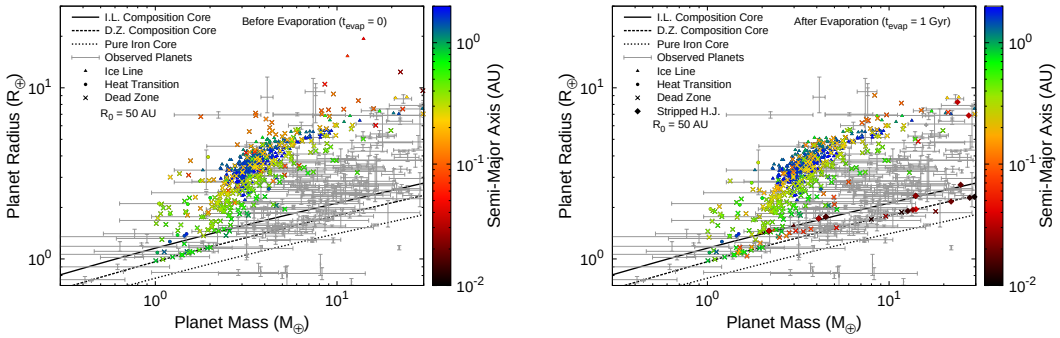

Figure 4.7: The resulting M-R distribution for super Earths in the $R_0 = 50$ AU population is shown before (**left**) and after (**right**) atmospheric photoevaporation is included. Data point shapes indicate the trap they formed in, and colour indicates their orbital radii. We have highlighted stripped hot Jupiters (H.J.) that appear in the post-photoevaporation (right) distribution; their masses initially exceeding the zone 5 range and not appearing in the before photoevaporation (left) panel. We include three core only (no atmosphere) M-R contours corresponding to different core compositions: mean ice line composition, mean dead zone composition, and a pure iron core. For comparison, we also show the observed distribution. Evaporation is seen to completely strip planets at $\lesssim 0.1$ AU of their atmospheres.

where the power-law index β=0.261 and 0.269 for the ice line and dead zone contours, respectively. This has a good correspondence with the power-law index given in Chen & Kipping (2017), $\beta = 0.2790^{+0.0092}_{-0.0094}$, fit to observed masses and radii of Terran worlds with no atmospheres.

Considering our M-R distribution prior to computing atmospheric evaporation, we observe that the majority of planets in this mass range form with atmospheres that contribute a significant fraction of their radii in our population model. This is indicated in the left panel of figure 4.7, as the majority of planets have radii significantly above their core-only radius as indicated by the contours. Only a small number of planets form with no atmosphere (directly on the core-only contour), and those that do are the lowest-mass super Earths formed in the dead zone trap.

This has a significant effect on our comparison to the data, before accounting for photoevaporation. Planets with masses $\lesssim$ 2-3 $M_\oplus$ are typically denser with less atmospheric mass, and our computed M-R distribution compares reasonably well with the observed data in this mass range. However, at larger masses, planets have accreted enough atmospheric mass to greatly increase their radii. In turn, the population's planets have systematically larger radii than the majority of the observed data. The discrepancy with the data is more extreme in the case of Neptunes (planet masses $\gtrsim$ 10 $M_\oplus$) whose radii are well above the observations. These results indicate that (prior to

including photoevaporation) our model forms planets with larger radii than most of the observed data due to the amount of gas they accrete during the disk phase. It will therefore be important to include a mechanism to reduce their radii (i.e. photoevaporative mass-loss) in order to achieve a better comparison with the data.

We show the 50 AU population after the evaporation model is calculated in figure 4.7, right panel. We see immediately that the evaporation model strips the atmospheres of planets with smallest orbital radii ($\lesssim$ 0.1 AU) as more planets lie directly on the core radius contour. More dead zone planets, as opposed to ice line planets, are completely stripped as they have smaller orbital radii. In addition, the evaporation model reduces the highest radii planets from the original population, removing several of the "outliers" that lay significantly above the observed distribution.

We identify the subset of stripped planets in figure 4.7, right, that originally formed as hot Jupiters (zone 1 planets) and underwent significant mass loss from photoevaporation, evolving into the super Earth - Neptune mass range. These planets formed with masses $\sim$ 30-100 $M_\oplus$ (ie. not the most massive gas giants formed in the population) at particularly small orbital radii $<$ 0.1 AU. In terms of the entire hot Jupiter population, we find that most planets are unaffected by atmospheric loss, and only $\sim$ 10 planets that fit the low mass and low orbital radius criteria are stripped to contribute to the super Earth and Neptune population after photoevaporation.

Extending the mass-loss calculation to the hot Jupiters formed in our population is important, however, as it adds more low radius planets at planet masses $>$ 3 $M_\oplus$, improving our comparison to the observed data. This also has implications for our resulting M-a distribution, which we discuss later in this section.

The evaporation model certainly improves our population's comparison to the observed data, as it reduces the radii of some planets that originally lied at large R_p. However, the evaporation model does not have a large effect on the majority of planets in the population with orbital radii $\gtrsim$ 0.2 AU. Since this is true for nearly all the ice line planets and a large portion of the dead zone planets, it remains the case that when comparing with the data, most planets with masses $\gtrsim$ 2-3 $M_\oplus$ have larger radii than the majority of the observed data points at a given planet mass, even after photoevaporation is considered.

In figure 4.8, we link our computed M-R distribution with planet composition. The colour scale now indicates planets' ice contents, the main indicator of planets' solid compositions, and the population is shown post-evaporation. As previously discussed, the ice contents of super Earths

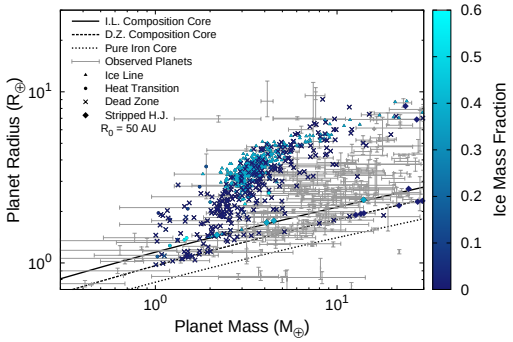

Figure 4.8: The mass-radius diagram is shown for the super Earths in the 50 AU population, with colour indicating the planets' ice contents and point shape the planet trap they formed in, or if the planets were stripped hot Jupiters. We use the same M-R contours from figure 4.7 (a mean ice line-composed core, a core with mean dead zone composition, and a pure iron core), along with the observed data for comparison.

formed in our model is bimodal, with dead zone planets being nearly devoid of ice and ice line planets accreting $\sim$ one-third of their solid mass as ice. Since most of the stripped cores are dead zone planets (due to their lower orbital radii), this results in most planets without atmospheres in this population being ice-poor.

Both the dead zone and ice line contribute to the majority of planets that are unaffected by evaporation with masses $\gtrsim$ 2-3 AU. We see that, despite these planets having different core compositions, and thus different core radii, they occupy the same region of the M-R diagram. We therefore conclude that planet atmospheres have the largest effect on a planet's overall radius, and can hide most differences in core radii derived from solid compositions. The effect of solid compositions on planet radii can only be seen in the case of completely stripped cores, which would lie near their respective M-R contours. In this case, ice line cores would exist at larger R_p than dead zone cores due to their different ice contents. However, as most planets in the population retain their atmospheres this is not the case (particularly for ice line planets).

In figure 4.9, left, we show the M-a distribution of zone 5 planets for the 50 AU population, with data points' colours indicating their ice mass fraction. The distribution is shown after photoevaporation, so planet masses are updated with respect to the amount of gas that was lost. Following the results shown in figure 4.6, we again see that planets formed in the dead zone are ice-poor, while those formed in the ice line have significant ice mass fractions. Additionally, the small number of

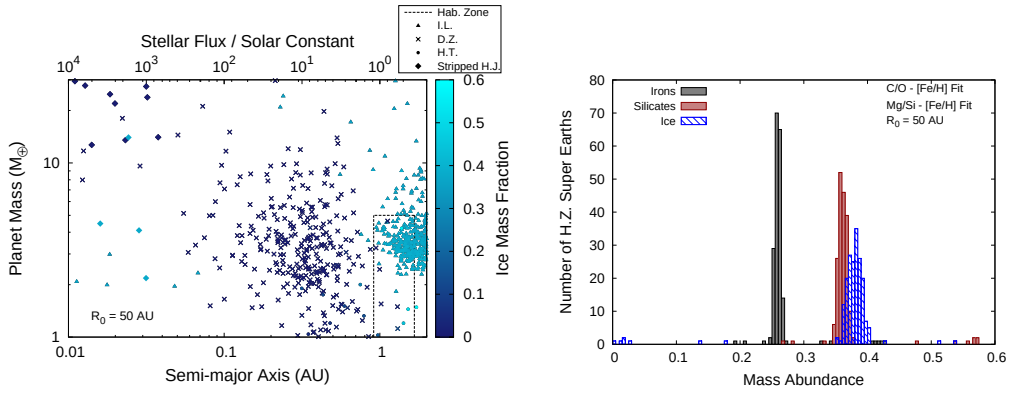

Figure 4.9: **Left:** The mass semi-major axis distribution is shown for the $R_0 = 50$ AU population over the extent of zone 5. Colours of data points indicate the planets' ice content, with point shape corresponding to the trap they formed in. We separately highlight stripped hot Jupiters (H.J.) that, following photoevaporation, evolve to become short-period super Earths or Neptunes. **Right :** Solid abundance distribution is shown for all planets that populate the Kopparapu et al. (2014) habitable zone. This subset of the population is predominantly formed in the ice line, so the distribution mainly resembles the overall population's ice line super Earth distribution, with a small amount of outliers formed in other traps.

heat transition super Earths show a range in ice mass fractions - a result that will become more apparent in the 66 AU population.

We again identify the subset of atmosphere-stripped hot Jupiters (zone 1 planets) that evolved into the super Earth - Neptune mass range in figure 4.9 (left). These planets formed as sub-Saturns at small orbital radii, corresponding to a small fraction ($\sim$ 10 planets) of the entire hot Jupiter (zone 1) population. These planets add to the super Earth population that was directly formed (i.e. prior to photoevaporation), leading a total zone 5 (super Earth & Neptune) formation frequency of 52.7% after photoevaporation is included. This corresponds to roughly a 1% increase in the zone 5 population beyond what was formed directly during the disk phase, having a frequency of 51.7% as in figure 4.3, left.

Evaporation has the largest effect on planet masses when planets form at small orbital radii, and can result in total atmospheric stripping from planets at $a_p < 0.1$ AU. At these orbital radii, our planet formation model does not directly form super Earths, but does form planets having masses $\gtrsim 10$ M$_\oplus$. In particular, the Neptunes (10-30 M$_\oplus$) and sub-Saturns (30-100 M$_\oplus$) that form at these small a_p have their masses greatly affected by photoevaporation, as they are not massive enough to retain their accreted atmospheres. This results in partial or complete stripping of these planets by the high FUV flux they receive, and their masses evolve to super Earths (1-10 M$_\oplus$).

On this basis, we see that photoevaporation may be a very important way of forming super Earths at small orbital radii (0.01 - 0.1 AU). Planets can first form as Neptunes or sub-Saturns at small a_p, accreting significant gas from the disk phase. Following this, photoevaporation strips their atmospheres, reducing their masses to the super Earth range of 1-10 $M_\oplus$. This is a region of the M-a diagram that our planet formation models were unable to directly populate (Alessi & Pudritz (2018) and Alessi et al. (2020)) before atmospheric mass loss was considered. Our formation model, setting the conditions for the post-disk phase evolution, produces sufficient Neptunes and sub-Saturns at these small a_p that are greatly affected by atmospheric mass loss and evolve to become short-period super Earths.

From a formation standpoint, super Earths are traditionally viewed as failed cores in the core accretion scenario, as their gas accretion timescales surpass the disk lifetime and their formation halts at moderate masses. Adding atmospheric evaporation into our models adds another route by which super Earths can form. In this case, they indirectly form; first by accreting a fairly substantial amount of gas (i.e. a Neptune or sub-Saturn) at small orbital radii, with subsequent atmospheric stripping from photoevaporation evolving the planets' masses to become super Earths. This is only a viable formation scenario for planets at small $a_p \lesssim 0.1$ AU, whereas the former "direct" formation scenario can take place over a wider range of semi-major axes.

Typically, in all but these planets at small a_p, evaporation does not have a large effect on planet masses even in the case of completely stripped cores. As a small atmosphere mass can result in a large increase in planet radius, stripping typically has a much greater effect on R_p than M_p. Therefore, the M-a diagram after evaporation is largely unchanged (comparing with figure 4.3), aside from Neptunes and sub-Saturns within 0.1 AU.

We see in figure 4.9 that there is a clear division in orbital radius at roughly 0.8 AU between planets formed in the dead zone at small orbital radii, and those formed in the ice line at larger separations. In terms of compositions, this translates into a separation in orbital radius between ice-rich and ice-poor super Earths, with the majority of the former orbiting at 1-2 AU from their host stars, and the latter mostly orbiting within 0.8 AU.

An intriguing question for astrobiology is what the composition of habitable super Earth planets are. We can answer this, for our models, by examining the composition of super Earths that receive a flux comparable to that of habitable planets in our Solar system. We use the results of Kopparapu et al. (2014) to define the habitable zone region in figure 4.9. Although this habitable zone calculation

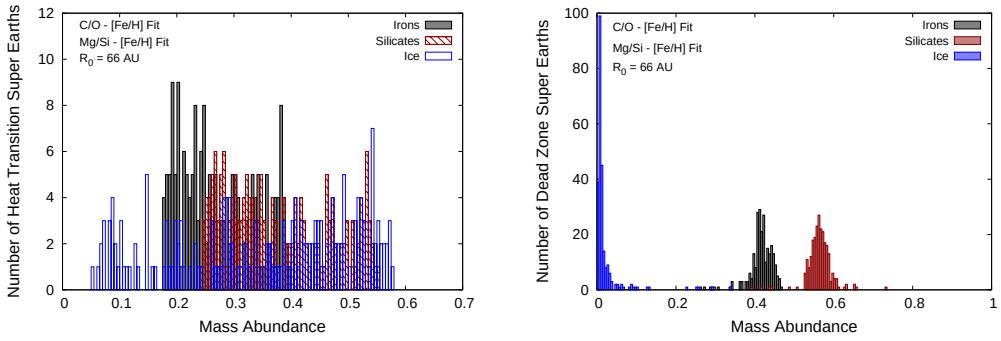

Figure 4.10: We show solid abundance distributions for zone 5 planets formed in the heat transition (left) and dead zone (right) in the $R_0 = 66$ AU population, using the disk chemistry run with metallicity-fit C/O and Mg/Si ratios. Heat transition planets show a large range in abundances of all three components, with ice fractions ranging from ~ 5 % to 58 %. Dead zone planets show a similar composition distribution to the 50 AU population, with most of the planets being dry ($\lesssim$ 0.2 %) and a ~ 5 % spread in iron and silicate abundances.

is based upon assuming an Earth-like planet, it does consider the effects of different atmosphere composition and a range of planet masses between 0.1-5 $M_\oplus$. We use their presented ranges of effective incident flux corresponding to a Solar stellar temperature to define the habitable zone, as our planet formation model assumes a Sun-like star. This leads to a habitable zone orbital radius range of 0.91 AU $\leq a_p \leq$ 1.67 AU.

In figure 4.9, right, we focus, accordingly, upon the solid abundance distribution of super Earths occupying the habitable zone from the 50 AU population. We see that the majority of these planets formed in the ice line - a result of nearly all super Earths with $a_p \gtrsim 1$ AU formed in the ice line in this population. Therefore, the habitable zone planets are almost entirely a subset of the total ice line population. Their solid abundance distribution largely resembles that shown for all ice line planets (figure 4.6, left) with a small number of outliers formed in the other two traps having different compositions.

4.3.2 66 AU Population

We now show composition and radius results for the zone 5 planets formed in the $R_0 = 66$ AU population, using the disk chemistry run considering metallicity-fit C/O and Mg/Si ratios. The super Earths in this population are primarily formed in the dead zone and heat transition, with only a small amount formed in the ice line. While the 50 AU population saw a clear separation between

the dead zone and ice line super Earths, there is substantially more overlap between the dead zone and heat transition super Earths within the 66 AU population. In comparison to the 50 AU case, the dead zone super Earths in the 66 AU population form with slightly larger orbital radii, and should be less-affected by evaporation. Additionally, there are more low-mass super Earths (planet masses 1-3 $M_\oplus$) in this population compared to the 50 AU case.

In figure 4.10, we show solid abundance distributions of the 66 AU population's super Earths, separately plotting those formed in the heat transition and dead zone traps. We do not include a distribution for the small number of super Earths formed in the ice line in this population.

The heat transition planets show a large range in ice abundance from 5 % up to 58 %. This large variance in super Earth abundance is a result of the interesting evolution of the trap itself, which typically begins outside the ice line for the first $\sim$ 2-3 Myr before evolving to exist inside the ice line at later stages of disk evolution (in sufficiently long-lived disks). The heat transition therefore can sample solids across a wide span of orbital radii throughout the disk, accreting both ice-rich and ice-poor material.

The large range of ice mass fractions on super Earths formed in the heat transition is a consequence of accretion both outside and inside the ice line, with the more ice-poor super Earths spending more of their formation accreting solids inside the ice line. Within a disk's evolution, the relative amount of time the heat transition exists outside the ice line to inside the ice line is dependent on disk parameters, spending more time inside the ice line in disks with lower surface densities (lower mass and larger radius) and longer lifetimes. Since disk initial mass and lifetime are both varied parameters in the population, this leads to the heat transition spending different relative amounts of time outside and inside the ice line in different disks, and to the large range of ice abundances encountered in this subset of the super Earth population.

The heat transition is able to form the most ice abundant super Earths in our models - even larger ice mass fractions than those resulting from formation in the ice line. This occurs in the case where solid accretion occurs entirely outside the ice line, in the region of the disk with maximum ice abundance. This would pertain to disks with sufficiently *short* disk lifetimes such that the heat transition does not evolve to within the ice line.

As was the case for the ice line planets in the 50 AU population, the large variances seen in the mass abundances of irons and silicates are in response to the range of mass abundance in ice within the population. This is because the heat transition planets accrete solids from outside $\sim$ 1 AU - the

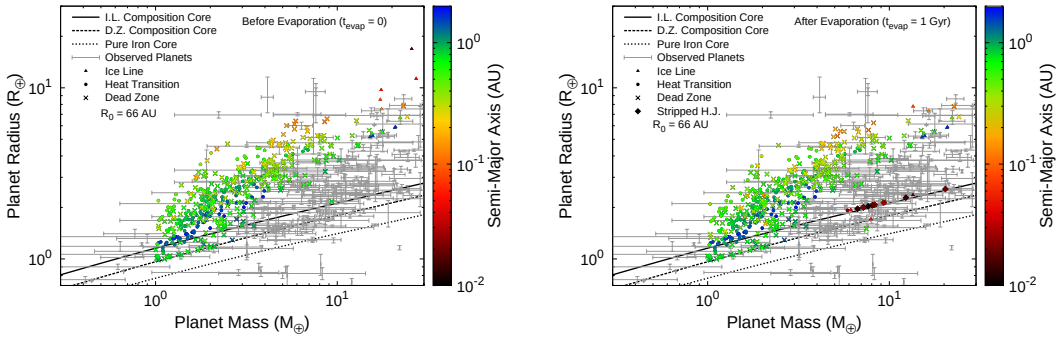

Figure 4.11: The $R_0 = 66$ AU population's M-R distribution is shown before (**left**) and after (**right**) atmospheric photoevaporation is calculated. Data point colour indicates planets' orbital radii, with shape indicating the planet trap they formed in or if the planets are stripped hot Jupiters (H.J., in the after photoevaporation panel). The core-only contours are the same as in figure 4.7: mean ice line composition (for the 50 AU population), mean dead zone composition, and a pure iron core. Stripping plays a smaller role here than in the 50 AU population due to planets having larger orbital radii.

region of the disk where iron and silicate abundances show no radial variation.

The distribution of dead zone planets in the 66 AU population is very similar to that of the 50 AU population. As expected from our previous results, these planets are the most ice poor super Earths formed in the populations, typically having ice mass fractions less than 0.2 %. Additionally, there is a $\gtrsim 5$ % spread in iron and silicate mass abundances despite minimal variation in ice mass fraction. This is caused by the dead zone super Earths accreting from the inner region of the disk ($\lesssim 1$ AU) where the iron and silicate abundances show variation with orbital radius.

In figure 4.11 we show the M-R distribution for zone 5 planets in the 66 AU population, both before and after atmospheric evaporation is calculated. We include the same core M-R contours from figure 4.7: cores with the mean ice line composition from the 50 AU population, and cores with the mean dead zone composition. As we have shown, the heat transition planets formed in this 66 AU population show a wide range of solid compositions that no individual mass-radius contour can characterize. We therefore show the contour corresponding to the mean ice line composition from the 50 AU population to indicate where ice-rich cores with no atmospheres would lie.

The colour scale shows that planets formed in the heat transition and dead zone traps have similar orbital radii, typically outside a few tenths of an AU. In contrast to the 50 AU population, there are fewer planets at very small orbital radii $\lesssim 0.1$ AU, so evaporation plays a less significant

role.

As was the case with the 50 AU population, most planets form in this $R_0 = 66$ AU run having accreted enough atmosphere to significantly contribute to their overall radii. This is seen in the "before evaporation" (left) panel of figure 4.11, as most planets lie well above the core-only contours.

We also find the same conclusion here that planets in the 1-3 $M_\oplus$ range compare quite well to the observed data, while those at higher masses accrete sufficient gas such that their radii are larger than the bulk of the observed distribution. However, it is interesting that in the 66 AU population, the planets with masses $\gtrsim 3$ $M_\oplus$ generally have smaller radii and compare better to the data than those from the 50 AU population. We notably form less planets with extremely large R_p in the 66 AU population that lie well above all of the data at a given M_p as we saw in the 50 AU population.

The 66 AU population is also skewed to lower planet masses than the 50 AU run. As a larger portion of the 66 AU population lies in the 1-3 $M_\oplus$ range, there is a somewhat better fit to the observed data even before evaporation is included.

Turning to the right panel of figure 4.11, we examine the 66 AU population's M-R distribution after atmospheric evaporation has been calculated. We see that only a small number of planets are stripped in this population, evolving to lie near the core-only radii denoted by the contours. The planets that are stripped typically have orbital radii $\lesssim 0.1$ AU. Since the majority of the population orbits outside a few 0.1 AU, atmospheric evaporation does not result in a significant change to planet radii for all but a small number of of short-period planets that are completely stripped. We do note that some planets at a few 0.1 AU, while not completely stripped, lose some of their atmospheric mass resulting in a $\sim 10\%$ change in their radii.

Additionally, there are ~ 10 planets that originally form as zone 1 hot Jupiters that are significantly affected by atmospheric mass loss, resulting in them evolving to the super Earth mass range (these are highlighted in figure 4.11). This improves our comparison to the observations by contributing more low R_p (stripped) planets at larger masses > 3 $M_\oplus$. Atmospheric mass loss does ultimately improve the 66 AU population's comparison to the data through reducing planets' radii, however most planets that form in this population are unaffected by the atmospheric mass-loss process.

In figure 4.12, we show the M-R distribution for the 66 AU population following the evaporation model, now highlighting planets' solid composition with colour scale indicating their ice mass fraction. We arrive at the same result as we did from figure 4.8 - namely that planet atmospheres play the most significant effect on overall radii, and can hide any differences in solid core radii that arise from

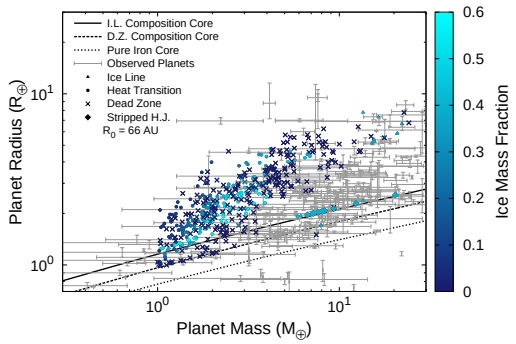

Figure 4.12: The mass-radius distribution is shown for the 66 AU population post-evaporation model. Data point colours indicate the planets' ice mass fractions. Point shapes indicate the trap each planet formed in, or if planets formed as hot Jupiters (H.J.) whose atmospheres were stripped. The same core only M-R contours from figure 4.11 are shown: a mean ice line-composed core (from the 50 AU population), a core with mean dead zone composition, and a pure iron core. There is significant overlap in the M-R distribution between ice-rich and ice-poor cores, indicating that atmospheres play the most significant role in affecting planet radii.

differences in compositions. This is seen from the majority of planets whose accreted atmospheres are retained. These planets occupy the same region of the M-R diagram (well above the core-only contours) regardless of solid composition or the trap they formed in.

Only in the case of the small number of planets with no atmospheres, arising either through no gas accreted from formation or through stripping, do we find radius differences between planets being caused by differences in compositions. These planets are near the core contours on the M-R distribution, and we can clearly distinguish the denser dead zone cores from the heat transition cores at somewhat larger radii as caused by their higher ice mass fractions.

In figure 4.13 (left), we show the 66 AU population's zone 5 M-a distribution, with data point colours indication planets' ice mass fractions. Following the results already discussed for this population, the heat transition planets show a large range in compositions, and typically those orbiting at larger semi-major axes have higher ice mass fractions. This is as a result of heat transition planets with larger a_p typically accreting more of their solids outside the ice line, and therefore being more ice-rich than those with smaller a_p. The dead zone planets all have similar ice-poor compositions, with little variation. The small number of ice line planets are also shown on this figure, with masses in the 10-30 $M_\oplus$ range and therefore can be considered Neptunes. Their solid compositions are very similar to the 50 AU ice line planets, with ice mass fractions of $\simeq$ 0.35-0.4.

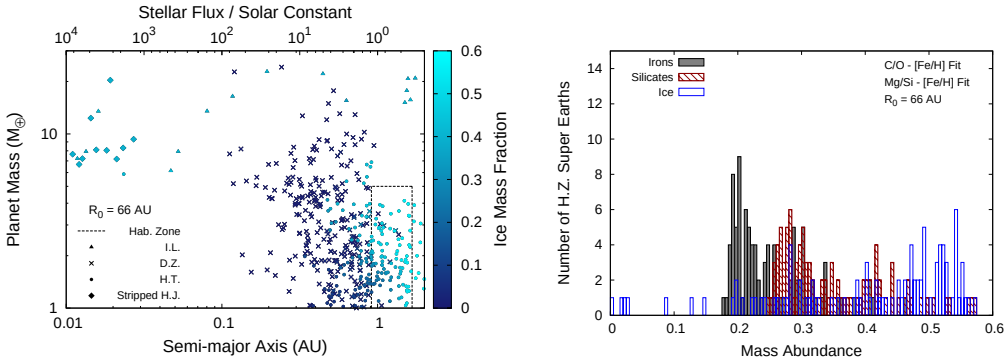

Figure 4.13: **Left:** We show the M-a distribution for the 66 AU population over the extent of zone 5. Data points' colours and shape indicate planets' ice contents and planet traps, respectively. We highlight planets as stripped hot Jupiters (H.J.) that form as zone 1 planets at small a_p, but evolve via photoevaporation into the zone 5 M-a space. **Right :** The solid abundance distribution is plotted for the subset of the population within the Kopparapu et al. (2014) habitable zone. Most of these planets are formed in the heat transition, so the habitable zone planets show a wide range in compositions, similar to the distribution for all heat transition planets.

We arrive at the same result as the 50 AU population; namely that evaporation does reduce the planet masses of Neptunes (10-30 $M_\oplus$) and sub-Saturns (30-100 $M_\oplus$) on small orbits ($\lesssim$ 0.1 AU) to $\lesssim$ 10 $M_\oplus$. We re-iterate our previous conclusion that this is another means of forming super Earths in addition to the "failed core" scenario - planets can first accrete substantial gas during the disk phase, forming as Neptunes or sub-Saturns, and have subsequent photoevaporative mass-loss strip their atmospheres and reduce their masses to that of a super Earth. There is a smaller number of these planets in the 66 AU population than there was in the 50 AU case, however, and they evolve to masses $\gtrsim$ 8-10 $M_\oplus$ instead of filling out the full 1-10$M_\oplus$ super Earth mass range. This results in the short period ($a_p < 0.1$ AU) super Earth ($M_p < 10$ $M_\oplus$) region of the M-a space largely unpopulated in the 66 AU model, even after photoevaporation is included. We contrast this with the 50 AU population (figure 4.9), whereby a number of planets populate this region of the M-a diagram. We further discuss the implications of this result in section 4.4.6.

In the 66 AU population, we generally find little difference in the overall M-a distribution of zone 5 planets before and after evaporation is included (comparing figure 4.3 with 4.13). Outside of $\sim$ 0.1 AU, where most zone 5 planets form in the 66 AU model, evaporation has little effect on planet masses, leaving the overall M-a distribution mostly unaffected. Similar to the 50 AU model, there are $\sim$10 stripped sub-Saturns that evolve into the zone 5 mass-range, increasing the zone 5

population to 32.4% beyond what was formed directly, without considering atmospheric mass-loss (31.7%, see figure 4.3 right). As we found in the 50 AU model, through atmospheric stripping of sub-Saturns, photoevaporation increases the zone 5 formation frequency by $\sim 1\%$ from what formed directly during the disk phase.

In contrast to the 50 AU population, there is significantly more overlap (and no clear transition) in semi-major axis between the dead zone and heat transition super Earths. The orbital radii of dead zone planets in the 66 AU population are typically slightly larger than those formed in the 50 AU population, which leads to some overlap with heat transition planets between 0.3-0.9 AU. Outside of this region at $a_p > 0.9$ AU, super Earths are almost entirely formed in the heat transition.

In figure 4.13, right, we show the distribution of super Earth compositions that lie within the Kopparapu et al. (2014) habitable zone for the 66 AU population. Since the heat transition forms most super Earths outside of 0.9 AU, heat transition planets are the most prominent habitable zone planets in this population, with only a small number of dead zone planets contributing to the population. The solid abundance distribution therefore closely resembles that of the heat transition. This results in a large degree of compositional variety in habitable planets formed in the 66 AU population as a result of planet formation in the heat transition. Whereas in the 50 AU population, the predominance of ice line planets in the habitable zone lead to a quite uniform composition, in the 66 AU case we see a large range of habitable zone super Earth compositions as a result of them mainly being formed in the heat transition.

4.4 Discussion

4.4.1 Comparison with M-R distribution

In both the $R_0 = 50$ AU and 66 AU populations, the models' M-R distributions prior to evaporative evolution compared reasonably with the observations for planet masses $\lesssim$ 2-3 $M_\oplus$. At larger masses, we still achieve a reasonable comparison with the data, but only match well with observed planets with highest radii at a given mass. Planets formed in our populations at masses $\gtrsim 3$ $M_\oplus$ typically have radii that are larger than most of the observed distribution.

We therefore identify masses of about 2-3 $M_\oplus$ as the transition between planets whose radii are predominantly solid cores at lower masses, and planets at higher masses whose radii have a large contribution from a gaseous envelope, following the idea that a small amount of accreted atmosphere

can heavily increase a planet's radius (Lopez & Fortney, 2013). This also raises the question of if there are additional means beyond photoevaporation (as explored in this work) to reduce planet radii, and improve our model's comparison with the M-R distribution.

4.4.2 Reducing Planet Radii: Envelope Opacities of Forming Planets

We first explore this from a formation perspective. As we have identified, planets with masses $\gtrsim 3$ $M_\oplus$ have accreted enough gas during the disk phase such that their radii are larger than most of the observed data. Gas accretion rates in our models are determined by the atmospheres' envelope opacities, $\kappa_{\rm env}$. This parameter was studied in detail in Alessi & Pudritz (2018), where we concluded that a low value of roughly $\kappa_{\rm env}$ $\sim$0.001 cm^2 g^{-1} was required to achieve a reasonable comparison with the observed gas giant frequency - orbital radius distribution. While we did not explore different settings of the envelope opacity aside from our best-fit value (as determined from paper I) in this work, we discuss the impact of this parameter on the M-R relation here.

Higher envelope opacities would lead to two differences in the resulting super Earth population. First, the mass at which gas accretion begins (the critical core mass) would be larger, and this would lead to our "transition mass" (separating core-dominated planets, and those with radii heavily influenced by gaseous envelopes) of 2-3 $M_\oplus$ shifting to higher masses. This would lead to a larger range of small planet masses where radii remain small and maintain a good comparison with the observed distribution. The second effect a higher envelope opacity would have is that once gas accretion begins, its rate would be reduced compared to a smaller envelope opacity. Less gas on super Earths would lead to smaller planet radii above the "transition mass", which would also improve our comparison to the M-R relation, even before considering post-disk phase mass loss.

While increasing the envelope opacity may improve our comparison to the M-R data in the super Earth-Neptune mass range, changing its setting does not come without consequences in terms of our comparison with the M-a distribution. As we showed in Alessi & Pudritz (2018), even a small increase in envelope opacity from 0.001 cm^2 g^{-1} to 0.003 cm^2 g^{-1} reduces a rich warm gas giant population to near zero, with larger envelope opacities seeing an increase in gas giant formation frequencies at smaller orbital radii (ie. hot Jupiters). This disagrees with the gas giant frequency-period relation from occurrence rate studies, that show gas giant frequency to peak within the warm Jupier a_p range (Cumming et al., 2008), supporting our use of smaller envelope opacities in this work.

4.4.3 Reducing Planet Radii: Photoevaporative Mass Loss

In this work, we considered photoevaporation as a means of reducing planet radii through atmospheric loss to improve our comparison with the M-R distribution. Photoevaporation is indeed an important inclusion in our models for this purpose, as planets at low orbital radii $\lesssim 0.1$ AU can be entirely stripped of their atmospheres, reducing their radii. In the case of planets above 2-3 $M_\oplus$ that originally were at higher R_p than most of the observed data, atmospheric loss improved our models' comparison to the M-R distribution through reducing these planets' radii. Photoevaporation also impacts planets at a few tenths of an AU depending on their core masses.

Most of the super Earths we form in our models, however, have larger orbital radii such that they are not impacted by photoevaporation. Ice line planets in the 50 AU population, for example, all have orbital radii $\gtrsim 0.8$ AU. This resulted in the majority of planets in both populations having negligible atmospheric loss, and therefore no reduction in their radii that resulted from formation. As the statistical majority of super Earths, then, are unaffected by photoevaporation, its ability to improve our comparison to the observed M-R data through stripping atmospheres is limited.

It is possible that using a higher setting of atmospheric opacity, or a semi-grey model, would increase the effectiveness of stripping as planet radii would be larger, particularly within a_p <0.1 AU (Jin et al., 2014). This would be the case as planets would fill out a larger portion of their Roche lobes over a larger range of a_p, increasing photoevaporative mass-loss rates. However, we note that such a change in treatment in atmospheric opacity would not significantly affect our resulting M-R distribution for two reasons.

We first recall that the majority of super Earths in our populations form near ~ 1 AU, where changing from a grey to semi-grey opacity treatment has only a small increase on planet radii ($\lesssim$1%). Even if the effect orbital radius range where atmospheric stripping occurs is increased (for example, to a few tenths of an AU), most planets produced in our populations would still remain unaffected as they form at larger a_p. Furthermore, the $\lesssim 1\%$ change in their radii resulting from the different opacity treatment would only increase the degree to which they are displaced with the M-R data (in terms of R_p) at $M_p > 3$ $M_\oplus$.

For the second reason, we notice that planet radii are only significantly affected by atmospheric opacity within $a_p < 0.1$ AU, which is the region over which entire atmospheric stripping already occurs in our model with the current assumptions (ie. a grey opacity). We re-iterate that a change

to a semi-grey opacity treatment could extend the effective a_p range where stripping occurs (i.e. to a few 0.1 AU), but this would only affect a small number of additional planets (beyond those that are already stripped in the grey-opacity treatment) as most super Earths form in our populations closer to 1 AU.

Short-period super Earths: Additional Formation Scenario

One key improvement photoevaporation does have (in addition to reducing a small number of stripped planets' radii) is contributing an additional means of forming super Earths, specifically at small orbital radii. Previous versions of our population models have been unable to produce a significant number of super Earths at $a_p \lesssim 0.1$ AU, and planets that form at these small orbital radii are typically at least Neptune or sub-Saturn masses, having accreted a significant amount of gases. These planets are heavily impacted by photoevaporation due to their close proximities to their host stars. Stripping of these planets' atmospheres then reduces their masses to that of super Earths, populating a region of the M-a diagram we previously were unable to form planets in.

Photoevaporation adds an additional formation scenario for super Earths beyond the traditional "failed core" scenario (i.e. Alibert et al. (2006); Mordasini et al. (2009a); Rogers et al. (2011); Hasegawa & Pudritz (2012); Alessi et al. (2017)) albeit restricted to small a_p; planets can form as Neptunes or sub-Saturns close to their host star, whereby post-disk phase their atmospheres are photoevaporated, reducing their masses. Our result is in agreement with those found from previous works (i.e. Owen & Wu (2013); Jin et al. (2014)). Super Earths can therefore either be planets that fail to accrete significant amounts of gas during the disk phase, or planets who accrete, then lose gas by photoevaporation that sets in once the disk dissipates. Our model predicts super Earths at larger orbital radii ~ 1 AU to much more likely have formed via the first "failed core" scenario. We have found that stripping of sub-Saturns adds only a 1% increase to the super Earth population that forms directly from the disk phase, and is therefore a secondary effect in our models.

4.4.4 Reducing Planet Radii: Core-Powered Mass Loss

A post-disk mass loss mechanism would have a greater impact on our comparison to the observed M-R distribution if it affected planets over a larger extent of orbital radii. As we have discussed, photoevaporation only strips planet atmospheres at $a_p \lesssim 0.1$ AU, and can reduce a portion of atmospheric mass out to a few tenths of an AU depending on the planet's core mass. It is restricted to

small a_p as planets need to receive a high enough FUV flux in order to be affected by photoevaporation.

An alternative post-disk phase atmospheric mass loss mechanism is core-powered mass loss (Gupta & Schlichting, 2019). Both photoevaporation (Owen & Wu, 2013) and core-powered mass loss have been shown to reproduce the location of the radius valley near 1.5 $R_\oplus$ where the planet occurrence rate is reduced, separating super Earths that are stripped of atmospheres from sub-Neptunes that retain their primordial atmospheres. The core-powered mechanism drives atmospheric mass loss by young planets radiating away their heat of formation, and therefore may impact planets over a wider extent of a_p. However, as Gupta & Schlichting (2019) & Gupta & Schlichting (2020) have focused on planets with orbital periods < 100 days ($\lesssim$ several tenths of an AU), it is unclear how big of an impact the core-powered approach may have on low-mass planets at larger orbital radii (ie. the ~ 1 AU super Earths that frequently form in our model's ice line).

4.4.5 Core Compositions

By comparing their predicted location of the radius valley, as dependent upon planet core densities, with its observed location, Jin & Mordasini (2018) and Gupta & Schlichting (2019) conclude that the bulk of the low-mass planets within 100-day orbital periods must have Earth-like mean densities. This places a strong constraint on the amount of water that can exist on these planet cores, as low water contents provide the best comparison between their models and observations.

In our 50 AU population, there is a clear separation between ice-poor super Earths that formed in the dead zone having orbital radii < 0.8 AU, and ice-rich super Earths formed in the ice line with $a_p > 0.8$ AU. While there is no such division between heat transition and dead zone planets in the 66 AU population, it remains the case that super Earths at the smallest a_p formed in the dead zone, and accrete very little ice onto their cores during formation. It is indeed these planets that form in the dead zone at small a_p with Earth-like composition (low ice abundances) that are stripped of their atmospheres from photoevaporation - a result that is in agreement with the dry cores at orbital periods < 100 days predicted in Jin & Mordasini (2018) and Gupta & Schlichting (2019).

Core Compositions: Effect on M-R Distribution

We find that atmospheres play a dominant role in affecting a planet's overall radius. In the case of planets that retain their accreted atmospheres, ice rich planets that formed in the ice line or heat

transition, occupy the same region of the M-R diagram as dead zone planets with rocky cores. Thus, an atmosphere's effect on R_p can hide any differences in core radii that result from different solid compositions.

The effects of different bulk solid compositions only result in discernible effects on the M-R diagram in the case of planets with no/little atmospheres. This could be a result of no gas accreted during formation, or accreted gas being stripped from photoevaporation for planets at small orbital radii. In this case, ice-poor (dead zone) planets do have smaller radii at a given mass than ice-rich planets. We do note, however, that this difference in radii (ie. between the ice line-composition and the Earth like dead zone composition M-R contours) is somewhat small, and is comparable to typical errors in observed planet radii.

Following this result, we can conclude that, while investigating non-Solar C/O and Mg/Si ratios did have an affect on solid compositions, this ultimately translates to a minimal effect on our populations' M-R distributions. The trap that the planets form in has the largest effect on their solid compositions, producing a range of dry, Earth-like core compositions, to ice-rich planets with up to a third (ice line) or half (heat transition) of their solid mass in ice. The full variation of these elemental ratios, however, only resulted in a ~ 5 % variation in planets' ice compositions within any given trap. For example, the ice line planets from the 50 AU model have ice compositions ranging from $\sim$ 35-40 %.

When comparing drastically different solid compositions - that of a dead zone (ice-poor) and an ice line (ice-rich) planet - we only see somewhat small radius differences comparable to observational uncertainty. Furthermore, this difference in core radii only translates onto the M-R diagram in the case of cores with no atmospheres. We can therefore conclude that the small compositional variations derived from the ranges of C/O and Mg/Si considered (through the metallicity-fit of equations 4.1 & 4.2) ultimately have little effect on the resulting M-R distributions of our populations.

Effect of Vaporization During Planetesimal Accretion

We recall that our model assumes no vaporization of material during planetesimal accretion, meaning that the local disk solid composition is directly accreted onto the core. Alibert (2017) showed that planetesimals can withstand thermal disruption up to an envelope mass of ~ 3 $M_\oplus$, so this is a reasonable approach. However, we can conclude that our resulting M-R distribution would be largely unaffected even if we were to account for vaporization of ice for example, during planetesimal

accretion. This is because atmospheres hide the effects of solid compositions on planet radii, and the majority of our planets in both populations form at a sufficiently large orbital radius to retain their accreted atmospheres. As vaporization of ice during planetesimal accretion would reduce cores' ice contents, this would only affect the M-R distribution for the small number of planets with no atmospheres. We re-iterate however, that in this case, the difference in radii between a solid core with a third of its solid mass in ice (ie. an ice line core) and a core with Earth-like composition (ie. a dead zone core) is comparable to observational errors in planet radius.

Equilibrium Disk Chemistry Model vs. Tracking Ice Line Location

When tracking planets' solid compositions, we found that most compositional variations in a population are a result of planets having different ice contents (ie. accreting inside vs. outside the ice line). The ratio of bulk irons to silicates is constant over the majority of the disk's extent; in all but the innermost $\sim$ 1-2 AU. This begs the question of whether or not a full solid chemistry model is important, or if one could reproduce our composition results by only tracking the disk's ice line and where planets accrete with respect to it.

We argue that incorporating a full solid chemistry model is advantageous. The inner regions of the disk $\sim$ 1-2 AU play a significant role in producing planets in our models, as the vast majority of our planet populations have orbital radii at these a_p. Planets, therefore, do accrete from the region of the disk where the iron to silicate ratio has a dependence on a_p and is not constant. This is clearly seen in the compositional results of dead zone planets. This subset of our super Earth population showed a range of iron and silicate abundances despite having nearly no variation in ice, as all planets had a near zero water content.

It is important to accurately model the solid abundances of planets at small a_p, as these are the planets that can be stripped by photoevaporation, and it is the stripped planets whose radii reflect their solid compositions. Furthermore, the internal heating of these planets through radioactive decay scales with planets' silicate abundances, which impacts the atmospheric mass-loss calculation, affecting planets precisely in the region where the disk silicate abundance varies with orbital radius in a non-trivial manner.

4.4.6 Effect of Initial Disk Radius on Comparison with M-R distribution

In paper II in this series (Alessi et al., 2020), we found that an initial disk radius of 50 AU resulted in a population whose M-a distribution had the best correspondence to the observed data, compared to other settings of R_0. This was a result of the $R_0 = 50$ AU population resulting in the largest super Earth population, mainly from formation at the ice line. In terms of disk formation, these intermediate disk sizes correspond to moderate mass-to-magnetic flux ratios (i.e. moderate magnetic braking), as opposed to strong magnetic braking or the case of pure hydrodynamic collapse, which correspond to small and large disk sizes (ie. the 66 AU population included here), respectively (Masson et al., 2016). We note that the small disk size case of $R_0 = 33$ AU was not included in this work as it resulted in very few super Earths being formed.

In terms of our comparison in this work to the M-R distribution, we find that the $R_0 = 50$ AU and 66 AU models are comparable, as neither achieve an objectively better fit. Both models fit the data reasonably well in the $\sim$ 1-3 $M_\oplus$ range, whereas at larger planet masses, our populations typically produce planets at larger radii than most of the observed population. At these larger planet masses, the 50 AU model achieved a slightly worse comparison, as planets formed with slightly larger radii than in the 66 AU model. However, this was somewhat mitigated after the photoevaporative mass-loss model was included on the populations as it has a larger effect on the 50 AU model's planets than those from the 66 AU population. Nevertheless, the final (post-atmospheric mass loss) M-R distributions of both the 50 AU and 66 AU populations were comparable in terms of their comparison with the data.

The increased effectiveness of photoevaporation resulted in the 50 AU population having a better correspondence with the observed M-a distribution than the 66 AU population. As atmospheric mass loss is more significant in the 50 AU population, more planets that formed in the Neptune - sub-Saturn mass range at small orbital radii were stripped, having their masses reduced to $\lesssim 10 M_\oplus$. In the 50 AU model, this process resulted in more short-period super Earths, filling out a region of the M-a space that our planet formation model (without photoevaporation) does not directly populate (as it produces planets with higher masses $\gtrsim$ that of Neptune at these small a_p).

We therefore conclude that the 50 AU population produces the better *M-a distribution*, even though our comparison to the M-R data gives no clear preference for either initial disk radius (50 AU or 66 AU). In paper II, we arrived at this same conclusion while only considering planet formation,

as the initial disk radius of 50 AU resulted in the largest super Earth population. Here, by combining formation and atmospheric mass-loss, we find that the 50 AU model is optimal because (1) it results in more short-period super Earths; and (2) more sub-Saturns (zone 1) planets are stripped, further enhancing the super Earth population already obtained from formation in paper II. In terms of disk formation, our results support moderate magnetic braking (moderate settings of mass to magnetic flux) during disk formation.

The 50 AU population also has a more clear separation between dry, rocky planet compositions at small orbital radii resulting from formation in the dead zone trap, and ice-rich super Earths at larger $a_p \sim 1$ AU resulting from formation at the ice line. Thus, the 50 AU population also shares better agreement with the result of Jin & Mordasini (2018); Gupta & Schlichting (2019) derived from the position of the super Earth radius valley - that short-period super Earths (P<100 days) typically have Earth-like mean densities.

Another consequence of this result is that the 50 AU population predicts nearly all super Earths residing in the habitable zone (whose extent was estimated using the Kopparapu et al. (2014) calculation), formed in the ice line trap, and have ice-rich compositions ranging from 35-40% ice by mass. Our formation models therefore produce planets in this interesting region of the M-a diagram that acquire a substantial water budget from the disk phase.

This, however, can be contrasted with dry, rocky compositions of the Solar system's terrestrials, which are the only planets at these separations whose compositions are well known. In light of our model's frequent production of ice-rich super Earths near 1 AU, this raises the interesting question of whether Earth-like compositions are common or rare at these separations. The difference in compositions between our models' super Earths near 1 AU and the Solar system terrestrials may be a result of different formation scenarios.

Post-disk dynamical assembly is a standard approach in modelling the formation of the Solar system terrestrials (i.e. Izidoro & Raymond (2018)). In this circumstance, the planetesimals mostly originate inside the ice line after the disk has dissipated, and growth occurs from collisions induced by orbit crossings (through gravitational perturbations from Jupiter). Because most of the constituent planetesimals originally lie within the ice line, this approach naturally leads to dry and rocky planets. Dynamical assembly is a different formation scenario than we considered here, and may be important for the formation of low-mass planets, and for its contribution to their M-R distribution (i.e. Hasegawa (2016)). Conversely, super Earths at ∼1AU from our models arise as failed cores in

the core accretion model, which is a quite different scenario. In this case, planets (mostly) form in the ice line trap, acquiring substantial water during the disk phase as a consequence.

It is also interesting that the 50 AU population sees a bimodal distribution in super Earth compositions. The ice line and dead zone traps produce nearly the entire super Earth population in this model, each having their own compositional signatures and only a small variation across the entire population. The heat transition was the only trap in our models to produce a wide range of planet compositions, ranging from dry, rocky planets (similar to those produced in the dead zone), to those with up to 55% ice by mass. This is a result of the heat transition migrating across the ice line during disk evolution, and its position with respect to the ice line being dependent on disk properties stochastically varied in our population models. However, in the 50 AU population, the heat transition contributes almost no super Earths.

The differences we see between the 50 AU and 66 AU populations in terms of their final M-a and M-R distributions suggest an important extension of this model: investigating a population with a full distribution of initial disk radii. The observations of disk radius distributions are still in an early stage of development. However, one could use a plausible distribution of R_0 that is then sampled in the population models (in the same manner as the initial disk mass, lifetime, and metallicity are treated). In paper II (Alessi et al. (2020)), we investigated a larger sample of fixed R_0 values to determine our population's M-a distributions. Based on these results, we expect that a population that includes a sampled distribution of R_0 values will have a smoother distribution of low-mass planets on the M-a diagram than is seen in either the 50 AU or 66 AU populations investigated in this work.

However, there are three important results of the populations that will be maintained in either treatment of R_0 that we argue will not greatly affect the populations' final M-R distribution. First, at all investigated R_0 values in paper II, we find that super Earths near 1 AU are formed in the ice line and/or the heat transition, while shorter-period ($\lesssim$ 0.5 AU) super Earths are formed in the dead zone. As discussed in this paper, this gives rise to the range of solid compositions we find, as well as their effect on the M-R distribution. The second result is that, for the full range of R_0 values investigated in paper II, most low-mass planets form outside of 0.3 AU. We have shown with our atmospheric photoevaporation model that planets with these sufficiently large a_p encounter negligible post-disk mass loss. Lastly, we recall that planet masses of $\sim$ 2-3 $M_\oplus$ separate our populations' lower mass planets whose radii compare well with the observed data, and higher mass planets whose radii

are larger than most of the observed data at a given mass. The latter case is a result of their acquisition of a sufficiently large atmospheric mass fraction during the disk phase. In paper II, we find at all investigated values of fixed R_0, the resulting populations have a comparable fraction of low-mass planets with masses above and below this transition of $\sim$ 2-3 $M_\oplus$.

Therefore, the most important factors shaping our populations' M-R distributions identified in this work - planets' solid compositions, atmospheric mass fraction, and orbital radii that determine the effectiveness of photoevaporation - will not change significantly for populations using a more extended investigated range of R_0 values, as in paper II. On this basis, we argue that, if a full distribution of R_0 values were sampled over in our population synthesis model, the resulting M-R distribution would not be greatly affected, and would be similar to those shown for the 50 AU and 66 AU populations in this work.

4.5 Conclusions

In this work we have determined the effects of atmospheric photoevaporative evolution and solid compositions on the mass-radius distribution of planets in the super Earth - Neptune mass range in the populations from the Alessi et al. (2020) models. We have included planet structure calculations and solid disk chemistry, with elemental C/O & Mg/Si ratios scaling with metallicity in accordance with recent stellar data (Suárez-Andrés et al., 2018). In doing so, we link variability in disk properties to outcomes of planet formation, and also link the outcomes of planet formation to post-disk evolution.

Our main results are as follows:

- Atmospheric mass loss is an important inclusion in population synthesis models. Prior to evaporation, our populations had a reasonable comparison to the observed M-R data for 1-3 $M_\oplus$ planets, but produced systematically larger radii planets than most of the data at masses $\gtrsim 3\ M_\oplus$. Evaporation improves this comparison by reducing planet radii, and stripping planets on small orbits $\lesssim 0.1$ AU. Most super Earths form at larger radii, however, and are unaffected by stripping. Our comparison with the data would be improved using an evaporation model that impacts planet radii across a larger extent of orbital radii.

- Evaporation also improves our comparison to the observed M-a relation, resulting in a means by which short-period super Earths form. Before accounting for atmospheric mass loss, our

planet formation models do form planets at small $a_p \lesssim 0.1$ AU, but these planets have accreted substantial gas during the disk phase and form with masses larger than that of Neptune. Photoevaporative mass-loss strips these Neptunes and sub-Saturns resulting from our formation model, producing super Earths at these small a_p. By incorporating atmospheric mass loss, we populate this region of the M-a diagram previous versions of our model (that did not include post-disk atmospheric evolution) were unable to.

- We obtain a more optimal M-a distribution using an initial disk radius of 50 AU. Comparing populations resulting from a 50 AU and 66 AU initial disk radius, atmospheric mass loss is more significant in the 50 AU model as more short-period planets are formed. This leads to more Neptunes and sub-Saturns being stripped, increasing the super Earth population at small orbital radii. Our planet formation and atmospheric mass loss model therefore favours an intermediate initial disk size of 50 AU, corresponding to moderate magnetic braking during protostellar collapse. The two populations, however, produce comparable M-R distributions, where no clear preference in disk radius model can be deduced.

- Treatment of atmospheres and atmospheric mass loss has the most drastic effect on M-R diagram. Effects of variability in core composition are hidden by atmospheres except in the case of cores with no atmospheres where radii differences derived from different solid compositions can be seen. This is achieved either through no gas accreted during formation, or via stripping.

- The two different initial disk radii runs see different traps forming super Earths (50 AU: ice line & dead zone; 66 AU: heat transition & dead zone) at different radii, with the 50 AU run producing super Earths on smaller orbits. The initial disk radius thereby affects the M-R relation through the relative impact of photoevaporation and super Earth compositions.

- The traps' locations in the disk with respect to the water ice line set the resulting solid abundances. Planet formation at the water ice line results in super Earths having 35-40% of their solid mass in water ice. As the dead zone trap exists within the ice line, planets formed in this trap are all dry, having $\lesssim 0.2\%$ of their solid mass in ice. The heat transition produces the largest range of super Earth compositions, from dry, Earth-like compositions (similar to those produced in the dead zone), to super Earths with up to 55% of their solid mass in ice.

- We obtain an M-R relation for our solid planetary cores of $M_p \sim R_p^{\beta}$ with a power law index

β=0.261 and 0.269 for ice line and dead zone cores, respectively. This achieves good correspondence with the index found in Chen & Kipping (2017), $\beta = 0.2790^{+0.0092}_{-0.0094}$, fit to observed terrestrial planets.

- At small a_p, our models produce super Earths with low ice abundances $\lesssim 0.2\%$ by mass, a result of formation in the dead zone trap. This result is in agreement with the Earth-like planet composition inferred via the radius valley's location in atmospheric mass-loss studies (i.e. Jin & Mordasini (2018); Gupta & Schlichting (2019)) at orbital periods < 100 days.

- Planets' solid compositions ultimately has a small effect on the resulting M-R distribution, with atmospheres having the most significant effect. The traps' biggest effect on the M-R relation is through the production of super Earths at different distances from their host-stars, which determines the importance of photoevaporation.

- Elemental ratios, varied in accordance with stellar data have an effect on planet ice abundances and silicate-bearing minerals (enstatite & forsterite), but this has only a small effect on the overall M-R relation.

This paper concludes a three-part investigation on the key physical processes that connect the formation of planets, to the properties of planetary populations in the M-a and M-R diagrams, their core compositions, and structure of their atmospheres. The major ingredient in sculpting these relations is planet migration theory. Although in this regard our model uses a modified viscous disk theory approach, planet migration arises through the combined role of viscous and wind torques. With the rising importance of disk winds in interpreting the physics of outflows and protoplanetary disks in ALMA observations (Bai & Stone (2013); Gressel et al. (2015); Suzuki et al. (2016); Hasegawa et al. (2017); Flaherty et al. (2018); Rosotti et al. (2020); see also review Pudritz & Ray (2019)), we emphasize that our program can accommodate disk wind torques and their effects on disk evolution, planet formation, and migration. Accordingly, this will be the subject of our future work.

Appendix A: Disk Chemistry Model

We use an equilibrium chemistry model to track evolving solid abundances throughout the disk and materials accreted onto forming planets. This approach assumes that the composition of the disk material is chemically reset and forms *in situ* as opposed to being directly inherited from the

protostellar core. The short chemical timescales in the inner disk ($\lesssim$ 10 AU, Öberg et al. (2011); Pontoppidan et al. (2014)) support this assumption in the main planet-forming region of the disk. Chemical inheritance is likely important for abundances in the outer disk, however this region plays a less significant role for planet formation in our model. This is because core accretion rates in the outer disk are small as the disk's surface density is lower. Additionally, radial drift in the Birnstiel et al. (2012) dust model efficiently removes solids from the outer disk, further reducing solid accretion rates in this region.

The equilibrium chemistry approach is best suited to tracking the abundances of solids throughout the disk that condense from the gas phase on short timescales (Toppani et al., 2006). Non-equilibrium chemistry, particularly photochemistry, play an important role in affecting chemistry in the gas phase (i.e. Cridland et al. (2016)). While the approach does not include non-equilibrium processes and therefore will be less accurate in determining gas abundances throughout the disk, equilibrium chemistry remains a justified approach here as our focus is to compute the composition and radial structures of low-mass (predominantly solid) planets.

Our equilibrium chemistry calculations are performed with the ChemApp solver (distributed by GTT Technologies; http://www.gtt-technologies.de/newsletter). We consider a temperature range between 50-1850 K with 200 linearly-spaced resolution elements, and a pressure range of 10^{-11} - 10^{-1} bar with 400 logarithmically-spaced resolution elements. These ranges were chosen to span the disk midplane temperatures and pressures encountered in our population synthesis models. The Chambers (2009) disk model is used to map these temperatures and pressures to time-dependent midplane radii throughout the disk that are interpolated over to determine a species' abundance profile. We also consider a range of disk metallicities between -0.6 and 0.6 with 240 linearly-spaced resolution elements in our chemistry calculations. This is the same range of disk metallicities used in our population synthesis models, covering the observed range of planet-hosting stellar metallicities (Alessi & Pudritz, 2018).

In table 4.1, we list the 31 solid- and 37 gas-phase chemical species that are included in our chemistry models. The species we include are those that form with a non-negligible abundance ($\gtrsim 10^{-10}$ mol in a 100 kmol chemical system) in the investigated range of parameters. This is the same species list that was used in Alessi et al. (2017), with the addition of SiC in both gas and solid phase. SiC (along with graphite) has been shown to become abundant in disks with very high C/O ratios of $\gtrsim$ 0.8 (Bond et al., 2010), and we include these as C/O is a varied parameter in our

Table 4.1: A list of species present in the chemistry model. Solids that are present in figure 4.15 have their common names bracketed following their chemical formulae.

Gas Phase			Solid Phase		
Al	H_2				
Ar	H_2O	Ne	Al_2O_3	Fe_3O_4 (magnetite)	
C	HCN	Ni	$CaAl_2SiO_6$	$FeSiO_3$	SiO_2
C_2H_2	HS	O	$CaMgSi_2O_6$ (diopside)	Fe_2SiO_4 (fayalite)	FeS (troilite)
CH_2O	H_2S	O_2	CaO	H_2O	NiS
CH_4	He	OH	$CaAl_{12}O_{19}$	MgO	Ni_3S_2
CO	Mg	S	$CaAl_2Si_2O_8$	$MgAl_2O_4$	Al
CO_2	N	Si	$Ca_2Al_2SiO_7$	$MgSiO_3$ (enstatite)	C
Ca	N_2	SiC	$Ca_2MgSi_2O_7$	Mg_2SiO_4 (forsterite)	Fe
CaO	NH_3	SiO	$FeAl_2O_4$	$NaAlSi_3O_8$	Ni
Fe	NO	SiO_2	FeO (Wüstite)	Na_2SiO_3	Si
FeO	NO_2	SiS	Fe_2O_3	SiC	
H	Na				

populations. However, stellar data shows that such systems are extremely uncommon (Brewer & Fischer, 2016), and C/O $\simeq$ 0.7 is the highest value that is input into our chemistry models. We nonetheless include both phases of silicon-carbide for completeness.

An update to our previous version of our chemistry model (Alessi et al., 2017) is our treatment of the initial disk abundances. We have updated the Solar compositions used in our calculations to photospheric abundances from Asplund et al. (2009), for which our previous work used those from Pasek et al. (2005).

In table 4.2, we show the updated list of initial disk abundances scaled up to a 100 kmol system. We only include the 15 most abundant elements in our chemistry model to simplify the calculations. With this assumption, we are omitting the presence of various low-abundance species that would form as a result of additional elements included in the chemistry models. However, since those species would comprise a very small mol-fraction of the chemical system if included, they would merely be a small correction to the abundance results shown throughout this work.

A1: Effects of C/O and Mg/Si Ratios

In addition to incorporating non-Solar metallicities, we also investigate non-Solar C/O and Mg/Si ratios. In our main chemistry calculation, we vary these in accordance with disk metallicity through fits taken from Suárez-Andrés et al. (2018). Here, however, we show results of disk chemistry runs with constant C/O and Mg/Si ratios (independent of metallicity) to discern their effects on resulting

Table 4.2: Solar elemental abundances used in our equilibrium chemistry calculations are shown. We take the 15 most abundant elements from Solar photospheric data from Asplund et al. (2009), normalized to a 100 kmol chemical system. We scale these abundances for non-Solar metallicity, C/O, and Mg/Si ratios as described in the text.

Element	Abundance (kmol)
H	92.07
He	7.84
O	4.51×10^{-2}
C	2.48×10^{-2}
Ne	7.84×10^{-3}
N	6.22×10^{-3}
Mg	3.12×10^{-3}
Si	2.98×10^{-3}
Fe	2.59×10^{-3}
S	1.30×10^{-3}
Al	2.48×10^{-4}
Ar	2.31×10^{-4}
Ca	1.80×10^{-4}
Na	1.71×10^{-4}
Ni	1.46×10^{-4}

solid abundances.

For both elemental ratios, we consider the Solar quantity (C/O = 0.54 & Mg/Si = 1.05) in addition to a sub-Solar and super-Solar values (independently, for both ratios) for a total of 9 different chemistry runs. For the low C/O case, we select a value near the peak of the observed stellar C/O ratio distribution for F, G, and K stars, 0.47 (Brewer & Fischer, 2016), and we set the high C/O ratio value to 0.61 (having the same difference in C/O with the Solar value as the low setting). This high C/O ratio is quite extreme with respect to the majority of the observed data, lying on the high-C/O 'tail' of the distribution.

The Solar Mg/Si ratio (1.05) lies close to the average in the observed distribution from Brewer & Fischer (2016). We set the low and high Mg/Si ratios, 0.9 and 1.2 respectively, to span most ($\sim \pm 2\sigma$) of the observed distribution.

In figure 4.14, we show solid abundance profiles at different disk C/O ratios. The solids are categorized based on where the minerals would be located in a chemically differentiated planet. The irons, or core materials, are iron- and nickle-bearing minerals. Silicates, or mantle materials, are magnesium or aluminum silicate-bearing minerals. Lastly, the "ice" component consists only of water ice.

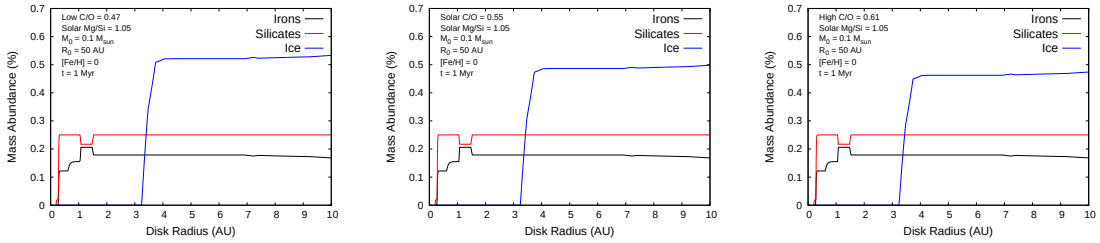

Figure 4.14: Solid disk abundances are shown for the low C/O = 0.47 setting (left), Solar C/O = 0.54 (centre), and high C/O = 0.61 (right), all calculated with Solar Mg/Si = 1.05. The solids are divided into three categories: iron-bearing minerals, silicate-bearing minerals, and water ice. These abundance profiles are computed 1 Myr into the evolution of a Solar-metallicity disk with an initial mass of 0.1 $M_{\odot}$, and initial radius of 50 AU. Higher ice abundances result from lower C/O ratios, with total iron and silicate abundances being unaffected by the C/O ratio.

We see that the main effect of the C/O ratio is on the disk water abundance, with low values resulting in a higher ice abundance due to the larger molar abundance of oxygen. While similar plots are not shown for the different Mg/Si ratios considered, its effect on mineral abundances (discussed below) has a secondary effect on the disk's water abundance causing for a slightly higher ice abundance in disks with larger Mg/Si ratios. However, the change in ice abundance for the investigated range in Mg/Si is smaller than that shown in figure 4.14 for the range of C/O ratios.

Figure 4.14 also shows that the summed abundances of irons and silicates remains constant across the majority of the disk's extent ($\gtrsim$ 1.5 AU). The abundance profiles of these two summed components are unchanged by the disk's C/O or Mg/Si ratios. This feature of the disk chemistry is important to consider when interpreting planet composition results, as variation in bulk iron and silicate mass fractions between planets is often a result of their differing ice mass fractions[5]. Changes in ice mass fraction are usually the main driver of compositional variation between planets, and mass fractions of irons and silicates change in response to these different ice mass fractions. The ratio of irons to silicates is typically roughly constant in planets as a result of their uniform abundance disk chemistry profiles. Variation in solid abundances of irons and silicates is only present in the innermost regions of the disk, between $\sim$ 0.1 AU where solids condense out of the gas phase and $\sim$ 1.5 AU.

In figure 4.15, we show the main effect of the disk Mg/Si ratio on abundances of the silicate-bearing minerals in the disk by plotting abundance profiles for the most abundant minerals at the

[5]Since the summed mass fraction of irons + silicates + ice has to sum to unity

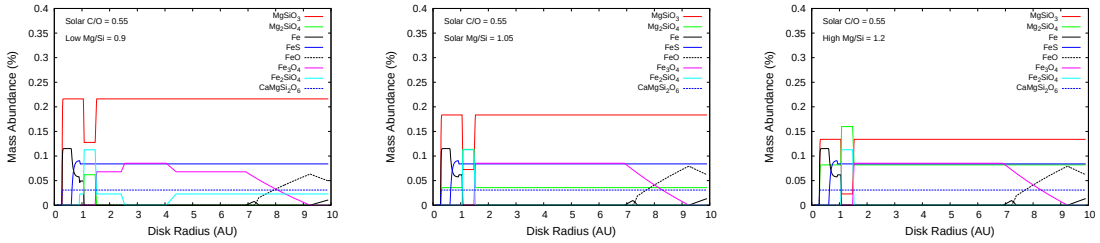

Figure 4.15: Abundance profiles of the most abundant minerals are shown for the low Mg/Si = 0.9 setting (left), Solar Mg/Si = 1.05 (centre), and high Mg/Si = 1.2 (right), all computed at the Solar C/O ratio. All disk parameters are the same as in figure 4.14. The abundances of enstatite ($MgSiO_3$) and forsterite (Mg_2SiO_4) are seen to depend on the disk Mg/Si ratio, with forsterite becoming more abundant as Mg/Si increases.

three Mg/Si ratios considered. We most notably see that the abundances of enstatite ($MgSiO_3$) and forsterite (Mg_2SiO_4) are affected by the disk Mg/Si ratio, with more forsterite being produced as Mg/Si is increased in accordance with the increased molar abundance of Mg. The abundance profiles of enstatite and forsterite are relatively constant throughout the disk outside of the innermost dust-sublimation zone, with the exception being a small range of $\sim$ 1-1.5 AU where fayalite (Fe_2SiO_4) attains its peak abundance. The abundance curves of both fayalite and magnetite (Fe_3O_4) change slightly in the lowest Mg/Si ratio case. While not shown, we have investigated these mineral abundances at the various C/O ratios considered, and find that changing the disk C/O while holding the Mg/Si ratio constant does not affect these mineral abundances.

As was previously mentioned, the disk's ice abundance is slightly higher in disks with larger Mg/Si ratios. This is somewhat unexpected since high Mg/Si results in more forsterite (Mg_2SiO_4, carrying more oxygen) and less enstatite ($MgSiO_3$, carrying less oxygen). However, when taking the net molar amount of both minerals and accounting for the total number of oxygen atoms carried by both, we find that the net oxygen atoms carried by both enstatite and forsterite is *smaller* in the high Mg/Si ratio case despite the higher forsterite abundance, accounting for the slightly increased ice abundance.

Appendix B: Planetary Structure

B1: Interior Structure Model

The equations we use to describe our planets' interiors are the hydrostatic balance equation,

$$\frac{dP}{dr} = \frac{-Gm(r)}{r^2}\rho, \tag{4.5}$$

and the mass continuity equation,

$$\frac{dm}{dr} = 4\pi r^2 \rho, \tag{4.6}$$

where m(r) is the mass internal to the given shell, G is Newton's gravitational constant, r is the radius of the shell from the planet's centre, and ρ is the material density as determined by the equation of state,

$$\rho = \rho(P, T) \simeq \rho(P). \tag{4.7}$$

The Equation of State (EOS) is a function of the pressure and temperature of the given shell and is determined by the local material properties. Since we are ignoring thermal effects in the core, the EOS will only be a function of pressure.

Within the silicate and iron layers, the pressure is typically so high that our zero-temperature assumption is valid. In the silicate layer, we assume our material is in the initial perovskite phase of $MgSiO_3$. This undergoes a transition to the post-perovskite phase at pressures above 120 GPa (Komabayashi et al. (2008)). Both phases are modelled based on a high pressure extension to experimental results using a diamond anvil. We assume that iron is in its high pressure, hexagonal closely packed (hcp) phase, with the EOS taken from the diamond anvil cell results of Fei et al. (2016). For all three materials, in the high-pressure regime we adopt the electron degenerate Thomas Fermi Dirac (TFD) EOS from Seager et al. (2007) for pressures above 1 TPa.

As per the assumption that our planets are differentiated, there would, in reality, be a degree of mixing of materials between layers. However, it is expected that mixing would likely only change the core radius by *sim* a few hundred kilometres. This is a small effect as the corresponding change is well within other uncertainties in the model (Valencia et al. (2006)), such as those related to the various water phases' equations of state. We therefore do not consider these mixing effects between differentiated layers in cores in our calculations.

B2: Atmospheric Structure Model

We add a third interior structure equation to equations 4.5 and 4.6 that accounts for energy transport in the atmosphere,

$$\frac{dT}{dr} = \frac{T}{P}\frac{dP}{dr}\nabla(T,P) \ , \tag{4.8}$$

where $\nabla(T,P)$ is determined using,

$$\nabla(T,P) = \frac{d\ln T}{d\ln P} = \min(\nabla_{ad}, \nabla_{rad}). \tag{4.9}$$

∇_{ad} and ∇_{rad} refer to the adiabatic and radiative gradient, respectively, and determine the efficiency of energy transport by either convection or radiation in a given shell. The radiative gradient is calculated with,

$$\nabla_{rad} = \frac{3}{64\pi\sigma G}\frac{\kappa l P}{T^4 m}, \tag{4.10}$$

where κ is the Rosseland mean opacity corresponding to the pressure and temperature of a given shell. We find this value using the tables of Freedman et al. (2008) corresponding to Solar metallicity. The adiabatic gradient is also taken from the EOS tables of Chabrier et al. (2019). The method of energy transport in a given shell is determined by comparing the radiative and adiabatic gradients and choosing the method with the smaller corresponding gradient.

In order to self-consistently solve for the structure of our planets, we apply the Eddington boundary equations, given in Mordasini et al. (2012b). We determine the radius of our planet, R_p to be the photosphere corresponding to the τ=2/3 optical depth surface. This has a corresponding photospheric pressure of,

$$P = \frac{2GM_p}{3R_p^2\kappa} \ , \tag{4.11}$$

and a temperature that is set by a combination of external heating from the host-star's radiation and internal heating from the core (with luminosity L_{int}, and temperature T_{int}),

$$T^4 = (1-A)T_{eq}^4 + T_{int}^4. \tag{4.12}$$

The equilibrium temperature T_{eq} is determined using a sun-like star and the given planet's semi-major axis, a. All planets are assumed to have a Jovian albedo, A=0.343. Their equilibrium

temperature is therefore,

$$T_{eq} = 280K\left(\frac{a}{1AU}\right)^{-1/2}\left(\frac{M_*}{M_\odot}\right). \tag{4.13}$$

This boundary condition assumes that the planet rotates quickly and redistributes heat evenly across the surface. It also ignores non-grey atmosphere effects from wavelength-dependent opacities, since these only significantly impact planets on very small orbital radii ($\sim$ 0.1 AU, Mordasini et al. (2012b)). A more rigorous treatment would be to incorporate the semi-grey approximation of Guillot (2010), however this would generally be a small correction on our predicted planet radii as the majority of our planets orbit outside of 0.1 AU.

The internal luminosity of our planets results from the decay of radioactive isotopes in the silicate layer. Since we are focused on modelling the structure of super Earths, we neglect energy produced by gravitational contraction which generally only applies for gas giants. Following the approach of Mordasini et al. (2012c), we incorporate three important radiogenic isotopes, ^{40}K, ^{238}U and ^{232}Th, in our structure model. The heat produced by the decay of these isotopes exponentially decays with time as the quantity of radioactive material slowly decreases over billion-year time scales. For this reason we neglect isotopes with short lived half lives ($<$ 100 million years). The total internal luminosity from radiogenic sources also scales with the mass of the planet's core and the amount of rocky material in the silicate layer, so a more massive super Earth with a higher abundance of silicate material will have a more luminous core than a smaller core whose composition is ice- or iron-dominant.

Appendix C: Atmospheric Photoevaporation

We study the long-term impacts of photoevaporation on the atmospheres of our planets by combining the UV and X-ray driven models of Murray-Clay et al. (2009) and Jackson et al. (2012). We use the power law fits to measured integrated fluxes from Ribas et al. (2005) for young solar-type stars in the X-ray (1-20 Å) and extreme ultra-violet (EUV) (100-360 Å) wavelengths.

In the early evolution of the planet, X-ray driven photoevaporation dominates due to the high x-ray fluxes from a young star (Ribas et al. (2005),Jin et al. (2014)). Jackson et al. (2012) model mass loss by assuming that the energy from incident photons is converted into work to remove gas

from the gravitational potential of the planet. This results in a mass loss rate, $\dot{m}$, of,

$$\dot{m} = \epsilon \frac{16\pi F_{XR} R_p^3}{3GM_p K(\xi)}, \tag{4.14}$$

where R_p corresponds to the photosphere of the planet, and F_{XR} is the incident X-ray flux at the planet's orbital distance. The factor $K(\xi)$ is a scaling parameter that accounts for the ratio of the planet's Roche lobe to its radius (Jackson et al. (2012)). This factor becomes significant for highly inflated close-in planets where $K(\xi)$ approaches zero. The final parameter ϵ accounts for how efficiently X-rays are able to remove the gas from the planet's atmosphere, for which we adopt the value used by Jin et al. (2014) of 0.1. This value was chosen as the majority of the work done to strip the atmosphere is attributed to X-rays within the narrow wavelength range of 5-10 Å(Owen & Jackson (2012)).

For extreme EUV-driven photoevaporation, we consider the two regimes highlighted in the model of Murray-Clay et al. (2009). For low EUV fluxes beneath a critical threshold, the EUV-driven mass loss rate is formatted similarly to equation 4.14, but without the $K(\xi)$ term. In this case, the radius of the planet is considered to be where the atmosphere becomes opaque to UV radiation, which occurs at a pressure of approximately 1 nanonbar (Murray-Clay et al. (2009)). In the case of EUV-driven mass loss, Jin et al. (2014) choose an efficiency parameter of 0.06. For high EUV fluxes, a portion of the incoming radiation is lost to cooling radiation and increasing the EUV flux no longer increases the mass loss rate. In this radiation-limited regime, the mass-loss rate is given by (Murray-Clay et al. (2009)),

$$\dot{m}_{rr-lim} \approx 4\pi \rho_s c_s r_s^2 \,, \tag{4.15}$$

where c_s is the sound speed, and r_s is the sonic point where the UV-driven wind becomes supersonic. The two parameters are determined as described in Murray-Clay et al. (2009). As in Jin et al. (2014), we chose a flux of 10^4 erg/s to mark the transition between the radiation-limited and the energy-limited regime (equation 4.14).

One last important transition to consider is that between X-ray and UV-driven mass flows. Above a certain UV flux, X-rays are no longer able to penetrate the UV ionization front, resulting in a UV-dominated flow (Owen & Jackson (2012)). To determine if this transition is present, we check if the

total EUV luminosity $L_{\rm EUV}$ from the star exceeds (Owen & Jackson, 2012),

$$L_{\rm EUV,crit} = 10^{40} s^{-1} \Big(\frac{a}{0.1 AU}\Big)^2 \Big(\frac{\dot{m}_x}{10^{12} g/s}\Big)^2 \Big(\frac{R_p}{10 R_E}\Big) \, . \tag{4.16}$$

If $L_{\rm EUV} > L_{\rm EUV,crit}$, then the flow is UV-driven and the X-ray mass loss rate is set to zero. When the reverse is true, the flow is X-ray driven, and X-ray and UV mass-loss rates are treated as previously described.

We start the mass loss evolution of our planets immediately after the protoplanetary disk evaporates, a parameter that is stochastically-varied throughout our population of planets according to the observed range of disk lifetimes. We evolve each planet forward until it is 1 Gyr old. Beyond this point, the mass loss rates are so small, even for close in-planets, that any planet managing to hold onto a substantial envelope at this point will be safe from further photoevaporation while its star is on the main sequence (Jin et al. (2014), Jin & Mordasini (2018)).

Appendix D: Individual Effects of C/O & Mg/Si Ratios on Super Earth Abundances

We now discuss the effects of the disk C/O and Mg/Si ratio individually by considering population results from chemistry runs where these ratios are held constant with disk metallicity (no variation in a population run). We consider three values of each ratio: their Solar value as well as a high and low value where the variation spans $\gtrsim 1\ \sigma$ in the chemical ratio's observed distribution in stellar data (see notes in appendix 4.5).

In figure 4.16, we show the distribution in solid abundances of super Earths (zone 5 planets) formed in the ice line from the $R_0 = 50$ AU population for each of these nine disk chemistry calculations. We most notably see that the disk C/O ratio has a significant effect on the planets' ice contents, with low C/O ratios resulting in higher ice abundances due to the larger molar abundance of oxygen. This trend can be seen at all values of the Mg/Si ratio.

The Mg/Si ratio does have a small effect on the planets' ice abundance with high Mg/Si ratios resulting in larger ice contents. While this trend is seen at all values of disk C/O, the effect of Mg/Si on the planets' ice contents is less significant than that of C/O. As discussed in section 2.2, the effect of Mg/Si on the disk's ice content is a secondary effect. The molar abundances of enstatite ($MgSiO_3$)

and forsterite (Mg_2SiO_4) are set by the disk Mg/Si, with high values using *less* total oxygen atoms leaving more remaining to contribute the disk's water budget.

We recall from section 4.5 that the *absolute* abundances of these iron and silicate components are unchanged when varying these elemental ratios. Therefore, the ratio of each planets' iron to silicate abundance in figure 4.16 are consistent regardless of the elemental ratios considered. As each planets' total abundance needs to sum to unity, the percent abundances of iron and silicate do scale (with constant ratio) in response to the ice abundance as affected by the elemental ratios. We emphasize, however, that the C/O and Mg/Si ratios are affecting the disk and planets' ice contents only, and the percent abundances of irons and silicates change in response to the changing ice contents.

We also see that the distributions of planet abundances at each C/O and Mg/Si ratio investigated show less scatter (have tighter peaks) than the corresponding distribution of ice line super Earths from the metallicity-fit run - figure 4.6, left. In the latter case, the population samples a range of both elemental ratios as the disk metallicity is varied, leading to a larger scatter in planets' ice abundances, whereas only individual values of C/O and Mg/Si are considered in the case of figure 4.16.

The ice line super Earths from the $R_0 = 50$ AU population are optimal for showing the effects of the disk elemental ratios on super Earth compositions since there is relatively little variance in ice abundances of super Earths within a population. This is a result of the trap itself being defined to exist at the water phase transition (a particular temperature and pressure in the chemistry model), leading to a somewhat consistent super Earth composition within a population.

This is contrasted with planets forming in the heat transition in the $R_0 = 66$ AU population which display a large range in ice abundances (regardless of elemental abundances considered) due to the trap migrating across the ice line during disk evolution. The trends shown in figure 4.16 do, however, apply to heat transition planets with the highest ice abundances. This subset of heat transition planets accrete all of their solids outside the ice line, acquiring the disk ice abundance that is dependent on the elemental ratios. While not shown, distribution of heat transition super Earths' ice abundances would be similar to figure 4.10 (left), with the maximum ice abundance set by the elemental ratios and the distribution extending to low ice contents.

Additionally, we do not show the composition distributions for dead zone planets formed in either R_0 population. The trends seen in figure 4.16 are driven by variances in ice abundances which only matter for planets that accrete material from outside the water ice line. Since dead zone planets

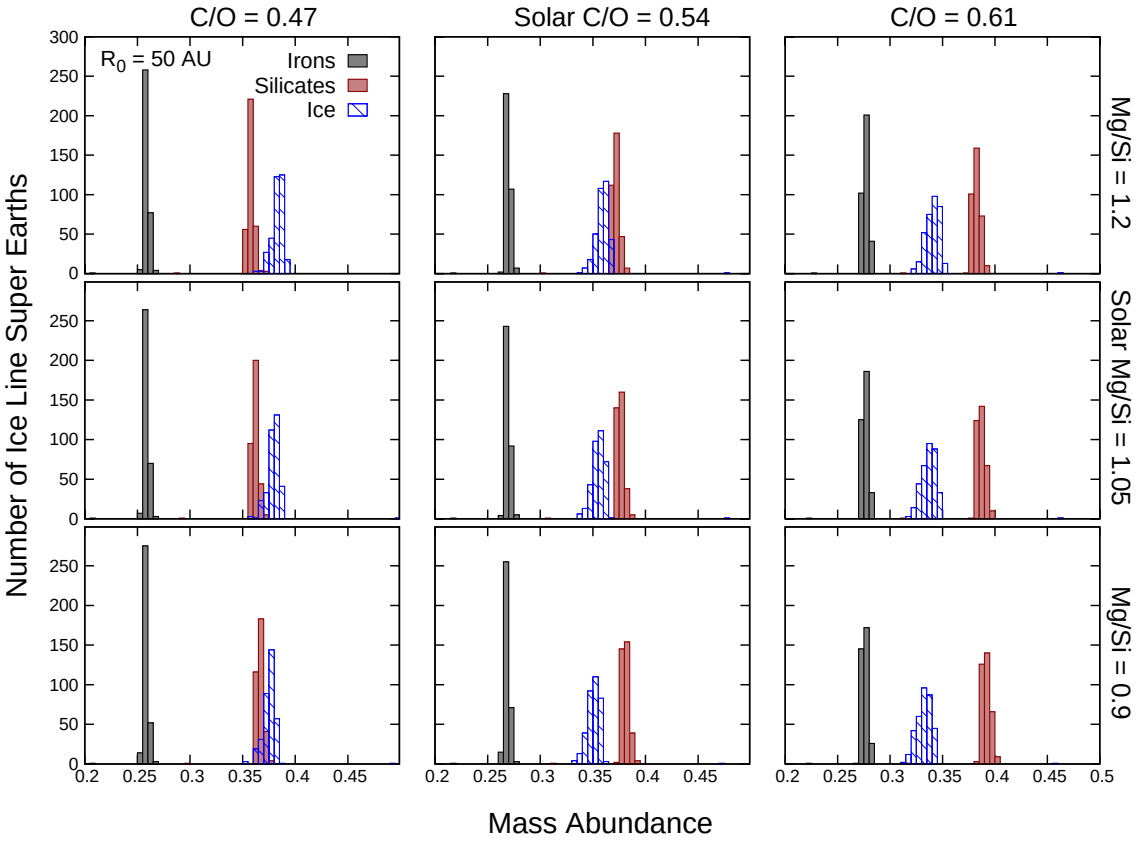

Figure 4.16: Solid abundance distributions are shown for zone 5 planets formed in the ice line from the $R_0 = 50$ AU population, computed using disk chemistry runs with different elemental abundances. The disk C/O ratio increases from left to right, and the Mg/Si ratio increases bottom to top. The ice contents on the planets increases most significantly as the C/O ratio is *decreased* and increases less significantly as Mg/Si is *increased*.

accrete from inside the ice line, they all acquire a similar ice-poor composition and distributions to those shown in figures 4.6 and 4.10. Since the ratio of the summed iron- and silicate-bearing minerals is unaffected by the disk C/O or Mg/Si values, the distribution of dead zone planets' compositions for all C/O and Mg/Si ratios is very similar to the metallicity-fit population previously shown.

Acknowledgements

The authors thank the anonymous referee for their insightful comments that have improved the quality of this paper. M.A. acknowledges funding from the National Sciences and engineering Research Council (NSERC) through the Alexander Graham Bell CGS/PGS Doctoral Scholarship and from an Ontario graduate scholarship. J.I. acknowledges funding from an NSERC-USRA research award. R.E.P. is supported by an NSERC Discovery Grant. This work made use of Compute/Caclul Canada. This research has made use of the NASA Exoplanet Archive, which is operated by the California Institute of Technology, under contract with the National Aeronautics and Space Administration under the Exoplanet Exploration Program.

Data availability

The data underlying this article will be shared on reasonable request to the corresponding author.

Corrigendum for Formation of Planetary Populations III: Core Composition & Atmospheric Evaporation

In our description of the observed M-R diagram in the super-Earth and Neptune mass range in figure 4.2, we incorrectly attributed the somewhat large uncertainties in planet masses to an uncertain inclination angle of the systems. Exoplanets on the M-R diagram have both a transit observation (measuring their transit radii) and a radial velocity observation (measuring their mass M_p, modulo the system's inclination angle i, as $M_p \sin i$). In order for these transit observations to be possible, it is necessary that the systems' inclination angles are near edge-on ($i \simeq 90$ degrees). Therefore, the uncertainties on the planet masses in the M-R diagram are *not* due to the uncertainty in their systems' inclination angles, but rather due to other factors contributing to uncertainty in planet masses in radial velocity measurements (such as stellar variability and measurement uncertainty).

Chapter 5

Effects of MHD Disk Winds - Driven Evolution

In this chapter we extend our investigation by considering a protoplanetary disk model whose evolution is driven by *both* magnetorotational instability (hereafter MRI)-turbulence and magnetohydrodynamics (hereafter MHD) disk winds. The following represents preliminary work towards an upcoming paper that is in preparation.

5.1 Introduction

In this thesis, we have carried out a detailed investigation of planet formation in disks evolving via MRI-turbulence, showing correspondence with many features of the planetary M-a and M-R relations by considering observationally-constrained ranges of disk properties. Underlying all of our studies is the physical structure and evolution of protoplanetary disks. We now aim to investigate the degree to which results of planet formation will change when the alternate disk-winds evolution mechanism is considered. A fundamental difference between MRI and MHD-winds is that the former sees disk evolution driven through the generation of turbulence and its associated effective viscosity, while the latter does not. Rather, in the disk-winds scenario, disks are predicted to be laminar with angular momentum exchange being achieved through an outflow of disk material along magnetic field lines threading the disk (Blandford & Payne, 1982; Pudritz & Norman, 1986). Using numerical MHD

models, Bai & Stone (2013) have shown that when MRI is suppressed, such as within a disk dead zone, disk winds can operate and drive disk evolution.

Assuming disk evolution takes place through MRI-turbulence has traditionally been a standard approach in core accretion models. The strength of disks' turbulent viscosities is established in models by the $\alpha_{\rm turb}$ parameter in the viscosity scaling of Shakura & Sunyaev (1973): $\nu = \alpha_{\rm turb} c_s H$, where c_s is the sound speed and H is the pressure scale height. In this treatment, the setting of $\alpha_{\rm turb}$ has a significant effect on disks' evolution timescales. While, in this regard, it is a fundamental parameter in disk studies, it is only loosely constrained observationally. This constraint is achieved by either matching the related evolution timescale to observationally inferred disk lifetimes (Hernández et al., 2007), or by matching the related accretion rates to those observationally inferred through Hα emission (Hartmann et al., 1998). These approaches result in an estimation for $\alpha_{\rm turb} \sim 10^{-4} - 10^{-2}$. It is important to note that these estimations assume that disk evolution is *solely* driven by turbulence.

However, there have been recent observational indications that disks exhibit a lower level of turbulence than expected on these bases. Observed levels of disk line-broadening (Flaherty et al., 2018) and studies of dust properties within pressure traps (Dullemond et al., 2018; Rosotti et al., 2020) carried out with ALMA observations have constrained the strength of turbulence in protoplanetary disks to an upper limit of $\alpha_{\rm turb} \lesssim 0.007$. High settings of $\alpha_{\rm turb} \sim 10^{-2}$ that have been considered in core accretion models are in disagreement with these observations. Therefore, acknowledging that disk evolution can take place through the *combined* effect of turbulence and winds, one may consider a more modest setting of turbulence while setting the disk wind strength such that the *overall* evolution timescale is consistent with observationally inferred disk lifetimes.

While the value of $\alpha_{\rm turb} = 10^{-3}$ we have used throughout this thesis is within observational limits, these recent observations indicate the importance of incorporating MHD-winds into disk evolution models. Our goal is to determine to what degree this alternate disk evolution scenario will affect results of planet formation. Recently, Chambers (2019) has developed an analytic model of disk evolution via the combined effects of turbulence and disk winds that has shown close resemblance to the numerical treatment of Suzuki et al. (2016). This analytic treatment has been readily incorporated into the framework we have developed throughout this thesis. It is advantageous for our purposes as it allows for the strengths of MRI and MHD-winds to be individually specified, and therefore models that incorporate both mechanisms at various relative strengths can be investigated.

We recognize that a fully self-consistent treatment of disk evolution via winds demands a numerical MHD approach with non-ideal MHD effects included (Ohmic dissipation, ambipolar diffusion, and the Hall effect). Other works have considered this detailed approach, wherein disk evolution is tied to the detailed ionization structure that depends on non-equilibrium chemistry (e.g. Bai & Stone (2013); Lesur et al. (2014); Gressel et al. (2015); Bai et al. (2016); Gressel et al. (2020); Rodenkirch et al. (2020)). Details of this computed disk structure under the effects of MHD processes can have significant consequences for migration of low-mass planets (McNally et al., 2017, 2018). The Chambers (2019) disk model we consider simplifies/neglects many of these complex issues, but remains useful as a simple means to understand the basic effects of winds on disk evolution and outcomes of planet formation in a computationally inexpensive framework.

The remainder of this chapter shows our early efforts towards understanding how disk evolution through a combination of disk winds and MRI-turbulence affects planet formation in our framework. While we have not yet computed full planet populations, our strategy at this stage is to instead investigate a handful of models that highlight the effects of disk winds. This is done by considering different settings of the relative strength of MRI-turbulence and MHD-winds and their related stresses driving disk evolution. As a means of foreshadowing results of a population synthesis run, we will establish the effect of changing the disk surface density (which is set by a combination of disk mass and radius) and lifetime on individual planet formation tracks. These tests will give a sense of the range of planet formation outcomes one might expect when full distributions of these disk parameters are sampled in a population run. In section 5.2, we will summarize the Chambers (2019) disk model which is a new addition to our treatment for this chapter. We will also detail the additions and constraints we have made to this disk model, before defining the individual models' parameter settings that we will investigate in results sections 5.3 and 5.4. Lastly, in section 5.5, we summarize our main conclusions and discuss extensions of this treatment that we will consider in future work.

5.2 Protoplanetary Disk Model: Combined Evolution Through Turbulence and Disk Winds

We consider the analytic disk model of Chambers (2019) which solves the disk evolution equation for the surface density $\Sigma(r,t)$,

$$\frac{\partial \Sigma}{\partial t} = \frac{3}{r}\frac{\partial}{\partial r}\left[r^{1/2}\frac{\partial}{\partial r}\left(r^{1/2}\nu\Sigma\right)\right] + \frac{1}{r}\frac{\partial}{\partial r}\left(r v_w \Sigma\right) - \dot{\Sigma}_w \ , \tag{5.1}$$

where the first term corresponds to the evolution driven via MRI-turbulent viscosity ν that is solved on its own in pure viscous models (i.e. Chambers (2009) that we have previously been using). The second and third terms both correspond to the effects of the disk wind, that can contribute both a stress driving disk accretion (second term), and an outflow (third term). Here, the former is characterized by v_w, the inward radial velocity caused by the disk wind, and the latter is characterized by $\dot{\Sigma}_w$, the rate of surface density loss due to the wind outflow.

Chambers (2019) introduces three parameters that correspond with each of these three physical effects:

- v_0; the inward velocity of material at $r_0 = 1$ AU, and T_0=150 K which is the disk temperature at r_0 caused *solely* from radiation (see equation 5.8 and following description). This parameter in large part sets the initial disk accretion rate $\dot{M}_0$.

- f_w; the fraction of v_0 that is caused by disk winds. Setting f_w=1 corresponds to a pure disk winds scenario, while setting f_w=0 corresponds to a pure viscous evolution.

- K; which characterizes the strength of the winds-driven outflow.

Solving the protoplanetary disk structure in this framework now introduces two additional parameters beyond the one ($\alpha_{\rm turb}$) that was needed in the pure viscous scenario. These three model parameters are related to the three individual disk evolution mechanisms in equation 5.1 as follows. The turbulent viscosity ν is related to f_w and v_0 as,

$$\nu = \frac{2}{3}(1-f_w) r_0 v_0 \left(\frac{r}{r_0}\right)^{3/2}\left(\frac{T}{T_0}\right) \ , \tag{5.2}$$

where T is the midplane temperature at radius r. The winds-driven velocity through the disk is,

$$v_w = f_w v_0 \left(\frac{T}{T_0}\right)^{1/2} . \tag{5.3}$$

Lastly, the surface density outflow rate depends on the parameter K as,

$$\dot{\Sigma}_w = \frac{K f_w v_0 \Sigma}{r_0} \left(\frac{r}{r_0}\right)^{-3/2} . \tag{5.4}$$

This equation can be integrated to determine the total mass outflow rate,

$$\dot{M}_{\rm wind} = \int_{R_{in}}^{R_{out}} 2\pi r \dot{\Sigma}_w {\rm dr} , \tag{5.5}$$

where R_{in} and R_{out} are the inner and outer disk radii, respectively.

A similar form of the disk evolution equation 5.1 was numerically solved in Suzuki et al. (2016). While three parameters are still used in their formalism (setting the strength of each of the three evolution mechanisms), the individual strengths of turbulence and disk winds are instead set using the standard α parameters; $\alpha_{\rm turb}$ and $\alpha_{\rm wind}$. The following equations can be used to convert between these parameters and the Chambers (2019) f_w and v_0 parameters,

$$\alpha_{\rm turb} = \frac{(1-f_w) r_0 v_0 \Omega_0}{c_{s0}^2} , \tag{5.6}$$

and,

$$\alpha_{\rm wind} = \frac{f_w v_0}{c_{s0}} . \tag{5.7}$$

Here, Ω_0 is the Keplerian angular frequency at the reference radius $r_0 = 1$ AU, and c_{s0} is the sound speed at reference temperature $T_0 = 150$ K.

The midplane temperature T is solved using (Lecar et al., 2006),

$$T^4 = T_0^4 \left(\frac{r}{r_0}\right)^{-2} + \left(\frac{3GM_* F}{8\pi\sigma_{\rm sb} r^3}\right)\left(\frac{3\kappa\Sigma}{8}\right) , \tag{5.8}$$

where G is the gravitational constant, M_* is the host-star mass, $F \simeq 3\pi\nu\Sigma$ is the mass flux due to turbulent viscosity-driven accretion, $\sigma_{\rm sb}$ is the Stefan-Boltzmann constant, and κ is the disk opacity. Here, the first term corresponds to heating from host-star radiation, and the second to heating via

viscous dissipation. In the absence of viscous heating, a pure radiative equilibrium $T_{\rm req}$ profile is obtained (i.e. Chiang & Goldreich (1997)),

$$T_{\rm req} = T_0 \left(\frac{r}{r_0} \right)^{-1/2} , \tag{5.9}$$

where T_0=150 K is the temperature at reference radius $r_0 = 1$ AU.

We note that, in equation 5.8, the viscous heating is only generated through turbulent viscosity, and not through a general dissipation of gravitational potential energy. In a pure winds scenario, then, there will be no viscous heating contribution, and the disk midplane temperature will be the radiative equilibrium profile. In this circumstance, the gravitational potential energy lost by accreting material will be carried away by the wind. This process has been recently investigated in Mori et al. (2019) using MHD simulations, who find that this general heating from gravitational dissipation is small compared to radiative or viscous heating ($\lesssim$ a 10% change to the midplane temperature), which confirms this result of the treatment of equation 5.8.

The disk opacity κ has an effect on the strength of viscous heating. As was the case in the previously considered pure viscous Chambers (2009) model, the Chambers (2019) model also takes the disk opacity to be constant $\kappa = \kappa_0$ throughout the majority of the disk's radial extent. The exception is in the innermost region above the evaporation temperature $T_{\rm evap} = 1500$ K where dust grains sublimate, and the opacity becomes a steeply decreasing function of temperature (Stepinski, 1998). While Chambers (2019) uses a small value of $\kappa_0 \simeq 0.1$ cm^2 g^{-1} that may arise following grain growth, we continue to use a disk opacity of $\kappa_0 = 3$ cm^2 g^{-1} in accordance with our previous disk model's treatment.

The disk accretion rate $\dot{M}_{\rm acc}$ is determined by calculating the mass flux across an inner radius R_{in}, for which Chambers (2019) uses 0.05 AU. The disk accretion rate is therefore,

$$\dot{M}_{\rm acc} = 2\pi R_{in} \Sigma(R_{in}) v(R_{in}) , \tag{5.10}$$

where the velocity of disk material at the inner radius $v(R_{in})$ scales with the velocity at 1 AU v_0 (a model input parameter) following,

$$v(R_{in}) = v_0 \left(\frac{T(R_{in})}{T_0} \right)^{1/2} , \tag{5.11}$$

where we recall that $T_0 = 150$ K is the temperature at reference radius 1 AU solely due to radiation. However, $T(R_{in})$ is the total midplane temperature at $R_{in} = 0.05$ AU from combined viscous and radiative heating.

In addition to the parameters listed, one also needs to specify the initial disk mass and radius for the model, which combine to set the characteristic surface density. The initial disk mass can be directly input, using for example $f_M = 0.1$ $M_\odot$, which is the average initial disk mass used in our population synthesis models. The initial disk radius is handled in the Chambers (2019) formalism through an exponential cutoff radius $r_{\rm exp}$ which scales with the outer disk radius. Chambers (2019) uses a setting of $r_{\rm exp} = 15$ AU that we also adopt. As the name suggests, the value of $r_{\rm exp}$ indicates the radius where the surface density profile begins to decrease sharply with further increase in r. As we will see, however, significant disk surface densities can exist well outside $r_{\rm exp}$, so this parameter does not immediately indicate the outer disk radius. Lastly, we consider all of our disk and planet formation models to take place around a Solar mass star.

We refer the reader to section 3 of Chambers (2019) for a detailed listing of the analytic equations that are solved. While this model provides the main framework for the disk models investigated throughout this chapter, we make the following additions.

First, to reduce disk model parameters, we relate the strength of the outflow as parameterized by K (i.e. equations 5.4 and 5.5) to the disk accretion rate (equation 5.10) following a result of disk wind theory (Pudritz & Norman, 1986),

$$\frac{\dot{M}_{\rm wind}}{\dot{M}_{\rm acc}} \simeq 0.1 \ . \tag{5.12}$$

This relation has also been observationally confirmed for a large sample of systems in Watson et al. (2016). By solving equation 5.12 at time $t = 0$ for a particular disk model's specification of $\alpha_{\rm turb}$ and $\alpha_{\rm wind}$, the constant K can be solved for as opposed to being an input parameter. This method reduces our list of disk input parameters by one. We highlight that only low settings of $K \lesssim 0.1$ are needed to solve equation 5.12. The large values of $K = 1$ that are used in example disk models in Chambers (2019) are then in contention with this constraint provided by equation 5.12, as a setting of $K = 1$ results in $\dot{M}_{\rm wind} \gtrsim \dot{M}_{\rm acc}$.

We also determine the location of the dead zone throughout disk evolution, as resulting from Ohmic dissipation. We recall that within the dead zone, the disk ionization fraction is insufficient

for the MRI instability to operate. To determine the dead zone's location, we use the same approach taken in previous chapters, following Matsumura & Pudritz (2003) and assuming disk ionization is caused by host-star X-rays. This approach results in the following criteria for an MRI-active disk, written in terms of the Ohmic Elsasser number (Simon et al., 2013),

$$\Lambda = \frac{v_A^2}{\eta_O \Omega} \lesssim 1 \, , \tag{5.13}$$

where v_A is the Alvén speed, η_O is the Ohmic diffusivity, and Ω is the local Keplerian orbital frequency. We refer the reader to section 2.3.2 for a complete description of our dead zone model. As we will show in later sections, this method results in the outer edge of the dead zone $\lesssim$20-30 AU and evolving inwards with time, similar to its evolution in the previously considered Chambers (2009) framework.

An improvement we make in our treatment of the dead zone is that, in the Chambers (2019) framework, we can set different turbulence strengths with the $\alpha_{\rm turb}$ parameter inside and outside the dead zone. For example, following Hasegawa & Pudritz (2010), we reduce $\alpha_{\rm turb}$ by two orders of magnitude inside the Ohmic dead zone, while maintaining a constant disk accretion rate as set by the parameter v_0. What this means physically, is that within the Ohmic dead zone, the stress related to disk winds increases so as to maintain a radially-constant disk accretion rate (i.e. following the result of Bai & Stone (2013)). We specify our choice of $\alpha_{\rm turb}$ settings for our various disk models in section 5.2.2. This treatment is an improvement of our previous handling of the dead zone, for which the dead zone was "passive" in the sense that we determined its outer edge's location, but it had no physical effect on the disk structure so as to not break the assumed self-similarity of the Chambers (2009) model. Here, the dead zone has a more self-consistent effect on the disk structure, as its outer edge separates two distinct regions with different strengths of $\alpha_{\rm turb}$ and $\alpha_{\rm wind}$.

We have also investigated ambipolar diffusion (hereafter AD; another non-ideal MHD effect) in its ability to affect the dead zone's structure along the disk midplane. Following Bai & Stone (2011), this investigation was done by solving for the AD parameter Am throughout the disk,

$$\mathrm{Am} = \frac{\mathrm{v_A^2}}{\eta_{\rm A} \Omega} \, , \tag{5.14}$$

where η_A is the ambipolar diffusivity. The parameter Am is AD's counterpart to the Ohmic Elsasser number, in that it quantifies how effective AD and its diffusivity will be in suppressing MRI growth. This calculation resulted in Am values of 100-1000 throughout the disk's extent along the midplane for fiducial disk settings and $\alpha_{\rm turb} = 10^{-3}$. At this setting of $\alpha_{\rm turb}$, Bai & Stone (2011) show that MRI would only be suppressed at values of the plasma $\beta \equiv P_{\rm gas}/P_{\rm B}$ (a ratio of gas to magnetic pressure) near 0.1-1. Therefore, AD will only suppress the MRI and create an "AD dead zone" in the most tenuous regions of the disk, such as in the disk's outer extent, or well above the disk midplane. This result is in accordance with the commonly-found conclusion that AD affects MRI turbulence only in the lowest density regions of the disk (e.g. Armitage 2011; Simon et al. 2013). We therefore do not include AD in our disk models, and the dead zone location we determine is only due to the effect of Ohmic dissipation.

5.2.1 Planet Formation & Migration

We follow the same approach of computing core accretion models and trapped type-I migration as has been used throughout this thesis (i.e. chapters 2 & 3). The planet traps we include in our model are the ice line, heat transition, and outer edge of the dead zone. In the cases of the ice line and heat transition, the method by which their locations are calculated has been altered slightly in this new disk framework.

We simply define the ice line as the location along the disk midplane where the temperature is 170 K. Our models previously computed the full disks' equilibrium chemical structures to determine the phase-transition point of water. We have found that in all cases the resulting ice line location (defined where the abundance of water vapour and ice are equal) has a midplane temperature of 170 K. While, in the Chambers (2009) model, the heat transition separating viscous and radiative heating was directly calculated, in the new Chambers (2019) model it is not. We define the heat transition at the point where the temperature due to viscous heating $T_{\rm vis} = 0.5\,T_{\rm req}$. Since the total midplane temperature is $T^4 = T_{\rm vis}^4 + T_{\rm req}^4$, this definition corresponds to viscous heating contributing a $\sim 6\%$ to the radiative equilibrium temperature. The method of computing the dead zone's outer edge remains the same, following Matsumura & Pudritz (2003) for an X-ray ionized disk.

Details of our planet formation model remain unchanged, and we continue to use the best fit values related to forming planets' envelope opacities found in chapter 2. As we will be calculating individual planet formation tracks as opposed to full populations, we set $f_{\rm max} \equiv M_{\rm max}/M_{\rm gap} = 50$ to

terminate gas accretion onto massive planets, instead of sampling from a distribution to determine $f_{\rm max}$. As a simplifying assumption, we consider a constant dust-to-gas ratio of $f_{\rm dtg} = 0.01$, and do not include dust evolution effects (i.e. radial drift) in this preliminary study. This assumption removes the computational expense of solving the Birnstiel et al. (2012) dust evolution model. While radial drift will have an effect on planet formation models and certainly adds a layer of complexity to this problem, our goal is to focus first on understanding the basic effects of disk evolution via winds on planet formation. In this regard, we are following the approach we took for the turbulent disk model (Chambers, 2009), where we first considered a constant dust-to-gas ratio model (chapter 2) before the more complex scenario of incorporating dust evolution (chapter 3). Lastly, we maintain a Solar metallicity in our models such that $f_{\rm dtg} = 0.01$. As we extend this model into a population synthesis framework in the future, this assumption will be relaxed so as to include a full metallicity distribution in its effect on $f_{\rm dtg}$ and solid accretion rates.

5.2.2 Defining Investigated Models: Disk Parameter Settings

We now define the various disk models and their parameters' settings we will investigate in the following results chapters.

First, in section 5.3, we will compare disk models at two different relative strengths of $\alpha_{\rm turb}$ and $\alpha_{\rm wind}$. In the first case, which we refer to as the "turbulent dominated model" (or "turbulent model" for short), we set $\alpha_{\rm turb} = 10^{-3}$ which is the same setting we have used throughout this thesis. The second, "combined turbulence & winds model" (which we refer to as the combined model, for short) considers $\alpha_{\rm turb} = 10^{-4}$, an order of magnitude lower. In both cases, the fiducial models are normalized using the setting of parameter v_0 such that they have the same initial accretion rate $\dot{M}_{0,\rm fid} \simeq 6 \times 10^{-8}$ M$_\odot$ yr^{-1}. This value of $\dot{M}_{0,\rm fid}$ compares reasonably with initial accretion rates calculated using the previous disk model (Chambers, 2009), and also with observationally-inferred accretion rates from Watson et al. (2016). This normalization results in the turbulent model having an $\alpha_{\rm wind} \simeq 2.5 \times 10^{-4}$, and the combined model $\alpha_{\rm wind} \simeq 2.7 \times 10^{-4}$.

In figure 5.1, we summarize the turbulent-dominated and combined models by plotting snapshots of their α parameters across the disks' extents. In both models, within the MRI dead zone, $\alpha_{\rm turb}$ is decreased by two orders of magnitude. This reduction is shown clearly on the plots of figure 5.1 as a transition at the outer edge of the dead zone r_{dz}, whose location is shown for this example at time $t = 0$ in the disk's evolution. This transition point, being the dead zone trap, evolves inwards with

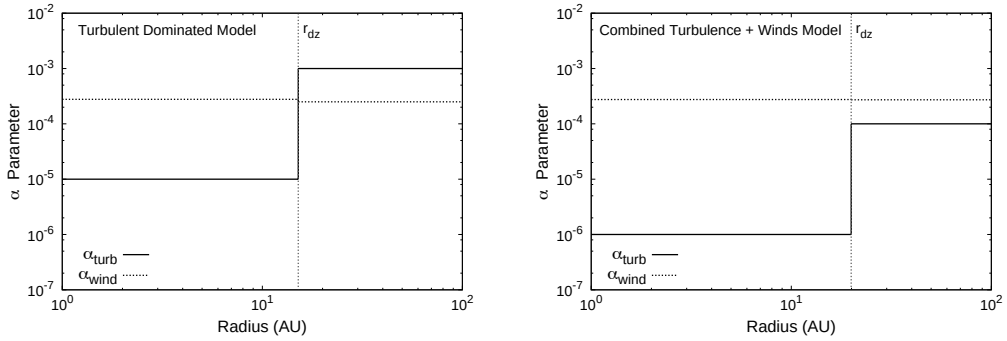

Figure 5.1: We show snapshots at t=0 of the turbulent dominated (left) and combined turbulence & winds (right) models by plotting the $\alpha_{\rm turb}$ and $\alpha_{\rm winds}$ parameters across their disks' extents, where the decrease in $\alpha_{\rm turb}$ by two orders of magnitude at the outer edge of the dead zone (r_{dz}) is shown. This transition point (the dead zone trap) evolves inwards with time throughout the disk's evolution. We normalize both models by using the same initial disk accretion rate $\dot{M}_0 \simeq 6 \times 10^{-8}$ $\rm M_\odot$ $\rm yr^{-1}$.

time as the disk evolves. We see that only a small increase in $\alpha_{\rm wind}$ is needed at r_{dz} to maintain a radially-constant disk accretion rate despite $\alpha_{\rm turb}$ decreasing by two orders of magnitude at this location.

We note that in the Chambers (2019) model, quite a large disk winds fraction $f_w \simeq 0.8$ is required to produce $\alpha_{\rm turb} = 10^{-3}$. Using a "pure" turbulence setting of $f_w = 0$ leads to $\alpha_{\rm turb} \simeq 0.02$ at this value of $\dot{M}_{0,\rm fid}$, over an order of magnitude larger than the setting we considered in previous chapters. Therefore, even in the turbulent model, a substantial fraction ($\sim 80\%$) of disk accretion is generated from disk winds and its related stress.

Other factors that affect the disks' initial accretion rates are the settings of the initial disk mass f_M and radius, which scales with the exponential cutoff radius $r_{\rm exp}$. Following Chambers (2019), we set $r_{\rm exp} = 15$ AU for all models. We then set the initial disk mass f_M such that the initial surface density at reference radius 1 AU is,

$$\Sigma_0 \equiv \Sigma(r_0 = 1\,{\rm AU}, {\rm t} = 0) = 1500\,{\rm g\,cm^{-2}} \equiv \Sigma_{0,\rm fid}\ . \tag{5.15}$$

This value of $\Sigma_{0,\rm fid}$ corresponds to initial disk masses $\simeq 0.05$ $\rm M_\odot$ in both the turbulent and combined models. A surface density of 1500 g $\rm cm^{-2}$ is similar to Σ_0 values in fiducial models investigated in the previous Chambers (2009) framework.

In section 5.3, we also determine how the setting of Σ_0 affects results planet formation, as a means of foreshadowing the outcomes of a full population synthesis calculation. For both the turbulent and combined models, in addition to the fiducial setting, we consider a high setting $\Sigma_0 = 3\,\Sigma_{0,\rm fid}$ and a low setting $\Sigma_0 = (1/3)\,\Sigma_{0,\rm fid}$. While ultimately these changes are achieved by altering the initial disk mass, we label these models in terms of their Σ_0 value since the differences in surface densities can arise from a combination of changes to the initial disk mass and radius. Furthermore, the disk surface density is the physical parameter responsible for setting planet formation timescales. We note that we would arrive at similar planet formation results if we were to instead keep f_M constant and alter the disk radius $r_{\rm exp}$, provided the same values of Σ_0 and $\dot{M}_0$ were considered. The wind outflow is constrained according to equation 5.12 in all models presented in section 5.3.

Lastly, in section 5.4, we shift our focus to a winds-dominated disk model and examine the effect of the outflow strength. In these models, we set $\alpha_{\rm turb} = 10^{-6}$, which is the turbulent strength within the dead zone of the combined model in section 5.3. We continue to use an initial disk mass of f_M = 0.05 $\rm M_\odot$, the fiducial setting in both the turbulent and combined models. Obtaining an initial disk accretion rate $\dot{M}_0 = 6 \times 10^{-8}$ $\rm M_\odot$ $\rm yr^{-1}$ requires $\alpha_{\rm wind} \simeq 2.7 \times 10^{-4}$. This value is similar to settings of $\alpha_{\rm wind}$ in the previous models. However, given the low setting of $\alpha_{\rm turb} = 10^{-6}$, the relative strength of disk winds is much higher.

In the first "constrained outflow" model, we follow our approach of constraining the wind outflow parameter K according to equation 5.3. This constraint results in a small value of $K \simeq 0.05$. In the second model, we do not account for the constraint provided by equation 5.12, and instead adopt a high setting of $K = 1$ as was used in Chambers (2019). We refer to this as the "unconstrained outflow" model. While this model leads to very high wind outflow rates that are comparable to, or higher than the disk accretion rate (in contention with disk winds theory and observations), we will see that a very efficient wind outflow has interesting effects on disk evolution, giving rise to a surface density maximum within the disk.

Table 5.1 summarizes each of the models we investigate in sections 5.3 and 5.4 and their parameters.

Table 5.1: A summary of model parameters. The turbulent-dominated and combined turbulence & winds models are investigated in results section 5.3, while the winds-dominated models are investigated in section 5.4.

Model	Outside r_{dz}	Inside r_{dz}
Turbulent-Dominated	$\alpha_{\rm turb} = 10^{-3}$	$\alpha_{\rm turb} = 10^{-5}$
Fiducial Σ_0	$\Sigma_0 = \Sigma_{0,\rm fid} = 1500$ g cm^{-2}	
High Σ_0	$\Sigma_0 = 3\,\Sigma_{0,\rm fid}$	
Low Σ_0	$\Sigma_0 = (1/3)\,\Sigma_{0,\rm fid}$	
Combined Turbulence & Winds	$\alpha_{\rm turb} = 10^{-4}$	$\alpha_{\rm turb} = 10^{-6}$
Fiducial Σ_0	$\Sigma_0 = \Sigma_{0,\rm fid} = 1500$ g cm^{-2}	
High Σ_0	$\Sigma_0 = 3\,\Sigma_{0,\rm fid}$	
Low Σ_0	$\Sigma_0 = (1/3)\,\Sigma_{0,\rm fid}$	
Winds-Dominated	$\alpha_{\rm turb} = 10^{-6}$	No dead zone
Fiducial Σ_0	$\Sigma_0 = \Sigma_{0,\rm fid} = 1500$ g cm^{-2}	
Constrained outflow	K from equation 5.12	
Unconstrained outflow	$K = 1$	

5.3 Results I: Effect of relative strength of turbulence and disk winds

In figure 5.2, we compare the evolution of the turbulent-dominated and combined disk models to discern the effect of the the relative strength of turbulence and disk winds. We plot the disks' accretion rates, as well as radial profiles of surface densities and midplane temperatures throughout 3 Myr of evolution at the fiducial Σ_0 setting. For both models the disk accretion rate decreases by roughly 1.5 orders of magnitude below the initial accretion rate of $6{\times}10^{-8}$ M$_\odot$ yr^{-1} after 3 Myr, decreasing slightly more in the combined model. This range of $\dot{M}$ is quite comparable to those resulting from the previous Chambers (2009) models with fiducial parameters.

The inhomogeneities present within the radial surface density and temperature profiles correspond to the outer edge of the dead zone, where there is a local change in the strength of $\alpha_{\rm turb}$. Comparing the two models' surface density evolutions in the outer disk (at radii near 70-100 AU), we see a key difference between disk evolution via turbulence and winds. In the viscous evolution case, we see a small amount of spreading in the outer disk - a necessary consequence of angular momentum conservation within the viscous evolution mechanism. This spreading does not occur in the combined model where winds-driven evolution is more prominent, and in this circumstance the disk, in fact, slightly contracts. We recall that the former 'turbulent' model required quite a high disk winds fraction $f_w \simeq 0.8$ to set $\alpha_{\rm turb} = 10^{-3}$. Since a small fraction ($\simeq 20\%$) of accretion is a consequence

of turbulent viscosity, there is only a small amount of spreading in the outer disk. We note that a more extreme turbulent model of $\alpha_{\rm turb} = 10^{-2}$, as considered in Chambers (2019), shows more significant amount of viscous spreading.

While these differences between the two models exist in the outer disk regions owing to differences in relative disk wind strength, the inner 10 AU of the two disks are relatively comparable in terms of their surface densities. Recalling our previous planet formation results, this is the region where most planet formation occurs due to low solid accretion rates at larger radii (with core accretion rate scaling with Σ). We see that the Σ profiles of the two models are quite comparable in the inner 10 AU, particularly for the first 2 Myr. The more rapid evolution of the combined model becomes apparent on the surface density profile at 3 Myr, where Σ is noticeably smaller in the combined model than in the turbulent scenario. On the basis of comparing the two models' (somewhat similar) surface densities, and noting that planetary growth via solid accretion is a relatively fast formation regime (< 1 Myr), we do not expect significant differences in core accretion rates between the two models.

When plotting the disk midplane temperature profiles in figure 5.2, we include the radiative equilibrium profile (equation 5.9) to indicate the regions where viscous heating is effective in both models. The turbulent and combined models are revealed to be quite different in terms of their temperature structures. Viscous heating is more pronounced in the turbulent model due to the higher value of $\alpha_{\rm turb}$, resulting in the viscously heated region (where $T > T_{\rm req}$) extending to larger radii. We also see that at the location of the dead zone, where $\alpha_{\rm turb}$ decreases by a factor of 100, the midplane temperatures decrease towards the radiative equilibrium profile. This decrease is due to the lower turbulence strength within the disks' dead zones, which results in less effective viscous heating. We therefore find that there are substantial differences between the turbulent and combined models in terms of their midplane temperatures. Since two of the traps in our model (the ice line and heat transition) depend on the disk midplane temperature, we expect the locations of these traps to be quite different between the two models. While not considered here, the difference in the traps' locations will also cause a significant difference between the models' chemical abundance profiles, which will depend most sensitively on the disks' temperature structures.

In figure 5.3, we investigate differences in the planet traps' locations and evolutions between the two models at the fiducial setting of Σ_0. We indeed find that the temperature-dependent traps, the heat transition and ice line, exist at larger radii in the turbulent model due to the increased viscous heating. Conversely, the outer edge of the dead zone lies farther out in the combined model than

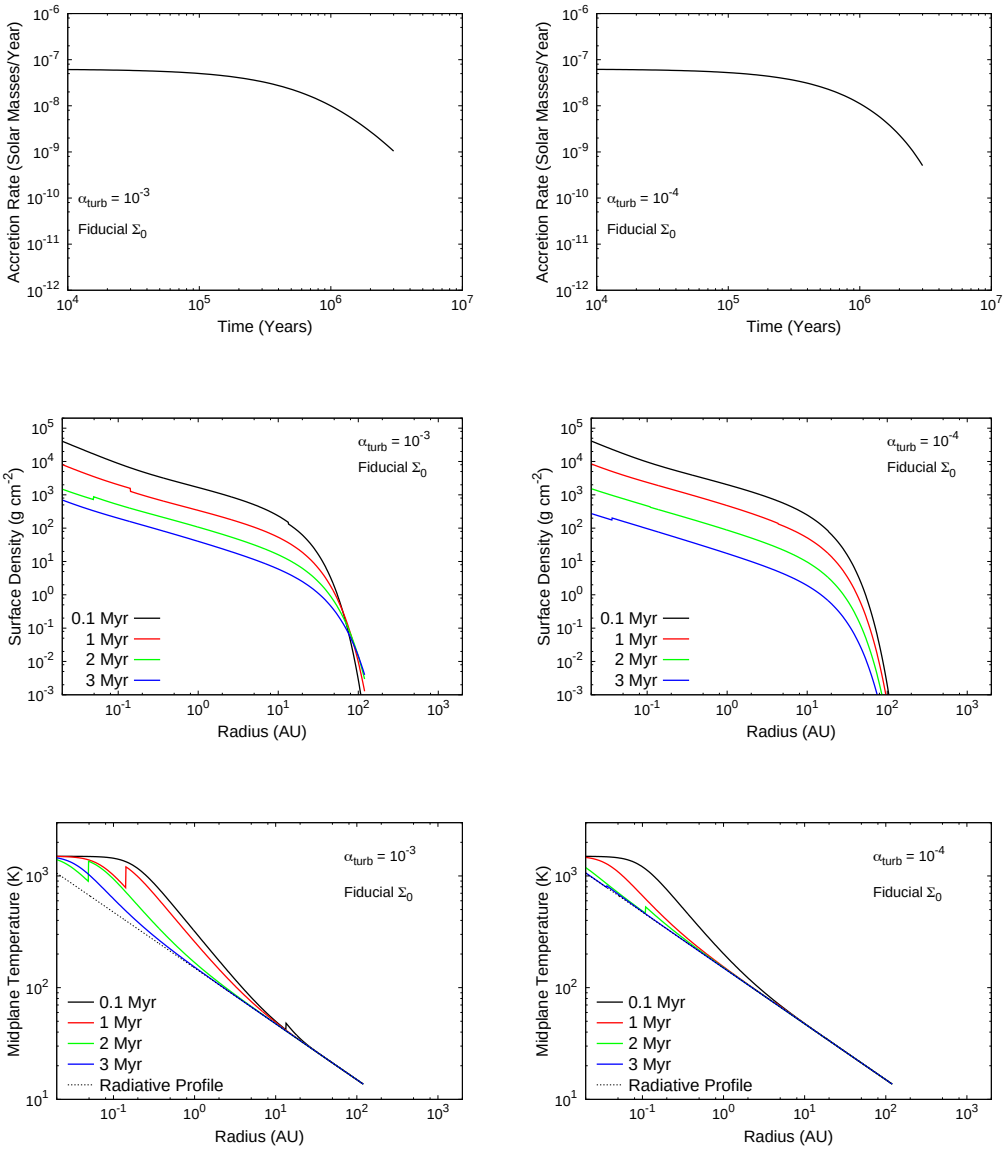

Figure 5.2: We compare protoplanetary disk evolution in the 'turbulent' ($\alpha_{\rm turb}$=10^{-3}; left column) and 'combined' turbulence and winds ($\alpha_{\rm turb}$=10^{-4}; right column) cases. Both disks are normalized to the fiducial setting of Σ_0. Time evolution of the disk accretion rate is plotted in the top row, and profiles of surface density and midplane temperature are plotted throughout disk evolution in the middle and bottom rows, respectively.

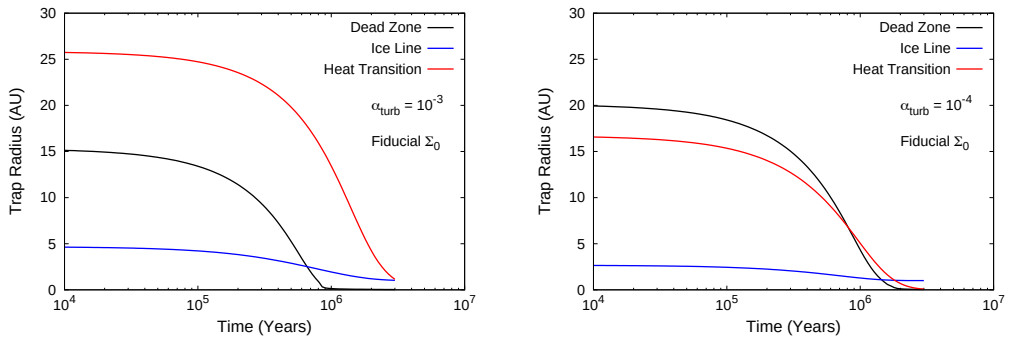

Figure 5.3: Planet traps' evolutions are plotted for the turbulent (left) and combined (right) disk models, both considering a fiducial setting of Σ_0.

in the turbulent case, despite their surface density profiles being similar. While the midplane X-ray ionization is sensitively dependent on the Σ profile, there are several temperature-dependent factors in the dead zone model (recombination rates, Ohmic diffusivity η_O, etc). These factors, combined with the differences in the disks' temperature structures and evolution, ultimately affect the location of the outer edge of the dead zone where the Elsasser number $\Lambda = 1$.

We see from figure 5.3 that within a typical disk lifetime of 3 Myr, all the traps in our model converge to within $\lesssim$ 3 AU. We therefore predict that substantial solid accretion rates can exist on planetary cores undergoing trapped type-I migration at these traps' locations, as high surface densities persist in both disk models' inner regions even after 2-3 Myr of evolution. In the combined model, all traps exist within 10 AU after only 1 Myr of disk evolution. Conversely, in the turbulent model, this is only the case for the ice line and dead zone, and the heat transition evolves within 10 AU after $\sim$ 2 Myr of disk evolution. Planet formation will be most efficient within 10-20 AU based on the disks' surface density profiles (which set the solid accretion timescales) that decrease sharply outside of this radius range. At the fiducial Σ_0, the traps' evolution to within this region by 1 Myr in the combined model indicates that planet formation will be effective in each of the three traps. In the turbulent model, we expect this to be also true for formation in the ice line and dead zone traps. Formation within the heat transition in the turbulent model, however, will likely result in much longer formation timescales, due to its large radius at times up to 2 Myr.

The evolution of planet traps in the turbulent-dominated model using the new disk framework of Chambers (2019) can be compared with that of the previously investigated pure turbulence disk model (Chambers, 2009). We refer the reader to figure 2.5, which shows the traps' evolution for a

fiducial set of model parameters within this purely viscous disk model. The pure turbulence case sees a different initial ordering of planet traps, with the X-ray dead zone being the farthest out in the disk, followed by the heat transition and ice line which lie consecutively closer to the star. In the case of the turbulent-dominated model in the Chambers (2019) formalism, there is a different initial ordering, with the heat transition now being the outermost trap, followed by the dead zone, and again the ice line. In this regard, we see that, despite using the same $\alpha_{\rm turb} = 10^{-3}$ value, the different disk models do change the locations and relative ordering of the planet traps. We attribute this difference to the fact that the turbulent-dominated model in the Chambers (2019) disk requires 80% of disk accretion to be driven by disk winds. The two disk models are similar, however, in that the traps rather quickly evolve into the inner disk ($\lesssim$ 10 AU). In both disk models, the dead zone does so faster ($\lesssim$ 1 Myr) than the heat transition, which shifts to within 10 AU after about 2 Myr.

We now investigate our predictions by showing planet formation tracks in figure 5.4. Planet formation models are calculated for each of the two models (turbulent and combined), and at 3 settings of Σ_0: fiducial, high, and low (as described in section 5.2.2). We incorporate this variance in Σ_0 to give an indication of the effect that varied disk masses and radii will have on results of planet formation. While our planet formation models are calculated in long-lived 10 Myr disks, we include time marks along each planet formation track at 1 Myr intervals. This demonstrates the effect that disk lifetime will have on these models, as shorter lifetimes will simply truncate the formation tracks at positions in the M-a diagram as indicated by the time marks. This grid of planet formation models therefore contains a significant amount of information alluding to the outcomes of full population synthesis calculations, as it shows the effect of two of the most crucial varied disk parameters; namely the disk mass and lifetime.

We first examine the fiducial Σ_0 case for the turbulent model. We see that formation within each of the 3 traps gives rise to gas giants across a wide span of orbital radii when a 10 Myr disk lifetime is used. The ice line produces a warm gas giant at $\sim$0.6 AU after 3 Myr. Its position in the disk within 5 AU for the entirety of the disk's evolution results in efficient planet formation in this trap. The dead zone forms a hot Jupiter at $\sim$0.07 AU after only 2 Myr, due to its rapid inward migration into the inner, high density regions of the disk. The heat transition also forms a hot Jupiter at $\sim$0.06 AU, but requires the full 10 Myr disk lifetime to do so. Disk lifetimes of 4-9 Myr would truncate the heat transition planet's formation within the super Earth region of the M-a diagram between 0.06-0.4 AU. This result confirms that the heat transition's large radius and slow inward migration

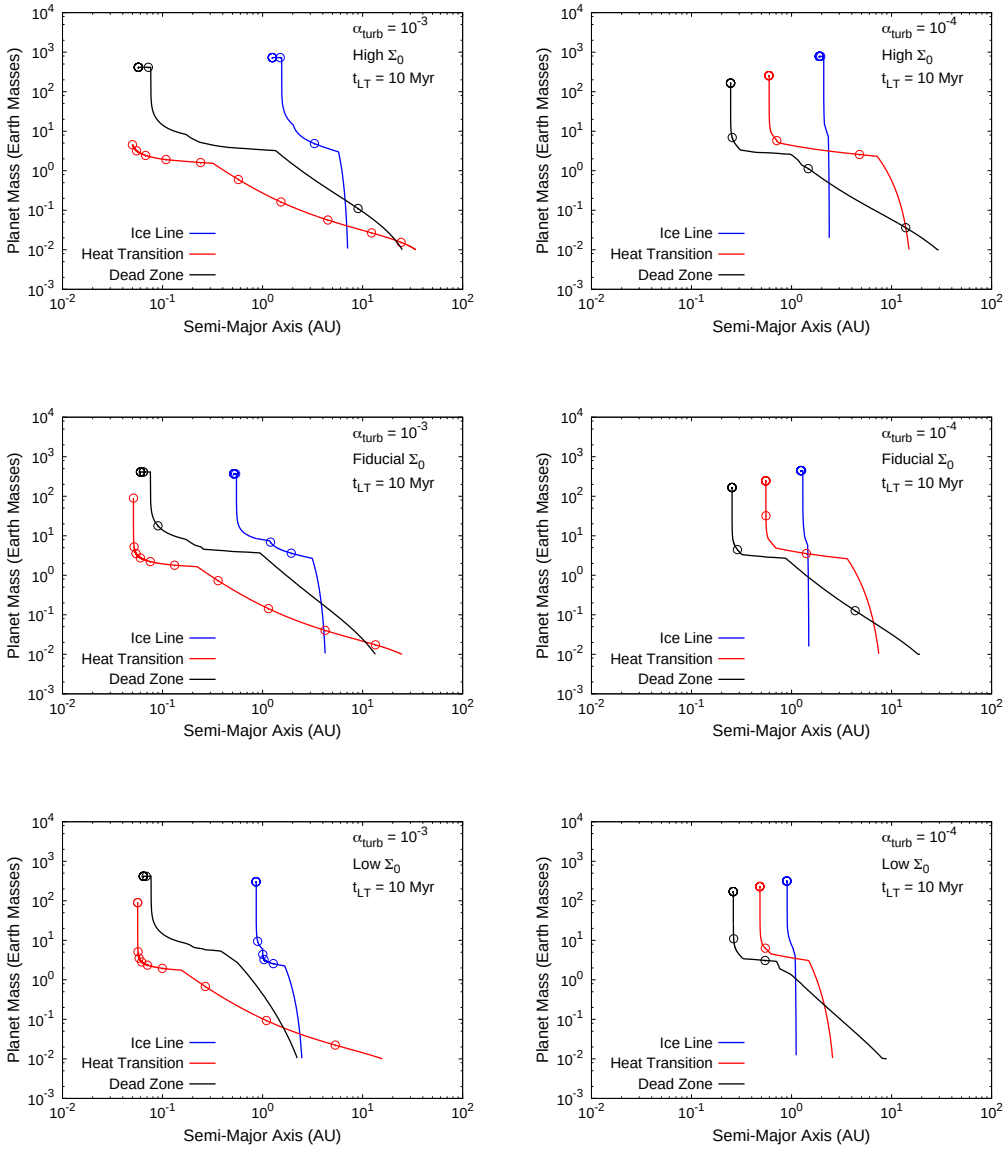

Figure 5.4: We show a grid of planet formation tracks pertaining to the turbulent (left column) and combined (right column) disk models. We investigate the effect of disk surface density Σ_0 by considering three settings: high $\Sigma_0 = 3\ \Sigma_{0,\mathrm{fid}}$ (top row), fiducial $\Sigma_{0,\mathrm{fid}}$ (middle row), and low $\Sigma_0 = 0.33\ \Sigma_{0,\mathrm{fid}}$ (bottom row). All models assume a long disk lifetime of 10 Myr. Open circles along the formation tracks indicate planets' positions at 1 Myr intervals, indicating their positions if a shorter disk lifetime were to be considered.

results in the trap being relatively inefficient for planet formation in this model.

Changing the disk surface density has two counteracting effects on planet formation rates. Increasing the disk surface density gives rise to higher accretion rates at a given orbital radius r. However, the second effect that opposes this higher accretion rate is that increasing the surface density also results in the positions of planet traps being shifted radially outwards to regions with lower Σ. This shift is as a result of the higher surface densities throughout the disk, and correspondingly larger viscous heating. Therefore, planets forming at a given trap in models with different Σ_0 values will accrete at different radii. When comparing the effect of disk surface density on planet formation, then, one should consider the net effect on the *local* accretion rate at the traps' positions.

In the case of the high Σ_0 turbulent model, the ice line again produces a warm gas giant, but its final position is outside 1 AU and it forms in only 2 Myr. The dead zone planet's formation is similar to the fiducial model, resulting in a hot Jupiter at roughly 0.07 AU after 2 Myr. Even after 10 Myr of formation, the heat transition is only able to produce a super Earth at roughly 0.06 AU. In this case, the outward shift of the trap with the increase in Σ_0 was sufficient to reduce its accretion such that the trap failed to produce a gas giant. The high Σ_0 model is interesting in that it produces each of the three main classes of observed exoplanets: a super Earth, a hot Jupiter, and a warm Jupiter.

When examining the low Σ_0 turbulent scenario, we find that this model also results in the ice line producing a warm gas giant at roughly 1 AU. However, its formation time increases to 5 Myr. Since the ice line's location in the disk is relatively insensitive to Σ_0, the formation timescale at this trap intuitively scales with disk surface density. This formation track shows that an appreciable range of disk lifetimes, 1-4 Myr, will truncate this planet's formation and result in a super Earth or Neptune between 1-2 AU. The decrease in Σ_0 from the fiducial setting has a significant effect on the locations of the dead zone and heat transition traps, and ultimately results in their formation timescales decreasing. The dead zone again forms a hot Jupiter at 0.07 AU, but in this model does so within 1 Myr. The heat transition forms a hot Jupiter at 0.06 AU in 9 Myr. This formation track also shows that a large range of disk lifetimes, in this case 3-8 Myr, will result in the formation of a super Earth with orbital radius between 0.06-0.3 AU.

We highlight that, when considering the formation tracks for the turbulent-dominated model, we have reproduced our result from chapter 2 (for which this model is most directly comparable; i.e. $\alpha_{\rm turb} = 10^{-3}$, constant $f_{\rm dtg} = 0.01$) even though we are using a different disk model. Namely, when using an X-ray ionized disk and its related dead zone, there is a clear separation between warm gas

giants formed near 1 AU in the ice line, and hot Jupiters formed within 0.01 AU from the dead zone. Based on the results of figure 5.4, we expect that this result will remain even when a full population is considered with distributions of disk lifetimes and Σ_0. With that said, it should be recalled that this is indeed a different model, with disk winds carrying a significant amount ($\sim 80\%$) of angular momentum.

We now analyze planet formation tracks corresponding to the combined turbulence and winds models in figure 5.4. We find a much more compact configuration among gas giants that are formed in each of the three traps at all settings of Σ_0 than we found in the turbulent model. In this circumstance, the formed gas giants have the most compact orbital configuration at low Σ_0, and the largest span of orbital radii is encountered in the high Σ_0 case. The ice line forms a gas giant within 1 Myr at each investigated Σ_0. The ice line forms gas giants at the largest separation from the host star among each of the traps. Their radii range from 1-2 AU, shift outwards slightly as Σ_0 is increased. The ice line is thus extremely efficient in gas giant formation in the combined model, which is a result of its location within 3 AU for the entire disks' evolution.

In contrast to the turbulent model, the heat transition produces gas giants at ~ 0.6 AU in 2-3 Myr of disk evolution in the combined model, with shortest formation times corresponding to the low Σ_0 case. The final orbital radius of the resulting gas giant is insensitive to the setting of Σ_0. In the combined model, the smaller amount of viscous heating results in the heat transition existing at a smaller orbital radius where disk surface densities are higher. This shift to smaller orbital radii increases the efficiency of planet formation in this trap when compared to the turbulent model.

In the combined model, formation in the dead zone trap is also quite different. The trap produces gas giants between 0.2-0.3 AU whose orbital radii are also quite insensitive to Σ_0. These planets' formation timescales are between 3-4 Myr, with shortest formation timescales pertaining to the lower Σ_0 cases. Comparing to the turbulent model, the dead zone's location in the combined scenario is at a larger radius. The trap rapidly evolves inwards in both cases. While in the turbulent model, this trap exclusively produced hot Jupiters within 1-2 Myr, the larger initial radius of the dead zone in the combined scenario results in gas giants forming with longer formation times and larger final orbital radii.

In table 5.2, we summarize the results of our planet formation models shown in figure 5.4. As an overall comparison between the turbulent and combined models, we find that a larger range of planet formation outcomes are achieved in the turbulent case when varying the disk lifetime and surface

Table 5.2: A summary of the final planet masses and orbital radii (at the end of each disk's 10 Myr-lifetime) in each model shown in figure 5.4, where we investigated the effect of different Σ_0 values on planet formation results in both the turbulent-dominated and combined turbulence & winds models.

Model	Ice Line a_p, M_p	Heat Transition a_p, M_p	Dead Zone a_p, M_p
Turbulence-Dominated Model			
High Σ_0	1.3 AU, 729 $M_\oplus$	0.05 AU, 4.6 $M_\oplus$	0.06 AU, 414 $M_\oplus$
Fiducial Σ_0	0.5 AU, 372 $M_\oplus$	0.05 AU, 89 $M_\oplus$	0.06 AU, 411 $M_\oplus$
Low Σ_0	0.86 AU, 303 $M_\oplus$	0.06 AU, 90 $M_\oplus$	0.06 AU, 418 $M_\oplus$
Combined Turbulence & Winds Model			
High Σ_0	1.9 AU, 786 $M_\oplus$	0.6 AU, 256 $M_\oplus$	0.25 AU, 165 $M_\oplus$
Fiducial Σ_0	1.2 AU 446 $M_\oplus$	0.55 AU, 246 $M_\oplus$	0.25 AU, 166 $M_\oplus$
Low Σ_0	0.9 AU, 316 $M_\oplus$	0.5 AU, 229 $M_\oplus$	0.26 AU, 170 $M_\oplus$

density. Not only are the final configurations of planets more compact in the combined scenario, but their orbital radii and formation times are quite insensitive to variation in Σ_0. For example, across the range of Σ_0 settings investigated, the combined model does not produce any hot Jupiters or short-period super Earths. Additionally, we generally found shorter gas giant formation timescales at all settings of Σ_0 in the combined disk models, indicating that the super Earth population will be limited at the lower setting of $\alpha_{\rm turb} = 10^{-4}$. As a result, gas giants will form too efficiently to achieve a reasonable comparison with the data.

Varying Σ_0 has a larger effect on planet formation models in the turbulent scenario, which affects planets' formation times and/or orbital radii. We also find that the turbulent model readily shows that the formation of each of the observed classes of planets can be achieved. The ice line produces warm gas giants and super Earths near 1 AU; the dead zone forms hot Jupiters, and the heat transition results in super Earths forming over a range of orbital radii, as well as hot Jupiters in the longest-lived disks.

On this basis, our planet formation results demonstrate that a full population model in the turbulent scenario with $\alpha_{\rm turb} = 10^{-3}$ will achieve a better comparison with the observed M-a distribution than the "combined" turbulence and disk winds model with $\alpha_{\rm turb} = 10^{-4}$. While we have not yet performed a detailed parameter study of $\alpha_{\rm turb}$ beyond the settings investigated in this chapter, our results here give indication that the value of $\alpha_{\rm turb} = 10^{-3}$ used throughout this thesis is closer to a "best-fit" value (in terms of comparing with the observed M-a data) than $\alpha_{\rm turb} = 10^{-4}$ is.

5.4 Results II: Wind-dominated models & the effect of outflow strength

We now consider the case of a winds-dominated disk model with $\alpha_{\rm turb} = 10^{-6}$, which is same value used within the combined model's dead zone. We will examine the effect of the strength of the wind-driven outflow by comparing two models: the constrained case where K is solved for using equation 5.12, and the unconstrained case where we use a high setting of $K = 1$. In this disk model we do not consider a dead zone as the turbulence strength is quite low throughout the entire disk's extent. The related trap at the Ohmic dead zone's outer edge is therefore not present in these models.

In figure 5.5, we plot the resulting disk evolution corresponding to each scenario. We find that, even though the strength of turbulence has been reduced by a factor of 100 compared to the combined model of the previous section, the "constrained outflow" model's accretion rate and surface density evolution is quite comparable to the $\alpha_{\rm turb} = 10^{-4}$ case. The accretion rate decreases from its initial value of $6{\times}10^{-8}$ $M_\odot$ yr^{-1} to roughly 10^{-9} $M_\odot$ yr^{-1} after 3 Myr of disk evolution. The surface density profiles also show the disk to contract with time in terms of its outer radius; a result of winds-dominated evolution.

The constrained outflow model's temperature profile is, however, significantly different from the $\alpha_{\rm turb} = 10^{-4}$ case, as viscous heating has been substantially decreased due to the reduced strength of turbulence. This decrease results in the disk's viscous region being limited to the innermost region within 1 AU and early times in disk evolution $\lesssim$ 1 Myr. Between 1 and 2 Myr, viscous heating has decreased to the point where the entire disk's heating is dominated by host-stellar radiation. Once this has occurred, the midplane temperature profiles simply correspond to the radiative equilibrium profile (equation 5.9). As a consequence, the midplane temperature profile will become completely static, since the radiative temperature profile has no time-dependence. This will result in the ice line's position being stationary in the disk throughout its evolution. Furthermore, if disk chemistry were to be computed in this disk, the profiles would not evolve with time after the viscously-heated region has disappeared. We note that these implications of a static, radiative-equilibrium temperature profile are a result of the common assumption that we have used throughout this thesis that the host-star's luminosity is constant.

Now considering the unconstrained outflow scenario in the right column of figure 5.5, we can immediately see the interesting effect of a strong, winds-driven outflow on disk evolution. In this

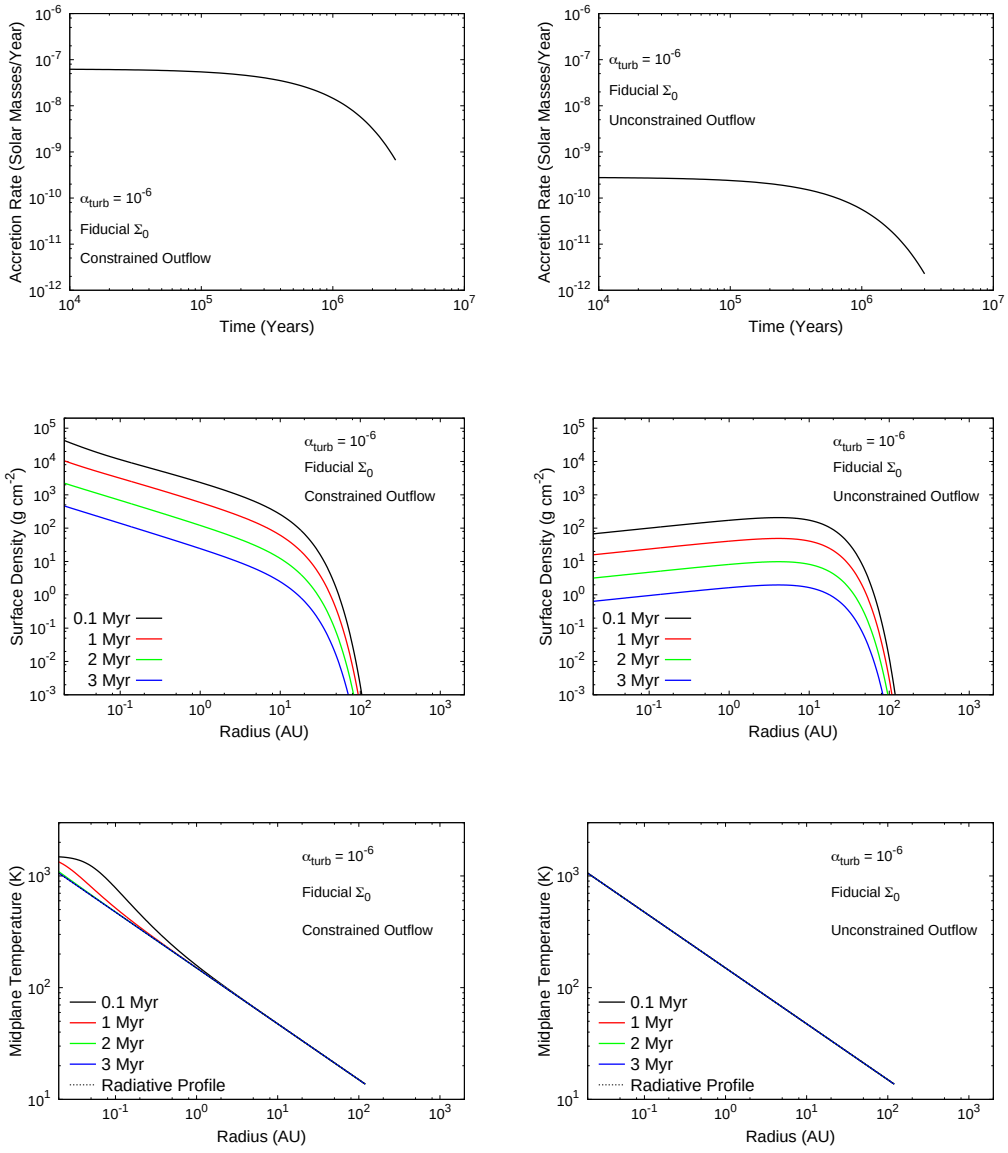

Figure 5.5: We compare disk evolution in winds-dominated disks ($\alpha_{\rm turb} = 10^{-6}$) at two settings of disk outflow strength. The left column pertains to the 'constrained' outflow where K is determined according to equation 5.12. The right column considers a high outflow strength with K=1. The top row shows evolution of disk accretion rate, and middle and bottom rows show radial profiles of surface density and midplane temperature, respectively.

model, a larger fraction of the disk winds' stress is carried away in the outflow as opposed to contributing to disk accretion. This results in the disk accretion rate $\dot{M}$ being reduced by roughly two orders of magnitude compared to the constrained outflow scenario.

Another compelling effect of a strong outflow can be readily seen in the disk surface density profiles. Rather than being a decreasing function of disk radius over the entire disk's extent, we see that Σ increases until roughly 10 AU where it achieves a maximum value before decreasing in the outer disk. This is a result of of the outflow surface density rate being a decreasing function of radius r (see equation 5.4), removing material more efficiently in the inner disk than the outer disk. This feature is also present in many of the surface profiles shown in the numerical treatment of Suzuki et al. (2016).

Since, in addition to having a low setting of turbulence, the unconstrained outflow model's accretion is substantially lower, there is no viscously-heated region in the disk. At all times, the midplane temperature is a result of heating through radiation alone, and the midplane temperature profiles are equal to $T_{\rm req}$ (equation 5.9) for the entirety of disk evolution. There are two consequences of this result. First, the heat transition and its related trap are not present in this model, as there is no transition into a viscously-heated region present in the disk. Second, as we have described above, the midplane temperature profile is completely static, which will result in an ice line radius that does not change as the disk evolves.

To summarize, since we are considering an extremely low setting of $\alpha_{\rm turb}$, there is no longer a dead zone or its related trap in either winds-dominated model. Additionally, in the unconstrained outflow case, there will be no heat transition, with only a static ice line remaining from our standard set of three planet traps. Both the heat transition and ice line will remain in the constrained outflow scenario.

However, the surface density maximum that is encountered in the unconstrained outflow model has significant implications for planet migration. Type-I migration models have shown that forming cores will experience zero net torque at locations of surface density maxima (i.e. Sándor et al. (2011)). In fact, this is our main motivation for analyzing the unconstrained outflow model, despite the fact that it produces large outflow mass-loss rates that are in contention with disk winds theory and observations (i.e. equation 5.12).

We adopt the standard type-I migration torque formula of Paardekooper et al. (2010) to determine

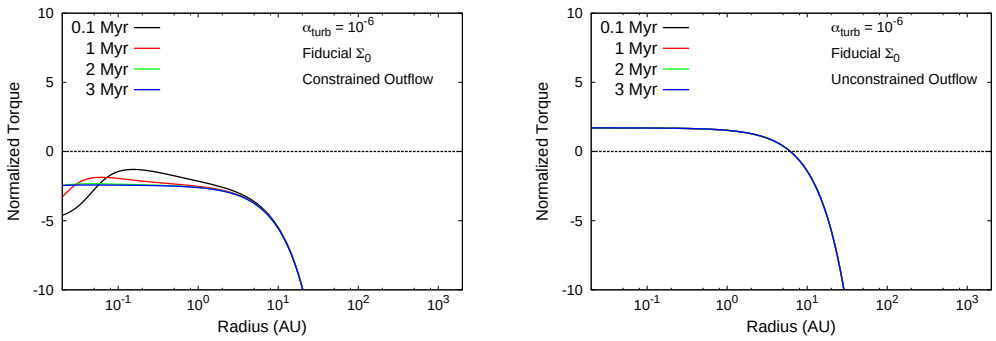

Figure 5.6: Profiles of the normalized type-I migration torque Γ_I/Γ_0 are shown for both the constrained and unconstrained outflow models, calculated using equation 5.16. Inward type-I migration will persist across the entire 'constrained outflow' disk's extent. Conversely, we find a planet trap near 10 AU related to the surface density maximum in the 'unconstrained outflow' model.

if a null torque location (i.e. a planet trap) will exist in either model;

$$\gamma\frac{\Gamma_I}{\Gamma_0} = -2.5 - 1.7\beta + 0.1\alpha + 1.1(1.5-\alpha) + 7.9\frac{\xi}{\gamma}\ , \tag{5.16}$$

where Γ_I is the normalized type-I migration torque whose sign indicates the direction of planet migration ($\Gamma_I < 0$ indicating inward migration). α and β correspond to the magnitudes of the local power-law indices of the surface density, and temperature profiles, respectively (i.e. $\Sigma \sim r^{-\alpha}$, $T \sim r^{-\beta}$). This torque formula illustrates that the type-I migration torque is sensitive to the local disk surface density and temperature profiles. We use an adiabatic index of $\gamma = 5/3$ corresponding to a monatomic gas. ξ is the disk's entropy gradient; $\xi = \beta - (\gamma - 1)\alpha$. Lastly, the torque normalization factor Γ_0 is,

$$\Gamma_0 = \left(\frac{q}{h}\right)^2 \Sigma_p r_p^4 \Omega_p^2\ , \tag{5.17}$$

where q is the planet to star mass ratio, h is the disk aspect ratio, and all quantities are computed at the planet's location.

We will, however, only calculate the *normalized* type-I migration torque Γ_I/Γ_0 using equation 5.16, to determine if any planet traps exist in either the constrained or unconstrained outflow models. These will correspond to locations where $\Gamma_I = 0$. We note that, since we are calculating the *normalized* torque, we do not need to prescribe a core mass (which would be needed to determine the torque normalization, equation 5.17).

The result of this calculation is shown in figure 5.6, where radial profiles of the normalized torque are shown throughout both disks' evolutions. We see that in the constrained outflow model, the type-I migration direction will be inward across the entire disk's extent, and for the entire disk's evolution. The constrained model's surface density profiles are similar to the 'combined' turbulence and winds model of the previous section, so we expect this result to apply to that disk model as well.

In the case of the unconstrained outflow model, we do indeed find a planet trap near 6 AU where $\Gamma_I/\Gamma_0 = 0$, related to the maximum in the disk surface density profile. Interior to the trap, the direction of the type-I torque is outward, while exterior to the trap it is inward. The directions of the type-I migration torque are therefore appropriated to migrate planets towards the trap. We also find that the torque profiles in the unconstrained outflow scenario are time-independent. In addition to the static temperature profile, the radial profile of the surface density's power-law index α is also time-independent, which causes the static torque profiles. This can be seen in figure 5.5, where the unconstrained outflow model's Σ profile decreases while maintaining its radial structure.

Based on this result of figure 5.6, we obtain a second planet trap in the unconstrained outflow case, in addition to the ice line. We refer to this trap simply as the "null torque" for this model. However, since the torque profiles and null torque radius are static, this trap will also be stationary in the disk throughout its evolution.

In figure 5.7, we plot the evolution of the traps' radii and planet formation tracks in both the constrained and unconstrained outflow models. Here, we only consider the fiducial setting of Σ_0. In the constrained outflow model, we see that the heat transition is located at a much smaller radius in the disk than either the turbulent or combined models of the previous section. This is as a result of the lower $\alpha_{\rm turb} = 10^{-6}$ and reduced viscous heating. As previously outlined, the ice line's position is stationary in the disk near 1 AU, due to the static radiative equilibrium temperature profile. Since the traps exist at small disk radii, and the constrained outflow model maintains large surface densities within 10-20 AU, both traps efficiently produce warm Jupiters near 1 AU within only 1 Myr of formation.

In the unconstrained outflow model, the radial locations of both the null torque and ice line traps are time-independent. In contrast to the constrained outflow model, planet formation in each of the two traps is extremely inefficient due to the rapid decrease in disk surface density caused by the strong outflow with $K = 1$. Even considering a long disk lifetime of 10 Myr does not result in massive planets forming, since the disk surface density has decreased significantly by 1 Myr due to the outflow

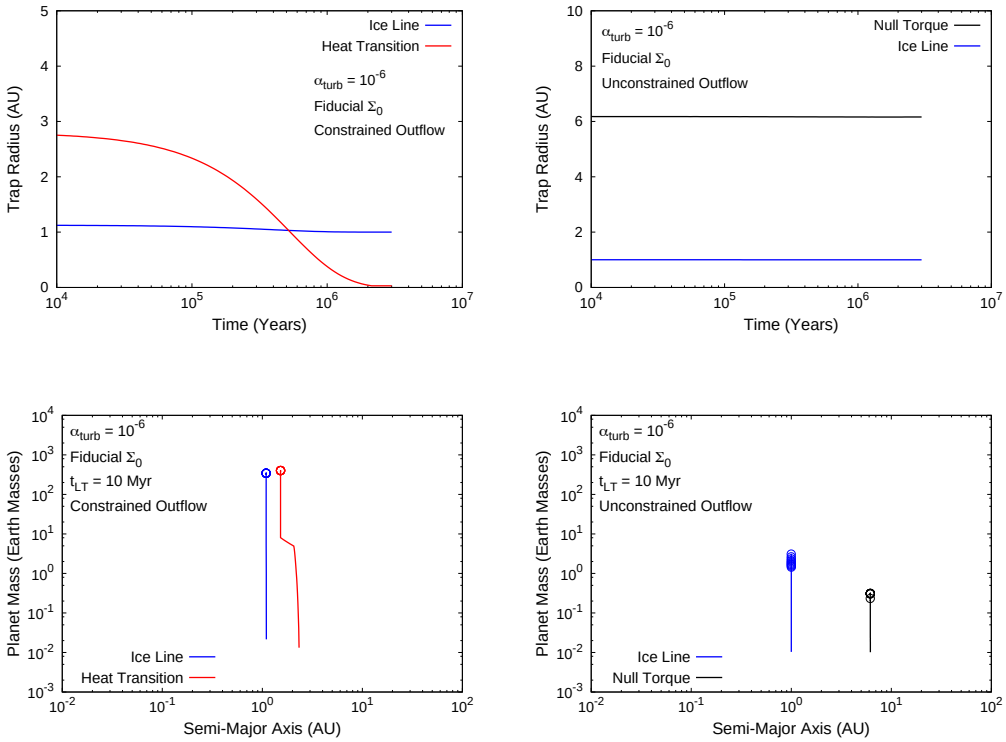

Figure 5.7: We plot evolution of planet traps (top row) and planet formation tracks (bottom row) for both the constrained outflow (left column) and unconstrained outflow (right column) models. In the planet formation plots, open circles designate the planets' positions at 1 Myr intervals throughout their disks' 10 Myr-lifetimes.

(see figure 5.5). The null torque only forms a sub-$M_\oplus$ core in this disk model, while the ice line forms a ~ 3 $M_\oplus$ super Earth. In both cases, the planets form in-situ due to the time-independence of their traps' locations.

We have also separately investigated how the positions of the traps change in both models with different settings of Σ_0. We find that the trap locations are extremely/entirely insensitive to the setting of Σ_0. This is mainly the case because the radiative equilibrium temperature profile, which dominates midplane heating, is independent of disk surface density (only depending on the radiative flux received by the disk). The resulting planet formation tracks are also very similar to those shown in figure 5.7. Based on these results that show limited planet formation and no variance with disk parameters, we do not expect a population synthesis model to be particularly interesting in either the constrained or unconstrained outflow models in terms of the planet traps framework. However, the low settings of $\alpha_{\rm turb}$ in a winds-dominated model may allow planets to form under a general type-I migration regime, as calculated with equation 5.16, while not being restricted to the locations of traps. We explore this idea further in the following section 5.5.

5.5 Discussion & Conclusions

In this chapter, we have investigated disk evolution via the combined processes of MRI-turbulence and MHD disk winds using the Chambers (2019) formalism. We first examined the effect of the relative strength of turbulence and disk winds by comparing a model with $\alpha_{\rm turb} = 10^{-3}$ to one with $\alpha_{\rm turb} = 10^{-4}$ and an increased strength of disk winds, such that their initial disk accretion rates were the same. The former model was used as a benchmark as it considers the same $\alpha_{\rm turb}$ value that has been used in our pure viscous evolution models throughout this thesis. In this comparison, we investigated these parameters' effects on planet formation models, and considered three different initial disk surface densities to discern the effects that different disk masses and/or radii will have. Lastly, in a winds-dominated scenario ($\alpha_{\rm turb} = 10^{-6}$), we compared two different strengths of the winds-driven outflow; a standard outflow that is in agreement with the theoretical and observational constraints ($\dot{M}_{\rm wind}/\dot{M}_{\rm acc} \simeq 0.1$), and a relatively strong outflow that is increased in by a factor of $\sim$ 10-100 from this standard case.

When comparing the turbulent and combined cases, the suite of planet formation models that we explored with different disk Σ_0 values indicate what these models' full M-a distributions will be

when a full population synthesis calculation is done. The combined model resulted in more compact planet configurations, producing gas giants between $\sim$ 0.3-2 AU with formation times of 1-4 Myr, depending on the trap they form in. Formation models in this scenario were quite insensitive to the disk Σ_0, both in terms of planets' formation times and final orbital radii. On this basis, if a full population were to be calculated for this combined model, we expect the planets to be distributed over a relatively small region of the M-a space, with no hot Jupiters or short-period super Earths. Additionally, the relatively short formation timescales indicate that this population model will overproduce gas giants.

Planet formation tracks in the turbulent model showed a more interesting variety in terms of planet orbital radii and formation times. In this model, the dead zone forms hot Jupiters with short formation timescales, the ice line forms warm gas giants at timescales comparable to typical disk lifetimes (3 Myr), and the heat transition forms hot Jupiters over long 9-10 Myr timescales, indicating that this trap will predominantly form super Earths and Neptunes when an observationally-constrained distribution of disk lifetimes is implemented in a population synthesis framework. Changing the disk Σ_0 did not have a large effect on the final orbital radii of gas giants formed with the dead zone or heat transition, but it did change their formation timescales by 1-2 Myr. The ice line planet formation tracks changed with Σ_0 both in terms of the planet formation times (2-4 Myr) and planets' final orbital configurations (0.6-2 AU). The planet formation tracks calculated with the turbulent model thereby show that a full range of final planet types on the M-a diagram can be achieved: hot and warm Jupiters, as well as super Earths with a range of orbital radii $\sim$ 0.05 AU - 2 AU.

On this basis, we expect a full population to achieve better correspondence with the observed M-a diagram using the parameters of the turbulent model ($\alpha_{\rm turb} = 10^{-3}$). The planet formation models indicate that a wide variety of planet types can form, whose formation times and final orbital radii depend on the setting of the disk Σ_0, which would be varied in a population synthesis calculation. This model also shows a clear separation between the gas giants that form near 1 AU in the ice line, and the hot Jupiters at $<$ 0.1 AU formed in the dead zone or heat transition. We have therefore reproduced one of our main findings of chapter 2, for which this turbulent model is most directly comparable (as they both use a constant dust-to-gas ratio). It is interesting that this result is recovered within the new disk model's framework. While this perhaps should not be surprising, we highlight that the "turbulent" model in the Chambers (2019) formalism we use in this chapter

requires a substantial disk winds fraction of $f_w \simeq 0.8$ to achieve $\alpha_{\rm turb} = 10^{-3}$. In other words, while we referred to this model as the turbulent scenario (since it has the same $\alpha_{\rm turb}$ as what we have used in previous chapters), a significant fraction of the disk evolution is attributed to winds-related stresses.

Using population synthesis calculations and their M-a distributions' comparison to observations, one could determine "best-fit" values of the disk $\alpha_{\rm turb}$ and $\alpha_{\rm wind}$ parameters. Constraining these parameters could be accomplished by examining a grid of populations with different $\alpha_{\rm turb}$ values. While we have only explored two settings of $\alpha_{\rm turb}$ in section 5.3, our planet formation results give a clear indication that this best fit value lies closer 10^{-3} than 10^{-4}. Adding complexity to this problem, however, is the likely case that disks as a population will exhibit a *range* of characteristic $\alpha_{\rm turb}$. This problem could be approached in a similar manner to our strategy in chapter 3 for constraining the initial disk radius using population synthesis; first finding an optimal value for the parameter despite it having an inherent distribution among protoplanetary disks. Furthermore, there is no theoretical basis for individual disks having α parameters that are constant with disk radius or time. In fact, numerical MHD results show that the disk α parameters can vary within disks' radial and vertical extents in a non-trivial manner (i.e. Bai & Stone 2011; Lesur et al. 2014; Gressel et al. 2020).

When analyzing the strong outflow case in the winds-dominated scenario ($\alpha_{\rm turb} = 10^{-6}$), we found that a type-I null torque location arose at roughly 6 AU due to a maximum in the disk surface density profile. As shown in Suzuki et al. (2016) and Chambers (2019) when starting with a typical surface density profile that decreases with radius, a strong, wind-driven outflows can cause material to be efficiently removed from the disk inner regions, resulting in a Σ maximum at intermediate radii. As the Paardekooper et al. (2010) type-I migration torque depends on the local power-law index of the disk Σ and T profiles, a surface density maximum will have a related planet trap (Sándor et al., 2011). In the winds-dominated scenario, however, planet traps were almost entirely stationary throughout the disk, due to the midplane heating being dominated by time-independent host-star radiation. Planet formation models were quite different in this framework, and showed virtually no variance with changing the disk Σ_0. In the case of the standard, constrained, outflow, both the ice line and heat transition form planets extremely rapidly within 1 Myr. The unconstrained outflow sees failed cores produced by both the ice line and null torque traps, due to the wind efficiently reducing the overall disk surface density and removing material that planets can accrete.

This result leads us to conclude that the winds-dominated scenarios cannot explain the diversity

of planetary masses and orbital radii observed on the M-a diagram. However, we explored this from the perspective of a trapped type-I migration scenario, where forming planetary cores are confined to positions of traps in the disk. This has been our standard approach since, in viscously-evolving disks, cores have been shown to rapidly type-I migrate throughout the disk, either falling into the host star, or encountering a trap. We make the simplifying assumption that our models' initial cores are situated within traps because, if they are not, type-I migration will rapidly transport them inwards until they reach a trap.

However, the winds-dominated scenarios may not result in planet migration being as rapid as it is in the standard viscous case. It is possible, that under the effect of standard type-I migration, planets may be able to form in a winds-dominated disk without rapid migration into the host star. This will be the case if the *overall* disk α (i.e. from a combination of turbulence and disk winds) is lower, resulting in slower disk evolution. This is the approach of Ogihara et al. (2018), using the Suzuki et al. (2016) combined turbulence and winds numerical disk model. Their work finds that a range of final super Earth radii can be achieved by considering a range of initial orbital radii for planetary cores, whose migration is simply handled by standard type-I migration (i.e. Paardekooper et al. (2010)). Of course, if traps are present throughout the disk, these cores' orbits may converge to their locations.

However, we have shown that planet migration is inwards at all disk radii in the standard, constrained outflow case (figure 5.6), so it is unclear how cores will be prevented from falling into their host stars in our framework without encountering the static traps. The unconstrained outflow case does show that a null torque exists and the direction of migration is outwards in the inner disk. However, the surface density is rapidly reduced in this model by the wind-driven outflow, offering little time for core accretion to take place. While it remains true that alternate model assumptions may affect these results, basic theoretical considerations applied to a winds-dominated model reveal issues for planet formation and achieving correspondence with the M-a distribution. However, we have not yet investigated the effect of changing the overall disk α that arises from a combination of turbulence and disk winds. Changing α will change the disk's overall evolution timescale, and can greatly affect planet formation and/or migration. This can be changed by considering different initial disk accretion rates other than the $\dot{M}_0 = 6 \times 10^{-8}$ we have considered as the fiducial case here. This investigation can be readily carried out with these models in future work.

We now list our main conclusions of this chapter:

- The turbulent-dominated model (using $\alpha_{\rm turb} = 10^{-3}$ outside of the dead zone) forms an interesting variety of different planet types. When exploring different disk surface densities and lifetimes, this model produces hot Jupiters, warm gas giants, and super Earths over a range of orbital radii. This gives good indication that a full population synthesis model using this parameter setting will result in a reasonable correspondence with the observed M-a data.

- The turbulent-dominated model also produces a clear separation between warm gas giants near 1 AU formed in the ice line and hot Jupiters formed in the dead zone and heat transition. Thus, the new Chambers (2019) disk model, which combines evolution via turbulence and disk winds, reproduces a result we found in chapter 2 using a pure turbulence model (Chambers, 2009).

- Reducing the strength of turbulence to $\alpha_{\rm turb} = 10^{-4}$ and increasing the disk winds strength to maintain the same disk accretion rate resulted in much more confined planet configurations than the stronger turbulence model was able to achieve. Planets formed between 0.3-2 AU in this model, and formation tracks were insensitive to changes in disk surface density in therms of their formation times and final planet radii. This model did not produce any planets with orbits < 0.3 AU, so it is unclear how hot Jupiters or short-period super Earths can form in this framework.

- When considering a winds-dominated model $\alpha_{\rm turb} = 10^{-6}$ with a strong outflow, a planet trap arises at ~ 6 AU as a null type-I migration torque. This is linked to a surface density maximum, that is achieved through the strong winds-driven outflow efficiently removing material close to the host-star.

- Winds-dominated models did not show variation in planet formation results with disk properties. At this setting, it is unclear how variation in the modelled planets' M-a distribution can be achieved.

This preliminary investigation serves as a foundation for a more in-depth future investigation on the effect of the relative strengths of turbulence and disk winds. For this, we will use a full population synthesis treatment in line with the previous chapters of this thesis to determine how final M-a distributions depend on the settings of $\alpha_{\rm turb}$ and $\alpha_{\rm wind}$. Our results shown in this chapter clearly indicate that disk evolution and planet formation is sensitive to the strengths of these two disk

evolution mechanisms, even using a theoretical framework that simplifies many of the complex issues that are at the forefront of full MHD treatments of this problem. These results motivate further understanding and constraint of disk evolution processes, both from observational and theoretical perspectives.

Chapter 6

Conclusions & Future Work

In this thesis, we have used the core accretion theory of planet formation to investigate the link between the observed variability in protoplanetary disk properties and the range of outcomes of planet formation as displayed in the exoplanet M-a and M-R diagrams. The method of planet population synthesis has been invaluable for this purpose, allowing for the full observed ranges of disk masses and lifetimes to be incorporated in their effects on resulting synthetic planet distributions. Dynamical planet traps, locations of zero net torque on forming planets linked to disk inhomogeneities, are central to our theory. When considering type-I migration torques, planet traps provide locations throughout the main body of the disk where migration timescales do not limit planet formation. As the early phases of core accretion (solid accretion and part of the slow gas accretion phase), the traps' locations throughout the disk in large part determine planet formation rates and abundances of accreted materials.

Our approach in comparing synthetic planet populations with the observed M-a and M-R diagrams has lead to several key results. First, in chapter 2, by considering the period distribution of gas giants, we find that low settings of envelope opacities $\kappa_{\rm env} \sim 0.001$ cm^2 g^{-1} are necessary to obtain reasonable correspondence with the gas giant occurrence rate - orbital radius relation (Bryan et al., 2016). This is the case as the period distribution of gas giants are shaped by the relative accretion and migration timescales, with the former being set physically by envelope opacities in the case of gas accretion. This setting of $\kappa_{\rm env}$ we find is in agreement with previous works (Hasegawa & Pudritz, 2014; Mordasini et al., 2014), is a factor of 100-1000 lower than typical protoplanetary disk opacities $\sim 0.1 - 1$ cm^2 g^{-1}, implying significant reduction of opacity after disk material has

been accreted. This can, for example, be accomplished through rapid grain growth in the forming planet's atmosphere, removing the small μm grains (Mordasini, 2014).

In chapter 3, by incorporating a physical model of dust evolution, we find that radial dust drift has a significant affect on planet formation results. In particular, the large region of the disk outside the water ice line is substantially reduced in solids by their inward transport, leading to long solid accretion timescales over this large extent of the disk. However, this also increased the solid surface density at the water ice line, making the trap a site of efficient planet formation.

Through investigation of the effect of the initial disk radius, we found different outcomes of formation at the ice line in terms of the ratio of super Earths to warm Jupiters. In the case of both small and large initial disk radius models warm gas giants were produced at a higher frequency, with intermediate disk sizes of 50 AU producing the largest super Earth population. In small disks, planets forming in the ice line had larger gap-opening masses, leading to a smaller effect of gas accretion termination, while in larger disks, the solid surface densities accumulated at the ice line through radial dust drift were the greatest, leading to efficient solid accretion rates. Both of these processes lead to efficient formation of gas giants, and are minimized at the intermediate disk radius setting.

This result confirms that the range of disk radii seen observationally (i.e. Ansdell et al. 2018) and through numerical studies of disk formation through protostellar core collapse (Masson et al., 2016; Bate, 2018) have crucial implications for planet formation in their role in setting the overall disk surface densities. Further observational constraint on disk parameters, then, will be tremendously useful in constraining planet formation models. Our approach taken in chapter 3 considered individual settings of R_0 to *isolate* its affect on the M-a distribution. In combination with a full log-normal distribution of initial disk masses, the individual disk radii settings translate to log-normal distributions of disk *surface density*, which is the physical parameter for planet formation models (i.e. setting accretion timescales). By changing the characteristic disk radius between models, and keeping the same disk mass distribution, we are effectively changing the average disk surface density of its log-normal distribution between populations which causes the changes in population outcomes we found in chapter 3.

As an extension of the approach taken in chapter 3, one could consider a full distribution of initial disk radii as an additional input parameter to be stochastically varied in the population synthesis models. This would treat R_0 in the same manner as initial disk mass and disk lifetime.

We did not take this strategy as doing so would 'wash out' the effect of the initial disk radius on population results, in that it would be hard to disentangle the effect of R_0 in a population that incorporates a full distribution of initial disk radii. If we were to use a full distribution for initial disk radius, it would, in combination with that of the disk mass, achieve an overall surface density distribution - the parameter with the most physical significance for our planet formation models. What ultimately matters the most in terms of results of planet formation, then, is the details of this surface density distribution (i.e. average and standard deviation), shaped by disk masses and radii. As this distribution is updated with improved constraints on initial disk properties, its effect on results of planet formation will indeed be interesting. Based on our results from chapter 3, we expect significant changes to results of planet formation models if observations or numerical models reveal an updated surface density distribution whose *average* is changed significantly.

We have compared planet populations in chapters 2 and 3, which assumed constant dust-to-gas ratios and a full dust evolution treatment, respectively. We have found that radial drift, through its effect on the solid distribution, has a significant effect on resulting planet populations. Notably, the transition between warm Jupiters and super Earths formed at the ice line, dependent upon the initial disk radius, was only encountered when radial drift was included. No such transition takes place in the constant dust-to-gas ratio models. Additionally, radial drift resulted in the formation of super Earths on smaller orbits ($\sim$ 0.05 AU) than were formed in the case of an assumed constant dust-to-gas ratio, which formed super Earths outside of $\sim$ 0.3-0.5 AU. We conclude based on these results that including radial dust drift is important to achieve short period super Earths directly out of the disk phase, and prior to any atmospheric loss is accounted for.

We recall that the Birnstiel et al. (2012) dust evolution model we considered has a high efficiency of radial drift. This resulted in compact dust distributions, with solid surface densities being small outside the water ice line. This is in contention with dust-continuum disk observations, which have revealed extended dust distributions and large disk radii in some systems. Additionally, results of Birnstiel et al. (2010b) show that the high radial drift efficiency resulting from the Birnstiel et al. (2010a) and Birnstiel et al. (2012) models does not adequately reproduce disk SEDs. We can therefore consider the dust treatment we investigated as perhaps an upper limit to the effect one might expect radial drift to have on disks' solid distributions. The constant dust-to-gas ratio populations (no radial drift), and radial drift populations are then two extremes that bracket the true effect of radial drift. This is another avenue for future work with this model as a direct extension to the calculations

presented in chapter 3: populations that include radial dust drift but reduce its impact on the dust distribution either by reducing the radial drift rate, or by including dust pressure traps to maintain an extended solid distribution.

In chapter 4 we investigated our best-fit chapter 3 populations' M-R distributions, by incorporating disk chemistry, planetary structure, and photoevaporative atmospheric mass loss. We found that the planet traps used in our model gave rise to a diversity among super Earth compositions, ranging from dry, Earth-like planets formed in the dead zone to ice-rich planets formed in the ice line and heat transition. This translated to radii differences discernible on the M-R diagram in the case of low-mass $\lesssim$ 2-3 $M_\oplus$ core-dominant planets or larger planets that were stripped after the disk phase. Many planets with masses > 3 $M_\oplus$ retained their accreted atmospheres, and in this case populated the same region of the M-R diagram despite their significantly different solid compositions. Therefore, when present, planetary atmospheres have the most significant effect on planet radii, and can hide composition's effect on changing the core radius.

Atmospheric escape through XUV photoevaporation was significant for planets on small orbital radii $\lesssim$ 0.1 AU. Planets that form as Neptunes or sub-Saturns at these small radii had their atmospheres stripped, notably resulting in the formation of short-period super Earths. This populated a region of the M-a space (i.e. $a_p < 0.05$ AU, $M_p < 5 - 10$ $M_\oplus$) that versions of our model in chapters 2 and 3 (which did not include atmospheric mass loss) could not. While atmospheric mass loss played a crucial role in affecting planets' final masses and radii, it was only significant for planets on these short-period orbits $\lesssim$ 0.1-0.3 AU since photoevaporation is a radiative effect. Investigating an alternate atmospheric core-powered mass-loss mechanism (i.e. Gupta & Schlichting 2019) is a prospect for future work as a direct extension to the model presented in chapter 4. While results of atmospheric mass loss will depend on host-star radiation even in this alternate scenario (through its effect on the atmospheric scale height), they will likely be less sensitive to orbital radii as planets' heat of formation (which all planets acquire) drive atmospheric escape as opposed to XUV flux (which is only significant at small a_p).

We then investigated disk evolution via the combined effects of turbulence and disk winds in chapter 5. We compared two models with different relative strengths of turbulence and disk winds; considering $\alpha_{\rm turb} = 10^{-3}$ and $\alpha_{\rm turb} = 10^{-4}$, respectively (the former being the turbulence setting we use throughout this thesis in the pure viscous models of chapters 2-4). We found that a more interesting variety of planet formation results are achieved with the higher setting of $\alpha_{\rm turb}$, as

planet formation models show sensitivity to disk lifetime and surface density (whose variation can be achieved with disk mass and/or radius). The higher turbulence case readily produced a range of planet formation results in line with the observed M-a distribution; forming super Earths over a range of 0.05-2 AU as well as hot and warm Jupiters. We also again find a separation between hot Jupiters formed in the dead zone and warm Jupiters near 1 AU formed in the ice line at this $\alpha_{\rm turb}$ settings; one of our main conclusions of chapter 2. The lower setting of $\alpha_{\rm turb} = 10^{-4}$ with an increased strength of disk winds produced a much more compact planet configuration, with gas giants' orbital radii between 0.3-2 AU. There was also much less variety in planet formation models in terms of their final orbital radii and formation timescales.

As an extension of the results we present in chapter 5, our future work will investigate full population synthesis models in disks whose evolution is driven through the combination of turbulence and disk winds. In doing so, we aim to find the optimal setting of $\alpha_{\rm turb}$ based on its resulting synthetic planet population's comparison to the observed M-a distribution. For the assumed initial disk mass accretion rate that we adopted (6×10^{-8} $M_\odot$ yr^{-1}), our planet formation results of chapter 5 indicate that this optimal value lies closer to 10^{-3} than 10^{-4}. Recognizing that disks as a population will almost certainly have an inherent distribution of strengths of turbulence and disk winds, this future population synthesis study that finds their best-fit values may indicate what the average of these parameters' distributions will be. Ultimately, a full distribution of these parameters can be incorporated into our population synthesis framework, although details of these distributions remain unclear at this stage. Our chapter 5 results certainly motivate better understanding of disk evolution and the relative strength of turbulence and disk winds, either from observations or theoretical models, as these factors have a significant affect on planet formation results.

6.1 Future Work & Extensions of Theoretical Model

Another interesting extension of the approach used in this thesis is to consider population synthesis models around stars of different masses, as was considered in Ida & Lin (2005) and Alibert et al. (2011). Of particular relevance in comparing with planets that will be detected by *TESS* will be modelling planet formation around M-dwarf stars. An uncertainty with this approach however, is understainding how the disk properties scale with stellar spectral class. Disk masses and lifetimes, for example, are loosely constrained even in the prominently-studied case of G-type stars. Since these

disk properties have been shown to be of paramount importance in setting planet formation timescales and outcomes, having a proper scaling of disk properties to reflect planet-formation environments around M-dwarfs will be important. It seems likely for instance that disk lifetimes will be somewhat different around M-dwarfs given their different XUV luminosities that drive photoevaporation, in addition to their longer evolution timescales onto the main sequence (Siess et al., 2000).

Planet detection around M-dwarfs has revealed the existence of many short-period planets, such as the compact Trappist-1 system (Gillon et al., 2017). Short-period planets are of particular interest in this case as they coincide with the M-dwarf habitable zone. Further planet detections will give a more complete understanding of the planetary orbital-radius distribution around M-dwarfs, but the current observational results may indicate that results of planet formation should systematically produce shorter-period planets than in the case of formation around a G-type star. If this is the case, it must be understood what disk properties or changes in relevant planet formation timescales give rise to this result.

Another prospect of future work that will improve theoretical constraints on population synthesis is having a clear physical picture of terminating gas accretion onto massive planets. In this thesis, we employed a simple scaling of a planet's maximum mass with its gap-opening mass through the parameter $f_{\rm max}$. This is contrasted with the other commonly used disk-limited approach, for which one parameterizes the fraction of material accreting through the gap (i.e. disk accretion) that accretes onto the planet (see section 1.2). Both approaches involve the use of a parameter that ultimately sets planets' final masses based on accretion efficiency following gap-opening. Our $f_{\rm max}$ approach is supported by hydrodynamic models that show substantial material flowing through gaps (Morbidelli et al., 2014) and that this results in high accretion rates being sustained onto even massive planets (i.e. no self-driven termination process; Lambrechts et al. 2019). With these results in mind, however, it remains unclear what physical process(es) determine planets' final masses, providing that their disk does not dissipate during the (short) runaway growth phase. This is an unlikely scenario due to the differences in runaway growth timescale ($\lesssim 10^5$) and disk lifetimes ($\gtrsim 10^6$ years).

As introduced in Batygin (2018), and investigated further for semi-analytic planet formation theory in Cridland (2018), magnetic termination offers a more physical picture of setting planets' maximum masses during runaway gas accretion. We recall that in this process, a planet's accretion cross-section is determined by the radius over which magnetic effects caused by the protoplanet's dynamo dominate. This immediately leads to an inverse scaling between accretion cross-section and

planet mass, such that accretion will be physically limited as planet masses grow beyond masses of Jupiter, naturally leading to a reasonable comparison with observed gas giants.

However, we note that this model is sensitive to *two* parameters whose combination ultimately sets planets' maximum masses. The first is the planet's magnetic moment which depends on the complex problem of forming planets' magnetic fields. The second parameter is the fraction of disk accretion that supplies accretion onto a circumplanetary disk, which is the exact parameter necessary in the common disk-limited accretion picture. Constraining each of these parameters demands understanding of complex physical processes. Additionally, magnetic termination requires an additional model parameter beyond the one needed in either our $f_{\rm max}$ approach or the disk-limited approach. These factors allude to the disadvantage of considering the magnetic termination approach, which may offset its advantage of providing a complete physical picture of the final stage of planet formation. However, if these model parameters were constrained (i.e. by dedicated numerical simulations), investigating how well the magnetic termination process can reproduce the observed M-a relation in a population synthesis framework would be an interesting inclusion into our strategy.

Recently, there have been many dust-continuum observations of protoplanetary disk gaps and asymmetries at large $\gtrsim$ 10 AU host-star separations (i.e. Andrews et al. 2018). Many works are investigating the role that planets have in driving these features (i.e. Dong et al. 2015b,a; Fung & Dong 2015). For example, by assuming gaps are caused by planets, one can use the observed position and widths of gaps to constrain the planet's orbital radius and mass. It then becomes necessary to achieve relatively massive planets ($\gtrsim$ a few $M_\oplus$) at large orbital distances $>$ 10AU to produce these observed disk features at large separations. Our formation models do produce planets at such large separations, but rather within $\sim$ 5 AU. This is because solid accretion timescales via planetesimal accretion become negligibly small outside $\sim$ 10 AU. This is further exacerbated when radial drift is implemented, reducing solid surface densities outside the ice line. While our planet populations are able to give a reasonable comparison to the observed M-a distribution, they will not be able to explain these observed disk features at large orbital radii, well outside the limited radial extent over which our formation models produce planets.

If it is indeed planets that are creating these observed dust gaps in disks, this then raises the question of how planets with masses $\gtrsim$ a few $M_\oplus$ form at such large separations. Formation at a dust trap at large separations, and/or outward migration may be able to explain their existence within the core accretion framework. The latter scenario of outward migration has been shown to

be common outcome of type-I migration of planetary cores in 2D models of inviscid, winds-evolving disks (McNally et al., 2018). However the 3D case (McNally et al., 2020) shows the opposite result of rapid inward migration, comparable to the case of rapid Lindblad-driven inward migration in viscous disk models (i.e. the standard type-I migration problem, Ward 1997). The interest of future investigations of planet formation within winds-evolving disks motivates a more complete understanding of planet migration in this disk winds framework. Formation through gravitational instability is another possibility of forming planets at large orbital radii (i.e. Boss, 1997), especially given that dust continuum observations are biased to the detection of the brightest sources, indicating that spatially resolved disks (for which gaps have been observed) may be above-average in mass.

One of the most important factors in limiting planet formation to be significant only in the inner region of the disk is the setting of the disk α (that is, the overall disk α achieved through the combined effect of disk winds and turbulence). In this thesis, we have shown that models using α=10^{-3} achieve correspondence with the observed exoplanet populations, for which the majority of the data is within $\sim$ 5 AU, likely due to biases in detection techniques. As we have outlined, a limitation with this setting of α is that solid accretion rates become negligible outside of 10 AU. Considering lower settings of α may be advantageous for this purpose as it will result in higher solid accretion rates at disk radii $>$ 10 AU, as disk evolution timescales are longer, and higher surface densities can be maintained. Furthermore, with lower α values (i.e. 10^{-4}), type-I migration timescales are also longer, meaning that rapid inward migration will not be as significant of a factor. This is especially true for low planet masses that have not reached $\sim$ 1 $M_\oplus$ for which numerical mass-dependent migration models show trapping can occur (see, for example, figure 1.9 from Coleman & Nelson 2016b).

As the disk α has a significant effect on planet formation, migration, and disk evolution timescales, further observational and/or theoretical constraints will be tremendously important to predict outcomes of planet formation. For this purpose, given our results of chapter 5, it will also be important to understand the relative strengths of turbulence and disk winds in driving disk evolution. Furthermore, one should consider that disks as a population probably have a range of α values as might arise if one considers the variable ionization conditions that protoplanetary disks may be exposed to within a young, forming star cluster environment. This distribution is not well understood but will have crucial implications for planet formation models. Lastly, there is no theoretical reason (beyond convenience in models) that individual disks should have one radially-constant α value. It

is likely that disks have radial- and time-dependent α *profiles* which can affect planet formation. We have accounted for this in terms of the dead zone, resulting in different strengths of turbulence in the inner disk versus the outer disk. However, disks' radial α structures may be more complicated, as numerical MHD models have indicated with accretion stresses (Bai & Stone, 2011; Lesur et al., 2014). Of course, probing a detailed radial α profile observationally is not attainable given spatial resolution limitations, but global disk numerical models may be able to address these issues.

Pebble accretion is another possibility to achieve massive planets at large separations, as these models have shown their ability to produce large accretion rates well outside this inner 10 AU "planetesimal formation" zone our models are confined within. However, pebble ablation poses a theoretical limitation on these models, resulting achieving maximum core masses of 0.6 $M_\oplus$ (Alibert, 2017; Brouwers et al., 2018). The recent models of Brouwers & Ormel (2020) indicate that growth can be sustained even with ablation accounted for, but this requires that the increase in the atmosphere's metallicity resulting from ablation is retained and not recycled back into the disk even at low (sub-Earth) masses. With this result, perhaps larger solid accretion rates could be sustained over a larger extent of the disk, and in that case, the "planet forming" region ($\lesssim$ 10 AU) of our model would be extended.

Given the large range of solid size scales in debris disks (Hughes et al., 2018), as well as those inferred from models of early phases of solid growth in disks (Simon et al., 2016; Schäfer et al., 2017), it remains likely that a combined approach of accreting pebbles and planetesimals is appropriate. For this approach, one may consider pebble accretion to rapidly grow solids up to the ablation limit of 0.6 $M_\oplus$, with planetesimal accretion continuing growth afterwards. An important caveat in this circumstance is that the solid planetesimal accretion rate has an inverse-mass scaling, meaning that simply increasing the initial mass of the accreting core (i.e. 0.6 $M_\oplus$ instead of 0.01 $M_\oplus$) as we describe here will result in a similar overall oligarchic growth timescale. On this basis, we do not expect that this change would greatly affect our resulting planet populations.

However, one advantage of this combined approach (i.e. a hybrid type of model in which rapid pebble growth to a fraction of an Earth mass is followed by a predominantly planetesimal accretion mode as modelled in this thesis) is that pebble accretion rapidly grows solids to masses where mass-dependent torque models indicate they will be trapped ($\sim$ 1 $M_\oplus$; Coleman & Nelson 2016b). A common feature of these numerical models is their prediction of inward type-I migration for masses $\lesssim$ 1 $M_\oplus$, with trapping related to disk inhomogeneities occurring at higher masses (see also Baillié

et al. 2015; Coleman & Nelson 2016a; Cridland et al. 2019a). With this model, pebble accretion can rapidly grow solids through their inward type-I migration mass range such that significant inward migration will not be encountered. At the point where the ablation limit is reached, cores will have achieved masses where migration models show they can be trapped, with further solid growth being sustained by planetesimal accretion.

Lastly, another prospect for future work is in incorporating dynamics effects into our formation model, both during and after the protoplanetary disk phase. Our overall migration approach in this thesis categorized planets into either the trapped type-I phase or the type-II phase depending on whether or not they exceeded the local gap-opening mass. Many previous works have shown planet traps to be mass-dependent (i.e. Coleman & Nelson 2016a; Baillié et al. 2016; Cridland et al. 2019a) by including a full calculation of the type-I migration torque (Paardekooper et al., 2010). This approach would lead to a more self-consistent link between disk structure and migration of low-mass planets.

Additionally, all of our planet formation models assumed planets formed in isolation, and did not include dynamics between multiple planets concurrently forming, as was investigated for example in Hellary & Nelson (2012). We highlight that in our models, planet traps intersect throughout disk evolution. When considering planets forming in different traps, dynamics during these close encounters could lead to many interesting effects, such as scattering, or "breaking" a planet from the trap it was forming within. During the disk phase, there is also the possibility of *resonant trapping*, wherein dynamical traps can arise at resonant locations to the planet traps we include due to the dynamics effects from forming planets. Resonances during the disk phase have been shown to play a crucial role in planet formation scenarios such as in the Grand-Tack model of the Solar system (Walsh et al., 2011).

In order to compare with the observed planet eccentricity distribution, scattering following the protoplanetary disk phase needs to be considered (as was done, for example, in Ida et al. 2013). For this purpose, the results of planet formation in each of the traps during the disk phase serve as the necessary initial conditions to post-disk dynamics models. Thus, the work in this thesis can provide vital input into the post-disk dynamical evolution of newly formed planetary systems by constraining their initial configurations following the disk phase. Of particular importance will be scattering events between planets of comparable masses, which will eject one of the planets that form in a system while increasing the remaining planet's orbital eccentricity, and also reducing its semi-

major axis. Results of formation (i.e. of massive gas giants) could also be important in post-disk dynamical assembly scenarios wherein leftover planetesimals grow via collisions, with eccentricities induced from the gravitational perturbation of the massive planet(s). Dynamical assembly could offer an additional means by which low-mass planets could form, for example at small orbital radii. In this regard, dynamical assembly may provide another means to fill out the short-period super Earth region of the M-a space for which our models do not produce many planets. Post-disk dynamical assembly is the standard approach taken for formation of Solar system terrestrial planets, with Jupiter stirring up the inner planetesimal disk to induce collisional growth (Raymond et al., 2014).

In this thesis, we have affirmed the link between the observed variability in protoplanetary disks and exoplanet populations seen on the mass - semimajor axis and mass radius diagrams. Protoplanetary disk properties, namely their masses, radii, lifetimes, and metallicities, have been shown to significantly affect planet formation timescales in the core accretion framework, thereby resulting in scatter on the M-a and M-R diagrams. Results of planet formation models such as the one considered and developed throughout this thesis provide valuable constraints on many current issues in planetary astrophysics. For example, results of formation during the disk phase supply the necessary initial conditions for post-disk evolution processes such as dynamics and atmospheric mass loss. We have also explored the link that planet formation provides between chemical abundances throughout disks and planets' acquired compositions. Considering planet formation's role in this regard will be tremendously useful for interpreting future observations that probe planets' atmospheric compositions with *JWST* (the James Webb Space Telescope). Lastly, the populations synthesis framework presented in this thesis can be readily applied to model formation of planets in different stellar-mass systems. This will be particularly relevant in the case of M-dwarf systems in order to compare with exoplanets that are revealed with *TESS*. The ongoing discovery of exoplanets will continue to improve our knowledge of their properties and occurrences, offering further insight to refine our understanding of their formation.

Bibliography

ALMA Partnership et al., 2015, ApJ, 808, L3

Aikawa Y., Herbst E., 1999, ApJ, 526, 314

Alessi M., Pudritz R. E., 2018, MNRAS, 478, 2599

Alessi M., Pudritz R. E., Cridland A. J., 2017, MNRAS, 464, 428

Alessi M., Pudritz R. E., Cridland A. J., 2020, MNRAS, 493, 1013

Ali-Dib M., 2017, MNRAS, 464, 4282

Ali-Dib M., Johansen A., Huang C. X., 2017, MNRAS, 469, 5016

Alibert Y., 2017, A&A, 606, A69

Alibert Y., Mordasini C., Benz W., 2004, A&A, 417, L25

Alibert Y., Mordasini C., Benz W., Winisdoerffer C., 2005, A&A, 434, 343

Alibert Y., et al., 2006, A&A, 455, L25

Alibert Y., Mordasini C., Benz W., 2011, A&A, 526, A63

Andrews S. M., Wilner D. J., Hughes A. M., Qi C., Dullemond C. P., 2010, ApJ, 723, 1241

Andrews S. M., et al., 2018, ApJ, 869, L41

Ansdell M., et al., 2016, ApJ, 828, 46

Ansdell M., et al., 2018, ApJ, 859, 21

Armitage P. J., 2010, Astrophysics of Planet Formation. Cambridge University Press

Armitage P. J., 2011, ARA&A, 49, 195

Asplund M., Grevesse N., Sauval A. J., Scott P., 2009, ARA&A, 47, 481

Avenhaus H., et al., 2018, ApJ, 863, 44

Bae J., Zhu Z., Hartmann L., 2016, ApJ, 819, 134

Bai X.-N., 2011, ApJ, 739, 50

Bai X.-N., 2016, ApJ, 821, 80

Bai X.-N., Stone J. M., 2011, ApJ, 736, 144

Bai X.-N., Stone J. M., 2013, ApJ, 769, 76

Bai X.-N., Ye J., Goodman J., Yuan F., 2016, ApJ, 818, 152

Baillié K., Charnoz S., Pantin E., 2015, A&A, 577, A65

Baillié K., Charnoz S., Pantin E., 2016, A&A, 590, A60

Balbus S. A., Hawley J. F., 1991, ApJ, 376, 214

Barclay T., Pepper J., Quintana E. V., 2018, ApJS, 239, 2

Barenfeld S. A., Carpenter J. M., Ricci L., Isella A., 2016, ApJ, 827, 142

Barenfeld S. A., Carpenter J. M., Sargent A. I., Isella A., Ricci L., 2017, ApJ, 851, 85

Bashi D., Helled R., Zucker S., Mordasini C., 2017, A&A, 604, A83

Batalha N. M., et al., 2013, ApJS, 204, 24

Bate M. R., 2018, MNRAS, 475, 5618

Batygin K., 2018, AJ, 155, 178

Benz W., 2000, Space Sci. Rev., 92, 279

Benz W., Ida S., Alibert Y., Lin D., Mordasini C., 2014, in Beuther H., Klessen R. S., Dullemond C. P., Henning T., eds, Protostars and Planets VI, p. 691

Birnstiel T., Dullemond C. P., Brauer F., 2009, A&A, 503, L5

Birnstiel T., Dullemond C. P., Brauer F., 2010a, A&A, 513, A79

Birnstiel T., et al., 2010b, A&A, 516, L14

Birnstiel T., Ormel C. W., Dullemond C. P., 2011, A&A, 525, A11

Birnstiel T., Klahr H., Ercolano B., 2012, A&A, 539, A148

Birnstiel T., et al., 2018, ApJ, 869, L45

Bitsch B., Battistini C., 2020, A&A, 633, A10

Bitsch B., Lambrechts M., Johansen A., 2015, A&A, 582, A112

Blaes O. M., Balbus S. A., 1994, ApJ, 421, 163

Blandford R. D., Payne D. G., 1982, MNRAS, 199, 883

Blum J., Wurm G., 2000, Icarus, 143, 138

Bond J. C., O'Brien D. P., Lauretta D. S., 2010, ApJ, 715, 1050

Borucki W. J., et al., 2011a, ApJ, 728, 117

Borucki W. J., et al., 2011b, ApJ, 736, 19

Boss A. P., 1997, Science, 276, 1836

Brauer F., Dullemond C. P., Henning T., 2008, A&A, 480, 859

Brewer J. M., Fischer D. A., 2016, ApJ, 831, 20

Brouwers M. G., Ormel C. W., 2020, A&A, 634, A15

Brouwers M. G., Vazan A., Ormel C. W., 2018, A&A, 611, A65

Bryan M. L., et al., 2016, ApJ, 821, 89

Burke C. J., et al., 2014, ApJS, 210, 19

Butler R. P., Marcy G. W., 1996, ApJ, 464, L153

Carter-Bond J. C., O'Brien D. P., Delgado Mena E., Israelian G., Santos N. C., González Hernández J. I., 2012, ApJ, 747, L2

Carter J. A., et al., 2012, Science, 337, 556

Casassus S., et al., 2015, ApJ, 812, 126

Cassan A., et al., 2012, Nature, 481, 167

Cazzoletti P., et al., 2018, A&A, 619, A161

Chabrier G., Mazevet S., Soubiran F., 2019, ApJ, 872, 51

Chambers J. E., 2009, ApJ, 705, 1206

Chambers J., 2010, in Seager, S., ed, Exoplanets, pp 297–317

Chambers J. E., 2014, Icarus, 233, 83

Chambers J., 2019, ApJ, 879, 98

Chatterjee S., Ford E. B., Matsumura S., Rasio F. A., 2008, ApJ, 686, 580

Chen J., Kipping D., 2017, ApJ, 834, 17

Chiang E. I., Goldreich P., 1997, ApJ, 490, 368

Chiang E., Laughlin G., 2013, MNRAS, 431, 3444

Choukroun M., Grasset O., 2007, The Journal of Chemical Physics, 127, 124506

Cieza L. A., et al., 2019, MNRAS, 482, 698

Clarke C. J., 2007, MNRAS, 376, 1350

Cleeves L. I., Adams F. C., Bergin E. A., 2013, ApJ, 772, 5

Cleeves L. I., Bergin E. A., Qi C., Adams F. C., Öberg K. I., 2015, ApJ, 799, 204

Coleman G. A. L., Nelson R. P., 2016a, MNRAS, 457, 2480

Coleman G. A. L., Nelson R. P., 2016b, MNRAS, 460, 2779

Cox E. G., et al., 2017, ApJ, 851, 83

Crida A., Morbidelli A., Masset F., 2006, Icarus, 181, 587

Cridland A. J., 2018, A&A, 619, A165

Cridland A. J., Pudritz R. E., Alessi M., 2016, MNRAS, 461, 3274

Cridland A. J., Pudritz R. E., Birnstiel T., 2017, MNRAS, 465, 3865

Cridland A. J., Pudritz R. E., Alessi M., 2019a, MNRAS, 484, 345

Cridland A. J., Eistrup C., van Dishoeck E. F., 2019b, A&A, 627, A127

Crossfield I. J. M., et al., 2016, ApJS, 226, 7

Cumming A., 2004, MNRAS, 354, 1165

Cumming A., Butler R. P., Marcy G. W., Vogt S. S., Wright J. T., Fischer D. A., 2008, PASP, 120, 531

D'Alessio P., Cantö J., Calvet N., Lizano S., 1998, ApJ, 500, 411

D'Alessio P., Calvet N., Hartmann L., Lizano S., Cantó J., 1999, ApJ, 527, 893

Dittkrist K.-M., Mordasini C., Klahr H., Alibert Y., Henning T., 2014, A&A, 567, A121

Dong R., Fung J., 2017, ApJ, 835, 146

Dong R., Zhu Z., Whitney B., 2015a, ApJ, 809, 93

Dong R., Zhu Z., Rafikov R. R., Stone J. M., 2015b, ApJ, 809, L5

Duffell P. C., 2015, ApJ, 807, L11

Dullemond C. P., Dominik C., 2005, A&A, 434, 971

Dullemond C. P., et al., 2018, ApJ, 869, L46

Eistrup C., Walsh C., van Dishoeck E. F., 2018, A&A, 613, A14

Elser S., Meyer M. R., Moore B., 2012, Icarus, 221, 859

Ercolano B., Clarke C. J., 2010, MNRAS, 402, 2735

Facchini S., Birnstiel T., Bruderer S., van Dishoeck E. F., 2017, A&A, 605, A16

Facchini S., et al., 2019, arXiv e-prints, p. arXiv:1905.09204

Favre C., Bergin E. A., Cleeves L. I., Hersant F., Qi C., Aikawa Y., 2015, ApJ, 802, L23

Fei Y., Murphy C., Shibazaki Y., Shahar A., Huang H., 2016, Geophysical Research Letters, 43, 6837

Fischer D. A., Valenti J., 2005, ApJ, 622, 1102

Fischer D. A., Marcy G. W., Spronck J. F. P., 2014, ApJS, 210, 5

Flaherty K. M., Hughes A. M., Teague R., Simon J. B., Andrews S. M., Wilner D. J., 2018, ApJ, 856, 117

Flock M., Turner N. J., Mulders G. D., Hasegawa Y., Nelson R. P., Bitsch B., 2019, A&A, 630, A147

Ford E. B., Rasio F. A., 2008, ApJ, 686, 621

Frank M. R., Fei Y., Hu J., 2004, Geochimica et Cosmochimica Acta, 68, 2781–2790

Frank A., et al., 2014, in Beuther H., Klessen R. S., Dullemond C. P., Henning T., eds, Protostars and Planets VI, pp 451–474

Freedman R. S., Marley M. S., Lodders K., 2008, ApJS, 174, 504

French M., Mattsson T. R., Nettelmann N., Redmer R., 2009, Phys. Rev. B, 79, 054107

Fulton B. J., et al., 2017, AJ, 154, 109

Fung J., Chiang E., 2016, ApJ, 832, 105

Fung J., Dong R., 2015, ApJ, 815, L21

Gammie C. F., 1996, ApJ, 457, 355

Gandolfi D., et al., 2018, A&A, 619, L10

Gillon M., et al., 2017, Nature, 542, 456

Ginzburg S., Schlichting H. E., Sari R., 2018, MNRAS, 476, 759

Glassgold A. E., Najita J., Igea J., 1997, ApJ, 480, 344

Goldreich P., Tremaine S., 1980, ApJ, 241, 425

Gorti U., Dullemond C. P., Hollenbach D., 2009, ApJ, 705, 1237

Gorti U., Hollenbach D., Dullemond C. P., 2015, ApJ, 804, 29

Gressel O., Pessah M. E., 2015, ApJ, 810, 59

Gressel O., Turner N. J., Nelson R. P., McNally C. P., 2015, ApJ, 801, 84

Gressel O., Ramsey J. P., Brinch C., Nelson R. P., Turner N. J., Bruderer S., 2020, ApJ, 896, 126

Guillot T., 2010, A&A, 520, A27

Gullbring E., Hartmann L., Briceño C., Calvet N., 1998, ApJ, 492, 323

Gupta A., Schlichting H. E., 2019, MNRAS, 487, 24

Gupta A., Schlichting H. E., 2020, MNRAS, 493, 792

Han E., Wang S. X., Wright J. T., Feng Y. K., Zhao M., Fakhouri O., Brown J. I., Hancock C., 2014, PASP, 126, 827

Hartmann L., Calvet N., Gullbring E., D'Alessio P., 1998, ApJ, 495, 385

Hasegawa Y., 2016, ApJ, 832, 83

Hasegawa Y., Pudritz R. E., 2010, ApJ, 710, L167

Hasegawa Y., Pudritz R. E., 2011, MNRAS, 417, 1236

Hasegawa Y., Pudritz R. E., 2012, ApJ, 760, 117

Hasegawa Y., Pudritz R. E., 2013, ApJ, 778, 78

Hasegawa Y., Pudritz R. E., 2014, ApJ, 794, 25

Hasegawa Y., Okuzumi S., Flock M., Turner N. J., 2017, ApJ, 845, 31

Hasegawa Y., Bryden G., Ikoma M., Vasisht G., Swain M., 2018, ApJ, 865, 32

Hasegawa Y., Hansen B. M. S., Vasisht G., 2019, ApJ, 876, L32

Haworth T. J., Clarke C. J., Owen J. E., 2016, MNRAS, 457, 1905

Hellary P., Nelson R. P., 2012, MNRAS, 419, 2737

Hendler N. P., et al., 2017, ApJ, 841, 116

Hennebelle P., Commerçon B., Chabrier G., Marchand P., 2016, ApJ, 830, L8

Hernández J., et al., 2007, ApJ, 662, 1067

Howard A. W., et al., 2012, ApJS, 201, 15

Huang C. X., et al., 2018a, ApJ, 868, L39

Huang J., et al., 2018b, ApJ, 869, L42

Hueso R., Guillot T., 2005, A&A, 442, 703

Hughes A. M., Duchêne G., Matthews B. C., 2018, ARA&A, 56, 541

Ida S., Lin D. N. C., 2004a, ApJ, 604, 388

Ida S., Lin D. N. C., 2004b, ApJ, 616, 567

Ida S., Lin D. N. C., 2005, ApJ, 626, 1045

Ida S., Lin D. N. C., 2008, ApJ, 673, 487

Ida S., Lin D. N. C., Nagasawa M., 2013, ApJ, 775, 42

Ikoma M., Nakazawa K., Emori H., 2000, ApJ, 537, 1013

Isella A., Carpenter J. M., Sargent A. I., 2009, ApJ, 701, 260

Ivanov P. B., Papaloizou J. C. B., Polnarev A. G., 1999, MNRAS, 307, 79

Izidoro A., Raymond S. N., 2018, Formation of Terrestrial Planets. Springer-Verlag, p. 142, doi:10.1007/978-3-319-55333-7_142

Jackson A. P., Davis T. A., Wheatley P. J., 2012, Monthly Notices of the Royal Astronomical Society, 422, 2024

Jang-Condell H., Turner N. J., 2012, ApJ, 749, 153

Jin S., Mordasini C., 2018, The Astrophysical Journal, 853, 163

Jin S., Mordasini C., Parmentier V., van Boekel R., Henning T., Ji J., 2014, ApJ, 795, 65

Johansen A., Oishi J. S., Mac Low M.-M., Klahr H., Henning T., Youdin A., 2007, Nature, 448, 1022

Johnson J. A., et al., 2017, AJ, 154, 108

Kenyon S. J., Hartmann L., 1987, ApJ, 323, 714

Keppler M., et al., 2018, A&A, 617, A44

Kimmig C. N., Dullemond C. P., Kley W., 2019, arXiv e-prints, p. arXiv:1910.12889

Kley W., 1999, MNRAS, 303, 696

Kley W., Nelson R. P., 2012, ARA&A, 50, 211

Koch D. G., et al., 2010, ApJ, 713, L79

Kokubo E., Ida S., 2002, ApJ, 581, 666

Komabayashi T., Hirose K., Sugimura E., Sata N., Ohishi Y., Dubrovinsky L. S., 2008, Earth and Planetary Science Letters, 265, 515–524

Kopparapu R. K., Ramirez R. M., SchottelKotte J., Kasting J. F., Domagal-Goldman S., Eymet V., 2014, ApJ, 787, L29

Kratter K., Lodato G., 2016, ARA&A, 54, 271

Lambrechts M., Johansen A., 2012, A&A, 544, A32

Lambrechts M., Lega E., Nelson R. P., Crida A., Morbidelli A., 2019, arXiv e-prints, p. arXiv:1907.06362

Lecar M., Podolak M., Sasselov D., Chiang E., 2006, ApJ, 640, 1115

Lee E. J., 2019, arXiv e-prints, p. arXiv:1904.10470

Lesur G., Kunz M. W., Fromang S., 2014, A&A, 566, A56

Levison H. F., Kretke K. A., Duncan M. J., 2015, Nature, 524, 322

Li Z.-Y., Banerjee R., Pudritz R. E., Jørgensen J. K., Shang H., Krasnopolsky R., Maury A., 2014, in Beuther H., Klessen R. S., Dullemond C. P., Henning T., eds, Protostars and Planets VI, pp 173–194

Lin D. N. C., Papaloizou J. C. B., 1993, in Levy E. H., Lunine J. I., eds, Protostars and Planets III. pp 749–835

Lissauer J. J., Hubickyj O., D'Angelo G., Bodenheimer P., 2009, Icarus, 199, 338

Livingston J. H., et al., 2018a, AJ, 156, 78

Livingston J. H., et al., 2018b, AJ, 156, 277

Long F., et al., 2018, ApJ, 869, 17

Long F., et al., 2019, ApJ, 882, 49

Lopez E. D., Fortney J. J., 2013, ApJ, 776, 2

Lovis C., Fischer D., 2010, in Seager, S., ed, Exoplanets, pp 27–53

Lubow S. H., D'Angelo G., 2006, ApJ, 641, 526

Lubow S. H., Seibert M., Artymowicz P., 1999, ApJ, 526, 1001

Lynden-Bell D., Pringle J. E., 1974, MNRAS, 168, 603

Lyra W., Paardekooper S.-J., Mac Low M.-M., 2010, ApJ, 715, L68

Machida M. N., Kokubo E., Inutsuka S.-I., Matsumoto T., 2010, MNRAS, 405, 1227

Madhusudhan N., Amin M. A., Kennedy G. M., 2014, ApJ, 794, L12

Marcy G. W., Butler R. P., 1996, ApJ, 464, L147

Masset F. S., 2001, ApJ, 558, 453

Masset F. S., 2002, A&A, 387, 605

Masset F. S., Morbidelli A., Crida A., Ferreira J., 2006a, ApJ, 642, 478

Masset F. S., D'Angelo G., Kley W., 2006b, ApJ, 652, 730

Masson J., Chabrier G., Hennebelle P., Vaytet N., Commerçon B., 2016, A&A, 587, A32

Matsumura S., Pudritz R. E., 2003, ApJ, 598, 645

Matsumura S., Pudritz R. E., 2006, MNRAS, 365, 572

Matsumura S., Pudritz R. E., Thommes E. W., 2007, ApJ, 660, 1609

Matt S., Pudritz R. E., 2005, ApJ, 632, L135

Mayor M., Queloz D., 1995, Nature, 378, 355

Mayor M., et al., 2011, preprint, (arXiv:1109.2497)

McNally C. P., Nelson R. P., Paardekooper S.-J., Gressel O., Lyra W., 2017, MNRAS, 472, 1565

McNally C. P., Nelson R. P., Paardekooper S.-J., 2018, MNRAS, 477, 4596

McNally C. P., Nelson R. P., Paardekooper S.-J., Benítez-Llambay P., Gressel O., 2020, MNRAS, 493, 4382

Mellon R. R., Li Z.-Y., 2009, ApJ, 698, 922

Meru F., Bate M. R., 2010, MNRAS, 406, 2279

Molaverdikhani K., Henning T., Mollière P., 2019, ApJ, 873, 32

Mollière P., van Boekel R., Dullemond C., Henning T., Mordasini C., 2015, ApJ, 813, 47

Morbidelli A., Szulágyi J., Crida A., Lega E., Bitsch B., Tanigawa T., Kanagawa K., 2014, Icarus, 232, 266

Mordasini C., 2014, A&A, 572, A118

Mordasini C., 2020, A&A, 638, A52

Mordasini C., Alibert Y., Benz W., 2009a, A&A, 501, 1139

Mordasini C., Alibert Y., Benz W., Naef D., 2009b, A&A, 501, 1161

Mordasini C., Alibert Y., Benz W., Klahr H., Henning T., 2012a, A&A, 541, A97

Mordasini C., Alibert Y., Klahr H., Henning T., 2012b, A&A, 547, A111

Mordasini C., Alibert Y., Georgy C., Dittkrist K.-M., Klahr H., Henning T., 2012c, A&A, 547, A112

Mordasini C., Klahr H., Alibert Y., Miller N., Henning T., 2014, A&A, 566, A141

Mordasini C., Mollière P., Dittkrist K.-M., Jin S., Alibert Y., 2015, International Journal of Astrobiology, 14, 201

Mordasini C., van Boekel R., Mollière P., Henning T., Benneke B., 2016, ApJ, 832, 41

Mori S., Bai X.-N., Okuzumi S., 2019, ApJ, 872, 98

Moriarty J., Madhusudhan N., Fischer D., 2014, ApJ, 787, 81

Morton T. D., Bryson S. T., Coughlin J. L., Rowe J. F., Ravichandran G., Petigura E. A., Haas M. R., Batalha N. M., 2016, ApJ, 822, 86

Murray-Clay R. A., Chiang E. I., Murray N., 2009, The Astrophysical Journal, 693, 23–42

Nakatani R., Hosokawa T., Yoshida N., Nomura H., Kuiper R., 2017, preprint, (arXiv:1706.04570)

Ndugu N., Bitsch B., Jurua E., 2018, MNRAS, 474, 886

Nordström B., et al., 2004, A&A, 418, 989

Öberg K. I., Boogert A. C. A., Pontoppidan K. M., van den Broek S., van Dishoeck E. F., Bottinelli S., Blake G. A., Evans II N. J., 2011, ApJ, 740, 109

Ogihara M., Morbidelli A., Guillot T., 2015, A&A, 584, L1

Ogihara M., Kokubo E., Suzuki T. K., Morbidelli A., 2018, A&A, 615, A63

Oppenheimer M., Dalgarno A., 1974, ApJ, 192, 29

Ormel C. W., 2014, ApJ, 789, L18

Ormel C. W., Cuzzi J. N., 2007, A&A, 466, 413

Ormel C. W., Paszun D., Dominik C., Tielens A. G. G. M., 2009, A&A, 502, 845

Ormel C. W., Shi J.-M., Kuiper R., 2015, MNRAS, 447, 3512

Owen J. E., Jackson A. P., 2012, Monthly Notices of the Royal Astronomical Society, 425, 2931

Owen J. E., Wu Y., 2013, ApJ, 775, 105

Owen J. E., Wu Y., 2017, ApJ, 847, 29

Owen J. E., Ercolano B., Clarke C. J., Alexander R. D., 2010, MNRAS, 401, 1415

Owen J. E., Ercolano B., Clarke C. J., 2011, MNRAS, 412, 13

Paardekooper S. J., Baruteau C., Crida A., Kley W., 2010, MNRAS, 401, 1950

Paardekooper S.-J., Baruteau C., Kley W., 2011, MNRAS, 410, 293

Pascucci I., Sterzik M., 2009, ApJ, 702, 724

Pasek M. A., Milsom J. A., Ciesla F. J., Lauretta D. S., Sharp C. M., Lunine J. I., 2005, Icarus, 175, 1

Paszun D., Dominik C., 2009, A&A, 507, 1023

Petigura E. A., et al., 2017, AJ, 154, 107

Petigura E. A., et al., 2018, AJ, 155, 89

Pignatale F. C., Maddison S. T., Taquet V., Brooks G., Liffman K., 2011, MNRAS, 414, 2386

Pinilla P., Birnstiel T., Ricci L., Dullemond C. P., Uribe A. L., Testi L., Natta A., 2012a, A&A, 538, A114

Pinilla P., Benisty M., Birnstiel T., 2012b, A&A, 545, A81

Pinte C., Dent W. R. F., Ménard F., Hales A., Hill T., Cortes P., de Gregorio-Monsalvo I., 2016, ApJ, 816, 25

Piso A.-M. A., Youdin A. N., 2014, ApJ, 786, 21

Pollack J. B., Hubickyj O., Bodenheimer P., Lissauer J. J., Podolak M., Greenzweig Y., 1996, Icarus, 124, 62

Pontoppidan K. M., Salyk C., Bergin E. A., Brittain S., Marty B., Mousis O., Öberg K. I., 2014, Protostars and Planets VI, pp 363–385

Pringle J. E., 1981, ARA&A, 19, 137

Pudritz R. E., Norman C. A., 1986, ApJ, 301, 571

Pudritz R. E., Ray T. P., 2019, Frontiers in Astronomy and Space Sciences, 6, 54

Qi C., D'Alessio P., Öberg K. I., Wilner D. J., Hughes A. M., Andrews S. M., Ayala S., 2011, ApJ, 740, 84

Qi C., et al., 2013, Science, 341, 630

Queloz D., et al., 2000, A&A, 354, 99

Raymond S., Kokubo E., Morbidelli A., Morishima R., Walsh K., 2014, in Beuther H., Klessen R. S., Dullemond C. P., Henning T., eds, Protostars and Planets VI, p. 595

Rémy-Ruyer A., et al., 2014, A&A, 563, A31

Ribas I., Guinan E. F., Güdel M., Audard M., 2005, ApJ, 622, 680

Ribas Á., Merín B., Bouy H., Maud L. T., 2014, A&A, 561, A54

Rodenkirch P. J., Klahr H., Fendt C., Dullemond C. P., 2020, A&A, 633, A21

Rogers L. A., 2015, ApJ, 801, 41

Rogers L. A., Bodenheimer P., Lissauer J. J., Seager S., 2011, ApJ, 738, 59

Rosotti G. P., Teague R., Dullemond C., Booth R. A., Clarke C. J., 2020, MNRAS, 495, 173

Rowe J. F., et al., 2014, ApJ, 784, 45

Ruden S. P., Pollack J. B., 1991, ApJ, 375, 740

Sándor Z., Lyra W., Dullemond C. P., 2011, ApJ, 728, L9

Sano T., Miyama S. M., Umebayashi T., Nakano T., 2000, ApJ, 543, 486

Santerne A., et al., 2016, A&A, 587, A64

Santos N. C., Israelian G., Mayor M., Rebolo R., Udry S., 2003, A&A, 398, 363

Santos N. C., et al., 2017, A&A, 608, A94

Schäfer U., Yang C.-C., Johansen A., 2017, A&A, 597, A69

Schlichting H. E., Sari R., Yalinewich A., 2015, Icarus, 247, 81

Schwarz K. R., Bergin E. A., Cleeves L. I., Blake G. A., Zhang K., Öberg K. I., van Dishoeck E. F., Qi C., 2016, ApJ, 823, 91

Seager S., Kuchner M., Hier-Majumder C. A., Militzer B., 2007, The Astrophysical Journal, 669, 1279

Seifried D., Banerjee R., Pudritz R. E., Klessen R. S., 2012, MNRAS, 423, L40

Shadmehri M., Ghoreyshi S. M., 2019, MNRAS, 488, 4623

Shakura N. I., Sunyaev R. A., 1973, A&A, 24, 337

Siess L., Dufour E., Forestini M., 2000, A&A, 358, 593

Simon J. B., Bai X.-N., Stone J. M., Armitage P. J., Beckwith K., 2013, ApJ, 764, 66

Simon J. B., Armitage P. J., Li R., Youdin A. N., 2016, ApJ, 822, 55

Stepinski T. F., 1998, Icarus, 132, 100

Suárez-Andrés L., Israelian G., González Hernández J. I., Adibekyan V. Z., Delgado Mena E., Santos N. C., Sousa S. G., 2018, A&A, 614, A84

Suzuki T. K., Muto T., Inutsuka S.-i., 2010, ApJ, 718, 1289

Suzuki T. K., Ogihara M., Morbidelli A. r., Crida A., Guillot T., 2016, A&A, 596, A74

Tanaka H., Takeuchi T., Ward W. R., 2002, ApJ, 565, 1257

Tanigawa T., Tanaka H., 2016, ApJ, 823, 48

Tazzari M., et al., 2017, A&A, 606, A88

Terebey S., Shu F. H., Cassen P., 1984, ApJ, 286, 529

Testi L., et al., 2014, Protostars and Planets VI, pp 339–361

Thiabaud A., Marboeuf U., Alibert Y., Leya I., Mezger K., 2015, A&A, 574, A138

Thomas S. W., Madhusudhan N., 2016, MNRAS, 458, 1330

Tomida K., Okuzumi S., Machida M. N., 2015, ApJ, 801, 117

Toppani A., Libourel G., Robert F., Ghanbaja J., 2006, Geochimica Cosmochimica Acta, 70, 5035

Trapman L., Facchini S., Hogerheijde M. R., van Dishoeck E. F., Bruderer S., 2019, arXiv e-prints, p. arXiv:1903.06190

Tripathi A., Andrews S. M., Birnstiel T., Wilner D. J., 2017, ApJ, 845, 44

Turner N. J., Sano T., Dziourkevitch N., 2007, ApJ, 659, 729

Ubeira-Gabellini M. G., Christiaens V., Lodato G., Ancker M. v. d., Fedele D., Manara C. F., Price D. J., 2020, ApJ, 890, L8

Udry S., et al., 2000, A&A, 356, 590

Umebayashi T., Nakano T., 1981, PASJ, 33, 617

Valencia D., O'Connell R. J., Sasselov D., 2006, Icarus, 181, 545

Valencia D., Sasselov D. D., O'Connell R. J., 2007, ApJ, 665, 1413

Valenti J. A., Fischer D. A., 2008, Physica Scripta Volume T, 130, 014003

Vanderspek R., et al., 2019, ApJ, 871, L24

Venturini J., Alibert Y., Benz W., 2016, A&A, 596, A90

Visser R., van Dishoeck E. F., Doty S. D., Dullemond C. P., 2009, A&A, 495, 881

Wada K., Tanaka H., Suyama T., Kimura H., Yamamoto T., 2009, ApJ, 702, 1490

Walsh C., Millar T. J., Nomura H., 2010, ApJ, 722, 1607

Walsh K. J., Morbidelli A., Raymond S. N., O'Brien D. P., Mandell A. M., 2011, Nature, 475, 206

Wang J., Fischer D. A., 2015, AJ, 149, 14

Ward W. R., 1997, Icarus, 126, 261

Watson D. M., et al., 2016, ApJ, 828, 52

Weber M. L., Ercolano B., Picogna G., Hartmann L., Rodenkirch P. J., 2020, arXiv e-prints, p. arXiv:2005.14312

Weidenschilling S. J., 1977a, Ap&SS, 51, 153

Weidenschilling S. J., 1977b, MNRAS, 180, 57

Winn J. N., Fabrycky D. C., 2015, ARA&A, 53, 409

Woitke P., Kamp I., Thi W. F., 2009, A&A, 501, 383

Woodall J., Agúndez M., Markwick-Kemper A. J., Millar T. J., 2007, A&A, 466, 1197

Yen H.-W., Liu H. B., Gu P.-G., Hirano N., Lee C.-F., Puspitaningrum E., Takakuwa S., 2016, ApJ, 820, L25

Yen H.-W., Gu P.-G., Hirano N., Koch P. M., Lee C.-F., Liu H. B., Takakuwa S., 2019, ApJ, 880, 69

Youdin A. N., Goodman J., 2005, ApJ, 620, 459

Zeng L., Sasselov D., 2013, PASP, 125, 227

Zhang K., Blake G. A., Bergin E. A., 2015, ApJ, 806, L7

Zhu Z., et al., 2019, ApJ, 877, L18

van Boekel R., et al., 2017, ApJ, 837, 132

van der Marel N., Pinilla P., Tobin J., van Kempen T., Andrews S., Ricci L., Birnstiel T., 2015, ApJ, 810, L7

van der Marel N., Dong R., di Francesco J., Williams J. P., Tobin J., 2019, ApJ, 872, 112